

UPO

UNIVERSITÀ DEL PIEMONTE ORIENTALE

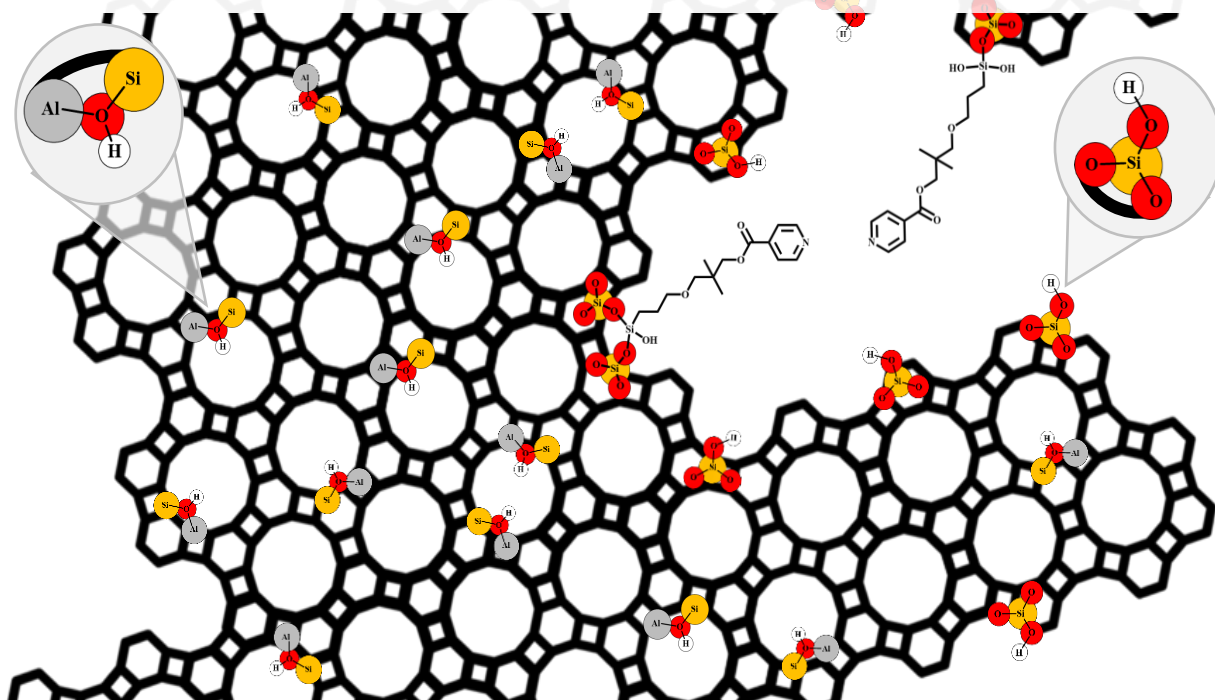
DIPARTIMENTO DI SCIENZE
E INNOVAZIONE TECNOLOGICA

Ph.D. Program in “Chemistry & Biology”

Cycle XXXIII, a.y. 2017-2020

SSD: CHIM/02

HIERARCHICAL POROUS HYBRID CATALYSTS: SYNTHESIS AND PHYSICO-CHEMICAL CHARACTERIZATION



Chiara Ivaldi

Supervisors: Prof. Enrica Gianotti and Dr. Ivana Miletto

Ph.D. Program Coordinator: Prof. Gian Cesare Tron



UNIVERSITÀ DEL PIEMONTE ORIENTALE

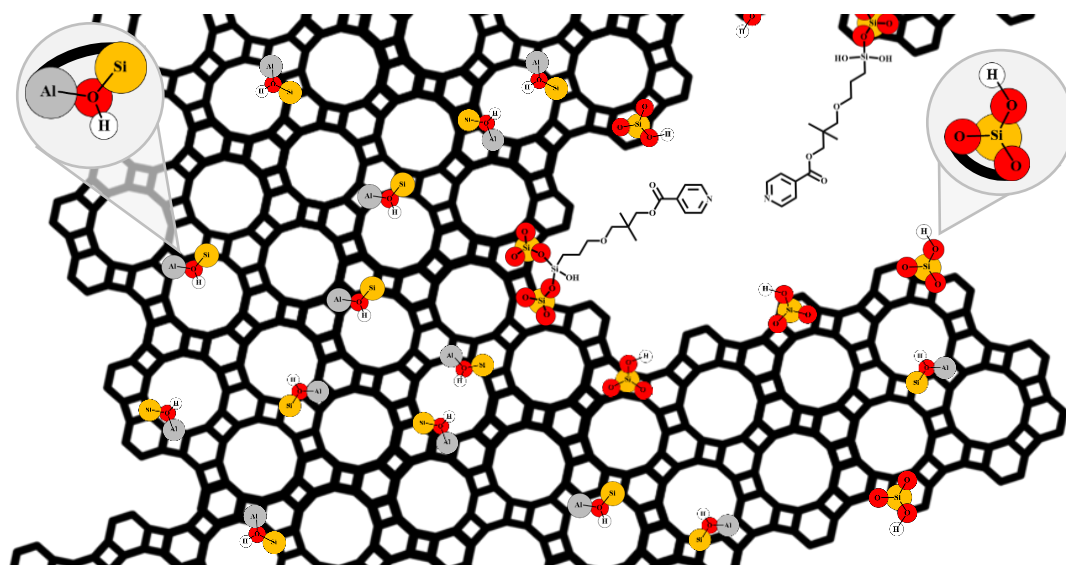
DIPARTIMENTO DI SCIENZE
E INNOVAZIONE TECNOLOGICA

Ph.D. Program in “Chemistry & Biology”

Cycle XXXIII, a.y. 2017-2020

SSD: CHIM/02

HIERARCHICAL POROUS HYBRID CATALYSTS: SYNTHESIS AND PHYSICO-CHEMICAL CHARACTERIZATION



Chiara Ivaldi

Chiara Ivaldi

Supervisors: Prof. Enrica Gianotti and Dr. Ivana Miletto

E. Gianotti

I. Miletto

Ph.D. Program Coordinator: Prof. Gian Cesare Tron



The Ph.D. project has received funding from the European Union's Horizon 2020 research and innovation program under grant agreement N. 720783—
MULTI2HYCAT.

Table of Contents

<i>Title Page</i>	I
<i>Acknowledgements to MULTI2HYCAT</i>	III
<i>Table of Contents</i>	V
<i>List of Abbreviations</i>	XI

Chapter 1 **01**

Introduction to hybrid materials

1.1	General concept	01
1.2	Organic-inorganic hybrid materials	02
1.3	Active sites of inorganic matrices	05
1.4	Synthetic pathways to obtain hybrid materials	08
1.5	Hierarchical porous hybrid materials	12
1.6	Notes and references	20

Chapter 2 **25**

Outline

Chapter 3 **29**

Sustainable saccharide templates to drive the synthesis of hierarchical silicoaluminophosphate SAPO-34 with tailored acid sites

3.1	Experimental section	30
3.1.1	General	30
3.1.2	Synthesis of SAPO-34	30
3.1.3	Characterization	32

3.1.4	Catalysis	32
3.2	Results and discussion	32
3.2.1	Morphological, structural and textural characterization	32
3.2.2	Spectroscopic characterization	37
3.2.3	Catalysis	43
3.3	Conclusions	44
3.4	Notes and references	45

Chapter 4 **49**

Hierarchical silicoaluminophosphate SAPO-34 architectures with tunable acid properties synthesised from mesoporous silica scaffolds

4.1	Experimental section	51
4.1.1	General	51
4.1.2	Synthesis of SAPO-34	52
4.1.3	Characterization	53
4.1.4	Catalysis	53
4.2	Results and Discussion	54
4.2.1	Synthesis	54
4.2.2	Morphological, structural and textural characterization	54
4.2.3	Spectroscopic characterization	58
4.2.4	Catalysis	68
4.3	Conclusions	70
4.4	Notes and references	71

Chapter 5 **75**

Hierarchical silicoaluminophosphate SAPO-5 architectures with tailored acid properties obtained from mesoporous silica scaffolds

5.1	Hierarchical SAPO-5 from mesoporous MCM-41 with variable silicon loading	76
5.1.1	Experimental section	77
5.1.1.1	General	77
5.1.1.2	Synthesis of SAPO-5	78
5.1.1.3	Characterization	79

5.1.1.4	Catalysis	79
5.1.2	Results and discussion	80
5.1.2.1	Structural and textural characterization	80
5.1.2.2	Spectroscopic characterization	83
5.1.2.3	Catalysis	92
5.1.3	Conclusions	93
5.2	Hierarchical SAPO-5 with tuned mesopore size	95
5.2.1	Experimental section	96
5.2.1.1	General	96
5.2.1.2	Synthesis	96
5.2.1.3	Characterization	97
5.2.2	Results and discussion	97
5.2.2.1	Structural and textural characterization	97
5.2.2.2	Spectroscopic characterization	99
5.2.3	Conclusions	102
5.3	Hierarchical SAPO-5 from mesoporous SBA-15 scaffold	103
5.3.1	Experimental section	103
5.3.1.1	General	103
5.3.1.2	Synthesis	103
5.3.1.3	Characterization	104
5.3.2	Results and discussion	105
5.3.2.1	Structural and textural characterization	105
5.3.2.2	Spectroscopic characterization	106
5.3.3	Conclusions	108
5.4	Notes and references	109

Chapter 6 **113**

Hybrid catalysts based on N-heterocyclic carbene

6.1	Experimental section	115
6.1.1	General	115
6.1.2	Synthesis of inorganic supports	115
6.1.3	Synthesis of N-heterocyclic carbene	116
6.1.4	Synthesis of hybrid catalysts	118
6.1.5	Characterization	118
6.1.6	Catalysis	119

6.2	Results and discussion	119
6.2.1	Materials	119
6.2.2	Characterization of NHC-Davisil silica	120
6.2.3	Characterization of NHC-MCM-41 and NHC-MCM-41-NPs	125
6.2.4	Characterization of NHC-HP-ZSM-5 and NHC-HP-SAPO-5	129
6.2.5	Catalysis	140
6.2.6	Unravelling the inferior catalytic performance of NHC-HP-SAPO-5 catalyst	142
6.3	Conclusions	147
6.4	Notes and references	148

Chapter 7 **153**

Influence of silicodactyly and silicopodality in the design of hybrid materials

7.1	Influence of silicodactyly	156
7.1.1	Experimental section	156
7.1.1.1	General	156
7.1.1.2	(3-Mercaptopropyl)methoxydimethylsilane synthesis	156
7.1.1.3	Synthesis of hybrid materials	157
7.1.1.4	Characterization	157
7.1.1.5	Computational details	157
7.1.2	Results and discussion	159
7.1.2.1	Hybrid structures	159
7.1.2.2	XRD and TGA analyses	160
7.1.2.3	FT-IR spectroscopy	162
7.1.2.5	Solid state NMR spectroscopy	165
7.1.2.5	Computational modeling	169
7.1.3	Conclusions on silicodactyly	172
7.2	Influence of silicopodality	174
7.2.1	Experimental section	175
7.2.1.1	General	175
7.2.1.2	Synthesis of multipodal pyridine derivatives	175
7.2.1.3	Synthesis of hybrid materials	176
7.2.1.4	Characterization	176
7.2.1.5	Computational details	176
7.2.2	Result and discussion	178

7.2.2.1	Hybrid structures	178
7.2.2.2	XRD and TGA analyses	178
7.2.2.3	FT-IR spectroscopy	180
7.2.2.4	Solid state NMR spectroscopy	186
7.2.2.5	Computational modeling	191
7.2.3	Conclusion on silicopodality	193
7.3	Notes and references	194

Chapter 8 **197**

Conclusions and perspectives

Chapter 9 **205**

Experimental section

List of Publications **211**

Acknowledgements **213**

Anti-plagiarism declaration **215**

List of Abbreviations

Frequently used materials and related

2,4,6-TMP: 2,4,6-trimethylpyridine

2,6-dTBP: 2,6-di-*tert*-butylpyridine

AlPO-*n*: aluminophosphate-*n*

BAS: Brønsted acid sites

CTAB: cetyl trimethylammonium bromide

HP-: hierarchically porous

LAS: Lewis acid sites

MCM-*n*: Mobil catalytic material-*n*

Micro: microporous

NHC: N-heterocyclic carbene

PMO: periodic mesoporous organic

Py: pyridine

SAPO-*n*: silicoaluminophosphate-*n*

SBA-*n*: Santa Barbara Amorphous-*n*

SDA: structure directing agent

ZSM-*n*: zeolite Socony Mobil-*n*

Frequently used experimental techniques and related

AF: accessibility factor

CP MAS NMR: cross polarization magic angle spinning nuclear magnetic resonance

FT-IR: Fourier-transform infrared spectroscopy

ICP-AES: inductively coupled plasma optical emission spectrometry

MD: molecular dynamics

NLDFT: non-localized density functional theory

SEM: scanning electron microscopy

SS NMR: solid state nuclear magnetic resonance

TGA/DTG: thermogravimetric analysis and derivative

VT FT-IR: variable temperature Fourier-transform infrared spectroscopy

XRDP: X-ray powder diffraction

1

Introduction to hybrid materials

In this chapter, a general introduction to hybrid catalysts has been given, focusing the attention on organic-inorganic Class II hybrid materials. The catalytic active centres characteristic of the inorganic supports used to obtain the hybrids, have then been described. Subsequently, the different synthetic methodologies adopted to prepare hybrid catalysts has been reported, with a view of emphasizing their advantages and drawbacks. Lastly, the potential of hierarchical porous hybrid materials as heterogeneous catalysts to perform tandem and cascade reactions has been deeply investigated.

1.1 General concept

From a conceptual point of view, hybrid materials are made up of a suitable combination of two or more structural builders. If the connection between these counterparts occur at a nanometric scale, besides preserving the intrinsic characteristic of each individual component, the resulting material will exhibit additional properties related to the synergy created by the presence of a very large hybrid interface.^[1,2] Historically, clay-based hybrids were the first hybrid materials spontaneously formed in nature, playing a crucial role in the abiogenesis process of the origin of life.^[3-5] As instance, due to their capacity of adsorb and concentrate prebiotic organic components from hypothetical primordial soup, clay-based materials promoted the synthesis of proteins from amino-acids and RNA long-chain nucleic acids from nucleotide bases.^[6-7] One of the most well-known examples of nanostructured hybrids is the Blue Maya pigment used by the ancient Pre-Columbian civilization, obtained by encapsulation of the indigo natural dye into a lamellar clay similar to palygorskite.^[8] Moreover, nature offers different examples of hybrid materials formed after soft biomineralization synthetic routes, such as the nacre

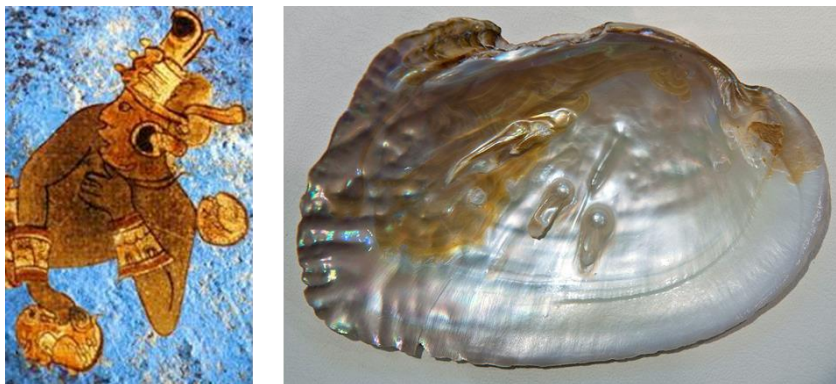


Figure 1.1. Examples of famous hybrid materials: blue Maya natural pigment (left) and nacre as crystallized compacted lamellar structure (right).^[1]

obtained from hexagonal plate layer of crystallized calcium carbonate (aragonite), which are connected at a nanometric scale through elastic biopolymers (conchiolin) (Figure 1.1).^[1]

Owing to the possibility of tuning their physico-chemical properties, hybrid materials have attracted a great deal of attention over the years in both the academic and industrial worlds.^[9-11] Indeed, several complementary structural builders, such as inorganic, organic, metallic or polymeric components, can be integrated into the resulting solid architecture and successfully employed in a large variety of applications, *i.e.* catalysis, adsorption or separation, microelectronics, sensing, magnetism, photochemistry, photoluminescence, fuel-cell processes and semiconductings.^[10,12] Overall, two main classifications and organizations of the hierarchy of hybrid materials can be distinguished: organic-molecules modified inorganic materials (organics-inorganic) and, *vice-versa*, inorganic-modified organic matrices (inorganic-organic).^[13] Within the framework of this Ph.D. thesis, attention will be focuses on inorganic materials modified by organic molecules.

1.2 Organic-inorganic hybrid materials

Organic-inorganic hybrids represent a class of heterogeneous materials which combine the advantages of both type of individual builders, resulting in solids with

high mechanical, structural and thermal stability, together with the flexibility and functional variety of organic compounds and polymers. This fact paves the way for designing materials containing different active sites within the framework, resulting in multi-functional catalysts with physico-chemical properties and reactivities unknown up to now.^[14] In addition, the possibility of tuning specific properties (*i.e.* hydrophilic/hydrophobic behaviour), is critical to prevent interfacial problems usually detected during catalytic processes. Specifically, the hydrophilic/hydrophobic properties of hybrid materials could be decisive to control adsorption-desorption phenomena occurring during the reaction processes, related to the concentration gradients of reagents and products.

Different synthetic strategies can be used to prepare hybrid materials, starting from simple procedures, such as physical mixtures or blends of different counterparts, up to more attractive methodologies, which allow to obtain hybrid composites, formed by different structural builders effectively combined at a nanometric scale.^[15] This latter synthetic pathway ensures homogeneous distribution of organic and inorganic sub-domains within the solid network, thus preventing phase separation. Since the organic-inorganic interface plays a crucial role in modulating the physico-chemical properties, hybrid materials have been classified by Sánchez and Ribot into two main families depending of the type of interactions existing between organic and inorganic individual builders.^[10] Class I includes hybrid systems consisting of simple organic molecule or oligomers embedded into a variety of porous inorganic matrices, usually obtained *via* soft sol-gel and self-assembling micellar processes.^[9] Nevertheless, the weak interactions (van der Waal, hydrogen bonds or electrostatic bonds) existing between the organic and inorganic interface typically lead to phase segregation, thereby limiting their further development. With the aim of obtaining more robust and stable functional solids, based on strong covalent or chemical bonds between the organic and inorganic building units, novel synthetic methodologies to design Class II hybrid have been explored.^[16,17] Indeed, the Class II hybrid favour the perfect integration of the active

organic functions at nanometric scale and their stabilization into the framework, as the organic moieties become structural components of the solids, preventing pores blockage.^[18] Moreover, the reactivity of catalytic active sites can be transferred from the cavities to the walls of heterogeneous catalyst, thus allowing to fully exploit the porosity of the materials during the catalysis.^[19]

To synthesise Class II hybrid, specific organic-inorganic precursors, containing covalently bonded organic and inorganic fragments, can be employed. This precursor can be prepared during one-pot synthesis^[20] or can be obtained by functionalizing monosilanes ((R'O)₃SiR) or bridged ((R'O)₃SiRSi(OR')₃) silsesquioxanes, to obtain *organosiliceous hybrids*.^[21,22]

A large variety of organic fragments have been incorporated for structural control and functionalization of hybrid materials, ranging from bridge-type organic moieties to sophisticated metallic complexes.^[23,24] However, the number of catalytic applications of hybrid materials, containing different structural active functionalities, have been to date certainly scarce, mainly as a result of the random distribution of active sites in the hybrid catalyst developed up to now. The non-homogeneous location of the active centres might result in a lower conversion and selectivity in chemical processes wherein structural building functions have to work in collaborative way (consecutive or cascade reactions), or in the deactivation of the hybrid catalyst due to mutual neutralization or agglomeration of the active sites.^[25] Similarly, diffusion and mass-transport limitations hinder access of reactants to the active centres, leading to decreased turnover and catalysts deactivation, as well as pore blockage. These drawbacks could be overcome by designing suitable specific organosilane monomer precursors with different functions in the same structural fragment, separated at controllable molecular distance to guarantee the reactivity of the active sites during the catalytic processes.^[26] Alternatively, creating hierarchical architectures within tunable porosity significantly enhances molecular diffusion, prolonging catalyst lifetime. However, more sustainable chemical processes, avoiding the isolation and purification of intermediate products and solvent removal,

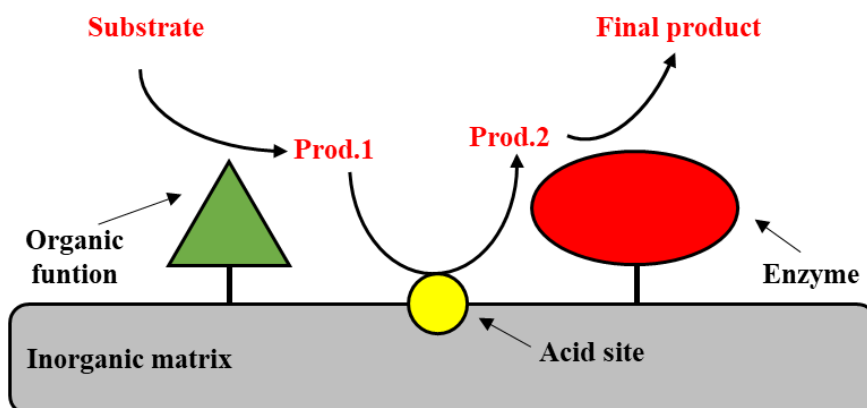


Figure 1.2. Example of multi-functional hybrid catalyst for cascade reactions.^[12]

can be developed by using a single catalyst containing all the necessary active sites into a single framework to catalyse the individual steps of cascade reactions (Figure 1.2). In this perspective, in the following sections a brief description of the active sites characteristic of the inorganic supports will be given. Subsequently, the synthetic methodologies commonly performed to obtain hybrid catalyst and the main types of hybrid solids which can be synthesised through these synthetic pathways will be described. Then, the relevance of hierarchical porous hybrid materials, one of the main focus of this Ph.D. research work, will be investigated.

1.3 Active sites of inorganic matrices

In the present paragraph, the plethora of active sites associated to inorganic supports used to prepare organosiliceous hybrid materials, will be described, together with their specific role in catalytic processes.

Zeolitic aluminosilicates, together with amorphous silica-alumina materials, formed by a three-dimensional network of TO_4 tetrahedra (T = tetrahedral atom, e.g. Si or Al) connected through oxygen bridges, exhibit *strong Brønsted acidity* as a result of the presence of protons that balance the negative charges in the lattice generated when tetravalent Si^{4+} is isomorphically replaced by a trivalent metal cation such as, for instance, Al^{3+} (Figure 1.3).

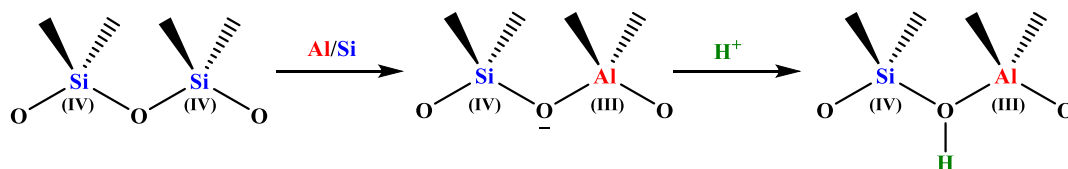


Figure 1.3. Schematic representation of isomorphous substitution of Si(IV) with Al(III) within the zeolite framework and subsequent formation of a Brønsted acid site.

From a structural point of view, the Brønsted acid site (BAS) can be regarded as a resonance of hybrid of structure I e II (Figure 1.4). Structure I is a fully bridged oxygen with a weakly bonded proton, and structure II is a silanol group with a weak Lewis acid interaction of the hydroxyl oxygen with an Al.^[27] According to Mortier's general theory,^[28] model I represents an acid site in a crystalline zeolite, while model II is more representative of the situation in an amorphous silica-alumina where no stabilization by long-range symmetric exists.^[29] The total number of Brønsted acid sites is directly correlated to the total number of framework T^{III} atoms.^[30] However, in a zeolite framework, especially for high aluminium-content zeolites, not all the acid sites have the same acid strength: this property changes with the number of aluminium atoms in the nearest neighbour position of the silicon atom which supports the acid site and also depends on the electronic density on the bridging hydroxyl group.^[31] Analogously to silicates, isomorphous substitution in aluminophosphates (AlPOs, composed of alternating AlO₄ and PO₄ tetrahedra, linked together exclusively through Al-O-P bonds) framework generates Brønsted acidity.^[32] Specifically, Brønsted acid sites are formed *via* isomorphous substitution of Al(III) (substitution mechanism I, SM I) with a monovalent M(I) or divalent M(II) dopant element and the isomorphous substitution of P(V) (substitution mechanism

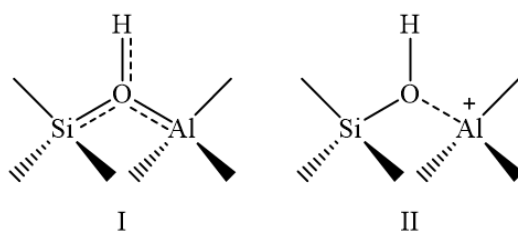


Figure 1.4. Resonance structures of a Brønsted acid site.^[29]

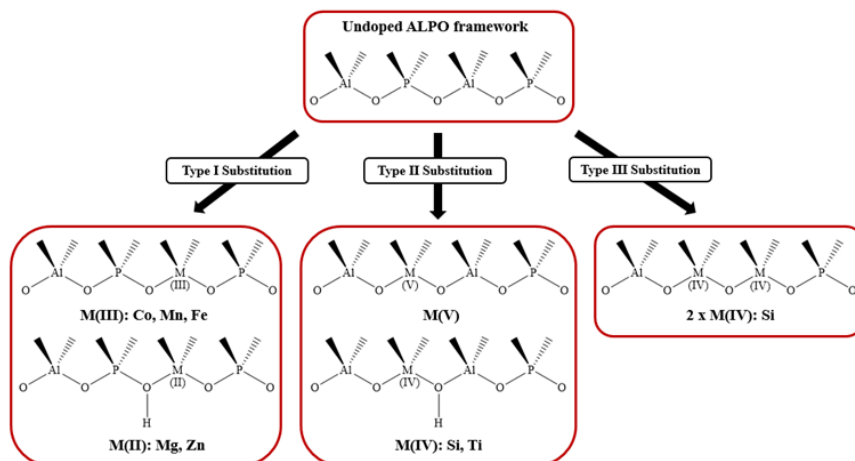


Figure 1.5. Different substitution mechanisms in AlPOs framework.^[39]

II, SM II) with a tetravalent M(V) cation. From a catalytic point of view, inorganic matrices possessing Brønsted acid sites are excellent candidates for designing bifunctional acid-base hybrids materials for tandem reactions.^[16,33-35]

In addition to Brønsted acidity, AlPOs derivatives can also exhibit isolated *redox centres*, obtained via SM I with dopant element having different oxidation states (*e.g.* Fe(II) and Fe(III), Co(II) and Co(III), Mn(II) and Mn(III)). CoAPO-34 is an example of combination of both redox and acidic properties, deriving respectively from the redox couples Co(II)/Co(III) and from the Brønsted acid sites generated by the substitution of Al(III) with Co(II).^[36-38] A schematic representation of the different substitution mechanism occurring in AlPO framework is reported in Figure 1.5.^[39]

Furthermore, amorphous silica-based materials, mesoporous silica, as well as zeolites and zeotype materials exhibit *weak silanol acid sites* as defective groups, arising from hydrolysed Si–O–Si bridges, missing tetrahedral framework atoms or located on the external surface of the crystals. Different types of Si–OH groups can be identified on inorganic surface (isolated or terminal silanols, geminal silanols, vicinal silanols and silanol nest interacting *via* hydrogen bond), depending on the adopted synthetic methodology (Figure 1.6).^[40] During catalysis, silanols group on

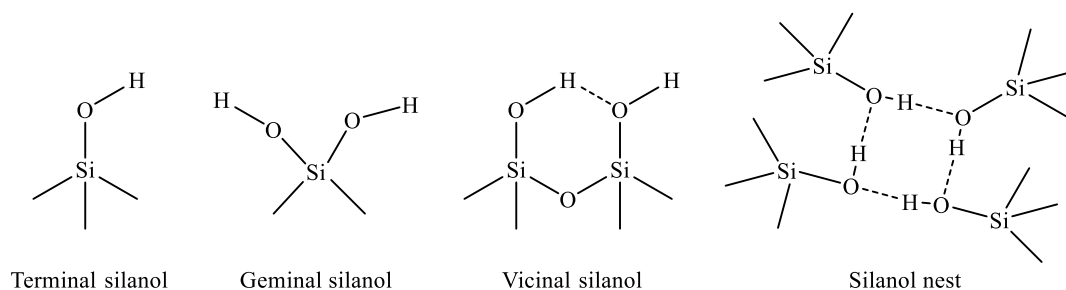


Figure 1.5. Different substitution mechanisms in AlPOs framework.^[39]

the hybrid material surface has proven to interact through weak H-bonds with reactants and transition intermediates. Moreover, the possibility of capping Si–OH groups with specific silylating agents allows to control the hydrophobic (silanol-rich)/hydrophilic (silanol-poor) character of the inorganic surface, thus influencing the catalytic activity of the active sites.^[41]

1.4 Synthetic pathways to obtain hybrid materials

Three different synthetic methods can be used to prepare organosiliceous hybrids based on organosilica precursors: 1) post-synthetic modification of the surface of a purely inorganic silica-based material (*grafting*), 2) simultaneous condensation of silica and organosilica precursors (*co-condensation*), and 3) incorporation of bridging organosilane precursors directly into the pore walls of a porous inorganic material (*synthesis of periodic mesoporous organosilicas*).^[23]

The *grafting* procedure consists in a post-synthesis modification of the surface of inorganic silica-based materials, performed by reaction of a specific organosilanes of the type $((R'O)_3SiR$, or less frequently chlorosilanes $ClSiR_3$ or silazanes



Figure 1.7. Grafting of specific $((R'O)_3SiR$ organosilanes, with R = organic functional group, onto the inorganic surface.^[12]

HN(SiR₃), with Si–OH groups of the inorganic matrix (Figure 1.7). The hydrolysis and condensation process between alkoxide terminal groups of the organosilane and the silanol groups of the inorganic material allows to covalently anchor and stabilize a large variety of organic moieties and organocatalysts. Moreover, several functionalities, such as acid, basic, redox and chiral functions, can be easily heterogenized within the same inorganic framework, thus generating multifunctional heterogeneous catalysts with application in cascade and tandem reactions. Furthermore, due to the synthetic conditions used, the grafting mechanism benefits from the retention of the structural properties of the inorganic matrices. A large variety of inorganic solids have been used to graft different organic moieties, from amorphous silicas^[42-44] to layered zeolites,^[34,35] mesoporous silicas^[45-53] and hierarchical zeotype materials.^[16] Amorphous silica-based hybrid materials exhibit high accessibility, stability and concentration of the anchored organic moieties. In addition, amorphous silica-aluminas are excellent inorganic matrices to generate bifunctional acid-base hybrid catalysts, owing to the large number of Brønsted acid sites located on the external surface. Nevertheless, the poor structuration between organic and inorganic counterparts, as well as the inhomogeneous distribution of the active centres and the absence of shape selectivity, can restrict their application in catalytic processes. Layered zeolitic organic-inorganic hybrids, obtained by the reaction of arylic silsesquioxane molecules with external silanols of the zeolitic layer, are also viable candidates for catalysing acid-base cascade reactions, due to the Brønsted acidity of the zeolitic framework coupled with the grafted basic organic function. Organic-functionalized mesoporous materials benefit from large specific surface areas available for catalytic reactions, high accessibility and stability of the active organic moieties. Despite these advantages, depending upon the steric hindrance of the anchored organic moieties and the degree of occupation, the lining of the pore walls can be followed by a reduction in the pore size. Additionally, if the grafting mechanism occurs preferentially at the pore openings, the diffusion of further molecules within the framework can be impeded, thus resulting in

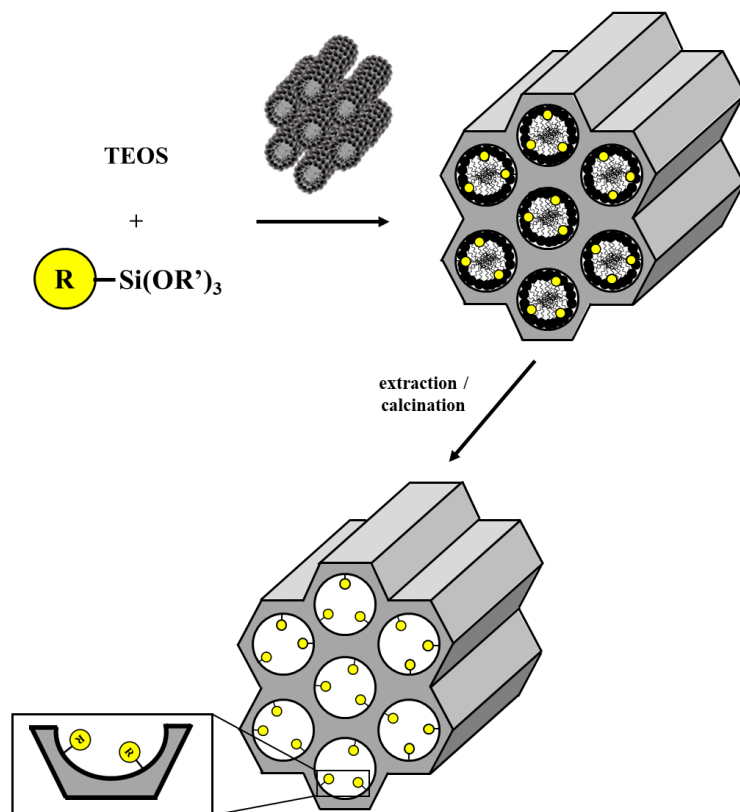


Figure 1.8. Hybrid ordered mesoporous silica obtained by co-condensation method. R = organic functional group.^[23]

inhomogeneous distribution of the active centres. In the case of very bulky moieties, this drawback can lead to pore blockage.

The *co-condensation* method (one-pot synthesis) involves the addition of terminal organoalkoxysilanes of the type $(\text{R}'\text{O})_3\text{SiR}$ directly during the synthesis of the inorganic matrix, such as to promote the condensation between terminal organosilane with silica tetralkoxysilane precursors ($(\text{RO})_4\text{Si}$ (TEOS or TMOS)), in the presence of a specific structure-directing agent (SDA). This synthetic strategy allows to obtain hybrid materials with organic moieties incorporated into silica matrix (Figure 1.8), thus preventing pore blockage. For instance, by employing SDA typically used to direct pure mesoporous silica phases (*e.g.* MCM or SBA silica phases), organosiliceous hybrid materials can be obtained with the organic

functionalities project into the pores.^[23] Nevertheless, the degree of mesoscopic order of the inorganic matrix progressively decreases with increasing concentration of organosilanes in the reaction media, till a complete loss of structural order is achieved. As a consequence, the $((R'O)_3SiR$ loading must not exceed 40 % mol. Moreover, an increase in the organosilane concentration promotes homocondensation reactions at the expense of cross-linking co-condensation with silica precursors, ultimately resulting in inhomogeneous distribution of the active sites. A further, purely methodological, drawbacks related to co-condensation method, is the chance of damaging the organic moieties during the removal of surfactant molecules, usually performed by extraction (calcination not suitable due to the presence of organic moieties).

In contrast to organically functionalized materials, which can be prepared by post-synthesis grafting or co-condensation, the framework of *periodic mesoporous organosilicas* (PMOs) is composed of organic and inorganic building blocks. Indeed, the use of bridged $((R'O)_3SiRSi(OR')_3)$ silsesquioxanes as organic-inorganic precursors as silica source in the PMOs synthesis, ensures the incorporation of the functional and active organic groups directly into the framework, instead of generating pending organic moieties located on the pore walls.^[54-56] PMO hybrid porous materials are synthesised using a self-assembling micellar route in the presence of surfactants which serve as structure-directing agents to direct the mesoporous network (Figure 1.9).^[23] Notably, PMOs benefits from homogeneous distribution of the active sites through the whole framework, highly ordered

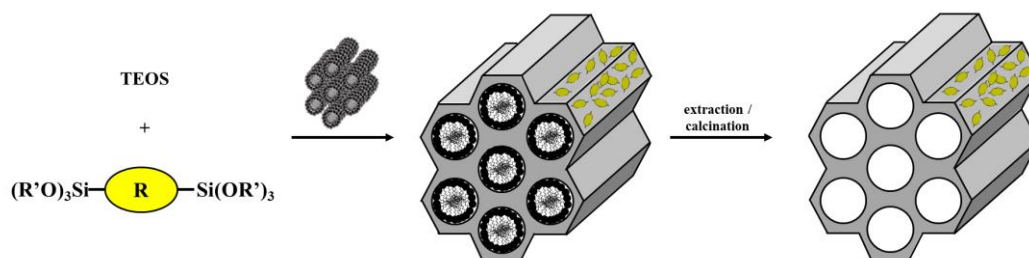


Figure 1.9. Self-assembly method to prepare PMOs hybrids. R = organic functional group.^[23]

mesoporous networks with uniform pores and, in contrast to hybrid synthesised *via* co-condensation, high loadings of the functional groups. Since organic bridged disilanes are integral components of the silica structure, the reactivity is entirely transferred from the cavities to the pore walls, thus preventing severe pore blockage.^[57] Furthermore, the possibility of simultaneously introducing different organic functionalities into the framework of PMOs paves the way for the design of a new class of multifunctional catalysts with different active sites integrated in the same network, thus facilitating the catalysis of multi-step and cascade reactions.^[58] Specifically, multifunctional PMOs can be obtained 1) by the combination of bridged disilanes, each bearing a different functionality; 2) by the combination of bridged silsesquioxanes together with grafted monosilanes, to obtain hybrid catalysts with active sites integrated in the pore walls and anchored on the wall surface; 3) by the use of specific silsesquioxanes bearing different organic active sites within the same linker, which are heterogenized and stabilised into the mesoporous network. Due to these noteworthy properties, PMOs represent a highly promising class of hybrid materials, with widespread technical applications.

1.5 Hierarchical porous hybrid materials

Hierarchical porous materials (especially hierarchical zeolite and zeotype materials), with enhanced diffusion and catalyst efficiency, have attracted great attention as heterogeneous catalysts within the past decades.^[59,60] Specifically, the expression “*hierarchy*” with respect to porous materials is generally used to indicate systems which contain different pore types in the form of bi- or multimodal pore size distribution, regardless if and how the two systems are connected. However, in a narrow sense, a porous material can be termed “*hierarchical*” only if an interplay between the different pore levels exists, resulting in an architecture which enable the splitting of the flow (liquid or gas) into smaller parts or *vice versa*, in order to maximize the benefits in catalysed reactions.^[61] Examples of different types of interconnectivity within the different levels of pores is reported in Figure 1.10.

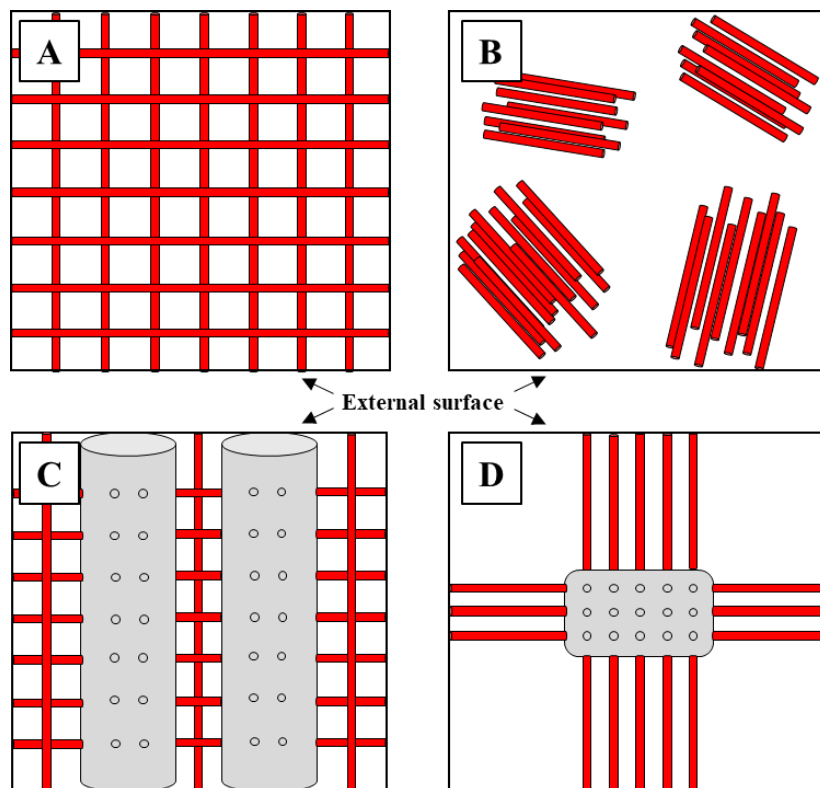


Figure 1.10. Different type of hierarchy in hierarchical materials: A) purely microporous framework; B) example of interconnected porosity, with mesopores generated by the fragmentation of the zeolite into small nanocrystals; C), D) schematic representations of intraconnected hierarchical systems, in which the micropores are crossed by larger pores introduced within the zeolitic crystals. The former is an example of accessible mesopores which can be entered from the external surface of the zeolitic crystals. The latter represent inaccessible mesoporosity, occluded in the microporous framework.^[64]

Interconnected hierarchy relates to a network of voids created in the intercrystalline space, as a result of the fragmentation of the microporous crystal into nanocrystals (Figure 1.10 B). Conversely, intraconnected hierarchy refers to the presence of mesopores in the microporous crystal (Figure 1.10 C and D). In all the cases (Figure 1.10 B-D), the micropores length is similarly reduced with respect to Figure 1.10 A. Moreover, all the three different configurations could lead to similar N_2 isotherms and pore size distributions characteristic of a mesoporous material. Nevertheless, the reduction in the length of the micropores is not a sufficient condition to increase the catalytic activity of the resulting hierarchical sample. For instance, the system

represented in Figure 1.10 D, is ineffective in increasing the mass-transport, since the mesopores are entrapped in the microporous architecture and thus accessible only through the micropores. In contrast, both the configurations depicted in Figure 1.10 B and C exhibit accessible mesovoids, the former directly from the outer surface of the crystal, the latter through the intercrystalline space in nanocrystals.^[62] Hence, with the aim of enhancing the catalytic performances through a hierarchical architectures, location of the additional porosity plays a crucial role and attention must be focused on designing an interconnected network of auxiliary mesopores (and/or macropores) within the microporous zeolitic framework.

Apart from enhancing diffusion of bulky molecules towards the catalytic active sites and preventing pore blockage typical of microporous materials, hierarchical zeotypes benefits from the retention of the crystalline order and associated acid functionality of the microporous framework. Since the introduction of an additional porosity implies a shortening in the length of the diffusional pathway, hierarchical architectures may be affected by a reduction in selectivity towards the target products. Nevertheless, in many reactions the product distribution is controlled by chemical factors (*i.e.* nature and distribution of the active centres) rather than by diffusional ones, thus the possible effect of hierarchical porosity on the selectivity cannot be easily predict.^[63]

A large-array of synthetic strategies to obtain hierarchical zeotype materials has been developed over the years, in order to widen their applications. In general, the additional pore system can be introduced 1) during the crystallization of the zeolitic material in the presence or absence of hard and soft meso- or macroporogen templates (bottom-up methods) to direct the formation of the additional porosity or 2) by post-synthesis treatments, such as metal extraction (*e.g.* dealumination or desilication, top-down approaches), aggregation of preformed zeolite crystallites (bottom-up method) or rearrangement (*e.g.* delamination/reassembly of layered zeolites).^[61] In the framework of this Ph.D. research study, only *desilication* as a top-down method and *soft-templating* as bottom-up approach will be explored.

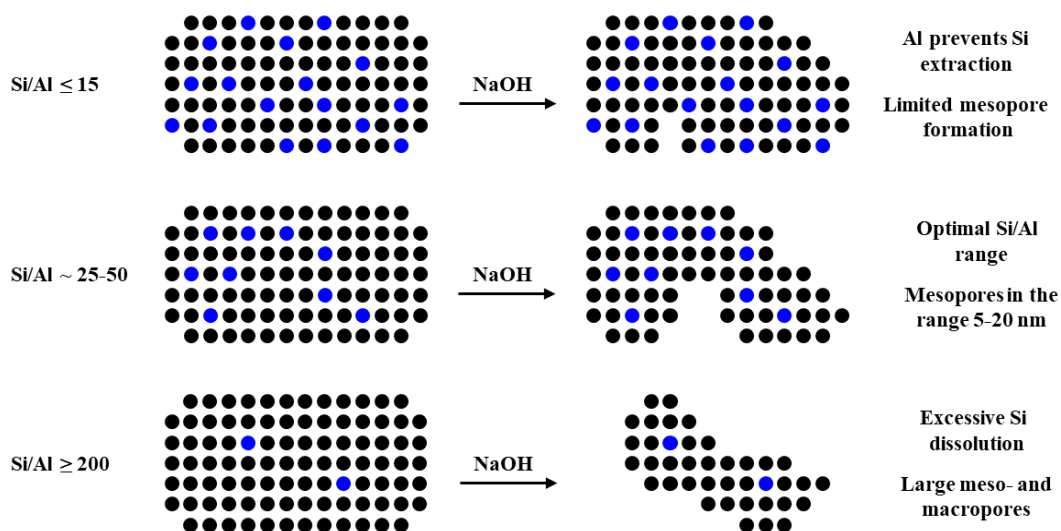


Figure 1.11. Schematic representation of the desilication mechanism performed via alkaline treatment on Al containing MFI-type zeolite.^[67]

Desilication is an effective demetallation method, consisting in selective extraction of silicon from the zeolitic framework by post-synthesis treatments with mild alkaline solution at temperatures between 50 and 80 °C.^[64,65] This useful approach leads to the introduction of a secondary porosity with high degree of connectivity in zeolite crystals of different framework types, whilst simultaneously retaining the long-range ordered and Brønsted acidity of the zeolite framework.^[66] Nevertheless, when Groen *et al.* defined a standard experimental desilication condition (0.2 M of NaOH, 65 °C, 30 min), they discovered that optimal introduction of intracrystalline mesopores could be achieved only for zeolite with limited range (25-50) of molar Si/Al ratios (Figure 1.11). For Si/Al ratio below 15, the high concentration of Al atoms in the zeolite framework prevent the Si atoms from being extracted, whereas at high Si/Al ratios (over 200), uncontrolled silicon extraction occurs, resulting in the formation of larger pores.^[67] Desilication exhibits several advantages, such as the possibility of scaling up the process, the chance of being applied to a wide range of zeolites, a relatively low cost and a high degree of interconnection between the different levels of porosity. However, this method leads to the production of defect sites which alter the acidic population of the parent

framework and, additionally, the generated mesopores are disordered and characterized by a relatively broad size distribution with respect to soft-templating methods.^[61,64] Apart from zeolites, desilication *via* basic treatments was applied even to aluminophosphates and silicoaluminophosphates.^[68] With respect to zeolite, these materials strongly amorphized in NaOH solution, thus requiring the use of more expensive and milder organic bases (e.g. tetrapropylammonium hydroxide or diethylamine). For SAPOs, a direct correlation between the increasing silicon content and the stability in alkaline media was evinced, with zeolitic-like Si domains more resistant than AIPO domains. Although desilication with mild organic bases resulted in SAPO hierarchical materials with intercrystalline porosity, the additional pore systems were scarcely tunable and disordered, like in the case of zeolites.

With the aim of generating a tunable and ordered mesoporosity, bottom-up soft-templating methods should be preferred to top-down approaches. In the dual *soft-templating* synthetic strategy, the formation of the additional pore system occurs during the material crystallization by the templating action of surfactants, whereas the synthesis of the zeolitic microporous framework is achieved by the use of a micropore structure-directing agent. The soft-templating approaches can be further subdivided into primary methods, in which all reactants are added at the beginning of a one-step synthesis procedure, and secondary methods, where all components, with exclusion of the surfactant, are added in the first synthesis step, while the soft-template is added in the last synthesis step prior to the hydrothermal synthesis (Figure 1.12).^[61,69,70] By performing soft-templating strategies, a higher tuning of the additional porosity can be achieved, yet the major issues are economic and environmental costs because of the use of sophisticated and disposable siliceous surfactants mesoporegen, such as dimethyloctadecyl[(3-(trimethoxysilyl)propyl)ammonium chloride (DMOD), which in most cases should be specifically synthesised.^[68,71-73] Thus, to exploit the potential of soft-templating methods to obtain ordered and tunable additional mesoporosity, the need to find alternative

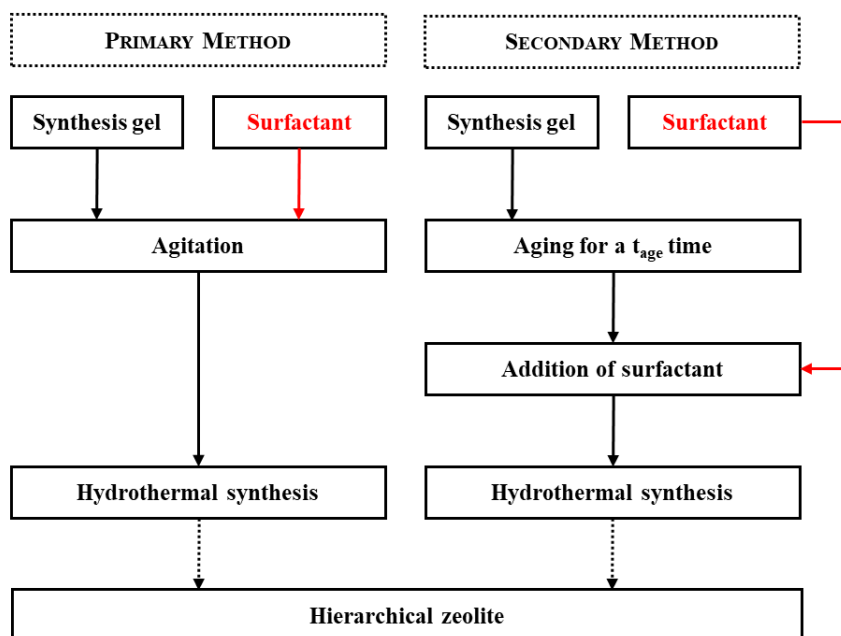


Figure 1.12. Schematic representation of the primary and secondary soft-templating methods.^[61]

environmental-friendly, low-cost and less-sophisticated soft-templates has become a challenging task.

The establishment of *structure-property relationships* plays a key role in investigating the nature of hierarchical materials and opens the door to further optimization of their application-oriented design. The most simple and direct method to define such relationship is to correlate their properties (enhanced accessibility, mesopore surface and volume, location of the active centres) with their specific catalytic application. In this respect, descriptors are helpful tools to gain a deeper insight in the critical evaluation of these properties.^[64] For instance, the *accessibility factor* (AF), determined by relating the amount of Brønsted acid sites probed by bulky strong bases (alkylpyridines) to the total amount of BAS in the zeolitic framework, allows to standardise acid site accessibility in zeotype materials. Indeed, the increased adsorption of bulky probe molecules due to the additional mesopore architecture, and their interaction with strong acid sites typically inaccessible in microporous samples, evidences an increment in the accessibility of the micropore

volume.^[74,75] Another descriptor which is useful to classify the porous characteristics of hierarchical materials, not taking into account other properties (*e.g.* acidity and composition), is the *hierarchy factor* (HF), defined as the relative mesopore surface area (S_{meso}/S_{total}) multiplied by relative microporosity (V_{micro}/V_{total}).^[76] A variant of HF factor, named indexed hierarchy factor (IHF), has also been proposed and obtained by normalizing micropore volume and mesopore surface area not by the total pore volume and surface area, but their maximum values ($IHF = (V_{micro}/V_{micro}^{max}) \times (S_{meso}/S_{meso}^{max})$).^[77] Both HF and IHF tools allow to compare hierarchical systems regardless to the synthetic methodology.

In light of their exceptional properties, hierarchical architectures represent a viable and promising alternative to microporous and mesoporous materials to host organic functionalities, rendering efficient organic-inorganic hierarchical porous heterogeneous hybrid catalysts. Due to their high mechanical and thermal stability, as well as to the resistance to structural changes in the presence of organic reactants and solvents, hierarchical frameworks ensure flexibility in the grafting method (where high-temperature reactions are required to functionalise the surface) and can be successfully used in a range of reactions with varying conditions. Moreover, the textural and acidic properties, together with their hydrophilic/hydrophobic character, can be easily controlled and varied during a one-pot synthesis protocol. In fact, by selecting an appropriated synthetic methodology, retention of the strong Brønsted acidity of the microporous framework is ensured, and the pore dimensions can be tuned in order to potentially maximise conversion and selectivity by a combination of regulating diffusion of molecules to and from the active sites as well as to achieve desirable confinement effects. Additionally, the presence of silanols groups, mainly located on the mesopore and external surface of the catalyst, can be exploited to perform “click” chemistry protocols for the sequential covalent attachment of tethers and organocatalyst molecules to the surface (Figure 1.13). The chance of covalently anchor the organic active sites preferentially within mesopores of the hierarchical

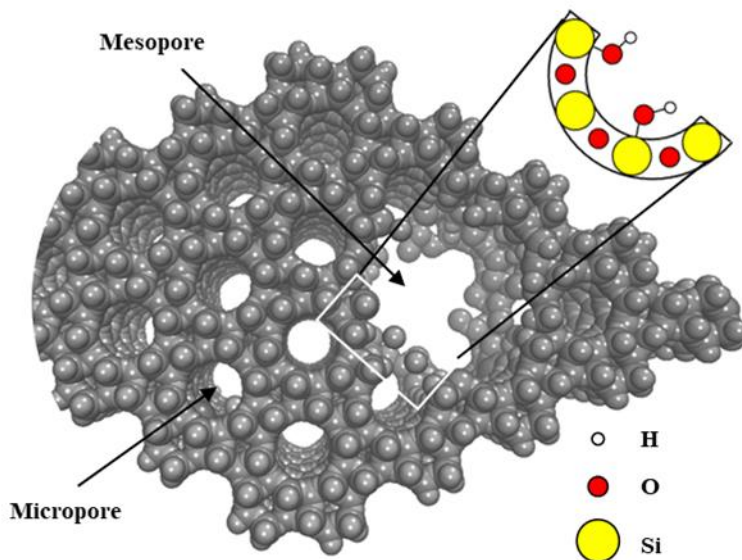


Figure 1.13. Graphical representation of a hierarchical architecture with discrete micropores and mesopores, with pendant silanols preferentially located on the mesopore surface, available for covalent functionalization of organocatalyst and active sites precursors.

structure prevents aggregation/crowding within the channels, which may lead to unfavourable substrate-substrate interactions and to alteration in reaction kinetics. The selective functionalization will also greatly help in enhancing mass transport and diffusion of substrate, reagents and products, whereas the well-defined and isolated active sites could ideally serve as *loci* for improved catalytic turnovers and enhanced rates.

Furthermore, the co-existence of different active sites, located at different position in the hierarchical framework (organic active sites on the mesopores and external surface and BAS within the microporous architecture) makes these catalysts extremely promising for applications in tandem and cascade reactions. As a conclusion, the development of successful strategies to heterogenize organic moieties within hierarchical porous inorganic supports ranks to the main challenges which are being demanded by European Union's directives, related to the effective development of more efficient (energy) and sustainable (environmental) chemical processes (catalysis). These heterogeneous multi-step catalytic routes will promote

the generation of basic resources and raw materials useful for society progresses, resolving general problems to which fundamental scientific and technical research could give sustainable responses.

1.6 Notes and references

- [1] U. Díaz, A. Corma, *Chem. Eur. J.* **2018**, 24, 1.
- [2] D. A. Loy, K. J. Shea, *Chem. Rev.* **1995**, 95, 1431.
- [3] M. Faustini, L. Nicole, E. Ruiz-Hitky, C. Sánchez, *Adv. Funct. Mater.* **2018**, 1704158.
- [4] C. Ponnampereuma, A. Shimoyama, E. Friebele, *Origins Life Evol. Biospheres* **1982**, 12, 9.
- [5] J.D. Bernal, *Proc. Phys. Soc., London, Sect. A* **1949**, 62, 537.
- [6] J.A. Rausellcolom, V.Fornes, *Am. Mineral.* **1974**, 59, 790.
- [7] W. Huang, J. P. Ferris, *J. Am. Chem. Soc.* **2006**, 128, 8914.
- [8] P. Gomez-Romero, C. Sanchez, *New J. Chem.* **2005**, 29, 57.
- [9] C. Sánchez, B. Julián, P. Belleville, M. Popall, *J. Mater. Chem.* **2005**, 15, 3559.
- [10] C. Sánchez, F. Ribot, *New J. Chem.* **1994**, 18, 1007.
- [11] C. Sánchez, P. Belleville, M. Popall, L. Nicole, *Chem. Soc. Rev.* **2011**, 40, 696.
- [12] U. Díaz, D. Brunel, A. Corma, *Coord. Soc. Rev.* **2013**, 42, 4083.
- [13] M.S. Seveleva, K. Eftekhari, A. Abalymov, T. E.L. Douglas, D. Volodkin, B.V. Parakhonskiy, A.G. Skirtach, *Frontiers in Chemistry* **2019**, 7, 179.
- [14] M.J. Climent, A. Corma, S. Iborra, *ChemSusChem* **2009**, 2, 500.
- [15] G. Férey, *Chem. Soc. Rev.* **2008**, 37, 191.
- [16] E. Gianotti, I. Miletto, C. Ivaldi, G. Paul, L. Marchese, M. Meazza, R. Rios, R. Raja, *RSC Adv.* **2019**, 9, 35336.
- [17] M.D. Jones, R. Raja, J.M. Thomas, J. Rouzard, B.F.G Johnson, K.D.M. Harris, *Angew. Chem. Int. Ed. Engl.* **2003**, 42, 4326.
- [18] U. Díaz, T. García, A. Velty, A. Corma, *Chem. Eur. J.* **2012**, 18, 8659.
- [19] M.J. MacLachlan, T. Asefa and G.A. Ozin, *Chem. Eur. J.* **2000**, 6, 2507.

- [20] J.L.C. Rowsell, O. M. Yaghi, *Microporous Mesoporous Mater.* **2004**, 73, 3.
- [21] A.P. Wight, M.E. Davis, *Chem. Rev.* **2002**, 102, 3589.
- [22] D.A. Loy, J. Shea, *Chem. Rev.* **1995**, 95, 1431.
- [23] F. Hoffmann, M. Cornelius, J. Morell, M. Fröba, *Angew.Chem., Int. Ed.* **2006**, 45, 3216.
- [24] S. Fujita, S. Inagaki, *Chem. Mater.* **2008**, 20, 891.
- [25] A. Kuschel, M. Drescher, T. Kuschel, S. Polarz, *Chem. Mater.* **2010**, 22, 1472.
- [26] P. García-García, A. Zagdoun, C. Coperet, A. Lesage, U. Díaz, A. Corma, *Chem. Sci.* **2013**, 4, 2006.
- [27] A. Corma, *J. Catal.* **2003**, 216 298.
- [28] J. Mortier, in: *Proceedings 6th International Zeolite Conference* **1984**, 734.
- [29] G.J. Gajda, J.A. Rabo, in *Acidity and Basicity of Solids*, in *NATOASI Series*, Kluwer Academic, London, **1994**, 444, p. 127.
- [30] W.D. Haag, *Stud. Surf. Sci. Catal.* **1994**, 84, 1375.
- [31] L.A. Pine, P.J. Maher, W. A. Wachter, *J. Catal.* **1984**, 85, 466.
- [32] J.A. Martens, P.A. Jacobs, in *Crystalline microporous phosphates - a family of versatile catalysts and adsorbents*, in *Advanced Zeolite Science and Applications*, Elsevier Science Publ, Amsterdam, **1994**, 85, p. 653.
- [33] K. Motokura, M. Tomita, M. Tada, Y. Iwasawa, *Top. Catal.* **2009**, 52, 579.
- [34] K. Motokura, M. Tada and Y. Iwasawa, *J. Am. Chem. Soc.* **2009**, 131, 7944.
- [35] A. Corma, U. Díaz, T. García, G. Sastre, A. Velty, *J. Am. Chem. Soc.* **2010**, 132, 1501.
- [36] L. Marchese, E. Gianotti, B. Palella, R. Pirone, G. Martra, S. Coluccia, P. Ciambelli, *Stud. Surf. Sci. Catal.* **2000**, 130, 3005.
- [37] E. Gianotti, M. C. Paganini, G. Martra, E. Giamello, S. Coluccia, L. Marchese, *Stud. Surf. Sci. Catal.* **2005**, 135, 178.
- [38] A. Martucci, A. Alberti, G. Cruciani, A. Frache, L. Marchese, H. O. Pastore, *J. Phys. Chem. B* **2005**, 109, 13483.
- [39] R. Raja, M. E. Potter, S. H. Newland, *Chem. Comm.* **2014**, 505940.

- [40] W. F.Höelderich, *Stud. Surf. Sci. Catal.* **1989**, 46 193–209.
- [41] J. D. Bass, S. L. Anderson, A. Katz, *Angew. Chem., Int. Ed.* **2003**, 42, 5219.
- [42] J.M. Notestein, A. Katz, *Chem. Eur. J.* **2006**, 12, 3954.
- [43] E. L. Margelefsky, R. K. Zeidan, M.E.Davis, *Chem. Soc.Rev.* **2008**, 37, 1118.
- [44] A. Fuerte, M. Iglesias, F. Sánchez, A. Corma, *J. Mol. Catal. A: Chem.* **2004**, 211; C. González-Arellano, A. Corma, M. Iglesias, F. Sánchez, *Chem. Commun.* **2005**, 3451; A. Corma, M. Iglesias, F. Sánchez, *Catal. Lett.* **1995**, 32, 313.
- [45] A. Corma, U. Díaz, T. García, G. Sastre, A. Velty, *J. Am. Chem. Soc.* **2010**, 132, 1501.
- [46] K. Motokura, M. Tada and Y. Iwasawa, *J. Am. Chem. Soc.* **2009**, 131, 7944.
- [47] Q. Fu, G.V.R. Rao, L.K. Ista, Y. Wu, B.P. Andrzejewski, L.A. Sklar, T.L. Ward, G.P. López, *Adv. Mater.* **2003**, 15, 1262.
- [48] D.R.Radu, C.-Y. Lai, J.W. Wiench, M. Pruski, V.S.-Y. Lin, *J. Am. Chem. Soc.* **2004**, 126, 1640.
- [49] K.K. Sharma, T. Asefa, *Angew. Chem., Int. Ed.* **2007**, 46, 2879.
- [50] N.R. Shiju, A.H. Alberts, S. Khalid, D.R. Brown, G. Rothenberg, *Angew. Chem., Int. Ed.* **2011**, 50, 9615.
- [51] G. Villaverde, A. Corma, M. Iglesias, F. Sánchez, *ACS Catal.* **2012**, 2, 399–406.
- [52] A. Erigoni, G. Paul, M. Meazza, M.C. Hernández-Soto, I. Miletto, R. Rios, C. Segarra, L. Marchese, R. Raja, F. Rey, E. Gianotti, U. Díaz, *Catal. Sci. Technol.* **2019**, 9, 6308.
- [53] A. Erigoni, M.C. Hernández-Soto, F. Rey, C. Segarra, U. Díaz, *Catalysis Today* **2019**, doi:10.1016/j.cattod.2019.09.041.
- [54] S. Inagaki, S. Guan, Y. Fukushima, T. Ohsuna, O. Terasaki, *J. Am. Chem. Soc.* **1999**, 121, 9611.
- [55] T. Asefa, M. J. MacLachlan, N. Coombs and G. A. Ozin, *Nature* **1999**, 402, 867.
- [56] B. J. Melde, B. T. Holland, C. F. Blandford and A. Stein, *Chem. Mater.* **1999**, 11, 3302.
- [57] S. Inagaki, S. Guan, T. Ohsuna and O. Terasaki, *Nature* **2002**, 416, 304.

- [58] U. Díaz, A. Corma, *Coord. Chem. Rev.* **2016**, 311, 85–124.
- [59] L.-H. Chen, M.-H. Sun, Z. Wang, W. yang, Z. Xie, B.-L. Su, *Chem Rev.* **2020**, DOI: <https://doi.org/10.1021/acs.chemrev.0c00016>.
- [60] S. Mitchell, A.B. Pinar, J. Kenvin, P. Crivelli, J. Kärger, J. Pérez- Ramírez, *Nature Comm.* **2015**, 6, 8633.
- [61] W. Schwieger, A.G. Machoke, T. Weissenberger, A. Inayat, T. Selvam, M. Klumpp, A. Inayat, *Chem. Soc. Rev.* **2016**, 45, 3353.
- [62] J. Pérez-Ramírez, C.H. Christensen, K. Egeblad, C.H. Christensen, J.C. Groen, *Chem. Soc. Rev.* **2008**, 37, 2530.
- [63] C. Fernandez, I. Stan, J.-P. Gilson, K. Thomas, A. Vicente, A. Bonilla, J. Pérez-Ramírez, *Chem. Eur. J.* **2010**, 21, 6224.
- [64] D. Verboekend, J. Pérez -Ramírez, *Catal. Sci. Technol.* **2011**, 1, 879.
- [65] J.C. Groen, L.A.A. Peffer, J.A. Moulijn and J. Pérez-Ramírez, *Colloids Surf. A* **2004**, 241, 53.
- [66] J.C. Groen, L.A.A. Peffer, J.A. Moulijn, J. Pérez-Ramírez, *Microporous Mesoporous Mater.* **2004**, 69, 29.
- [67] J.C. Groen, J.C. Jansen, J.A. Moulijn, J. Pérez-Ramírez, *J. Phys. Chem. B* **2004**, 108, 13062.
- [68] D. Verboekend, M. Milina, J. Pérez-Ramírez, *Chem. Mater* **2014**, 26, 4552.
- [69] D.P. Serrano, J.M. Escola, P. Pizarro, *Chem. Soc. Rev.* **2013**, 42, 4004.
- [70] K. Möller and T. Bein, *Compr. Inorg. Chem. II* **2013**, 7, 247.
- [71] S.H. Newland, W. Sinkler, T. Mezza, S.R. Bare, M. Caravetta, I.M. Haies, A. Levy, S. Keenan, R. Raja, *ACS Catal.* **2015**, 5, 6587.
- [72] Q. Sun, N. Wang, D. Xi, M. Yang, J. Yu, *Chem. Commun.* **2014**, 50, 6502.
- [73] S. Chapman, A.J. O'Malley, I. Miletto, M. Carravetta, P. Cox, E. Gianotti, L. Marchese, S.F. Parker, R. Raja, *Chem. Eur. J.* **2019**, 25, 9938.
- [74] I. Miletto, G. Paul, S. Chapman, G. Gatti, L. Marchese, R. Raja, E. Gianotti, *Chem. Eur. J.* **2017**, 23, 9952.

- [75] I. Miletto, C. Ivaldi, G. Paul, S. Chapman, L. Marchese, R. Raja, E. Gianotti, *ChemistryOpen* **2018**, 7, 297.
- [76] J. Pérez-Ramírez, D. Verboekend, A. Bonilla, S. Abelló, *Adv. Funct. Mater.* **2009**, 19, 3972.
- [77] D. Verboekend, S. Mitchell, M. Milina, J.C. Groen, Pérez-Ramírez, *J. Phys. Chem. C* **2011**, 115, 14193.

2

Outline

The Ph.D. research work which will be discussed in the next chapters was carried out in the frame of the European Union's Horizon2020 funded MULTI2HYCAT (multi-site organic-inorganic hybrid catalysts for multi-step chemical processes) project. The main goal of MULTI2HYCAT is to design, obtain proof of concept, upscale and obtain industrial validation in a pre-pilot reactor of periodic and non-periodic porous hybrid materials, exhibiting different flexibility or rigidity levels, which will be used as active catalysts to perform multi-step catalytic processes with predominantly high conversions (up to 90%) and selectivity (in the range of 80-90%) towards the desired final products. The project aims to solve the limits of current organosiliceous solids, while at the same time improving the flexibility and versatility and reducing costs of the obtained catalysts, making them attractive for a wide range of industrial applications. To this end, during the project, these novel catalysts will be demonstrated for pharmaceutical and intermediate chemistry applications, as a concrete prime-mover for subsequent replication.

With the aim of preparing Class II hybrid, based on strong chemical bonds between the organic and inorganic building units, hierarchical inorganic zeotypes, which retain the bulky microporous structure but possess an additional mesoporous network improving mass transport to internal active sites, represent a viable alternative to microporous and mesoporous materials to host organic functionalities, rendering a new and promising class of organic-inorganic hybrid catalysts to perform cascade and tandem reactions. The high mechanical and thermal stability of hierarchical materials, as well as their resistance to structural changes in the presence

of organic reactants and solvents, ensure flexibility in the grafting methodologies and in a wide range of applications. Moreover, the possibility of tuning their textural hydrophobic/hydrophilic and acidic properties, together with the speciation of the active sites, allow to maximise conversion and selectivity towards the desired products. Furthermore, the retention of acidic properties of the parent framework, associated with the possibility of speciation of the active centres (strong Brønsted acid sites mainly located within the microporous framework and organocatalyst on the mesopore surface) made hierarchical porous hybrids suitable catalyst to perform tandem and cascade reactions, with improved turnovers and enhanced rates. Among hierarchical porous zeotype materials, hierarchical silicoaluminophosphates (SAPOs) are good candidates for application requiring acid catalysis.

In light of the foregoing, the Ph.D. research activity was initially focused on the optimization of different synthetic strategies to prepare hierarchical zeolites and SAPOs acid catalysts. In particular, two novel bottom-up routes, benefiting for high degree of structural control, were used to synthesize hierarchical SAPO-34 and SAPO-5 catalysts, mitigating the need of sophisticated surfactants or templates by using: (i) surfactants (CTAB/Pluronic123) encapsulated within ordered mesoporous silica nanoparticles (MCM-41/SBA-15) as both the silicon source and mesoporegen; (ii) mono- and di-saccharides as structure directing agent to direct the mesopore network. In contrast, a well-established top-down approach, consisting in demetallation under basic conditions to extract framework constituents whilst retaining crystallinity, was employed to obtain a hierarchical ZSM-5 zeolite. In addition, with the aim of tuning acidic and textural properties, modulation of the silicon loading and mesopore diameter by using specific swelling agents, was performed.

Subsequently, optimised hierarchical materials were selected and used as inorganic support to covalently anchor different organic functionalities. The as-obtained hierarchical porous organic-inorganic hybrid catalysts were deeply characterized, using a multi technique approach (XRD, Volumetric analysis, TGA,

solid-state NMR and FT-IR spectroscopies), with the aim of establishing preliminary structure-property relationship. Furthermore, catalytic activity of the hybrids was evaluated in industrially-relevant reactions, selected in the framework of the MULTI2HYCAT consortium.

Alongside, in order to get a deeper insight in the nature of organic-inorganic interface in hybrid materials, the influence of silicodactyly (*i.e.* the number of hydrolysable alkoxy groups which can be used by the organosilane to grab the inorganic surface) and silicopodality (*i.e.* number of alkyl chains through which the organosilane is anchored to the surface) in the design of a Class II hybrid catalyst was deeply investigated through a combined experimental and computational approach. A detailed investigation of these two parameters is indeed helpful to forecast the influence of the different grafting configurations on the tendency of the organosilane to lay on the silica surface, possibly hampering the catalytic activity. This research study ultimately aimed at improving catalytic performances by establishing the best grafting configurations and conditions to host organic moieties fully available for interactions with substrates, preventing the organosilane-surface interactions.

The Ph.D. research activity was strictly correlated with the overall activities of the MULTI2HYCAT partners: Consejo Superior de Investigaciones Científicas (CSIC, Spain), University of Southampton (UoS, United Kingdom), Centre National de la Recherche Scientifique (CNRS, France), CAGE CHEMICALS SRL (Italy), PNO Consultants GmbH (Germany), ALMIRALL SA (Spain). Indeed, the Ph.D. research work was started during the first year of the project and three months were spent working at the University of Southampton, performing the synthesis of N-heterocyclic carbene organocatalyst, its grafting on selected inorganic supports and the evaluation of the catalytic activity of the as obtained organic-inorganic hybrid materials.

3

Sustainable saccharide templates to drive the synthesis of hierarchical silicoaluminophosphate SAPO-34 with tailored acid sites

In the present chapter, a novel bottom-up approach for the synthesis of hierarchical SAPO-34 catalysts, using mono- and disaccharides as mesopore structure directing agents, has been explored. A detailed physico-chemical characterization was performed to evaluate the structural, morphological, textural and spectroscopic properties of the zeotypes. Furthermore, the catalytic activity was tested in the liquid-phase acid-catalysed Beckmann rearrangement of cyclohexanone oxime to ϵ -caprolactam.

Introduction

Although microporous zeolite and zeolitic materials had been widely applied over the years as industrial heterogeneous catalysts,^[1-3] owing to their highly robust nature and tunable acidic, textural and catalytic properties,^[4-7] diffusion limitations and pore blockage^[8] paved the way for the development of hierarchical materials as a solution to overcome these drawbacks. Among all the synthetic strategies to obtain a hierarchical framework, bottom-up soft-templating methods should be preferred, ensuring high degree of structural control, whilst retaining the acidic properties of the microporous analogue.^[9,10] Nevertheless, bottom-up approach traditionally requires the use of sophisticated soft-template surfactants to address the mesoporosity.^[9,11] Owing to the immense catalytical potential of hierarchical porous systems, the need to identify alternative low-cost, sustainable mesopore

templating agents, compatible with conventional one-pot synthesis, is timely. However, recently saccharides have been proposed as viable alternative mesopore directing agents.^[12-14] In light of the foregoing, a low-cost bottom-up approach for the preparation of hierarchical SAPO-34 (silicoaluminophosphate with chabazite (CHA) topological framework), using monosaccharides (glucose and fructose) or disaccharides (sucrose) as mesopore directing agents (SDA_{meso}), will be described in the present chapter.^[15] This novel strategy aims at increasing mass transport and accessibility of the acid active sites, whilst retaining the nature of acid centres, by introducing an auxiliary mesoporous network. Structural, morphological, textural and spectroscopic characterization have been provided with a view to establish preliminarily structure-property relationship, which may lead to a rational design of sugar-templated hierarchical catalysts. Moreover, the catalytic activity of hierarchical SAPO-34 has been evaluated in the liquid-phase Beckmann rearrangement of cyclohexanone oxime, in which, conversely to vapour-phase Beckmann rearrangements, strong acid sites (*e.g.* Brønsted acid sites, BAS) play a crucial role.

3.1 Experimental section

3.1.1 General

Aluminum isopropoxide ($\geq 98\%$), tetraethylammonium hydroxide (35 wt% in H_2O), fumed silica, tetraethyl orthosilicate, phosphoric acid (85 wt% in H_2O), glucose, fructose and sucrose, all used for the synthesis of SAPO-34 materials, were supplied by Sigma-Aldrich (Milano, Italy). NH_3 ($\geq 99.7\%$), purchased from SIAD (Bergamo, Italy) and 2,6-di-*tert*-butylpyridine ($\geq 97\%$), purchased from Sigma Aldrich (Milano, Italy), were used as probe molecule in FT-IR experiments.

3.1.2 Synthesis of SAPO-34

Three different hierarchical SAPO-34 catalysts were synthesised following a bottom-up low-cost method, by using monosaccharides (glucose and fructose) and

the resulting disaccharide (saccharose) as mesoporous structure directing agent (SDA_{meso}). A microporous SAPO-34 was also synthesised to compare the physico-chemical properties and the catalytic activity. After crystallization, recovering and washing, all samples were calcined to remove the organic templates.

Synthesis of hierarchical sugar-templated SAPO-34: hierarchical catalysts were synthesised following the hydrothermal procedure reported in literature by Miletto *et al.*^[15] Aluminium isopropoxide (7.00g) was added slowly to phosphoric acid (2.35 ml, 85 % in H₂O), previously diluted in deionized water (29 ml) and the mixture was stirred for 1h. Fumed silica (1.24 g) was slowly added and the mixture was further stirred for 2 h. Tetraethylammonium hydroxide (TEAOH, 14.00 ml, 35 wt % in H₂O) was added dropwise under stirring and the gel was further stirred for 4 h. A different saccharide template, preventively dissolved in deionized water (8 ml), was added and the resulting gel of molar composition 1.0 Al : 1.0 P : 0.60 Si : 1 TEAOH : 0.067 SDA_{meso} : 60 H₂O was vigorously stirred for 30 min. The gel was transferred to a Teflon-lined stainless-steel autoclave and crystallize at 180 °C for 72 h under autogenous pressure. The solid product was centrifugated and washed with water. The as-prepared product was dried in air at 100 °C and calcined in a tube furnace under air flow at 600 °C for 10 h, producing a white crystalline solid.

Synthesis of microporous SAPO-34: microporous SAPO-34 was synthesised according to the following hydrothermal procedure. Aluminium isopropoxide (7.00g) was added slowly to tetraethylammonium hydroxide (TEAOH, 14.00 ml, 35 wt % in H₂O) under stirring. Deionized water (21 ml) was added and the mixture was stirred for 1 h. Tetraethylorthosilicate (TEOS, 1.14 ml) was added dropwise under stirring and the mixture was further stirred for 2 h. Phosphoric acid (2.33 ml, 85wt% in H₂O) was added dropwise under stirring. The gel was vigorously stirred for 30 min to produce a white gel of molar composition 1.0 Al : 1.0 P : 0.15 Si : 1 TEAOH : 50 H₂O. The gel was transferred to a Teflon-lined stainless-steel autoclave and crystallized at 200 °C for 60 h under autogenous pressure. The solid product from autoclave was then recovered by filtration and washed with water. The as-

prepared product was dried in air at 100 °C and calcined in a tube furnace under air flow at 600 °C for 16 h to produce a white crystalline solid.

3.1.3 Characterization

Prior to volumetric and spectroscopic analyses, calcined samples were outgassed at 300 °C overnight and for 2 h, respectively, to remove physisorbed water. Further details on the experimental techniques are reported in Chapter 9/Experimental section.

3.1.4 Catalysis

A portion of calcined catalyst was outgassed by heating overnight at 200 °C under vacuum. A 3-neck glass-lined reactor was charged with cyclohexanone oxime (0.1 g, Sigma Aldrich), anhydrous chlorobenzene (internal standard, 0.1 g, Sigma Aldrich), dried catalyst (0.1 g), and anhydrous benzonitrile (20 ml, Sigma Aldrich). The reaction vessel was sealed with a rubber septum, glass stopper, and reflux condenser. The reaction was transferred to a preheated oil bath at 130 °C and stirred at this temperature, under constant nitrogen atmosphere. Aliquots of the reaction mixture were extracted hourly over a 6-hour reaction period and analysed by gas chromatography using the Clarus 480 apparatus with flame ionisation detector (FID) and an Elite 5 column. Products were identified using authenticated standards and quantified against the internal standard, chlorobenzene.

3.2 Results and Discussion

3.2.1 Morphological, structural and textural characterization

The experimental framework composition of the hierarchical SAPO-34 catalysts (Table 3.1) was determined by inductively-coupled plasma atomic emission spectrometry (ICP-AES) analysis and the Si/(Si+Al+P) ratio was consistent with the theoretical value determined from the synthesis gel composition.

Table 3.1. Inductively-coupled plasma chemical analysis of hierarchical SAPO-34 catalyst.

Acronym	SDA _{meso}	Si	Al	P	Si/	Si/
		[wt %]	[wt %]	[wt %]	Si + Al + P ^[a]	Si + Al + P ^[b]
GLU-S01	Glucose	8.08	15.05	12.64	0.23	0.23
FRU-S02	Fructose	6.93	15.79	13.05	0.19	0.23
SUC-S03	Sucrose	8.22	20.50	14.10	0.19	0.23

[a] Experimental framework composition determined by ICP analysis after the synthesis.

[b] Theoretical framework composition determined from the synthesis gel composition.

X-Ray powder diffraction (XRDP) was performed to elucidate the structural features of saccharide-templated SAPO-34 (Figure 3.1). Despite a slight decrease in the intensity of the signals, which may be related to a partial loss of structural order due to the additional mesoporosity, all the observable reflections are characteristic of the CHA framework and no extraphases were detected.^[16] Thus, XRDP confirmed phase purity and crystallinity of all samples.

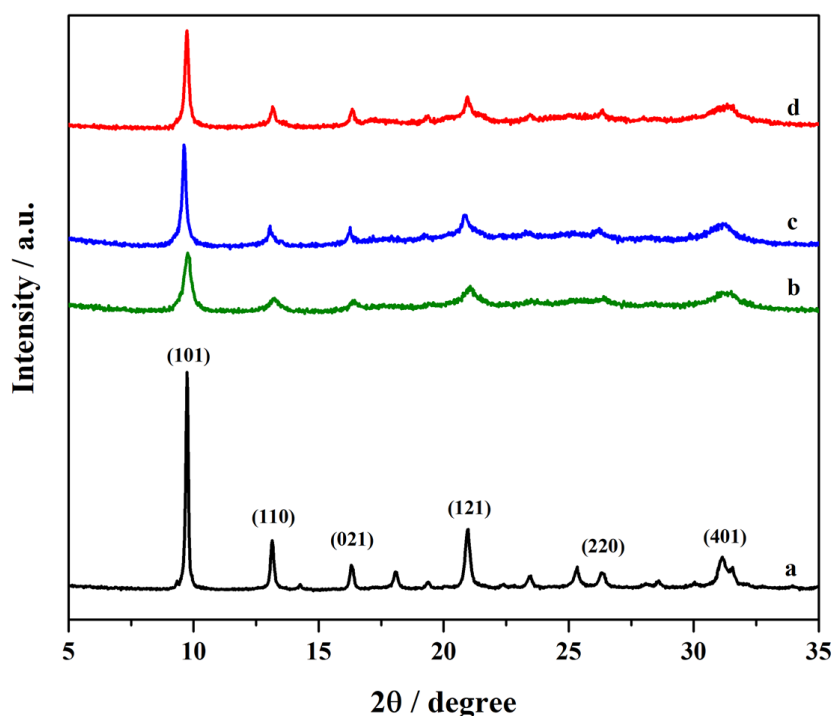


Figure 3.1. The powder XRD pattern of microporous SAPO-34 (a), GLU-S01 (b), FRU-S02 (c) and SUC-S03 (d).

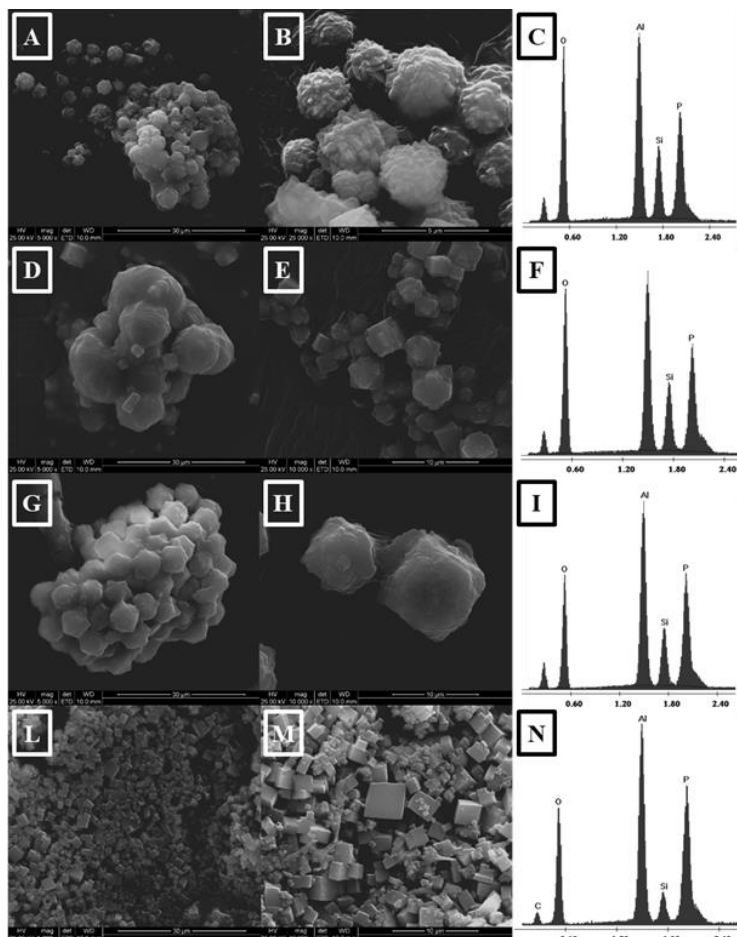


Figure 3.2. Representative SEM image of GLU-S01 (A, B), FRU-S02 (D, E), SUC-S03 (G, H), microporous SAPO-34 (L, M) and energy-dispersive X-Ray spectroscopic microanalysis of GLU-S01 (C), FRU-S02 (F), SUC-S03 (I) and microporous SAPO-34 (N).

The morphological properties of hierarchical SAPO-34 were investigated by scanning electron microscopy (SEM), which showed spherical aggregates of nanosized rhombohedra (Figure 3.2), relatively homogeneously distributed in size and shape, with some minimal hexagonal crystals. Hierarchical SAPO-34 particles are also generally larger than those of the microporous analogue (Figures 3.2 L and 3.2 M), the latter characterized only by the rhombohedral morphology typical of CHA crystals. Energy-dispersive X-Ray (EDX) spectroscopic analyses (Figure 3.2

C, 3.2 F, 3.2 I and 3.2 N), collected in different areas of the SAPO-34 samples, revealed a homogeneous distribution of Al, P and Si within the framework.

The textural properties of hierarchical SAPO-34 systems were investigated by N_2 adsorption/desorption volumetric analysis at 77 K (Figure 3.3).^[17] Whilst microporous SAPO-34 and GLU-S01 exhibited Type I isotherm, which is characteristic of a microporous framework, enhanced N_2 uptake at intermediate-to-high pressures by FRU-S02 and SUC-S03 yielded a Type IV isotherm with hysteresis loop, typical of mesoporosity (Figure 3.3 A). Pore size distributions (Figure 3.3 B) were determined by invoking NLDFT (non-localized density functional theory) to analyze the desorption branch of their respective isotherms.^[18-20] The pore size distribution of microporous SAPO-34 was found to be consistent with microporous CHA structure (Figure 3.3 B, inset). Beside the micropores of the CHA framework, GLU-S01 also exhibited small mesopores of 17 and 25 Å, whereas FRU-S02 and SUC-S03 afforded additional mesoporosity at approximately 38 and 52 Å. Details of the specific surface area and pore volume, determined by the NLDFT method, are summarized in Table 3.2. Encouragingly, when compared to the microporous analogue, FRU-S02 and SUC-S03 showed a substantial enhancement in mesopore volume (V_{meso}), total pore volume (V_{tot}) and mesopore

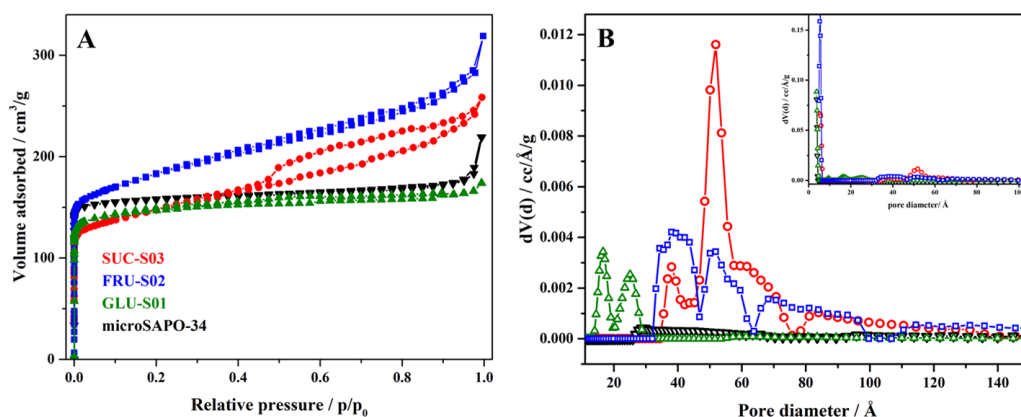


Figure 3.3. A) The N_2 adsorption/desorption isotherms at 77K. B) The pore size distribution in the mesopore range, with pore-size distribution in the micropore and mesopore range (inset).

surface area (S_{meso}). In contrast, GLU-S02 was characterized by a low mesopore pore volume and surface area, being more akin to microporous SAPO-34. In the light of the above, volumetric data confirmed the existence of a multiple level of porosity when the mesopore structure directing agent is fructose or saccharose.

Thermogravimetric and derivative thermogravimetric analyses (TGA/DTG) were carried out to determine the thermal stability of microporous and mesoporous structure directing agents. Thermograms and derivatives of hierarchical SAPO-34 catalysts (Figure 3.4 A and B) revealed a weight loss at 430 °C, which can be assigned to the removal of both organic templates (TEAOH and saccharides). Conversely, the decomposition of TEAOH (the micropore SDA) within the microporous SAPO-34 can be ascribed to a peak at 250 °C. Consequently, the existence of interconnectivity between the micro- and mesopores in hierarchical SAPO-34 catalysts may be hypothesized, such that the micropore SDA cannot be removed until the saccharide template has been decomposed at higher temperature.

Table 3.2. Textural properties of microporous and hierarchical SAPO-34 catalysts.

Catalysts	S_{BET} [m ² g ⁻¹]	S_{DFT} [m ² g ⁻¹]	S_{micro} [m ² g ⁻¹]	S_{meso} [m ² g ⁻¹] ^[a]	Relative mesopore area [%] ^[b]
GLU-S01	316	691	662	29	4.2
FRU-S02	554	968	853	115	11.9
SUC-S03	554	808	690	118	14.6
MicroSAPO-34	477	819	811	8	1.0

^[a] $S_{\text{meso}} = S_{\text{DFT}} - S_{\text{micro}}$; ^[b]Relative mesopore area = $S_{\text{meso}}/S_{\text{DFT}} \times 100$;

Catalysts	V_{DFT} [cm ³ g ⁻¹]	V_{micro} [cm ³ g ⁻¹]	V_{meso} [cm ³ g ⁻¹] ^[c]	Relative mesopore volume [%] ^[d]
GLU-S01	0.24	0.20	0.04	16.7
FRU-S02	0.41	0.22	0.19	46.3
SUC-S03	0.36	0.17	0.19	52.8
MicroSAPO-34	0.26	0.23	0.03	11.5

^[c] $V_{\text{meso}} = V_{\text{DFT}} - V_{\text{micro}}$; ^[d]Relative mesopore volume = $V_{\text{meso}}/V_{\text{DFT}} \times 100$;

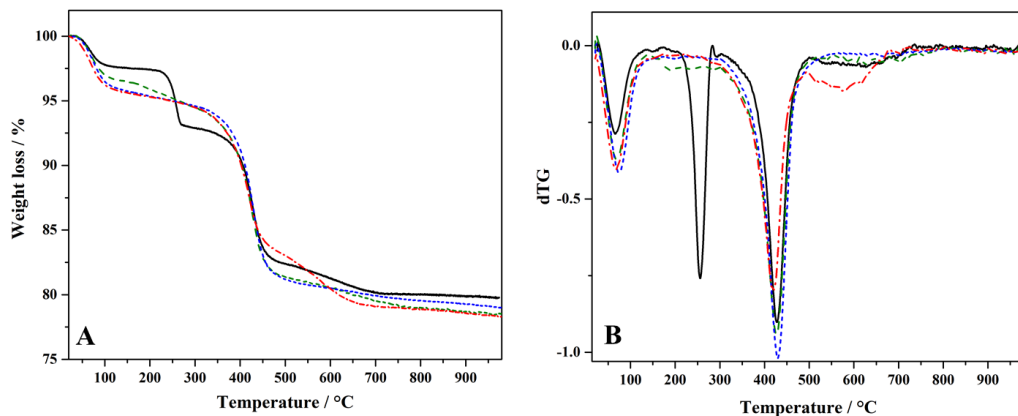


Figure 3.4. A) TGA and B) DTG curves of GLU-S01 (green curve/dash), FRU-S02 (blue curve/short dash), SUC-S03 (red curve/dash dot) and microporous SAPO-34 (black curve/plain).

3.2.2 Spectroscopic characterization

Spectroscopic characterization using solid-state magic angle spinning NMR (SS MAS NMR) and FT-IR spectroscopy of adsorbed probe molecules was performed with the intent to assess the nature, strength, and accessibility of the acid sites.

To probe the chemical environment of the framework atoms in both microporous and hierarchical SAPO-34 samples, ^{27}Al , ^{31}P and ^{29}Si MAS NMR characterization was performed (Figure 3.5). The ^{27}Al spectra of both microporous and hierarchical SAPO-34 exhibited a single signal at approximately 36 ppm, owing to the tetrahedrally-coordinated Al atoms (Figure 3.5 A). No signal at -13 ppm was observed, excluding the presence of octahedrally-coordinated extraframework Al species. For both hierarchical and microporous samples, the signal at ca. -29.8 ppm in the ^{31}P NMR spectra can be attributed to the tetrahedrally-coordinate P atoms (Figure 3.5 B). Since in both ^{27}Al and ^{31}P NMR spectra only a single resonance was observed, the strict alternation of Al and P atoms at the T position of the AlPO framework was confirmed.^[21] The ^{31}P spectrum of the hierarchical catalysts also exhibited a broad tail at approximately -24 ppm, which can be assigned to P-OH defects.^[21] The ^{29}Si NMR spectrum of microporous SAPO-34 revealed signals at -92 , -96 and -101 ppm, owing to the tetrahedrally-coordinated framework Si atoms

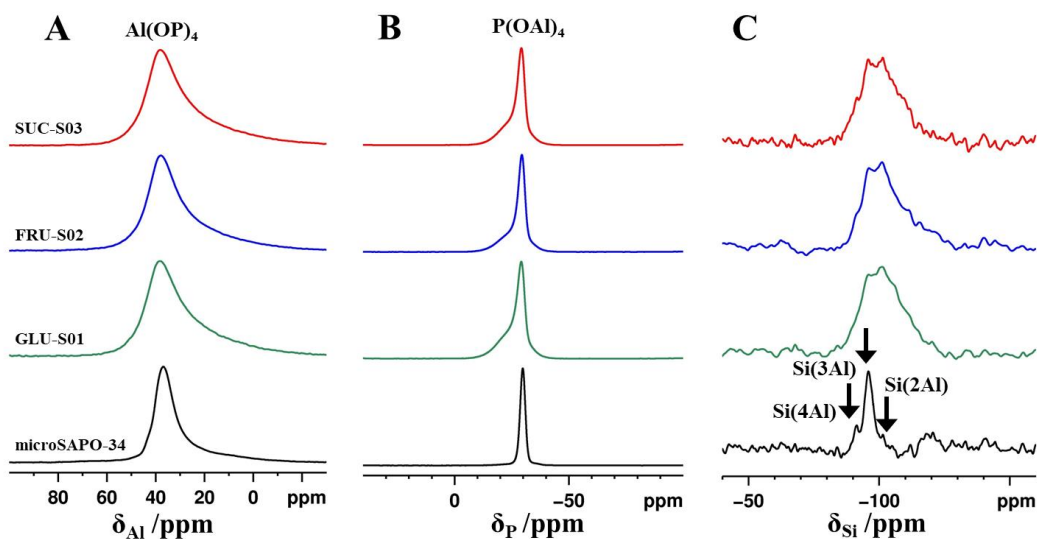


Figure 3.5. A) ^{27}Al , B) ^{31}P and C) ^{29}Si MAS NMR spectra of calcined hierarchical GLU-S01 (green), FRU-S02 (blue), SUC-S03 (red) and microporous SAPO-34 (black).

bonded to four, three and two Al atoms respectively (Figure 3.5 C). The same three resonances were also observed for the hierarchical SAPO-34, despite being broadened by the presence of silicon islands or aluminosilicate islands in the SAPO framework.^[1,22-24] An additional signal at -110 ppm can be appreciated, which is assigned to Q^4 silicon sites and consequently related to the presence of Si islands.

The nature of the acid sites in microporous and hierarchical SAPO-34 was investigated using ^1H SS NMR and FT-IR spectroscopies (Figure 3.6). ^1H SS NMR provided direct information about the different proton environments present in the samples (Figure 3.6 A). A signal at approximately 4 ppm, related to the Brønsted acid sites, was observed in both microporous and hierarchical materials. After the deconvolution, two components at 3.6 and 4 ppm can be distinguished and attributed to the two types of Brønsted acid sites with different acid strength in the O(4) and O(2) structural configuration of the CHA framework.^[23-26] For the hierarchical materials, two weak signals at 2.6 and 1.8 ppm can also be appreciated, owing to P-OH and Si-OH species respectively, whereas proton resonances beyond 4.5 ppm are related to hydrogen-bonded species.^[7,10] Quantitative analysis executed by means

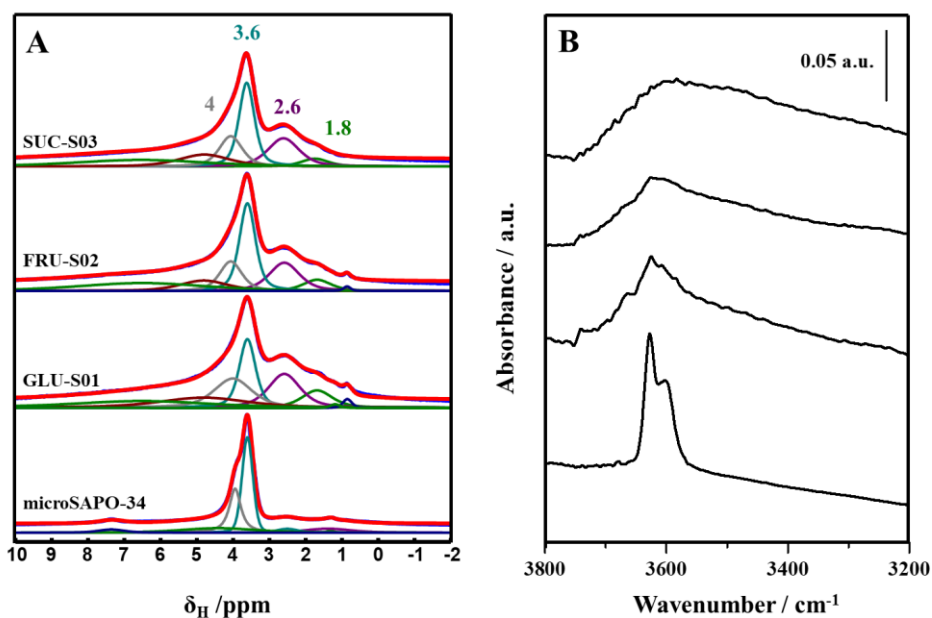


Figure 3.6. A) ^1H SS NMR spectra and B) FT-IR in the O-H stretching region of microporous SAPO-34 and hierarchical GLU-S01, FRU-S02 and SUC-S03.

of ^1H SS NMR (Table 3.3) evidenced that the total number of Brønsted acid sites in hierarchical SAPO-34 catalysts is comparable but lower than in the microporous sample. Conversely, the number of defective species (P–OH and Si–OH) and hydrogen-bonded species is greater in hierarchical materials than in microporous one, as an evidence to the fact that introducing mesoporosity leads to a decrease of

Table 3.3. FT-IR frequencies and population distribution of the protonic species obtained from ^1H SS NMR spectroscopy in microporous and hierarchical SAPO-34 catalysts.

ν_{OH} [cm^{-1}]	^1H chemical shift (δ) [ppm]	Assignment	^1H species [%]			
			GLU	FRU	SUC	microSAPO-34
3745	1.8	Si–OH	9	7	5	-
3678	2.6	P–OH	19	18	20	4
3630	3.6	BAS	21	30	29	42
3600	4.0	BAS	20	14	16	27
3550- 3350	5.5 (centred)	H-bonded species	29	30	30	18

the structural order.

Associated with ^1H SS NMR, FT-IR can help elucidating the differences between the proton species present in the samples. In the O–H stretching region of FT-IR spectra (Figure 3.6 B), microporous SAPO-34 revealed two intense signals at 3630 and 3600 cm^{-1} , which are attributed to the O–H stretching mode of the two types of Brønsted acid sites. The same bands, together with a weak signal at 3745 cm^{-1} arising from isolated Si–OH, can be observed in the spectrum of the hierarchical SAPO-34, though broadened by the high scattering profile.

The strength and accessibility of the acid sites in hierarchical SAPO-34 catalysts was investigated by FT-IR spectroscopy coupled with the adsorption of basic probe molecules. To quantify the total amount of the Brønsted acid sites, NH_3 (0.26 nm kinetic diameter) was employed. This strong base can interact with weakly acid sites through its lone electron pair *via* hydrogen bond, *e.g.* Si–OH and P–OH species, or undergo a proton transfer with strong acid sites, *e.g.* Brønsted acid sites. With respect to its small diameter, NH_3 can enter both the micropores and mesopores of hierarchical SAPO-34 framework and thus interact with BAS which are inaccessible to larger probe molecules, such as substituted pyridines.^[27-28] For this reason, 2,4,6-trimethylpyridine (2,4,6-TMP, 0.74 nm kinetic diameter) is widely used to assess the enhanced accessibility of acid sites in hierarchical zeolites and zeotypes, exploiting the impeded diffusion through small micropores.^[4,10,29-31] Therefore, a comparison between the interaction of the NH_3 and 2,4,6-TMP with the hierarchical framework provides information on the accessibility of the Brønsted acid sites, since 2,4,6-TMP can interact only with acid sites located in the mesopores or at the micropore mouths of hierarchical SAPO-34.^[7,10] Upon NH_3 adsorption (90 mbar), a band at 1619 cm^{-1} , owing to the bending mode of ammonia hydrogen bonded to Si–OH and P–OH, was observed (Figure 3.7 A-C). Moreover, the signal at 1450 cm^{-1} , assigned to the δ_{as} of NH_4^+ ions, revealed that a proton transfer had occurred between NH_3 and the BAS. Similarly, when 2,4,6-TMP interacts with Brønsted acid sites, its inherent basicity ($\text{p}K_{\text{a}} = 7.59$) induces a proton transfer, yielding the protonated species 2,4,6-

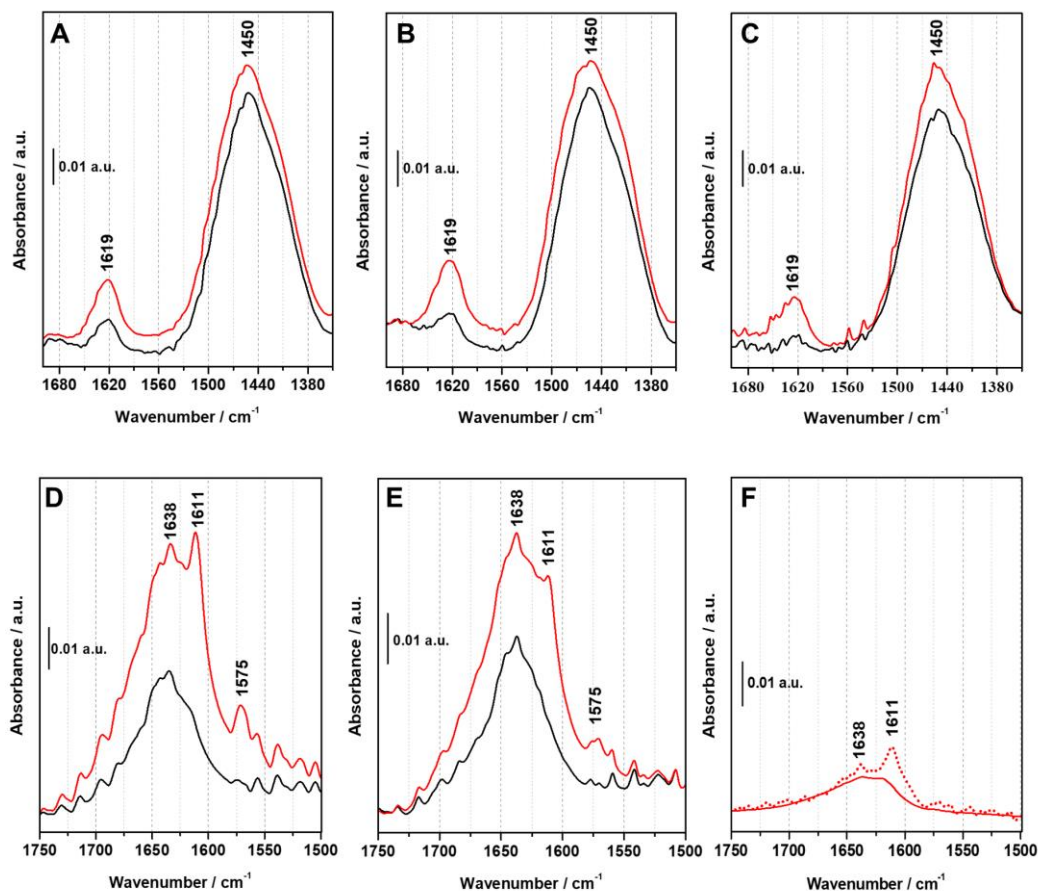


Figure 3.7. FT-IR difference spectra of NH_3 adsorption on A) GLU-S01, B) FRU-S02, C) SUC-S03 and of 2,4,6-TMP adsorption on D) FRU-S02, E) SUC-S03, F) GLU-S01 and microporous SAPO-34 (solid and dotted line, respectively). The spectra are shown before (red curve) and after outgassing the probe molecules at r.t. (black curve).

TMPH^+ . The ν_{8a} stretching mode of 2,4,6-TMP, which in liquid phase is detected at 1611 cm^{-1} , is strongly affected by the presence of Brønsted acid sites in the hierarchical framework, with its position changing in response of the acid-site strength. When the ν_{8a} mode appears at wavenumbers $> 1630\text{ cm}^{-1}$, the formation of the protonated species ($2,4,6\text{-TMPH}^+$) is inferred, whereas a lower wavenumber indicates the formation of a hydrogen-bonded adduct or physisorbed species.^[4,7,10,30] Upon 2,4,6-TMP adsorption (vapour pressure) on FRU-S02 and SUC-S03 (Figure 3.7 D and 3.7 E), signals at 1611 and 1575 cm^{-1} , related to physisorbed 2,4,6-TMP, and a band at 1638 cm^{-1} , owing to $2,4,6\text{-TMPH}^+$, were detected. After outgassing

the catalysts at r. t., signals at 1611 and 1575 cm^{-1} disappeared, whilst the band at 1638 cm^{-1} due to protonated species 2,4,6-TMPH⁺ was retained. This experimental evidence allowed to confirm that a fraction of Brønsted acid sites has been made accessible by the mesoporous network, in accordance with the fact that by introducing mesoporosity into CHA framework, the average micropore length is reduced and the number of accessible acid sites should increase accordingly. The signal at 1638 cm^{-1} was not detected in microporous SAPO-34 and GLU-S01 spectra, indicating that, in the latter case, the mesopores evidenced by volumetric analysis are irrelevant to accessibility arguments. The total number of accessible Brønsted acid sites (N) of hierarchical SAPO-34 catalyst, determined using NH_3 and 2,4,6-TMP and estimated by means of Lambert-Beer law (for further explanation refer to Chapter 9/Experimental section), is reported in Table 3.4., along with the nature and position of the IR bands of their corresponding protonated species. The total number of BAS detected by NH_3 was found to be comparable for all the saccharide-templated SAPO-34 catalysts. The accessibility factor (AF), defined as the number of sites detected by adsorption of the alkylpyridine, divided by the total number of Brønsted acid sites detected by NH_3 adsorption, was also evaluated for 2,4,6-trimethylpyridine. The AF was found to be similar for FRU-S02 and SUC-S03.

Table 3.4. The total number of accessible Brønsted acid sites (N) in hierarchical SAPO-34.

Catalyst	Protonated species	Position of IR band of the protonated species [cm^{-1}]	N [$\mu\text{mol g}^{-1}$]	AF
GLU-S01	NH_4^+ ^[a]	1450 (δ_{as})	43.88	1
	NH_4^+ ^[a]	1450 (δ_{as})	40.39	1
FRU-S02	2,4,6-TMPH ⁺ ^[b]	1638 (ν_{8a})	3.13	0.077
	NH_4^+ ^[a]	1450 (δ_{as})	40.73	1
SUC-S03	2,4,6-TMPH ⁺ ^[b]	1638 (ν_{8a})	2.95	0.072

^[a] $\epsilon = 0.147 \text{ cm}^2 \mu\text{mol}^{-1}$.^[32] ^[b] $\epsilon = 0.62 \text{ cm}^2 \mu\text{mol}^{-1}$.^[31]

3.2.3 Catalysis

On the basis of these promising characterization results, the catalytic activity of the saccharide-templated SAPO-34 catalysts was evaluated in the liquid-phase Beckmann rearrangement of cyclohexanone oxime to ϵ -caprolactam (the industrially-significant precursor to Nylon-6) and directly compared to that of the microporous SAPO-34 (Figure 3.8). Conventional microporous SAPO-34 showed a very poor activity, with only 15 % yield and 29 % conversion achieved after 6 h of reaction. This behaviour is due to inaccessibility of the internal Brønsted acid sites to cyclohexanone oxime. The catalytic activity of GLU-S01 was unsurprisingly found to be comparable (or even lower) to the microporous analogue, with only 10

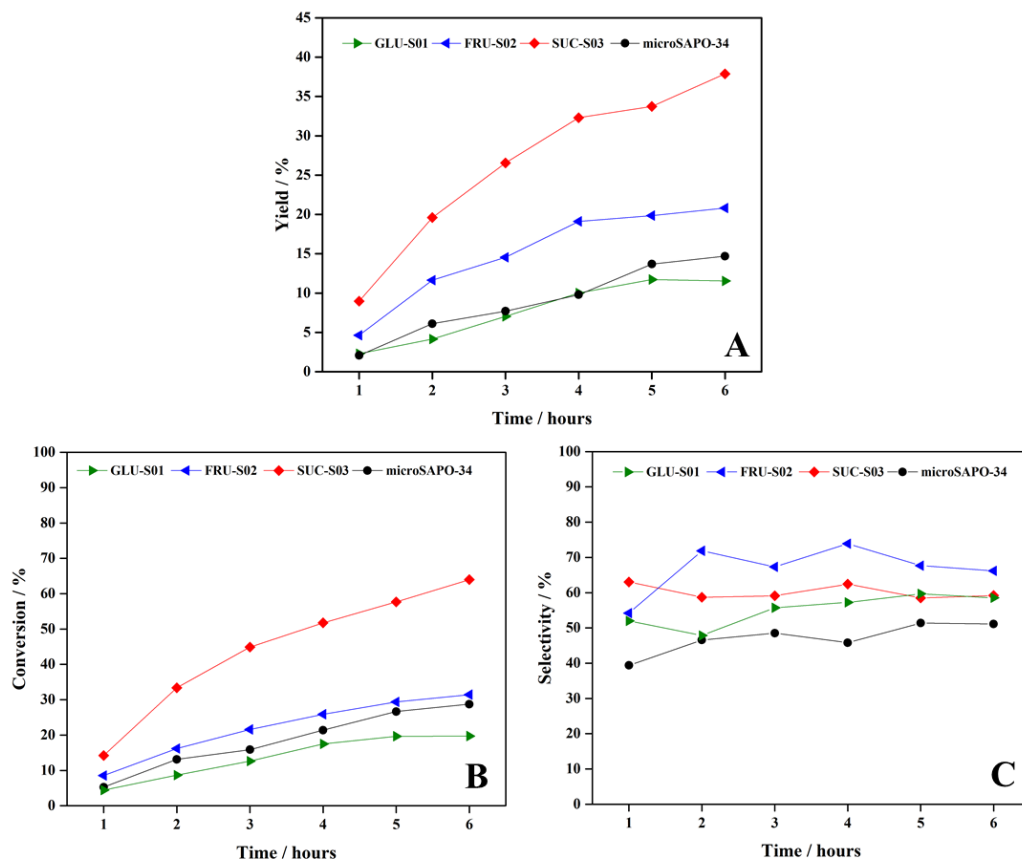


Figure 3.8. Comparison of A) the yield of ϵ -caprolactam, B) the conversion of cyclohexanone oxime and C) the selectivity towards ϵ -caprolactam in the liquid-phase Beckman rearrangement at 130°C under acid heterogeneous catalysis.

% yield and 20 % conversion achieved after 6 h of reaction. This inferior catalytic performance was consistent with textural and FT-IR with adsorption bulky 2,4,6-TMP characterization, which had assessed the inferior textural features of GLU-S01 together with the absence of BAS located on the mesopore surface. SUC-S03 exhibited the best performance among all the hierarchical catalyst, achieving 40 % yield and 64% conversion in the same 6 h period. Despite physico-chemical characterization had confirmed the hierarchical nature of FRU-S03, together with the enhanced accessibility of its BAS, its catalytic activity was proven to be noticeably inferior to that of SUC-S03, with only 20 % yield and 31 % conversion after 6 h of reaction. The differences in catalytic performance between the two samples could be related to a more impeded diffusion of the cyclohexanone oxime within the mesoporous framework of FRU-S02. Considering that the Beckmann rearrangement is conventionally performed at temperatures above 325 °C (vapour phase), a catalytic activity of SUC-S03 (when to the microporous analogue) should be considered a very promising result, ascribable to the superior diffusion afforded by the hierarchical architecture at lower temperatures (130 °C). Lastly, all the hierarchical SAPO-34 catalysts showed a higher selectivity towards ϵ -caprolactam than the microporous analogue (Figure 3.8 C), thus confirming the retention of the acidic properties and textural features with respect to the microporous analogue.

3.3 Conclusions

Physico-chemical characterization and catalytic tests have assessed that saccharide templating with fructose and saccharose is an effective low-cost soft-templating bottom-up method of synthesising hierarchical SAPO-34, introducing secondary porosity without the need for a sophisticated mesoporegen. Conversely, glucose has proven to be essentially ineffective in introducing mesoporosity in the SAPO-34 framework, resulting in a catalyst with textural properties, accessibility of the acid sites and catalytic activity comparable (if not inferior) to the microporous SAPO-34. The inefficacy of this saccharide in generating additional porosity may be

ascribed to the low concentration used in the synthesis gel. Nandan *et al.* reported that a low glucose concentration leads to smaller mesopores and textural features comparable to microporous analogues.^[12] Fructose and saccharose-templated catalysts exhibited superior textural properties, with substantial enhancement in mesopore volume and mesopore surface area. Besides having made a fraction of Brønsted acid centres accessible by the mesoporous network, the acid properties proved to be comparable to the microporous SAPO-34 analogue. Hence, by selecting an appropriate mono- or di- saccharide mesoporegen, effective modulation of the mesopore dimension could be achieved, mimicking at the same time the acidic properties of the microporous framework. Although the synthesis of a hierarchical framework had been successfully achieved with both mono- and di- saccharides, the use of saccharose as mesoporegen resulted in a hierarchical SAPO-34 with superior catalytic performances in the liquid-phase Beckmann rearrangement. Such an increase in the catalytic activity may be related to an enhancement of mass-transport capabilities with respect to the fructose-templated catalyst.

3.4 Notes and references

- [1] A. Corma, *Chem. Rev.* **1997**, 97, 2373.
- [2] J. Jiang, J.L. Jorda, J. Yu, L.A. Baumes, E. Mugnaioli, M.J. Diaz-Cabanas, U. Kolb, A. Corma, *Science* **2011**, 333, 1131.
- [3] M. Choi, K. Na, J. Kim, Y. Sakamoto, O. Terasaki, R. Ryoo, *Nature* **2009**, 461, 246.
- [4] E. Gianotti, M. Manzoli, M. E. Potter, V.N. Shetti, D. Sun, A.J. Paterson, T.M. Mezza, A. Levy, R. Raja, *Chem. Sci.* **2014**, 5, 1810.
- [5] R. Raja, M.E. Potter, S.H. Newland, *Chem. Commun.* **2014**, 50, 5940.
- [6] M.E. Potter, D. Sun, E. Gianotti, M. Manzoli, R. Raja, *Phys. Chem. Chem. Phys.* **2013**, 15, 13288.
- [7] A. Erigoni, S.H. Newland, G. Paul, L. Marchese, R. Raja, E. Gianotti, *ChemCatChem* **2016**, 8, 3161.

- [8] X. Zhu, J.P. Hofmann, B. Mezari, N. Kosinov, L. Wu, Q. Qian, B. M. Weckhuysen, S. Asahina, J. Ruiz-Martinez, E.J.M. Hensen, *ACS Catal.* **2016**, 6, 2163.
- [9] S.H. Newland, W. Sinkler, T. Mezza, S.R. Bare, M. Caravetta, I.M. Haies, A. Levy, S. Keenan, R. Raja, *ACS Catal.* **2015**, 5, 6587.
- [10] I. Miletto, G. Paul, S. Chapman, G. Gatti, L. Marchese, R. Raja, E. Gianotti, *Chem. Eur. J.* **2017**, 23, 9952.
- [11] Q. Sun, N. Wang, D. Xi, M. Yang, J. Yu, *Chem. Commun.* **2014**, 50, 6502.
- [12] D. Nandan, S. K. Saxena, N. Viswanadham, *J. Mater. Chem. A* **2014**, 2, 1054.
- [13] X. Yang, T. Lu, C. Chen, L. Zhou, F. Wang, Y. Su, J. Xu, *Microporous Mesoporous Mater.* **2011**, 144, 176.
- [14] Z. Liu, L. Liu, H. Song, C. Wang, W. Xing, S. Komarneni, Z. Yan, *Mater. Lett.* **2015**, 154, 116.
- [15] I. Miletto, C. Ivaldi, G. Paul, S. Chapman, L. Marchese, R. Raja, E. Gianotti, *ChemistryOpen* **2018**, 7, 297.
- [16] A.M. Prakash, S. Unnikrishnan, *J. Chem. Soc. Faraday Trans.* **1994**, 90, 2291.
- [17] K.A. Cychoz, R. Guillet-Nicolas, J. Garcia-Martinez, M. Thommes, *Chem. Soc. Rev.* **2017**, 46, 389.
- [18] J. Landers, G.Y. Gor, A.V. Neimark, *Colloids Surf. A* **2013**, 437, 3.
- [19] M. Thommes, K.A. Cychoz, *Adsorption* **2014**, 20, 233.
- [20] M. Errahali, G. Gatti, L. Tei, G. Paul, G. A. Rolla, L. Canti, A. Fraccarollo, M. Cossi, A. Comotti, P. Sozzani, L. Marchese, *J. Phys. Chem. C* **2014**, 118, 28699.
- [21] B. Zibrowius, E. Loffler, M. Hunger, *Zeolites* **1992**, 12, 167.
- [22] X. Chen, A. Vicente, Z. Qin, V. Ruaux, J.-P. Gilson, V. Valtchev, *Chem. Commun.* **2016**, 52, 3512.
- [23] G.A.V. Martins, G. Berlier, S. Coluccia, H.O. Pastore, G.B. Superti, G. Gatti, L. Marchese, *J. Phys. Chem. C* **2007**, 111, 330; b) G.A.V. Martins, G. Berlier, C. Bisio, S. Coluccia, H.O. Pastore, L. Marchese, *J. Phys. Chem. C* **2008**, 112, 7193.

-
- [24] A. Buchholz, W. Wang, A. Arnold, M. Xu, M. Hunger, *Microporous Mesoporous Mater.* **2003**, 57, 157.
- [25] L. Smith, A.K. Cheetham, L. Marchese, J.M. Thomas, P.A. Wright, J. Chen, E. Gianotti, *Catal. Lett.* **1996**, 41, 13.
- [26] S. Bordiga, L. Regli, C. Lamberti, A. Zecchina, M. Jorgen, K.P. Lillerud, *J. Phys. Chem. B* **2005**, 109, 7724.
- [27] J.M.R. Gallo, C. Bisio, G. Gatti, L. Marchese, H.O. Pastore, *Langmuir* **2010**, 26, 5791.
- [28] A. Zecchina, L. Marchese, S. Bordiga, C. Pazè, E. Gianotti, *J. Phys. Chem B* **1997**, 101, 10128.
- [29] F. Thibault-Starzyk, I. Stan, S. Abellk, A. Bonilla, K. Thomas, C. Fernandez, J.-P. Gilson, J. Perez-Ramirez, *J. Catal.* **2009**, 264, 11.
- [30] F. Thibault-Starzyk, A. Vimont, J.-P. Gilson, *Catal. Today* **2001**, 70, 227.
- [31] K. Mlekodaj, K. Tarach, J. Datka, K. Gkra-Marek, W. Makowski, *Microporous Mesoporous Mater.* **2014**, 183, 54.
- [32] J. Datka, B. Gil, A. Kubacka, *Zeolites* **1995**, 15, 501.

4

Hierarchical silicoaluminophosphate SAPO-34 architectures with tunable acid properties synthesised from mesoporous silica scaffolds

In the present chapter, a distinctive bottom-up synthetic methodology for the preparation of a hierarchical SAPO-34, using cetyl trimethylammonium bromide (CTAB) encapsulated within an ordered mesoporous silica (MCM-41) as both the silicon source as mesoporegen, has been described. Structural, morphological, and textural properties of the catalyst were investigated by means of detailed physico-chemical characterization and compared to its microporous analogue. Solid-state NMR and probe-based FT-IR spectroscopies were performed to gain insight on the nature, strength, and accessibility of Brønsted acid sites (BAS). Moreover, the catalytic activity of the hierarchical catalyst was evaluated in the industrially-relevant acid-catalysed Beckmann rearrangement of cyclohexanone oxime to ϵ -caprolactam, under vapour-phase conditions.

Introduction

Zeolites and zeotype materials are a significant and well-established class of industrial heterogeneous catalysts, especially for acid-catalysed chemical transformations, owing to their molecular sieving capabilities and high robust nature, together with the possibility of optimizing the nature and strength of acid active sites and tuning textural properties for specific reactions and applications.^[1-4]

Among zeolitic materials, silicoaluminophosphates (SAPOs) represent a viable alternative to zeolite for application requiring acid catalysis.^[5-6] Notably, SAPO-34, with chabazite (CHA) topological structure, has been extensively studied on account of its potential application in CO₂/CH₄ separation^[7] and hydrogen purification,^[8] in addition to its well-known industrial role in the methanol-to-olefine (MTO) process (100% methanol conversion and > 90 % selectivity to C₂-C₄ light olefins).^[9-11] Nevertheless, the narrow, 8-ring pore aperture (3.8 × 3.8 Å) of microporous SAPO-34 severely impedes molecular motions, resulting in pore blockage due to the coke formation/deposition with prolonged time on-steam.^[12] Recently, hierarchical zeotypes, which retain the bulky microporous structure but possess an additional mesoporous network which improves mass transport to internal active sites, strongly emerged as novel materials for catalytic applications to overcome typical drawbacks of traditional microporous systems.^[13,14] To obtain a hierarchical framework, both top-down^[15-17] and bottom-up^[18,19] synthetic strategies have been explored. Commonly, top-down approaches, such as demetallation, involve post-synthesis modification, in acid or alkali media, to partially extract framework constituents, whilst retaining crystallinity. Although localized collapse of the zeolitic architecture generates mesopore, it simultaneously leads to the production of defect sites which alter the textural and acidic characteristic of the parent framework. Furthermore, top-down method has been hardly ever performed on silicoaluminophosphates,^[17,20] owing to their relative instability under strongly acid or alkaline conditions.^[20] The alternative soft-templating bottom-up approach, which exploits the use of surfactants to direct the mesoporous network, is relatively facile, benefits from a high degree of structural control (the micellar structure can be controlled by the choice of the surfactant molecule and the use of additives, such as swelling agents), whilst preserving the acidic properties of the microporous framework.^[21] Despite these advantages, bottom-up approach traditionally requires the use of sophisticated and sacrificial siliceous surfactants/mesoporegen which, besides being really expensive, results in the incorporation of siliceous species into the mesopores walls, thus

altering the acidic properties of the parent framework.^[19,22-25] Owing to the immense catalytical potential of hierarchically porous systems, many attempts to identify alternative low-cost, less-sophisticated mesopore templating agents, compatible with conventional one-pot synthesis, have been made recently. In light of the foregoing, a novel bottom-up approach for the preparation of hierarchical SAPO-34 acid catalyst, using cetyl trimethylammonium bromide (CTAB) encapsulated within an ordered mesoporous silica (MCM-41) as both the silicon source as mesoporegen, will be described in the present chapter.^[26] This innovative synthetic strategy benefits from superior retention of acidic characteristic of the microporous parent framework, whilst simultaneously enhancing its mass transport capabilities together with accessibility of the acid active sites. Structural, morphological, textural and spectroscopic characterization have been provided with the aim of establishing preliminary structure-property relationship and facilitating mechanistic studies which ultimately aid further catalyst optimization. To this end, the catalytic activity of hierarchical SAPO-34 has been evaluated in the vapour-phase Beckmann rearrangement of cyclohexanone oxime to ϵ -caprolactam, the monomeric precursor of the Nylon-6 polymer.

4.1 Experimental section

4.1.1 General

Aluminum isopropoxide ($\geq 98\%$), tetraethylammonium hydroxide (35 wt% in H₂O), tetraethyl orthosilicate) and phosphoric acid (85 wt% in H₂O), all used for the synthesis of SAPO-34 materials, were supplied by Sigma-Aldrich (Milano, Italy). NH₃ ($\geq 99.7\%$) and CO (99.5%), purchased from SIAD (Bergamo, Italy) and pyridine ($\geq 99\%$), 2,4,6-trimethylpyridine ($\geq 98\%$), 2,6-di-tert-butylpyridine ($\geq 97\%$), purchased from Sigma Aldrich (Milano, Italy), were used as probe molecule in FT-IR experiments.

4.1.2 Synthesis of SAPO-34

Hierarchical SAPO-34 catalyst was prepared following a bottom-up soft-templating strategy, in which pre-synthesised MCM-41 with the surfactant (CTAB) inside the mesopores was used as both the silicon source as mesoporous structure directing agent (SDA_{meso}).^[27] A microporous SAPO-34 was also synthesised for comparison of the physico-chemical properties and the catalytic activity. After crystallization, recovering and washing, all the samples were calcined to remove the organic templates.

Synthesis of hierarchical SAPO-34: hierarchical catalysts were synthesised according to the following hydrothermal procedure. Aluminium isopropoxide (7.00 g) was slowly added to tetraethylammonium hydroxide (TEAOH, 14.00 ml, 35 wt% in H₂O) under stirring. Deionized water (21 mL) was added and the mixture was stirred for 1 h. CTAB-containing MCM-41 (2.11 g, prepared following the methodology reported in literature by Radu *et al.*^[27]) was slowly added and the mixture was further stirred for 2h. Lastly, phosphoric acid (2.33 ml, 85 wt% in H₂O), Fumed silica (1.24 g) was added dropwise and the resulting white gel of molar composition 1.0 Al/1.0 P/0.58 Si/1 TEAOH/0.067 CTAB/60 H₂O was vigorously stirred for 30 min. The gel was transferred to a Teflon-lined stainless-steel autoclave and crystallize at 200 °C for 60 h under autogenous pressure. The solid product was centrifugate and washed with water. The as-prepared product was dried in air at 100 °C and calcined in a tube furnace under air flow at 600 °C for 16 h, producing a white crystalline solid.

Synthesis of microporous SAPO-34: microporous SAPO-34 was synthesised according to the following hydrothermal procedure. Aluminium isopropoxide (7.00 g) was added slowly to tetraethylammonium hydroxide (TEAOH, 14.00 ml, 35 wt% in H₂O) under stirring. Deionized water (21 ml) was added and the mixture was stirred for 1 h. Tetraethylorthosilicate (TEOS, 1.14 ml) was added dropwise under stirring and the mixture was further stirred for 2 h. Phosphoric acid (2.33 ml, 85 wt% in H₂O) was added dropwise under stirring. The gel was vigorously stirred for 30

min to produce a white gel of molar composition 1.0 Al/1.0 P/0.15 Si/1 TEAOH/50 H₂O. The gel was transferred to a Teflon-lined stainless-steel autoclave and crystallized at 200 °C for 60 h under autogenous pressure. The solid product from autoclave was then recovered by filtration and washed with water. The as-prepared product was dried in air at 100 °C and calcined in a tube furnace under air flow at 600 °C for 16 h to produce a white crystalline solid.

4.1.3 Characterization

Before performing volumetric and spectroscopic measurements, calcined samples were outgassed at 300 °C overnight and for 2 h, respectively, to remove physisorbed water. Further details on the experimental techniques are reported in Chapter 9/Experimental section.

4.1.4 Catalysis

A cylindrical (4 mm diameter), quartz, fixed-bed reactor with a quartz frit was packed with 0.5 cm layer of glass beads (1 mm). The catalyst (0.2 g) was pelletized and added to the reactor, followed by a further 20 cm of glass beads (1 mm). The reactor was transferred into the heater unit of the flow-reactor setup. The catalyst was pre-treated by heating at 400 °C for 1 h under a 50 mL min⁻¹ flow of helium gas. The temperature and flow of helium gas were then reduced to 325 °C and 33.3 mL min⁻¹, respectively. A liquid-feed of 100 g L⁻¹ of cyclohexanone oxime in ethanol was fed, through an electronic syringe pump, into the reactor in order to maintain a weight hourly space velocity (WHSV) of 0.79 h⁻¹. As an external standard, a liquid feed of 100 g L⁻¹ of mesitylene in ethanol was simultaneously introduced into the exit feed using a WHSV of 0.79 h⁻¹. Once steady-state was established, samples were collected hourly and analysed using the Clarus 480 gas chromatograph flame ionisation detector (FID) and an Elite 5 column. Product formation was quantified against the mesitylene external standard.

4.2 Results and discussion

4.2.1 Synthesis

Hierarchical porous SAPO-34 (HP-SAPO-34) was prepared using a bottom-up soft-templating method, in which a pre-synthesised MCM-41, with the surfactant (CTAB) encapsulated inside the mesopores, was used both as the silicon source as mesoporegen. The addition of CTAB-containing MCM-41 to the reaction mixture promotes the gradual dissolution of the silica framework (Step 1, Figure 4.1), providing the silicic acid monomers that serve as silicon source for the synthesis of SAPO-34 framework (Step 2, Figure 4.1). The presence of CTAB inside the mesopores might slow the hydrolysis rate and collapse of the silica framework; therefore, SAPO-34 crystallization might preferentially occur along the CTAB-templated MCM-41 pore system.^[28]

4.2.2 Morphological, structural and textural characterization

Inductively-coupled plasma atomic emission spectrometry (ICP-AES) was performed to determine the experimental framework composition of the hierarchical SAPO-34 catalysts (Table 4.1). Notably, Si/(Si+Al+P) ratio was in good agreement with the theoretical value determined from the synthesis gel composition.

The morphological properties of hierarchical SAPO-34 were investigated by scanning electron microscopy (SEM). Significantly, the morphology of HP-SAPO-34 (Figure 4.2 A) turned out differently from both its microporous analogue (Figure

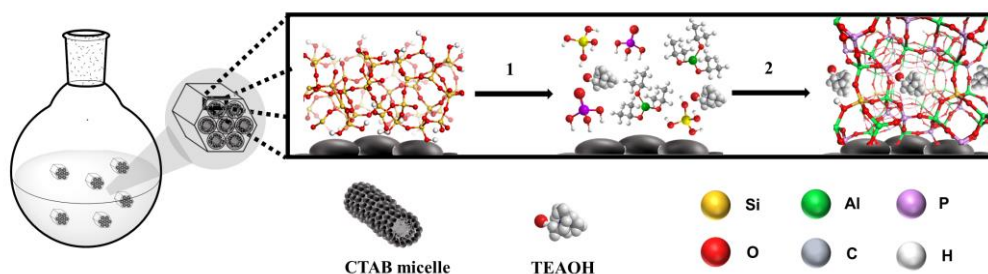


Figure 4.1. Schematic representation of the synthesis mechanism of HP-SAPO-34 using CTAB-containing MCM-41 as both the silicon source as the mesoporegen.

Table 4.1. Inductively-coupled plasma chemical analysis of SAPO-34 catalysts.

Acronym	Si [wt %]	Al [wt %]	P [wt %]	Si/ Si + Al + P ^[a]	Si/ Si + Al + P ^[b]
HP-SAPO-34	8.08	15.05	12.64	0.23	0.23
MicroSAPO-34	6.93	15.79	13.05	0.19	0.23

[a] Experimental framework composition determined by ICP analysis after the synthesis.

[b] Theoretical framework composition determined from the synthesis gel composition.

C) and mesoporous MCM-41 (Figure 4.2 C). Moreover, energy-dispersive X-ray (EDX) spectroscopic analyses (Figure 4.2 D), collected in different area of the hierarchical sample, evidenced a homogeneous distribution of Al, P, and Si, with no evidence of MCM-41-type particles.

X-Ray powder diffraction (XRDP) was carried out with the aim of elucidating the structural features of HP-SAPO-34 catalyst (Figure 4.3). The XRD pattern of HP-

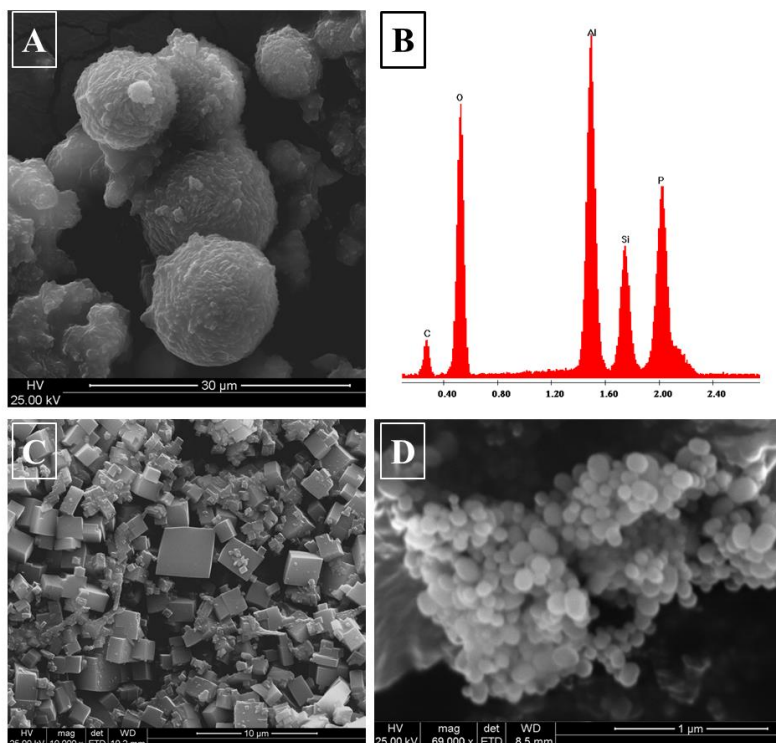


Figure 4.2. Representative SEM image of HP-SAPO-34 (A), microSAPO-34 (C), and MCM-41 (D) and energy-dispersive X-Ray spectroscopic microanalysis of HP-SAPO-34 (A).

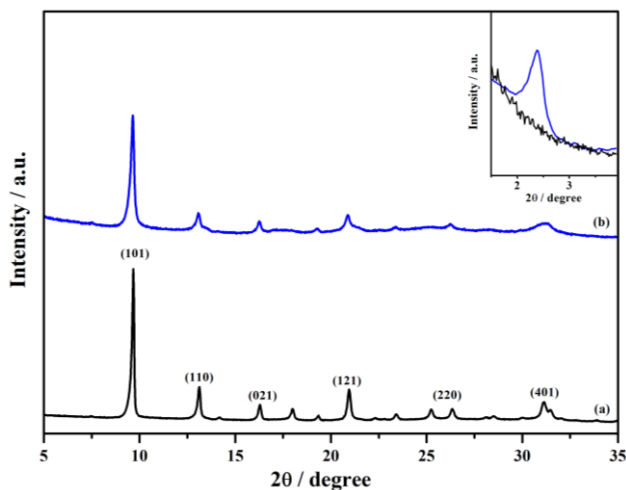


Figure 4.3. The powder XRD pattern of microporous SAPO-34 (a, black curve) and HP-SAPO-34 (b, blue curve), with the low-angle pattern (inset).

SAPO-34 exhibited all the characteristic reflections of CHA framework, therefore confirming phase purity and crystallinity of the sample.^[29] Additionally, small-angle XRD measurement of HP-SAPO-34 (Figure 4.3, inset) revealed a reflection at ca. 2° 2θ , which was absent in the microporous sample, indicating the presence of ordered mesoporosity.

The textural properties of HP-SAPO-34 catalyst were investigated by N_2 adsorption/desorption volumetric analysis at 77 K (Figure 4.4).^[30] Whilst microporous SAPO-34 exhibited Type I isotherm, which is typical of a microporous framework, enhanced N_2 uptake at intermediate-to-high pressures by HP-SAPO-34 yielded a Type IV isotherm with hysteresis loop, which is characteristic of mesoporous materials (Figure 4.4 A). Pore size distributions (Figure 4.4 B) were determined by invoking NLDFT (non-localized density functional theory) to analyze the desorption branch of their respective isotherms.^[31,32] The pore size distribution of microporous SAPO-34 was found to be consistent with microporous CHA framework (Figure 4.4 B, inset). Beside the micropores of the CHA framework, HP-SAPO-34 catalyst also afforded additional micropores at approximately 19 \AA , as well as mesopores at 33 and 51 \AA (Figure 4.4 B). Details of the specific surface area and

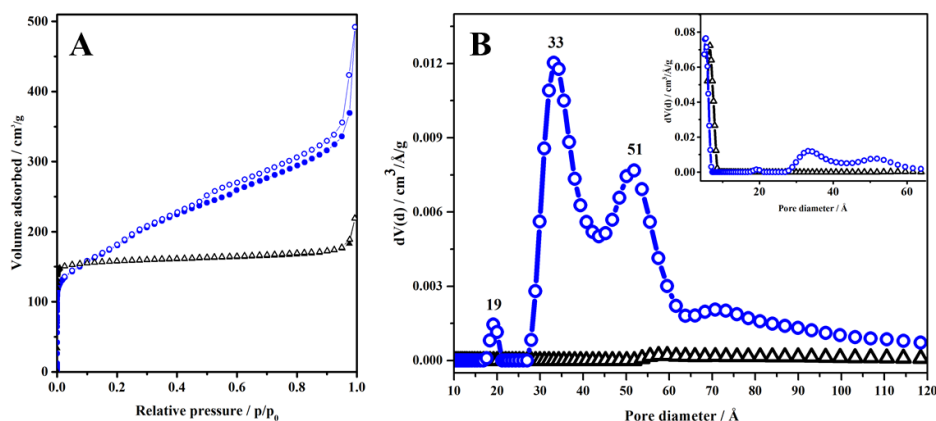


Figure 4.4. A) The N_2 adsorption/desorption isotherms at 77K of HP-SAPO-34 (blue curve) and microporous SAPO-34 (black curve) B) The pore size distribution in the mesopore range, with pore-size distribution in the micropore and mesopore range (inset).

pore volumes, determined by the NLDFT method, are summarized in Table 4.2. Encouragingly, when compared to the microporous analogue, HP-SAPO-34 revealed a substantial enhancement in mesopores volume (V_{meso}), total pore volume (V_{DFT}) and mesopore surface area (S_{meso}). In the light of the previous considerations, volumetric data strongly confirmed the existence of a multiple level of porosity (micro and mesoporosity) within HP-SAPO-34.

Table 4.2. Textural properties of HP-SAPO-34 and microporous SAPO-34 catalysts.

Catalysts	S_{BET} [$\text{m}^2 \text{g}^{-1}$]	S_{DFT} [$\text{m}^2 \text{g}^{-1}$]	S_{micro} [$\text{m}^2 \text{g}^{-1}$]	S_{meso} [$\text{m}^2 \text{g}^{-1}$] ^[a]	Relative mesopore area [%] ^[b]
HP-SAPO-34	641	783	511	272	34.7
MicroSAPO-34	477	819	811	8	1.0
MCM-41	1110	1267	-	-	-

^[a] $S_{\text{meso}} = S_{\text{DFT}} - S_{\text{micro}}$; ^[b]Relative mesopore area = $S_{\text{meso}}/S_{\text{DFT}} \times 100$;

Catalysts	V_{DFT} [$\text{cm}^3 \text{g}^{-1}$]	V_{micro} [$\text{cm}^3 \text{g}^{-1}$]	V_{meso} [$\text{cm}^3 \text{g}^{-1}$] ^[c]	Relative mesopore volume [%] ^[d]
HP-SAPO-34	0.58	0.13	0.45	77.5
MicroSAPO-34	0.26	0.23	0.03	11.5
MCM-41	1.3	-	1.3	-

^[c] $V_{\text{meso}} = V_{\text{DFT}} - V_{\text{micro}}$; ^[d]Relative mesopore volume = $V_{\text{meso}}/V_{\text{DFT}} \times 100$;

4.2.3 Spectroscopic characterization

Solid-state NMR (SS NMR) and probe-based FT-IR spectroscopies were performed to assess the nature, strength, and accessibility of the acid sites.

With the aim of probing the chemical environment of the framework atoms in both microporous and hierarchical SAPO-34 samples, ^{27}Al , ^{31}P and ^{29}Si MAS NMR characterization was carried out (Figure 4.5). For both microporous and HP-SAPO-34, the single signal at approximately 36 ppm in the ^{27}Al spectra can be assigned to the tetrahedrally-coordinated Al atoms (Figure 4.5 A). No resonance peak at -13 ppm was detected, excluding the presence of octahedrally-coordinated extraframework Al species. The ^{31}P NMR spectra of both hierarchical and microporous samples exhibited a signal at *ca.* -29.8 ppm, owing to tetrahedrally-coordinate P atoms (Figure 4.5 B). The presence of a single resonance peak in both ^{27}Al and ^{31}P NMR spectra confirmed the strict alternation of Al and P atoms at the T-positions of the AIPO framework.^[33] A broad tail at approximately -24 ppm was also detected in ^{31}P NMR spectrum of HP-SAPO-34, which can be assigned to P-OH groups or otherwise might indicate changes in the second coordination sphere due to Al speciation. These changes cannot be appreciated in the corresponding ^{27}Al NMR spectra as a result of the broadening beyond detection.^[34] The ^{29}Si cross-polarization (CP) MAS NMR spectrum of microporous SAPO-34 exhibited signals

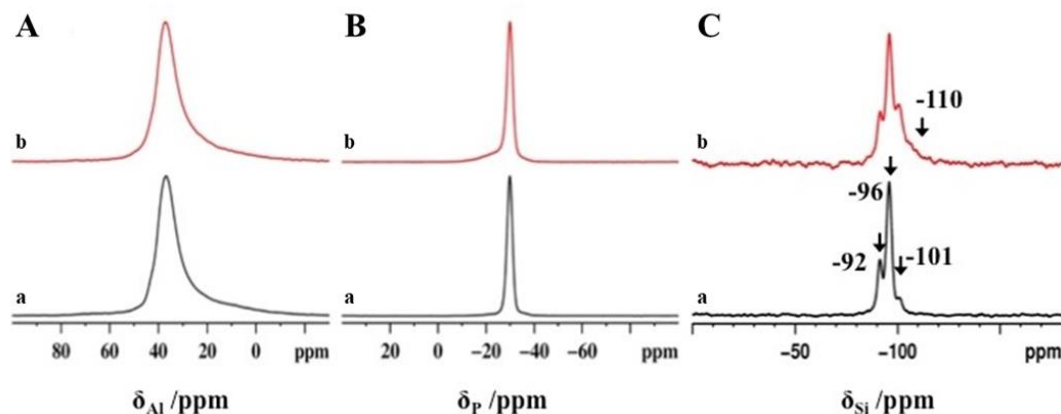


Figure 4.5. A) ^{27}Al , B) ^{31}P and C) ^{29}Si MAS NMR spectra of calcined microporous SAPO-34 (a, black) and HP-SAPO-34 (b, red curve).

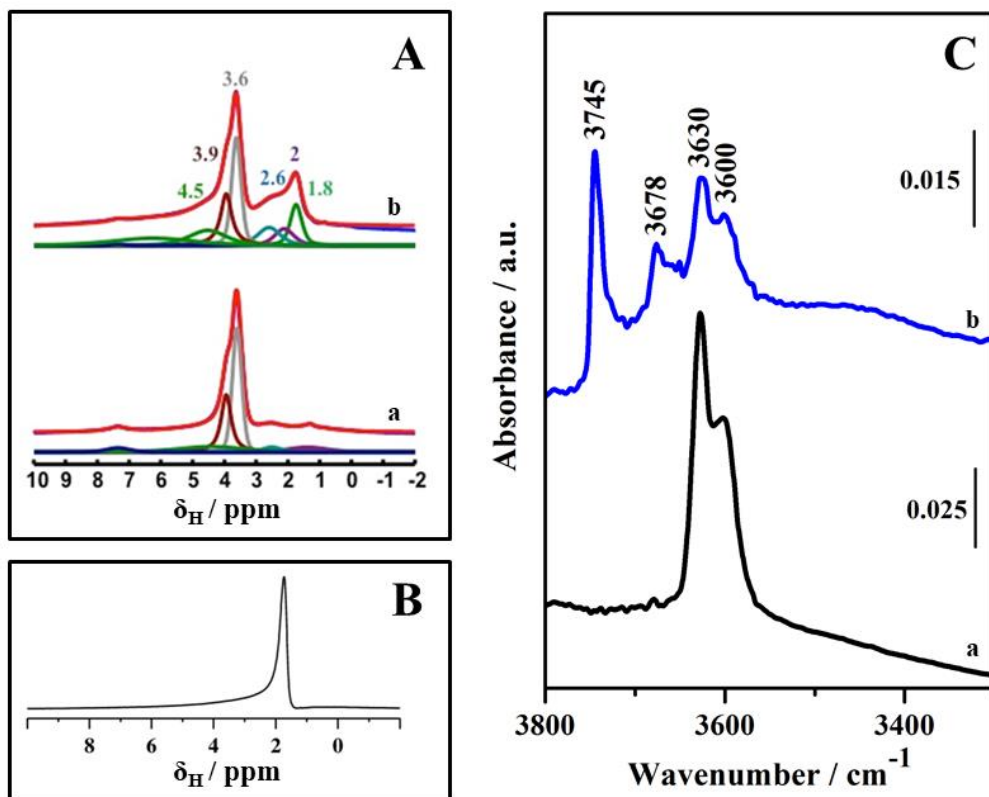


Figure 4.6. ^1H SS NMR spectra of A) of microporous SAPO-34 (a), HP-SAPO-34 (b) and B) MCM-41. C) FT-IR spectra in the O-H stretching region of microporous SAPO-34 (a, black curve) and HP-SAPO-34 (b, blue curve).

at -92 , -96 and -101 ppm, related to the tetrahedrally-coordinated framework Si atoms coordinated to four, three and two Al atoms respectively (Figure 4.5 C). The same three resonance peaks were also detected in the spectrum of HP-SAPO-34, despite being broadened by the presence of silicon islands or aluminosilicate islands in the SAPO framework.^[1,17,35,36]

The nature of the acid sites in microporous and HP-SAPO-34 was investigated by means of ^1H SS NMR and FT-IR spectroscopies (Figure 4.6). ^1H SS NMR provided direct information about the different proton environments present in the samples (Figure 4.6 A). A resonance peak at approximately 4 ppm, assigned to the Brønsted acid sites, was detected in the spectra of both microporous and hierarchical SAPO-34. After the deconvolution, two components at 3.6 and 4 ppm, attributed to

Table 4.3. FT-IR frequencies and population distribution of the protonic species obtained from ^1H SS NMR spectroscopy in microporous and hierarchical SAPO-34 catalysts.

ν_{OH} [cm^{-1}]	^1H chemical shift (δ) [ppm]	Assignment	^1H species [%]	
			HP-SAPO-34	MicroSAPO-34
3745	1.8	Si–OH	12	-
3745 tail	2.0	Si–OH	8	-
3678	2.6	P–OH	10	4
3630	3.6	BAS	23	42
3600	4.0	BAS	17	27
3550-3350	4.5	H-bonded species	30	18

the two types of Brønsted acid sites with different acid strength in the O(4) and O(2) structural configuration of the CHA framework, can be identified.^[35-38] Aside from BAS, HP-SAPO-34 displayed a composite signal at lower chemical shift which, after deconvolution, revealed two components at 1.8 and 2.0 ppm, due to external silanols ($\text{Si-OH}_{\text{ext}}$) at lattice defects and to intra-framework Si–OH groups interacting with neighbouring oxygen atoms ($\text{Si-OH}_{\text{int}}$), respectively. In addition, a signal at 2.6 ppm, related to P–OH groups, was also detected in the spectrum of HP-SAPO-34, whereas proton resonances beyond 4.5 ppm can be attributed to hydrogen-bonded species.^[39-42] In contrast, the ^1H NMR spectrum of calcined MCM-41 exhibited only a sharp signal at 1.8 ppm, due to Si–OH groups, and a broad feature in the range 2-6 ppm (Figure 4.6 B). Quantitative analysis made *via* ^1H SS NMR (Table 4.3) evidenced that the total number of Brønsted acid sites is lower in HP-SAPO-34 than in its microporous analogue. Conversely, the number of defective species (P–OH and Si–OH) is greater in HP-SAPO-34 than microporous SAPO-34.

Associated with ^1H SS NMR, FT-IR spectroscopy can help unravelling the differences between the proton species located within the SAPOs framework. In the O–H stretching region of FT-IR spectra (Figure 4.6 C), microporous SAPO-34 exhibited two intense bands with maxima at 3630 and 3600 cm^{-1} , owing to the O–

H stretching mode of BAS with different acid strength, at different structural configurations of the CHA framework. The same bands can be observed in the spectrum of the HP-SAPO-34, though at lower intensity, together with additional signals at 3745 cm^{-1} and 3678 cm^{-1} , arising from isolated Si–OH and P–OH groups, respectively. Notably, external and internal silanols cannot be clearly distinguished by FT-IR spectroscopy as a result of the overwhelming band of external Si–OH. Nevertheless, a pronounced tail, due to internal silanol groups, can be identified on the signal at 3745 cm^{-1} . Moreover, HP-SAPO-34 catalyst displayed a broad band from $3550\text{--}3350\text{ cm}^{-1}$, due to hydrogen-bonded hydroxyl groups.^[43] Significantly, the detection of characteristic bands owing to Brønsted acid sites in FT-IR and ^1H NMR spectra of HP-SAPO-34 provided confirmation of the dissolution of MCM-41 network and the successful incorporation of Si species in the CHA architecture.

FT-IR measurements of adsorbed CO at 80 K were performed to evaluate the strength of the acid sites in HP-SAPO-34 catalysts and to assess whether or not the overall acid characteristics of microporous SAPO-34 have been retained in the hierarchical system. Specifically, owing to its weak basicity, CO adsorbed at low temperatures is able to form OH...CO hydrogen-bonded adducts with acid sites, and the degree of the concomitant shift of hydroxyl band ($\Delta\nu_{\text{OH}}$) can be correlated with the catalyst acidity.^[44-47] The FT-IR spectra of HP-SAPO-34 and microporous SAPO-34 are reported in Figure 4.7. In the O–H stretching region ($3800\text{--}3100\text{ cm}^{-1}$), upon CO adsorption at low temperatures, signals due to the O–H stretching mode of BAS (3630 and 3610 cm^{-1}) were down-shifted in the spectra of both catalysts, as a result of the formation of OH...CO H-bonded adducts, yielding a broad, intense absorption centred at ca. 3350 cm^{-1} . Since the degree of red-shift was similar for both microporous and hierarchical SAPO-34, a comparable Brønsted acid strength was assessed. In the C–O stretching region ($2220\text{--}2040\text{ cm}^{-1}$), at low CO coverage, both samples displayed a signal centred at 2170 cm^{-1} , though of different intensity, due to the stretching mode of CO interacting with BAS. The observed blue-shift (32 cm^{-1}) with respect to the CO stretching mode detected for free CO molecule (ν_{CO} liquid-

like at 2138 cm^{-1}) was similar for both catalysts, again stressing their comparable acid strength. By progressively increasing the CO pressure, a low-frequency tail in the band at 2170 cm^{-1} , ascribable to the stretching mode of CO interacting with Si–OH and P–OH groups, was detected in the spectrum of HP-SAPO-34. Symmetrically, at high CO coverage, HP-SAPO-34 exhibited a shoulder at 3470 cm^{-1} , which can be assigned to the O–H stretching mode of P–OH defects interacting

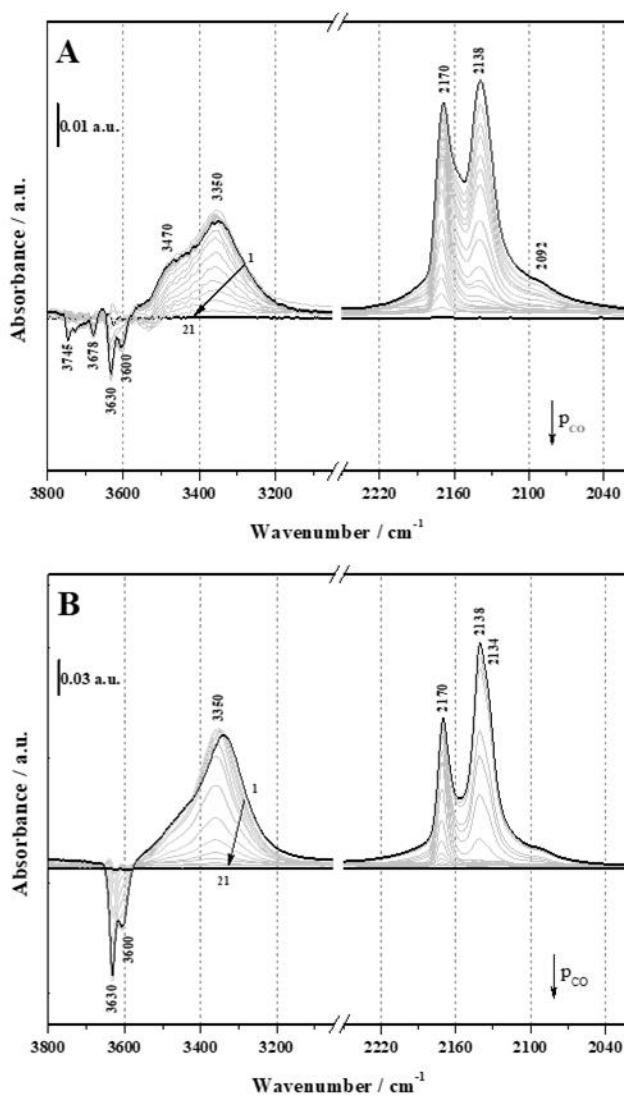


Figure 4.7. FT-IR difference spectra in the O–H (high frequency, $3800\text{--}3100\text{ cm}^{-1}$) and C–O (low frequency, $2220\text{--}2040\text{ cm}^{-1}$) stretching region of CO adsorbed at 80 K on A) HP-SAPO-34 and B) microporous SAPO-34 catalysts. Curves 1 to 21: decreasing CO doses from 15 mbar up to 1×10^{-4} mbar.

with CO.^[48] Signals arising from O–H stretching mode of Si–OH groups with CO cannot be distinguished due to overlapping with the negative bands in the 3650–3590 cm^{-1} . As a conclusion, FT-IR spectroscopy of adsorbed CO provided strong confirmation of the retention of the acid characteristic of the CHA framework in HP-SAPO-34. Nevertheless, due to its small kinetic diameter, CO is unable to discriminate acid sites based on their location within the hierarchical framework, thus providing no accessibility arguments.

To assess the accessibility of the acid sites in HP-SAPO-34 catalyst, FT-IR spectroscopy coupled with the adsorption of bulky probe molecules was performed. Due to their inherent basicity and steric hindrance, which impedes diffusion through small pore apertures, substituted pyridines are suitable probe molecules for discriminating BAS located inside the micropores from those present on the mesopores surface, thus providing both qualitative and quantitative information on the enhanced accessibility of acid sites in hierarchical zeolites and zeotypes.^[6,18,49-52] Specifically, pyridine (Py), 2,4,6-trimethylpyridine (2,4,6-TMP), 2,6-di-*tert*-butylpyridine (2,6-dTBP), with kinetic diameter of 0.54 nm, 0.74 nm and 1.05 nm, are too bulky to enter the microporous framework of SAPO-34 (micropore diameter of 0.38 nm) and can interact only with BAS located on the mesopores surface or at the micropores mouths. This interaction, which results in the protonation of the basic probe as a result of a proton transfer at a BAS, can be promptly identified using FT-IR spectroscopy by monitoring the frequency shift of the characteristic C–C aromatic ring mode of the probe molecule and its conjugate acid.

The FT-IR spectra of adsorbed 2,4,6-TMP at room temperature on HP-SAPO-34 catalyst are reported in Figure 4.8. In the O–H stretching region (Figure 4.8 A), bands at 3630 and 3600 cm^{-1} , assigned to the O–H stretching mode of BAS, were only partially eroded upon contact (10 min) with 2,4,6-TMP vapour pressure (blue curve). Simultaneously, new signals at 3295 cm^{-1} , attributed to N–H stretching mode of protonated 2,4,6-TMP, at 3040 cm^{-1} , due to C–H stretching vibration of pyridine ring, and at 2975 and 2930 cm^{-1} , related to ν_{asym} and ν_{sym} modes of CH_3 groups, were

observed.^[53] Overall, this experimental evidence suggested that only a fraction of the BAS in HP-SAPO-34 sample are accessible to bulky 2,4,6-TMP probe molecules.

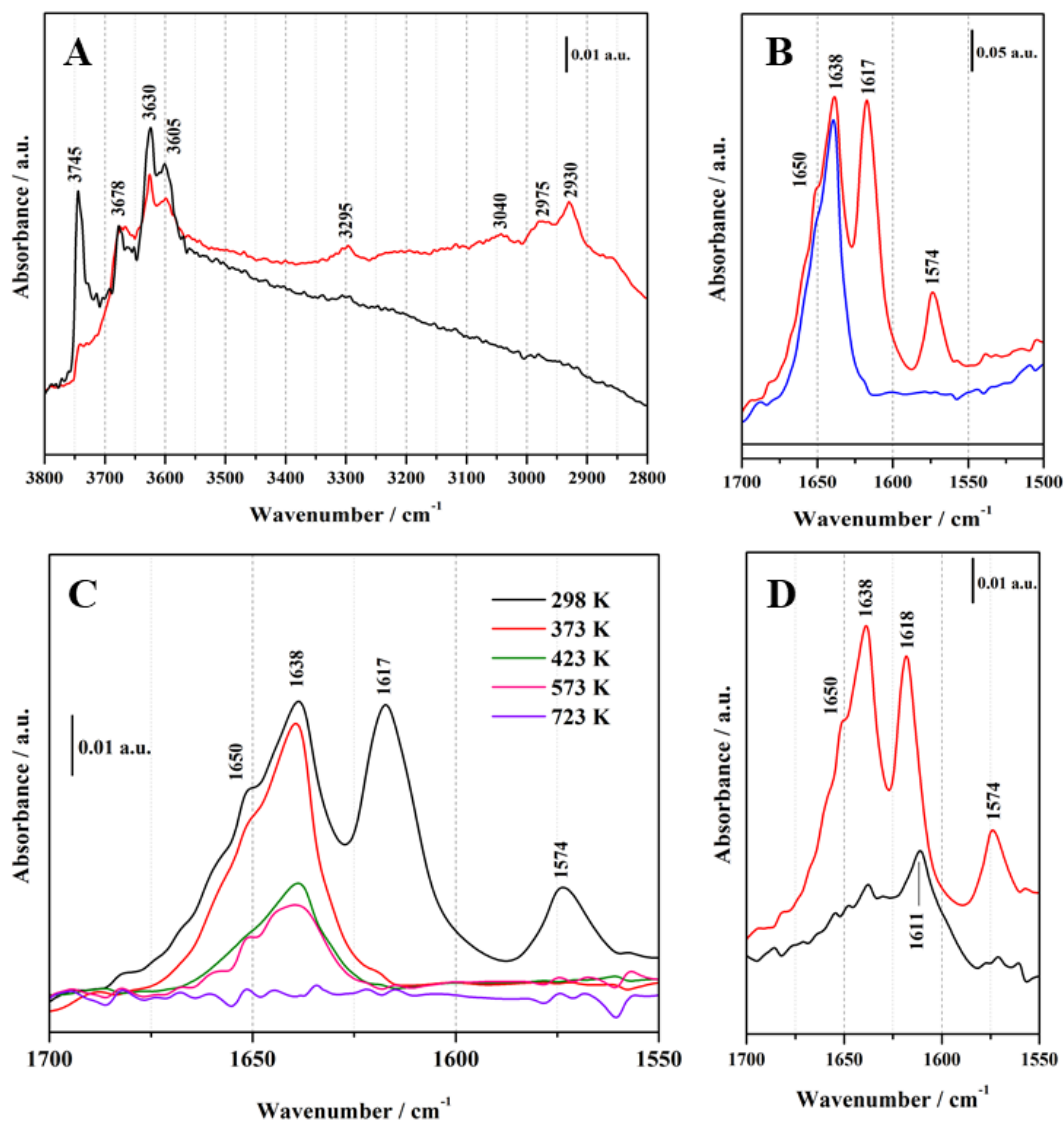


Figure 4.8. A) FT-IR absorbance spectra in the O–H stretching region and B) FT-IR difference spectra in the aromatic C–C ring vibration region of 2,4,6-TMP adsorbed on HP-SAPO-34. The black curve is the spectrum of HP-SAPO-34 in vacuum, the red curve is the spectrum of HP-SAPO-34 upon 10 minutes of contact time with 2,4,6-TMP vapour pressure and the blue curve is the spectrum recorded after outgassing the probe molecule at 373 K. C) FT-IR difference spectra of 2,4,6-TMP desorption at increasing temperatures. D) Comparison of FT-IR difference spectra of HP-SAPO-34 (red curve) and microporous SAPO-34 (black curve) upon contact with 2,4,6-TMP vapour pressure.

The ν_{8a} mode of 2,4,6-TMP, with its frequency changing in response of the acid site strength, was monitored in the aromatic C–C ring vibration region (Figure 4.8 B). When the ν_{8a} mode, which in liquid phase is detected at 1611 cm^{-1} , appears at wavenumbers $> 1630\text{ cm}^{-1}$, the formation of the protonated species (2,4,6-TMPH⁺) is inferred, whereas a lower wavenumber indicates the formation of a hydrogen-bonded adduct.^[6,43,51] Upon contact with 2,4,6-TMP, signals at 1617 and 1574 cm^{-1} , due to 2,4,6-TMP interacting with Si–OH groups *via* hydrogen bond, and a band at 1638 cm^{-1} with a shoulder at 1650 cm^{-1} , owing to ν_{8a} and ν_{8b} ring vibrations of 2,4,6-TMPH⁺ were detected. After outgassing the catalysts at 373 K , signals at 1617 and 1574 cm^{-1} , related to H-bonded adducts disappeared; conversely, the band at 1638 cm^{-1} was retained (Figure 4.8 C), indicating a relative resistance to thermal treatment (band at 1638 cm^{-1} was partially retained until 573 K) and confirming that a strong interaction had occurred between 2,4,6-TMP and accessible BAS. Notably, FT-IR spectrum of microporous SAPO-34 (Figure 4.8 D) exhibited only a signal at 1611 cm^{-1} , attributed to physisorbed 2,4,6-TMP. As a conclusion, the detection of the signal at 1638 cm^{-1} only in the spectrum of HP-SAPO-34 provided strong evidence that a fraction of Brønsted acid sites has been made accessible by the mesoporous network with respect to the microporous analogue.

With the aim of gaining further insight into the fraction of accessible Brønsted acid sites, other strongly basic probe molecules, of different steric hindrance, were adsorbed on HP-SAPO-34 catalyst. Specifically, NH_3 (0.26 nm kinetic diameter) was used to quantify the total amount of BAS, as it can readily enter both the micropores and mesopores of hierarchical SAPO-34 framework. Conversely, pyridine (0.54 nm kinetic diameter) and 2,6-dTBP (1.05 nm kinetic diameter), cannot enter the micropores and therefore can probe only the more accessible acid sites.

The FT-IR difference spectra of NH_3 , pyridine and 2,6-dTBP adsorbed on HP-SAPO-34, together with their desorption at increasing temperatures, are reported in the aromatic C–C ring vibration region (Figure 4.9 A-F). Upon NH_3 adsorption (100 mbar, Figure 4.9 A, red curve), a signal at 1619 cm^{-1} , owing to the bending mode

of ammonia hydrogen bonded to Si–OH, was detected. Furthermore, a band at 1450 cm^{-1} , assigned to the δ_{as} of NH_4^+ ions, indicated that a proton transfer had occurred

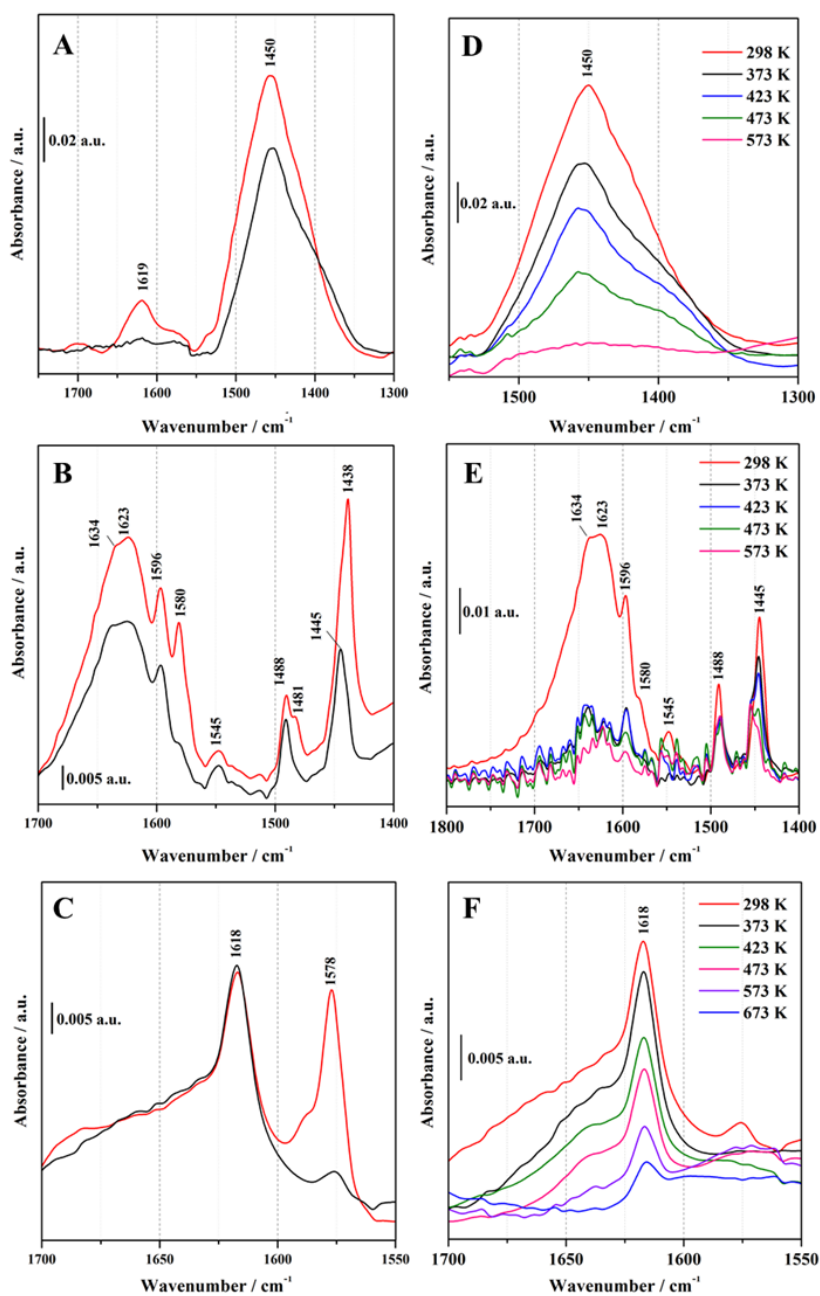


Figure 4.9. FT-IR difference spectra of A) NH_3 , B) pyridine and C) 2,6-dTBP adsorption showed before (red curves) and after (black curves) outgassing the probe molecules at room temperature. FT-IR difference spectra of D) NH_3 , E) pyridine and F) 2,6-dTBP desorption at increasing temperatures.

between NH_3 and the BAS. Upon adsorption of pyridine (vapour pressure, Figure 4.9 B, red curve), bands due to the physisorbed molecule (ν_{8b} at 1580 cm^{-1} , ν_{19a} at 1481 cm^{-1} and ν_{19b} at 1438 cm^{-1}), pyridine H-bonded to Si–OH (ν_{8b} at 1596 cm^{-1} and ν_{19b} at 1445 cm^{-1}), and protonated PyH^+ from interaction with strong BAS (ν_{8a} at 1634 cm^{-1} , ν_{8b} at 1623 cm^{-1} , ν_{19b} at 1545 cm^{-1} and ν_{19a} at 1488 cm^{-1}) were observed.^[54] Outgassing of the sample at 298 K removed the signal related to the physisorbed probe molecule (Figure 4.9 B, black curve). Finally, adsorption of 2,6-dTBP (vapour pressure, Figure 4.9 C, red curve) produced a signal at 1618 cm^{-1} (ν_{8a}), attributed to protonated 2,6-dTBPH⁺ species, and a band at 1578 cm^{-1} , due to hydrogen bonding interactions with silanols.^[52] Upon outgassing HP-SAPO-34 at 298 K, bands due to 2,6-dTBP H-bonded to silanols disappeared (Figure 4.9 C, black curve). Upon outgassing the sample at increasing temperatures, the intensity of the signals assigned to the protonated probe molecules was progressively reduced (Figure 4.9 D-E), indicating a relative resistance to thermal treatment.

The total number of accessible Brønsted acid sites (N) of HP-SAPO-34 catalyst, determined using the different probe molecules and estimated by means of Lambert-Beer law (for further explanation refer to Chapter 9/Experimental section), is reported in Table 4.4, along with the nature and position of the IR bands of their corresponding protonated species. Spectroscopic quantifications strongly evidenced that, although only a fraction of the Brønsted acid sites was made accessible to sterically hindered probe molecules, by introducing additional mesoporosity within

Table 4.4. The total number of accessible Brønsted acid sites (N) in HP-SAPO-34.

Probe molecules	Protonated species	Position of IR band of the protonated species [cm^{-1}]	N [$\mu\text{mol g}^{-1}$]	AF
NH_3	NH_4^+ ^[a]	1450 (δ_{as})	59.1	1
Py	PyH^+ ^[b]	1545 (ν_{19b})	6.33	0.107
2,4,6-TMP	2,4,6-TMPH ⁺ ^[c]	1638 (ν_{8a})	2.24	0.038
2,6-dTBP	2,6-dTBPH ⁺ ^[d]	1618 (ν_{8a})	2.19	0.037

^[a] $\varepsilon = 0.147\text{ cm}^2\ \mu\text{mol}^{-1}$.^[55] ^[b] $\varepsilon = 0.06\text{ cm}^2\ \mu\text{mol}^{-1}$.^[56] ^[c] $\varepsilon = 0.62\text{ cm}^2\ \mu\text{mol}^{-1}$.^[51] ^[d] $\varepsilon = 0.50\text{ cm}^2\ \mu\text{mol}^{-1}$.^[52]

the CHA framework, the average micropore length was reduced and the number of accessible BAS increased accordingly. Unsurprisingly, pyridine was able to interact with a higher fraction of BAS than 2,4,6-TMP and 2,6-dTPB, reflecting the fact that the smaller the kinetic diameter of the probe molecule, the higher the fraction of BAS which can be detected. The accessibility factor (AF), defined as the number of sites detected by adsorption of the alkylpyridine, divided by the total number of Brønsted acid sites detected by NH_3 adsorption, was also evaluated for the different probe molecules. The AF decreased with increasing alkylation of pyridine, thus with increasing steric bulk. Interestingly, SS NMR and FT-IR analyses strongly supported the successful preparation of a hierarchical framework, with comparable acidic properties with respect to the microporous analogue and concomitant enhanced accessibility of the strong BAS.

4.2.4 Catalysis

On the basis of the promising characterization results, the catalytic activity of the HP-SAPO-34 catalysts was evaluated in the vapour-phase Beckmann rearrangement of cyclohexanone oxime to ϵ -caprolactam and compared to that of the microporous SAPO-34 and MCM-41 (Figure 4.10). Notably, HP-SAPO-34 catalyst exhibited exceptional catalytic performances, with only 99 % conversion to the desired product over the course of the 6-h reaction (Figure 4.10 A). The selectivity of HP-SAPO-34 (95 % over the course of the 6-h reaction) was comparable to the one of microporous analogue, thus providing further confirmation that the acidic properties of the CHA framework had been retained in the hierarchical system (Figure 4.10 B). Anyway, the overall acidity of HP-SAPO-34 was found to be even superior to its microporous SAPO-34, even at short contact time. Interestingly, microporous SAPO-34 achieved a maximum conversion of only 82 %, which then steadily declined over the course of the reaction, presumably as a result of the catalyst deactivation due to pore-blockage.^[19] This result suggested impeded diffusion of cyclohexanone oxime to the

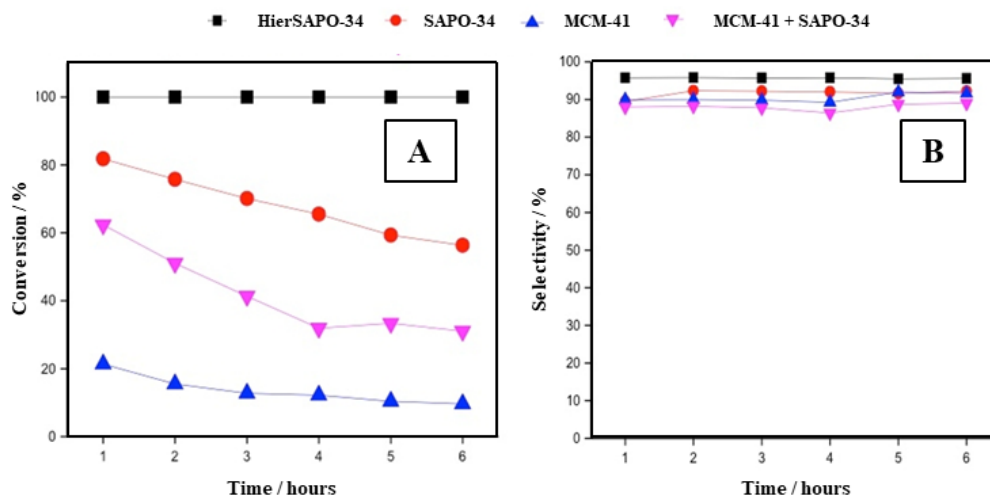


Figure 4.10. Comparison of A) the conversion of cyclohexanone oxime and B) the selectivity towards ϵ -caprolactam in the vapour-phase Beckman rearrangement, under acid heterogeneous catalysis, at 598 K and 0.79 h^{-1} WHSV.

internal acid active sites of microporous framework, reducing the number of acid catalytic centres which can participate in the catalytic reaction and limiting the catalysis to the more accessible BAS located on external surface of the catalyst or at the micropore mouths. As a consequence, the maximal conversion was restricted with respect to the hierarchical SAPO-34. With the aim of proving that the superior catalytic activity of HP-SAPO-34 was not solely due to an enhanced diffusion to indiscriminate acid sites, the catalytic activity of mesoporous MCM-41 was also evaluated. It is well known, indeed, that pendant silanol groups within the framework of MCM-41 can catalyse reactions requiring weak acid sites. Encouragingly, MCM-41 exhibited a low conversion which successively declined over the course of the reaction, stressing the importance of the nature of BAS, as well as their accessibility, in facilitating the desired transformation in high yield. Moreover, the lower conversion achieved by a 50:50 physical mixture of microporous SAPO-34 and MCM-41 with respect to both hierarchical and microporous sample evidenced the importance of designing a single framework, which combines, at the same time, desired acid characteristics and enhanced mass-transfer capabilities.

4.3 Conclusions

A distinctive bottom-up synthetic methodology for the preparation of a hierarchical SAPO-34 has been successfully performed. The use of CTAB encapsulated within ordered MCM-41, to serve as both silicon source as mesopore, has proven to be an effective soft-templating strategy in introducing secondary porosity without the need for a sophisticated mesopore. Hierarchical SAPO-34 exhibited superior textural properties, with respect to its microporous analogue, with substantial enhancement in mesopore volume and mesopore surface area. FT-IR of adsorbed CO, together with ^1H SS-NMR, strongly confirmed the retention of the acidic characteristic of microporous CHA framework. FT-IR of adsorbed alkylpyridine evidenced that the introduction of additional mesoporous network had greatly enhanced the accessibility of the acid active site. Furthermore, results from catalytic tests further demonstrated that this bottom-up synthetic methodology effectively retains the desirable acid characteristic of the parent framework, whilst simultaneously improving mass-transfer, thus reinforcing the spectroscopic evaluation. HP-SAPO-34 showed outstanding catalytic activity in the vapour-phase Beckmann rearrangement of cyclohexanone oxime to ϵ -caprolactam with respect to both microporous SAPO-34 and MCM-41. In addition, the mediocre yield of caprolactam achieved using a physical mixture of mesoporous MCM-41 and microporous SAPO-34, stressed the importance of designing a single, harmonized hierarchical system which can host, contemporarily, both micro- and mesopores. Besides enhancing accessibility and ensuring retention of Brønsted acidity, this bottom-up synthetic strategy is a viable mean of introducing defecting pendant silanols within hierarchical framework. Defective Si-OH groups of HP-SAPO-34 can indeed be used as anchoring point to graft organic moieties, to synthesise a hybrid material which combines the acidic properties of inorganic hierarchical framework with a tailored organic functionality, suitable for a particular application.

4.4 Notes and references

- [1] A. Corma, *Chem. Rev.* **1997**, 97, 2373.
- [2] Z. Wang, Y. Yu, R. Xu, *Chem. Soc. Rev.* **2012**, 41, 1729.
- [3] R. Raja, M.E. Potter, S.H. Newland, *Chem. Commun.* **2014**, 50, 5940.
- [4] M.E. Potter, D. Sun, E. Gianotti, M. Manzoli, R. Raja, *Phys. Chem. Chem. Phys.* **2013**, 15, 13288.
- [5] M. Hartmann, L. Kevan, *Chem. Rev.* **1999**, 99, 635.
- [6] E. Gianotti, M. Manzoli, M. E. Potter, V.N. Shetti, D. Sun, A.J. Paterson, T.M. Mezza, A. Levy, R. Raja, *Chem. Sci.* **2014**, 5, 1810.
- [7] M.A. Carreon, S. Li, J.L. Falconer, R.D. Noble, *J. Am. Chem. Soc.* **2008**, 130, 5412.
- [8] H. Hong, S. Li, R.D. Noble, *J. Membr. Sci.* **2008**, 307, 277.
- [9] B. Vora, J. Q. Chen, A. Bozzano, B. Glover, P. Barger, *Catal. Today* **2009**, 141, 77.
- [10] D. Chen, K. Moljordand, A. Holmen, *Microporous Mesoporous Mater.* **2012**, 164, 239.
- [11] P. Tian, Y. Wei, M. Ye, Z. Liu, *ACS Catal.* **2015**, 5, 1922.
- [12] X. Zhu, J.P. Hofmann, B. Mezari, N. Kosinov, L. Wu, Q. Quian, B.M. Weckhuysen, S. Asahina, J. Ruiz-Martinez, E.J.M. Hensen, *ACS Catal.* **2016**, 6, 2163.
- [13] J. Pérez-Ramírez, C. H. Christensen, K. Egeblad, C. H. Christensen, J. C. Groen, *Chem. Soc. Rev.* **2008**, 37, 2530.
- [14] L.-H. Chen, M.-H. Sun, Z. Wang, W. Yang, Z. Xie, B.-L. Su, *Chem Rev.* **2020**, DOI: <https://doi.org/10.1021/acs.chemrev.0c00016>.
- [15] J.C. Groen, J.C. Jansen, a. Moulijn, J. Pérez-Ramírez, *J. Phys. Chem. B* **2004**, 108, 13062.
- [16] A. Erigoni, S.H. Newland, G. Paul, L. Marchese, R. Raja, E. Gianotti, *ChemCatChem* **2016**, 8, 3161.

- [17] X. Cheng, A. Vincente, Z. Quin, V. Ruaux, J.P. Gilson, V. Vlatchev, *Chem. Comm.* **2016**, 52, 3512.
- [18] I. Miletto, C. Ivaldi, G. Paul, S. Chapman, L. Marchese, R. Raja, E. Gianotti, *ChemistryOpen* **2018**, 7, 297.
- [19] S.H. Newland, W. Sinkler, T. Mezza, S.R. Bare, M. Caravetta, I.M. Haies, A. Levy, S. Keenan, R. Raja, *ACS Catal.* **2015**, 5, 6587.
- [20] D. Verboekend, M. Milina, J. Pérez-Ramírez, *Chem. Mater.* **2014**, 26, 4552.
- [21] K. Na, M. Choi, R. Ryoo, *Microporous Mesoporous Mater.* **2013**, 166, 3.
- [22] M. Choi, R. Srivastava, R. Ryoo, *Chem. Commun.* **2006**, 4380.
- [23] Q. Sun, N. Wang, D. Xi, M. Yang, J. Yu, *Chem. Commun.* **2014**, 50, 6502.
- [24] S. Chapman, A.J. O'Malley, I. Miletto, M. Carravetta, P. Cox, E. Gianotti, L. Marchese, S.F. Parker, R. Raja, *Chem. Eur. J.* **2019**, 25, 9938.
- [25] D.P. Serrano, J.M. Escola, P. Pizarro, *Chem. Soc. Rev.* **2013**, 42, 4004.
- [26] I. Miletto, G. Paul, S. Chapman, G. Gatti, L. Marchese, R. Raja, E. Gianotti, *Chem. Eur. J.* **2017**, 23, 9952.
- [27] D. R. Radu, C.-Y. Lai, K. Jeftinija, E. W. Rowe, S. Jeftinija, V. S.-Y. Lin, *J. Am. Chem. Soc.* **2004**, 126, 13216.
- [28] E. A. Kang, T.-W. Kim, H.-J. Chae, M. Kim, K.-E. Jeong, J.-W. Kim, C.-U. Kim, S.-Y. Jeong, *J. Nanosci. Nanotechnol.* **2013**, 13, 7498.
- [29] A.M. Prakash, S. Unnikrishnan, *J. Chem. Soc. Faraday Trans.* **1994**, 90, 2291.
- [30] K.A. Cychoz, R. Guillet-Nicolas, J. Garcia-Martinez, M. Thommes, *Chem. Soc. Rev.* **2017**, 46, 389.
- [31] J. Landers, G.Y. Gor, A.V. Neimark, *Colloids Surf. A* **2013**, 437, 3.
- [32] M. Thommes, K.A. Cychoz, *Adsorption* **2014**, 20, 233.
- [33] B. Zibrowius, E. Löffler, M. Hunger, *Zeolites* **1992**, 12, 167.
- [34] W. Lutz, R. Kurzhals, S. Sauerbeck, H. Toufar, J.-C. Buhl, T. Gesing, W. Altenburg, C. Jger, *Microporous Mesoporous Mater.* **2010**, 132, 31.

- [35] G.A.V. Martins, G. Berlier, S. Coluccia, H.O. Pastore, G.B. Superti, G. Gatti, L. Marchese, *J. Phys. Chem. C* **2007**, 111, 330; b) G.A.V. Martins, G. Berlier, C. Bisio, S. Coluccia, H.O. Pastore, L. Marchese, *J. Phys. Chem. C* **2008**, 112, 7193.
- [36] A. Buchholz, W. Wang, A. Arnold, M. Xu, M. Hunger, *Microporous Mesoporous Mater.* **2003**, 57, 157.
- [37] L. Smith, A.K. Cheetham, L. Marchese, J.M. Thomas, P.A. Wright, J. Chen, E. Gianotti, *Catal. Lett.* **1996**, 41, 13.
- [38] S. Bordiga, L. Regli, C. Lamberti, A. Zecchina, M. Jorgen, K.P. Lillerud, *J. Phys. Chem. B* **2005**, 109, 7724.
- [39] M. Hunger, S. Ernst, S. Steuernagel, J. Weitkamp, *Microporous Mater.* **1996**, 6, 349.
- [40] M. Hunger, J. Krger, H. Pfeifer, J. Caro, B. Zibrowius, M. Below, R. Mostowicz, *J. Chem. Soc. Faraday Trans.* **1987**, 83, 3459.
- [41] M. Hunger, M. W. Anderson, A. Ojo, H. Pfeifer, *Microporous Mater.* **1993**, 1, 17.
- [42] J. Trébosc, J. W. Wiench, S. Huh, V. S.-Y. Lin, M. Pruski, *J. Am. Chem. Soc.* **2005**, 127, 3057.
- [43] A. Erigoni, S.H. Newland, G. Paul, L. Marchese, R. Raja, E. Gianotti, *ChemCatChem* **2016**, 8, 3161.
- [44] M. A. Makarova, A. F. Ojo, K. Karim, M. Hunger, J. J. Dwyer, *J. Phys. Chem.* **1994**, 98, 3619.
- [45] H. Knözinger, S. J. Huber, *J. Chem. Soc. Faraday Trans.* **1998**, 94, 2047–2059.
- [46] K. Chakarova, K. Hadjiivanov, *J. Phys. Chem. C* **2011**, 115, 4806.
- [47] M.E. Potter, M.E. Cholerton, J. Kezina, R. Bounds, M. Carravetta, M. Manzoli, Gianotti, M. Lefenfeld, R. Raja, *ACS Catal.* **2014**, 4, 4161.
- [48] E. Gianotti, V. Dellarocca, E. C. Oliveira, S. Coluccia, H. O. Pastore, L. Marchese, *Stud. Surf. Sci. Catal.* **2002**, 142, 1419.
- [49] F. Thibault-Starzyk, I. Stan, S. Abellk, A. Bonilla, K. Thomas, C. Fernandez, J.-P. Gilson, J. Perez-Ramirez, *J. Catal.* **2009**, 264, 11.

- [50] F. Thibault-Starzyk, A. Vimont, J.-P. Gilson, *Catal. Today* **2001**, 70, 227.
- [51] K. Mlekodaj, K. Tarach, J. Datka, K. Gkra-Marek, W. Makowski, *Microporous Mesoporous Mater.* **2014**, 183, 54.
- [52] K. Góra-Marek, K. Tarach, M. Choi, *J. Phys. Chem. C* **2014**, 118, 12266.
- [53] J. F. Arenas, I. Lkpez Tockn, J. C. Otero, J. I. Marcos, *J. Mol. Struct.* **1999**, 476, 139.
- [54] R. Buzzoni, S. Bordiga, G. Ricchiardi, C. Lamberti, A. Zecchina, *Langmuir* **1996**, 12, 930.
- [55] J. Datka, B. Gil, A. Kubacka, *Zeolites* **1995**, 15, 501.
- [56] J. Datka, *J. Chem. Soc. Faraday Trans.* **1980**, 76, 2437.

5

Hierarchical silicoaluminophosphate SAPO-5 architectures with tailored acid properties obtained from mesoporous silica scaffolds

In the present chapter, novel bottom-up synthetic methodologies to prepare hierarchical SAPO-5, using pre-synthesised ordered mesoporous silica (MCM-41 or SBA-15), with the surfactant inside the mesopores (CTAB or Pluronic), serving as both silicon source and mesoporogen, have been investigated. Moreover, catalysts optimization has been performed by varying the silicon loading and/or the mesopores dimensions through the choice of the mesoporogen. A detailed physico-chemical characterization was performed to evaluate the structural, morphological, textural and spectroscopic properties of the catalysts, with a view in establishing preliminarily structure-property relationships.

Introduction

As already widely discussed in Chapter 4, great progress in the ability to discover new synthetic methodology to prepare hierarchical acid catalysts has been made recently, in order to overcome shortcomings, *i.e.* mass transport limitations, lack of suitable acid strength, catalyst deactivation due to coke deposition, peculiar to microporous frameworks.^[1-6] Among the various heterogeneous acid catalysts that can be used, hierarchical silicoaluminophosphates (SAPOs) acid catalysts represent a viable candidate. Indeed, microporous SAPOs have been extensively employed in acid catalysed reactions of hydrocarbon conversion.^[7,8] Particularly, SAPO-5, with

AFI topological structure, a pore diameter of 7.3 Å and moderate acidity, has been used as heterogeneous catalyst in methanol-to-olefin conversion, toluene alkylation^[9] and xylene isomerization^[10]. In the present chapter, a bottom-up synthetic strategy to obtain hierarchical SAPO-5 catalysts, akin to the one described in Chapter 4, will be investigated. This particular soft-templating method exploits the use of a pre-synthesised ordered mesoporous silica (MCM-41 or SBA-15), with the surfactant inside the mesopores (CTAB or Pluronic), serving as both silicon source and mesopore-former. This novel bottom-up synthetic strategy mitigates the use of expensive and sophisticated surfactants to induce mesoporosity in the microporous framework and benefits from a superior retention of the acid properties of microporous SAPOs, whilst simultaneously enhancing mass transfer. In addition, high degree of structural control can be achieved by controlling the micellar structure through the choice of the surfactant molecule and the use of additives, such as swelling agents. Moreover, when this synthetic strategy was performed to prepare a hierarchical SAPO-34^[5] (for further details refer to Chapter 4), it has proven to be an effective means to introduce defective pendant Si–OH groups within the hierarchical network, with respect to different bottom-up strategies, such as the one described in Chapter 3, using mono- and disaccharides to introduce mesoporosity in the CHA framework^[6]. If the same result can be achieved for hierarchical SAPO-5, this property could be exploited to synthesise organic-inorganic hybrid catalysts, combining specific organic functionalities with desirable Brønsted acid sites of AFI framework, made more accessible through the hierarchical network.

5.1 Hierarchical SAPO-5 from mesoporous MCM-41 with variable silicon loading

From literature, it is well known that structural and chemical properties of microporous SAPOs depend on the mechanism of silicon incorporation within the framework, specifically a variation in the silicon loading allow a modulation of the

acid density and strength.^[11-14] For low Si concentration, SM2 substitution mechanism (partial substitution of the framework P with Si) results in the formation of isolated Brønsted acid sites of medium acid strength^[15,16] An increase in the Si loading can induce the formation of silicon islands (aggregates) in SAPO framework by a combination of SM2 and SM3 mechanism (simultaneous substitution of framework P and Al with Si)^[17,18] at the expense of a reduction of the total number of BAS, located in the SAPO domains. Nevertheless, BAS at the border of the islands benefit from higher acid strength.^[19,20] Moreover, it is well-established that the number of defective Si–OH groups, which can be exploited to graft organic moieties onto SAPO architecture, increases accordingly to the silicon loading. Depending on the specific catalytic application, it is therefore necessary to find a compromise between density, strength of BAS sites and number of silanol groups in SAPO framework. With the aim of investigating the difference in the population of acid sites, a series of hierarchical SAPO-5 catalysts with variable Si loadings were prepared by a bottom-up soft-templating strategy, using cetyltrimethylammonium bromide (CTAB) encapsulated within MCM-41, serving both as silicon source and mesopore. As a comparison, corresponding microporous catalysts were also synthesised. A detailed physico-chemical characterization has been performed in order to establish a preliminary structure-property relationship, which might be helpful to further catalysts optimization. The catalytic activity of the hierarchical SAPO-5 obtained at different silicon loading was preliminarily evaluated in the aldol condensation/crotonization of furfural (FF) with methylisobutylketone (MIBK), an acid catalysed reaction.

5.1.1 Experimental section

5.1.1.1 General

Aluminum isopropoxide ($\geq 98\%$), triethylamine ($\geq 99.5\%$), tetraethyl orthosilicate ($\geq 99\%$) and phosphoric acid (85 wt% in H₂O), all used for the synthesis of SAPO-5 catalysts, were supplied by Sigma-Aldrich (Milano, Italy). NH₃ (\geq

99.7%), purchased from SIAD (Bergamo, Italy) and 2,6-di-tert-butylpyridine ($\geq 97\%$), purchased from Sigma Aldrich (Milano, Italy), were used as probe molecule in FT-IR experiments.

5.1.1.2 Synthesis of SAPO-5

Hierarchical SAPO-5 catalyst with variable Si loading were synthesised following a bottom-up soft-templating strategy, in which pre-synthesised MCM-41 with the surfactant (CTAB) inside the mesopores was used as both the silicon source as mesoporous structure directing agent (SDA_{meso}). Microporous SAPO-5 materials were also prepared for comparison of the physico-chemical properties and the catalytic activity. After crystallization, recovering and washing, all the samples were calcined to remove the organic templates.

Synthesis of hierarchical SAPO-5 with variable Si loading: hierarchical catalysts were synthesised according to the following hydrothermal procedure. Aluminium isopropoxide (7.0 g) was added slowly to deionized water (10 mL) and TEA (2.77 mL) under stirring, and the mixture was stirred for 1 h. CTAB-containing MCM-41 (1.03 g, 2.06 g and 3.09 g for Si=0.30, Si=0.60 and Si=0.90, respectively, prepared following the methodology reported in literature by Radu *et al.*^[21]) was slowly added, and the mixture was further stirred for 2 h. Phosphoric acid (2.18 mL, 85 wt% in H₂O) was added dropwise under stirring. The mixtures with three variable Si content were vigorously stirred for 30 min to produce white gels of molar composition 1.0 Al/0.93P/x Si/yCTAB/0.58TEA/28 H₂O, where x = 0.3 and y = 0.033, x= 0.6 and y= 0.066 and x=0.9 and y=0.099, respectively. The gels were transferred to a Teflon-lined stainless-steel autoclave and crystallized at 473 K for 60 h under autogenous pressure. The solid products from autoclave was then recovered by filtration and washed with water. The as-prepared products were dried in air at 373 K and calcined in a tube furnace under airflow at 873 K for 16 h to remove organic surfactant and micropore template, producing a white crystalline solid. For the sake of clarity, the nomenclature HP-SAPO-5/xSi, where “HP” stands

for hierarchical porous, will be hereinafter used, where 'x' refers to the molar Si content in the synthetic gels.

Synthesis of microporous SAPO-5 with variable Si loading: microporous catalysts were synthesised according to the following hydrothermal procedure. Aluminium isopropoxide (7.0 g) was added slowly to deionized water (10 mL) and triethylamine (TEA, 2.77 mL) under stirring, and the mixture was stirred for 1 h. Tetraethylorthosilicate (TEOS, 2.31 mL, 4.62 mL and 6.92 mL for Si=0.30, Si=0.60 and Si=0.90, respectively) was added dropwise under stirring, along with 7.29 ml of deionized water, and the mixture was further stirred for 2 h. Phosphoric acid (2.18 ml, 85 wt% in H₂O) was added dropwise under stirring. The gel was vigorously stirred for 30 min to produce a white gel of molar composition 1.0Al: 0.93 P: x Si: 0.58 TEA: 28 H₂O where x= 0.3, 0.6, and 0.9, respectively. The gel was transferred to a Teflon-lined stainless-steel autoclave and subjected to hydrothermal synthesis at 473 K for 60 h under autogenous pressure. The solid product was then recovered from autoclave by filtration, washed with water, dried in air at 373 K and finally calcined in a tube furnace at 873 K for 16 h under airflow to generate a white crystalline solid. For the sake of clarity, the nomenclature SAPO-5/xSi will be hereinafter used, where 'x' refers to the molar Si content in the synthetic gels.

5.1.1.3 Characterization

Before undertaking volumetric and spectroscopic measurements, calcined samples were outgassed at 300 °C overnight and for 2 h, respectively, to remove physisorbed water. Further details on the experimental techniques are reported in Chapter 9/Experimental section.

5.1.1.4 Catalysis

The catalytic tests in the aldol condensation/crotonization reaction were performed by the Eco-Efficient Products and Processes Laboratory (E2P2L), UMI 3464 CNRS-Solvay, one of the European project partners, under the supervision of Prof. M. Pera-Titus. The aldol condensation/crotonization reaction was conducted in

a stainless-steel autoclave reactor (30 mL) from Taiatsu. In a typical test, the autoclave was charged with 0.2 g (2 mmol) of distilled furfural (FF), 3.8 g (38 mmol) of methylisobutylketone (MIBK), and 40 mg of catalyst in the reactor with a magnetic stirring bar, which correspond to the optimized conditions. The mixture was heated to the desired temperature under a stirring speed of 1000 rpm. Preliminary experiments were conducted ensuring the absence of external mass transfer limitations on the reaction rate.

5.1.2 Results and discussion

5.1.2.1 Structural and textural characterization

X-Ray powder diffraction (XRDP) was performed to investigate the structural properties of HP-SAPO-5/xSi and to contrast them with microporous analogues. XRD patterns of both HP-SAPO-5/xSi and microporous SAPO-5/xSi (Figure 5.1 A and B) exhibited the characteristic reflections of AFI framework^[22], thus stressing a high phase purity and crystallinity of all the catalysts, irrespective to their Si loading and porous architecture. Moreover, the signals intensities of the hierarchical catalysts were found to be comparable with microporous analogues, indicating a retention of the structural order even at high silicon and mesopore loadings.

The textural properties of HP-SAPO-5/xSi catalysts were investigated by N₂ adsorption/desorption volumetric analysis at 77 K (Figure 5.2).^[23] All hierarchical catalysts exhibited Type IV isotherms with a hysteresis loop in the P/P₀ range 0.6-1.0 (Figure 5.2 A), suggesting the presence of mesopores with an average size of approximately 30 Å, as inferred from the NLDFT (non-localized density functional theory) method (Figure 5.2 B). In addition, a band centred at ca. 10 Å was detected, which is typical of tensile strength effect due to N₂ adsorption.^[24] Ar adsorption/desorption volumetric analysis at 87 K was carried out on HP-SAPO-5/0.60Si with the aim of gaining a deeper insight in the textural properties of microporous framework. Indeed, it is well-established that the proper choice of the adsorptive used to perform volumetric analyses is crucial to obtain reliable surface

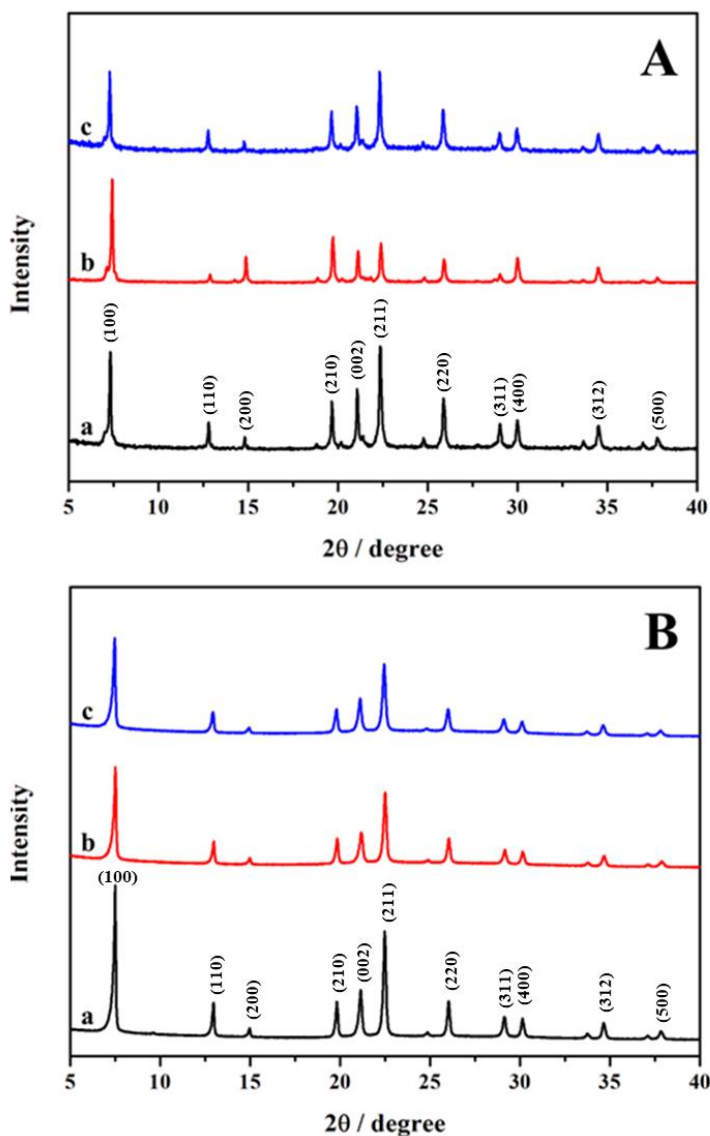


Figure 5.1. The powder XRD pattern of A) microporous SAPO-5/xSi and B) HP-SAPO-5/xSi, with x=0.30 (a, black curve), x=0.60 (b, red curve) and x=0.9 (c, blue curve).

areas and pore volumes. Recently, it has become evident that nitrogen is not an entirely satisfactory adsorbate for assessing the micropore size distribution. Specifically, with respect to many zeolites, the initial stage of physisorption, which is shifted to extremely low relative pressures ($P/P_0 \sim 10^{-7}$), where the rate of diffusion is extremely low, makes it difficult to measure equilibrated adsorption isotherms. Due to specific interactions with surface functional groups, the pore filling pressure is not

correlated with the pore size in a straightforward way. Conversely, argon adsorbed at 87 K is able to fill micropores ranging from 5 to 10 Å at significantly higher relative pressure, resulting in accelerated diffusion and faster equilibration time, thus being more suited from microporous analyses.^[25,26] Whilst isotherms obtained by N₂ and Ar adsorption/desorption analyses were found to be comparable (Figure 5.2 C), pore size distribution obtained using Ar as adsorptive and calculated by means of NLDFT, evidenced micropores at around 7.3 Å, as expected for the AFI structure. Details of the specific BET surface area, as well as the total, microporous and mesoporous specific surface area and pore volume, determined by the NLDFT

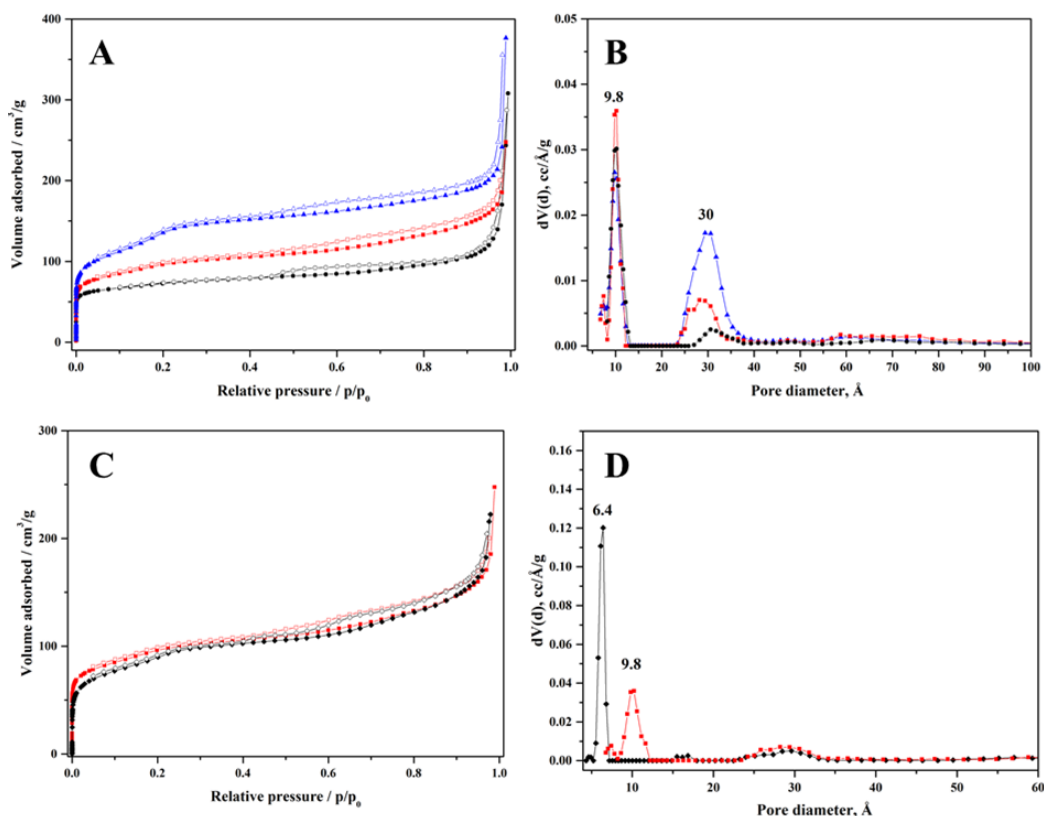


Figure 5.2. A) The N₂ adsorption/desorption isotherms at 77K of HP-SAPO-5/xSi with x=0.30 (black curve), x=0.60 (red curve) and x=0.90 (blue curve). B) Pore size distributions of the different samples in the mesopore range. C) Comparison between Ar (black curve) and N₂ (red curve) adsorption/desorption isotherms on HP-SAPO-5/0.60Si. D) Pore size distribution of HP-SAPO-5/0.60Si obtained by Ar adsorption at 87 K (black curve) and N₂ adsorption at 77 K.

Table 5.1. Textural properties of HP-SAPO-5/xSi

xSi	S_{BET} [m ² g ⁻¹]	S_{DFT} [m ² g ⁻¹]	S_{micro} [m ² g ⁻¹]	S_{meso} [m ² g ⁻¹] ^[a]	V_{DFT} [cm ³ g ⁻¹]	V_{micro} [cm ³ g ⁻¹]	V_{meso} [cm ³ g ⁻¹] ^[b]
0.30	267	375	351	60	0.304	0.079	0.225
0.60	340	450	327	123	0.323	0.077	0.246
0.90	464	552	333	219	0.448	0.075	0.373

$$^{[a]}S_{meso} = S_{DFT} - S_{micro}; \quad ^{[b]}V_{meso} = V_{DFT} - V_{micro};$$

method, are reported in Table 5.1. Both BET and NLDFT highlighted an increase of surface area with the silicon loading. The mesoporous surface area (S_{meso}) and mesopore volume (V_{meso}), together with total pore volume (V_{DFT}), also increased with the Si content, while the contribution of the microporous surface area (S_{micro}) and the micropore volume (V_{micro}) were found to be comparable in all samples, indicating that micropore textural features had not been affected by an increase of silicon and mesopore loading. Therefore, volumetric data strongly supported the successful synthesis of hierarchical architectures with superior textural properties, stressing the existence of multiple levels of porosity within the hierarchical frameworks, with simultaneous retention of microporous textural properties.

5.1.2.2 Spectroscopic characterization

The chemical environment of the framework atoms in HP-SAPO-5/xSi and microporous SAPO-5/xSi was investigated by ²⁷Al, ³¹P, and ²⁹Si MAS NMR spectroscopy (Figure 5.3-5.5). The ²⁷Al NMR spectra of all the samples exhibited a single resonance signal at *ca.* 36 ppm, which can be unambiguously assigned to tetrahedrally-coordinated Al atoms of Al(PO₄) (Figure 5.3 A and B). In both microporous and hierarchical catalysts, a peak at about -30 ppm in the ³¹P NMR spectra can be ascribed to tetrahedrally-coordinate P atoms. (Figure 5.4 A and B) The presence of a single resonance peak in both ²⁷Al and ³¹P NMR spectra confirmed the strict alternation of Al and P atoms at the T-positions of the aluminophosphates framework.^[27] The ³¹P NMR spectra of both microporous and hierarchical materials

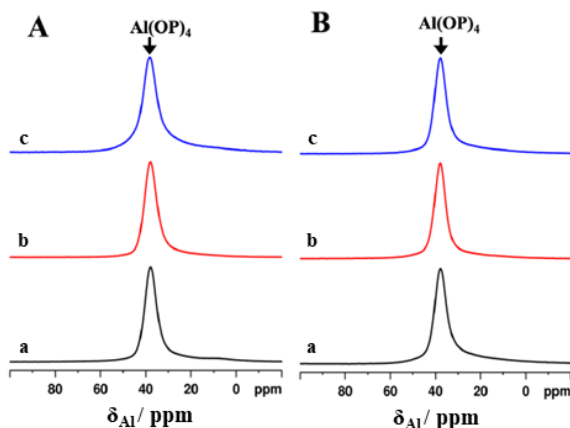


Figure 5.3. The ^{27}Al spectra of A) HP-SAPO-5/xSi and B) microporous SAPO-5/xSi, with $x=0.30$ (a, black curves), $x=0.60$ (b, red curves) and $x=0.90$ (c, blue curves).

at higher silicon loading (*i.e.* $x=0.9$) revealed an additional broad foot beneath the main resonance peak at approximately -24 ppm, owing to P–OH groups or otherwise indicating changes in the second coordination sphere due to Al speciation. These changes were not reflected in the ^{27}Al NMR spectra, probably because of the broadening beyond detection.^[28] Finally, the ^{29}Si MAS NMR spectra of microporous and hierarchical samples revealed multiple signals from -92 to -110 ppm, due to the tetrahedrally-coordinated Si atoms bonded to four, three, two, one and zero Al atoms (Figure 5.5 A and B). Notably, by increasing the Si loading, a decrease in the

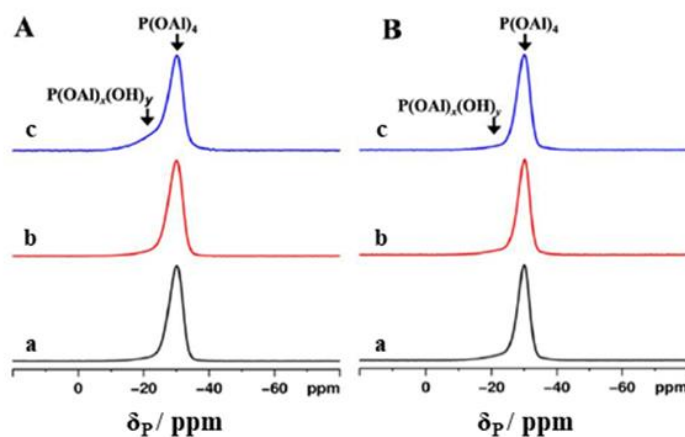


Figure 5.4. The ^{31}P NMR spectra of A) HP-SAPO-5/xSi and B) microporous SAPO-5/xSi, with $x=0.30$ (a, black curves), $x=0.60$ (b, red curves) and $x=0.90$ (c, blue curves).

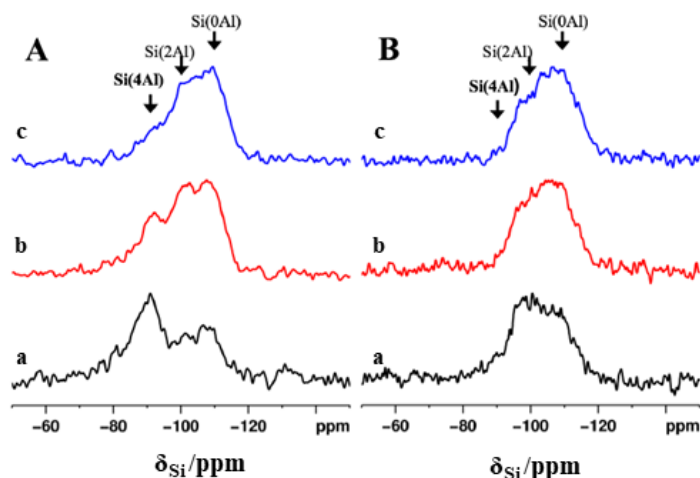


Figure 5.5. The ^{29}Si CP MAS NMR spectra of A) HP-SAPO-5/ $x\text{Si}$ and B) microporous SAPO-5/ $x\text{Si}$, with $x=0.30$ (a, black curves), $x=0.60$ (b, red curves) and $x=0.90$ (c, blue curves).

intensities of resonance signal related to isolated silicon atoms (Si(4Al)) was detected, with concomitant enhancement of the intensities of signals ascribable to tetrahedrally-coordinated Si atoms bonded to a smaller number of Si atoms (Si(3Al) to Si(0Al)). Significantly, this experimental evidence strongly confirmed that, at high silicon concentration, Si incorporation within the SAPO framework *via* SM2 and SM3 mechanism leads preferentially to the formation of silicon island instead of isolated BAS.

^1H SS NMR and FT-IR spectroscopies were performed to investigate the nature and strength of the acid sites present in SAPO-5/ $x\text{Si}$ and HP-SAPO-5/ $x\text{Si}$ catalysts with different Si loadings. Indeed, FT-IR spectroscopy can help to unravel the differences between the proton species located within the SAPOs framework (Figure 5.6 A and B). In the O–H stretching region, FT-IR spectra of HP-SAPO-5/ $x\text{Si}$ exhibited two distinctive bands centred at 3630 and 3513 cm^{-1} (Figure 5.6 A), owing to the O–H stretching mode of BAS with different acid strength, located in the 12-ring and 6-ring channels of the AFI framework.^[27,29-32] Additional signals arising from isolated Si–OH (3745 cm^{-1}) and isolated P–OH (3678 cm^{-1}) sites were also observed with increasing intensities from $x=0.3$ to $x=0.9$, indicating that the number

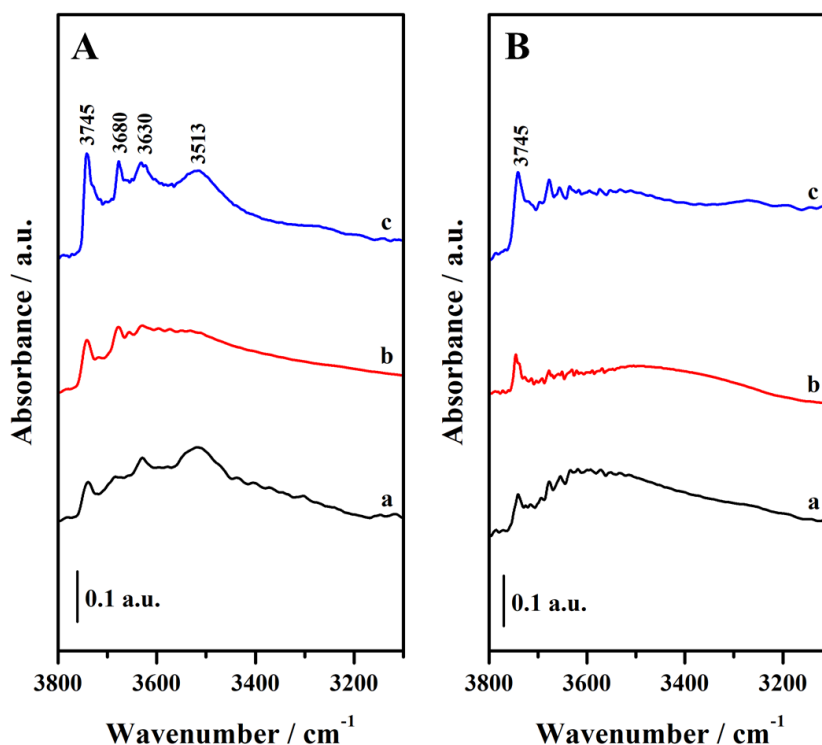


Figure 5.6. FT-IR spectra in the O-H stretching region of A) HP-SAPO-5/ x Si and B) microporous SAPO-5/ x Si, with $x=0.30$ (a, black curves), $x=0.60$ (b, red curves) and $x=0.90$ (c, blue curves).

of defects in the AFI framework has increased with Si loading. In the FT-IR spectra of microporous SAPO-5 (Figure 5.6 B), the bands due to the stretching of BAS were not detected due to the high scattering profile of the microporous SAPO-5 and only the contribution of Si–OH (3745 cm^{-1}) can be appreciated, with the same intensity trend detected for HP-SAPO-5/ x Si catalysts.^[32]

^1H SS NMR spectra, together with quantitative analysis, rendered direct information on the nature and density of protonic species present in the samples (Figure 5.7 A and B, Table 5.2). Two well separated resonance peaks centred at around 3.5 and 4.6 ppm, owing to two different types of Brønsted acid sites (BAS1 and BAS2) located respectively in the 12- and 6-membered ring channels within the AFI framework^[27], were detected in the spectra of both HP-SAPO-5/ x Si and microporous SAPO-5/ x Si. The intensity of both bands decreased with the Si loading

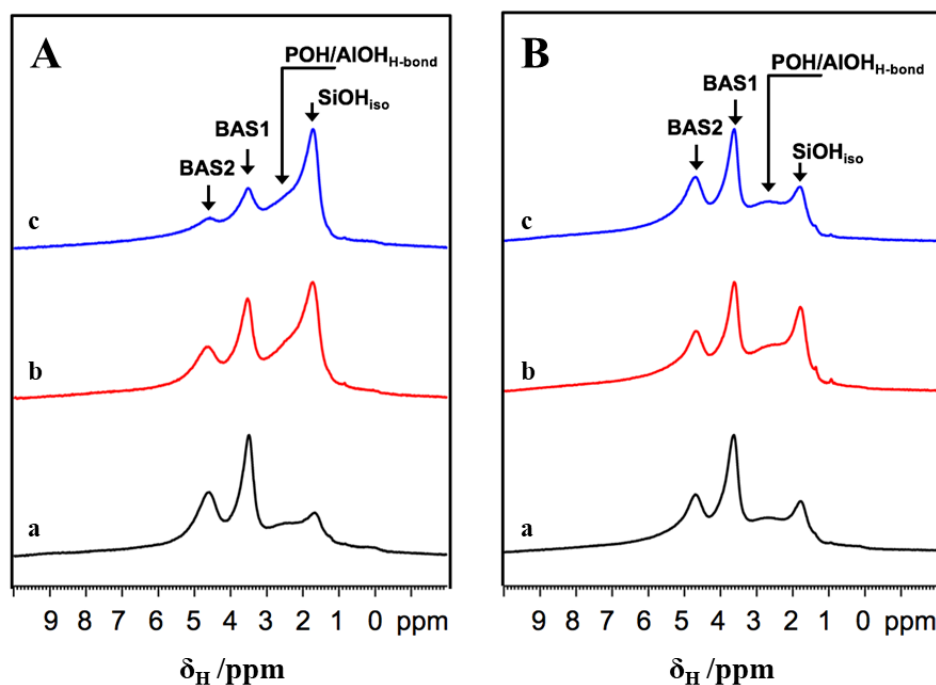


Figure 5.7. The ^1H SS NMR spectra of A) HP-SAPO-5/ x Si and B) microporous SAPO-5/ x Si, with $x=0.30$ (a, black curves), $x=0.60$ (b, red curves) and $x=0.90$ (c, blue curves).

for HP-SAPO-5/ x Si catalysts, whilst no definite trend was observed for their microporous counterparts. Whereas the intensity of both bands was found to be similar for HP-SAPO-5/0.6Si and SAPO-5/0.6Si, as well as for HP-SAPO-5/0.3Si and SAPO-5/0.3Si, HP-SAPO-5/0.9Si exhibited much lower intensity for both species compared to SAPO-5/0.9Si (21 vs. 12 for BAS1 at 3.5 ppm, and 14 vs. 5 for BAS2 at 4.6 ppm). Apart from Brønsted acid sites, a signal at ca. 1.7 ppm, attributed to isolated Si–OH groups, was observed in all ^1H MAS NMR spectra, together with a band centred at around 2.6 ppm, due to Al–OH and/or P–OH defects with very weak acidity.^[29–31] The intensity of the former band exhibited a neat increase with the Si loading for HP-SAPO-5/ x Si catalysts from 4 ($x = 0.3$) to 19 ($x = 0.9$), whereas the increase was more moderate for SAPO-5/ x Si catalysts (from 11 for $x = 0.3$ to 15 for $x = 0.9$). When comparing the SAPO-5/ x Si and HP-SAPO-5/ x Si catalysts at the same Si loading, the intensity was found to be similar for $x=0.6$ and $x=0.9$, whereas a much lower intensity was observed for HP-SAPO-5/0.3Si compared to SAPO-5/

Table 5.2. FT-IR frequencies and population distribution of the protonic species obtained from single-pulse ^1H SS NMR spectroscopy HP-SAPO-5/ x Si and microporous SAPO-5/ x Si, with $x = 0.3, 0.6, 0.9$.

ν_{OH} [cm^{-1}]	^1H Chemical shift [ppm]	Assignment	HP-SAPO-5/ x Si			Micro-SAPO-5/ x Si		
			$x=0.3$	$x=0.6$	$x=0.9$	$x=0.3$	$x=0.6$	$x=0.9$
3745	1.7-2.1	SiOH _{iso} AlOH,	4	16	19	11	16	15
3680	2.2-2.4	POH H-bonded	20	27	33	15	19	12
3630	3.5-3.9	BAS1	22	16	12	24	17	21
3513	4.6-4.9	BAS2	19	11	5	13	9	14

0.3Si (11 vs. 4). In contrast, the latter bands were systematically enhanced for HP-SAPO-5/ x Si catalysts compared to the SAPO-5/ x Si analogues (20 vs. 15 for $x = 0.3$, 27 vs. 19 for $x = 0.6$ and 33 vs. 12 for $x = 0.9$). Furthermore, for HP-SAPO-5/ x Si catalysts, the intensity increased monotonously with the Si loading from 20 for $x = 0.3$ to 33 for $x = 0.9$. Overall, all these results pointed out that, by increasing the Si more defects such as Si–OH, Al–OH and/or P–OH were produced in HP-SAPO-5/ x Si catalysts at the expense of Brønsted acid sites.

To assess the accessibility of the acid sites in HP-SAPO-5/ x Si catalysts, FT-IR spectroscopy coupled with the adsorption of basic probe molecules, with variable steric hindrance, such as NH_3 and 2,6-di-*tert*-butylpyridine (2,6-dTBP), was performed. The total amount of Brønsted acid sites was measured using NH_3 , which, due to its small kinetic diameter (0.26 nm), is usually considered a suitable probe molecule for titrating acid hydroxyl groups accessible through pores, channels or windows in zeolites with a size $< 4 \text{ \AA}$. This strong base can interact with weakly acid sites through its lone electron pair *via* hydrogen bond, *e.g.* Si–OH and P–OH species, or undergo a proton transfer with strong acid sites, *e.g.* Brønsted acid sites.^[33,34] In contrast, 2,6-dTBP, with a kinetic diameter of 1.05 nm, is not expected to enter the

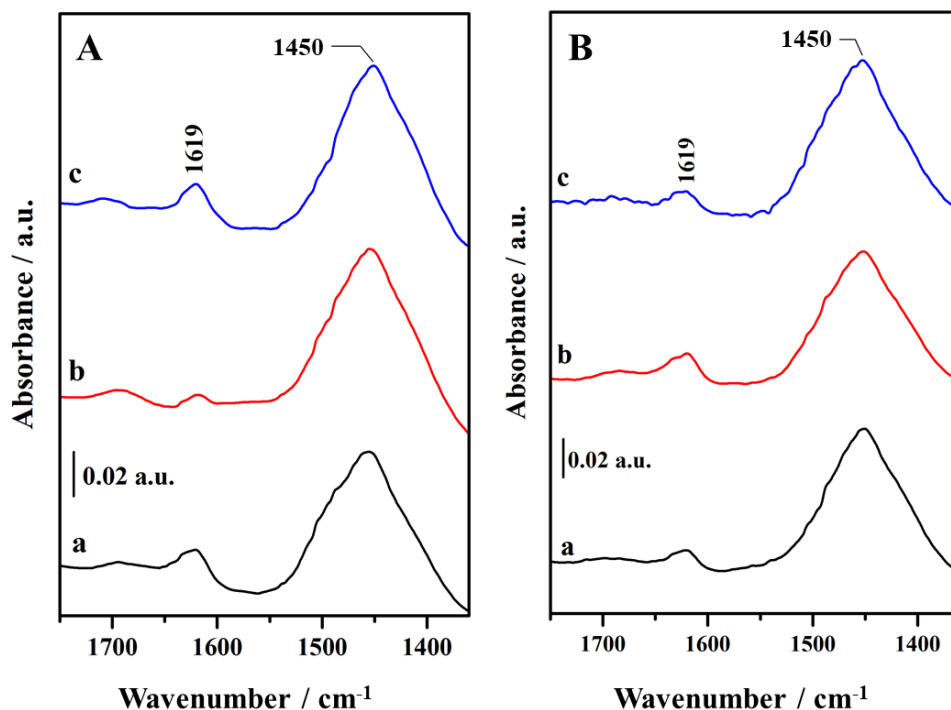


Figure 5.8. The FT-IR difference spectra of NH₃ adsorbed on A) HP-SAPO-5/xSi and B) microporous SAPO-5/xSi, with $x=0.30$ (a, black curves), $x=0.60$ (b, red curves) and $x=0.90$ (c, blue curves) after outgassing the probe molecule at room temperature.

micropores, and can therefore only probe the more accessible acid sites located on the mesopores surface or at the micropores mouths.^[35] Difference FTIR spectra of NH₃ and 2,6-dTBP adsorbed on HP-SAPO-5/xSi catalysts are reported in the low frequency zone, where the signals of protonated species are observed (Figure 5.8 A and Figure 5.9). For comparison, NH₃ was also probed on microporous SAPO-5/xSi to compare the amount of Brønsted acid sites in microporous and hierarchical catalysts (Figure 5.8 B). Upon NH₃ adsorption, a proton transfer from strong acid sites (BAS) occurs, resulting in the formation of NH₄⁺ protonated species. This interaction can be readily detected through the signal appearing at 1450 cm⁻¹, assigned to the δ_{as} of NH₄⁺ ions. After outgassing the samples at room temperature, this bands were retained in both HP-SAPO-5/xSi and microporous SAPO-5/xSi, stressing the strength of this interactions. Conversely, weak interactions *via* hydrogen bond with silanols were almost completely lost, thus only a weak signal at

Table 5.3. Integrated area (A) of the $\delta_{\text{asym}} \text{NH}_4^+$ (1450 cm^{-1}) band, calculated referring to the spectra of the catalyst outgassed at 298 K, and total number of Brønsted acid sites (N) determined by adsorbing NH_3 on HP-SAPO-5/ x Si and microporous SAPO-5/ x Si.

x	HP-SAPO-5/ x Si		Micro-SAPO-5/ x Si	
	A^a [cm^{-1}]	N^b [$\mu\text{mol g}^{-1}$]	A^a [cm^{-1}]	N^b [$\mu\text{mol g}^{-1}$]
0.3	6.29	42.8	6.88	46.8
0.6	6.80	46.2	6.48	44.1
0.9	6.66	45.3	6.66	53.2

^aThe integrated area of band at 1450 cm^{-1} . ^b $\epsilon = 0.147 \text{ cm}^2 \mu\text{mol}^{-1}$.^[37]

1619 cm^{-1} (δNH_3 H-bonded to Si–OH groups) was observed. The total number of Brønsted acid sites (N) of HP-SAPO-5/ x Si and microporous SAPO-5/ x Si, determined *via* NH_3 adsorption and estimated by means of Lambert-Beer law (for further explanation refer to Chapter 9/Experimental section), is reported in Table 5.3.

The density of accessible Brønsted acid sites (N) titrated by NH_3 was found to be similar for microporous SAPO-5/0.3Si ($46.80 \mu\text{mol g}^{-1}$) and SAPO-5/0.6Si ($44.08 \mu\text{mol g}^{-1}$), whereas it exhibited a higher value for SAPO-5/0.9Si ($52.30 \mu\text{mol g}^{-1}$). In the case of hierarchical HP-SAPO-5/ x Si catalysts, HP-SAPO-5/0.6Si and HP-SAPO-5/0.9Si revealed a higher density of Brønsted acid sites with 46.25 and $45.32 \mu\text{mol g}^{-1}$, respectively, compared to HP-SAPO-5/0.3Si, with $42.79 \mu\text{mol g}^{-1}$. However, HP-SAPO-5/0.9Si displayed a lower density of Brønsted acid sites than SAPO-5/0.9Si, as also evidenced by ^1H MAS NMR (Table 5.2).

A proton transfer with more accessible Brønsted acid sites in hierarchical catalysts also occurs when 2,6-dTBP is adsorbed and subsequently outgassed, and a band at 1618 cm^{-1} (ν_{8a}), due to protonated 2,6-dTBPH⁺ species, can be clearly observed in the spectra of HP-SAPO-5/ x Si (Figure 5.9). On the contrary, signal at 1578 cm^{-1} , due to hydrogen bonding interactions with silanols, almost totally disappeared.^[35] The density of accessible Brønsted acid sites (N) in HP-SAPO-5/ x Si catalysts titrated using 2,6-dTBP compared to the density of accessible sites titrated by NH_3 are listed in Table 5.4. Spectroscopic quantifications evidenced that only a

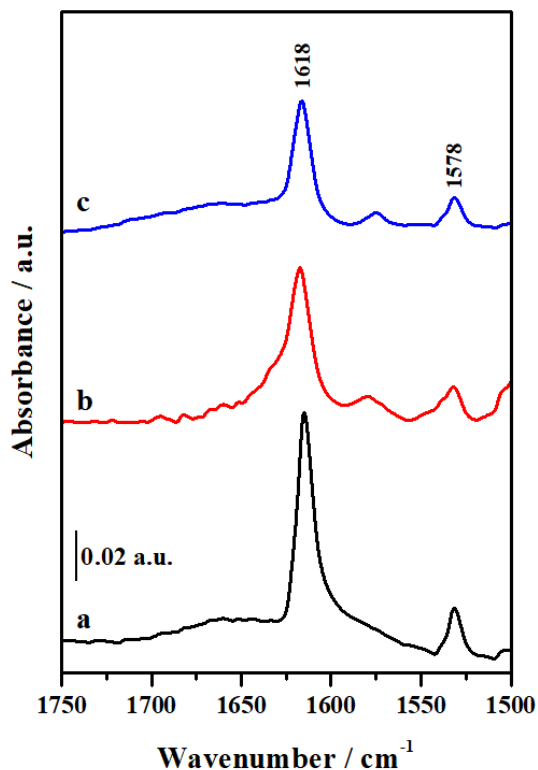


Figure 5.9. The FT-IR difference spectra of 2,6-dTBP adsorbed on A) HP-SAPO-5/xSi and B) microporous SAPO-5/xSi, with $x=0.30$ (a, black curves), $x=0.60$ (b, red curves) and $x=0.90$ (c, blue curves) after outgassing the probe molecule at room temperature.

small fraction of Brønsted acid sites were accessible to the bulkier probe molecules. The accessibility factor (AF)^[36], defined as the density of sites titrated by 2,6-dTBP divided by the density of Brønsted acid sites titrated by NH_3 , revealed a higher value for HP-SAPO-5/0.3Si ($AF = 0.049$), while HP-SAPO-5/0.6Si and HP-SAPO-5/0.9Si show a similar value ($AF = 0.025$). By assuming that the Brønsted acid sites titrated by 2,6-dTBP are preferentially located on the mesoporous surface, the density of Brønsted acid sites located in the micropores can be estimated by subtracting the density of acid sites titrated by 2,6-dTBP from that titrated by NH_3 . Interestingly, regardless of the Si loading, the density of Brønsted acid sites located in the micropores is similar in the different HP-SAPO-5/xSi catalysts, with a value of $0.13 \mu\text{mol m}^{-2}$ or $0.08 \text{ sites nm}^{-2}$ of microporous surface area. This experimental evidence suggested that Brønsted acid sites located in the micropores of HP-SAPO-5/xSi have

Table 5.4. Integrated area (A) of the $\delta_{\text{asym}} \text{NH}_4^+$ (1450 cm^{-1}) and $\nu_{8a} \text{2,6-dTBPH}^+$ bands, calculated referring to the spectra of the catalyst outgassed at 298 K and density of accessible Brønsted acid sites (N), density of the acid sites in micropores determined by adsorbing NH_3 and 2,6-dTBP on HP-SAPO-5/ x Si catalysts.

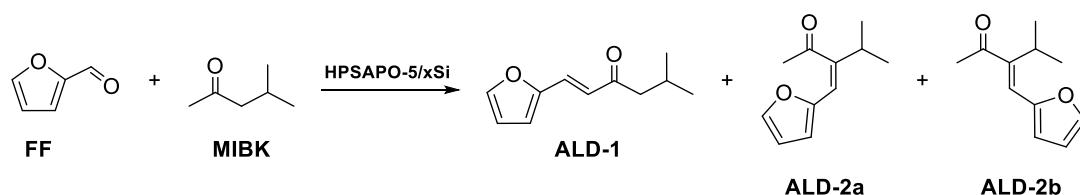
x	NH ₃ adsorption		2,6-dTBP adsorption		AF	Acid sites in micropores [$\mu\text{mol g}^{-1}$] ^c
	A^a [cm^{-1}]	N^b [$\mu\text{mol g}^{-1}$]	A^a [cm^{-1}]	N^b [$\mu\text{mol g}^{-1}$]		
0.3	6.29	42.8	1.04	2.08	0.049	40.7 (0.078)
0.6	6.80	46.2	0.58	1.16	0.025	45.1 (0.083)
0.9	6.66	45.3	0.58	1.16	0.025	44.2 (0.080)

^aThe integrated area of band at 1450 cm^{-1} . ^b $\epsilon = 0.147 \text{ cm}^2 \mu\text{mol}^{-1}$ for NH_4^+ band^[37] and $\epsilon = 0.50 \text{ cm}^2 \mu\text{mol}^{-1}$ for 2,6-dTBPH⁺ band^[35]. ^cIn parenthesis, acid sites per nm^2 of microporous surface area.

not been affected by an increase of the Si loading. Conversely, for high Si loading, silicon incorporation turned out to be facilitated on the mesoporous surface of the hierarchical catalyst, thus leading to an increase of Si–OH moieties within the mesopores at the expense of BAS.

5.1.2.3 Catalysis

The catalytic activity of HP-SAPO-5/ x Si materials was preliminary tested in the aldol condensation/crotonization of FF with MIBK, an acid catalysed reaction, to obtain (E)-1-(furan-2-yl)-5-methylhex-1-en-3-one (ALD-1) as main product and (E)- and (Z)-3-(furan-2-ylmethylene)-4-methylpentan-2-one (ALD-2a and ALD-2b, respectively) as by-products (Scheme 5.1).



Scheme 5.1. Main products obtained in the aldol condensation/crotonization reaction of FF with MIBK over acid HP-SAPO-5.

Table 5.5. Summary of the catalytic properties for HP-SAPO-5/xSi.

x	Conversion FF (%)	Selectivity FAAD (%)	Selectivity byproducts (%)
0.3	45	72	13
0.6	49	61	13
0.9	73	62	14

The alcohol intermediate issued from the aldol condensation was only observed at trace levels for a FF conversion higher than 10%. Besides, no products issued from the aldol self-condensation/crotonization of MIBK were detected. In Table 5.5 the FF conversion and ALD-1 and ALD-2a / ALD-2b selectivity are reported. HP-SAPO-5/0.9Si (higher amount of silanols, lower amount of BAS) exhibited a higher conversion (73 %) with respect to HP-SAPO-5/0.6Si (49 %) and HP-SAPO-5/0.3Si (45%). The selectivity of HP-SAPO-5/0.9Si and HP-SAPO-5/0.6Si was comparable (62 and 61 %), but lower with respect to HP-SAPO-5/0.3Si (72 %, higher amount of BAS and lower amount of silanols). The selectivity of the aldolization by-products ALD-2a and ALD-2b was found to be similar for the different HP-SAPO-5/xSi samples with a value about 13%. Overall, the obtained results evidenced an important effect of the Si loading and the presence of a hierarchical architecture on the catalytic properties of acid SAPO-5 catalysts in the aldol condensation/crotonization reaction of FF with MIBK, due the interconnectivity of micro- and mesopores in HP-SAPO-5/xSi catalysts which favour the cooperativity between the Brønsted acid sites and Si–OH groups during acid-catalysed reactions.

5.1.3 Conclusions

Hierarchical SAPO-5 catalysts at variable Si loading have been successfully synthesised using a soft-templating bottom-up synthetic approach. HP-SAPO-5/xSi physico-chemical properties were investigated by means of a detailed physico-chemical characterization and compared with SAPO-5/xSi microporous analogues. Besides confirming the coexistence of multiple levels of porosity, volumetric

analysis evidenced that microporous textural features of HP-SAPO-5/xSi had not been affected by an increase of the silicon and mesopore structure directing agent concentration. To gain a deeper insight in the nature and density of the protonic species present in SAPO-5/xSi and HP-SAPO-5/xSi catalysts, ^1H SS NMR and probe adsorbed FT-IR spectroscopies were performed. On the whole, ^1H NMR results stressed that, by increasing the Si loading, more defects such as Si–OH, Al–OH and/or P–OH were produced in HP-SAPO-5/xSi catalysts at the expense of Brønsted acid sites, whereas no definite trend was observed for their microporous counterparts. In addition, probe-based FT-IR spectroscopy has pointed out a comparable density of BAS located in the micropores for HP-SAPO-5/xSi, regardless of the Si loading. This experimental evidence, together with results obtained by means of NMR, strongly support the hypothesis that the silicon incorporation, for high Si loadings, preferentially occurs on the mesopore surface of hierarchical samples, thus resulting in an increase of Si–OH moieties within the mesopores at the expense of BAS. This assumption might also explain the higher value of the accessibility factor of HP-SAPO-5/0.30Si compared to HP-SAPO-5/0.6Si and HP-SAPO-5/0.9Si. Despite their different location on the catalyst, the interconnectivity of micro- and mesopores in HP-SAPO-5/xSi catalysts can favour the cooperativity between the Brønsted acid sites and Si–OH groups during acid-catalysed reactions. Moreover, silanols groups, mainly located on the mesopore surface of HP-SAPO-5/xSi, can be exploited to graft bulky organic moieties, which could not be accommodated inside the microporous AFI framework, to obtain organic-inorganic hybrid materials with spatially-separated catalytic active sites (organic active site within the mesopores and BAS within the microporous framework). Overall, $x=0.30$ might be a more suitable Si loading to perform studies on the catalyst optimization, as HP-SAPO-5/0.30Si resulted to be more akin to the microporous counterpart. Conversely, HP-SAPO-5/0.60Si and HP-SAPO-5/0.90Si proved to be viable candidates for use as inorganic supports for the synthesis of

organic-inorganic hybrid catalysts, which can also operate in catalytic reactions requiring spatially-separated active sites.

5.2 Hierarchical SAPO-5 with tuned mesopore size

From literature, it is well-established that mesoporous M41S can vary considerably in their pore characteristic (geometry, diameter, size distribution, volume and specific surface area) depending on the synthesis procedure.^[38,39] The precise tuning of pore sizes is among the many desirable properties that have made such materials the focus of great interest. In this perspective, several methods to enlarge the regular hexagonal array of uniform pore openings of MCM-41 have been developed over the years.^[40-51] One the most common attempted procedure for tuning the size of MCM-41 pores is the use of suitable organic additives to expand the surfactant micelles. Substituted aromatic compounds,^[44-48] alkanes,^[49] amines,^[50] tetraalkylammonium cations^[51] or mixtures of two different additives^[44,45,48] have been described as effective swelling agents. Due to its ability of distributing between core and palisade layer of rod-like micelles and to stabilise them, 1,3,5-trimethylbenzene (mesitylene) has proven to be one of the most suitable swelling agents to tune MCM-41 pores.^[48]

In light of the foregoing, a methodology to control the mesopore diameter of hierarchical SAPO-5 will be described in the present section. Swelling of CTAB surfactant micelles with varying amounts of trimethylbenzene was performed with the aim of tuning MCM-41 pores size. Indeed, by increasing the amount of swelling agent, a larger pore size should be obtained. The as-synthesised MCM-41 materials were then used to prepare hierarchical SAPO-5 catalysts, following the bottom-up synthetic methodology described in subsection 5.2.2. A detailed characterization using a multi-technique approach (XRDP, volumetric analyses, FT-IR and ss MAS NMR spectroscopies) was carried out, with the aim to assess whether or not swelled-templated hierarchical SAPO-5 catalysts benefits from the retention of the physico-

chemical properties of a hierarchical SAPO-5 analogue, whilst simultaneously enhance mass transport and accessibility of the acid sites.

5.2.1 Experimental section

5.2.1.1 General

Sodium hydroxide ($\geq 97\%$), hexadecyltrimethylammonium bromide ($\geq 98\%$), 1,3,5-trimethylbenzene (98 %), aluminum isopropoxide ($\geq 98\%$), triethylamine ($\geq 99.5\%$), tetraethyl orthosilicate ($\geq 99\%$) and phosphoric acid (85 wt% in H₂O), all used for the synthesis of SAPO-5 catalysts, were supplied by Sigma-Aldrich (Milano, Italy). NH₃ ($\geq 99.7\%$), purchased from SIAD (Bergamo, Italy) and 2,6-di-tert-butylpyridine ($\geq 97\%$), purchased from Sigma Aldrich (Milano, Italy), were used as probe molecule in FT-IR experiments.

5.2.1.2 Synthesis

Pure MCM-41 was prepared following the methodology reported in literature by Radu *et al.*^[21] MCM-41 materials with tailored pores size were obtained referring to the same procedure, by varying the swelling agent/TEOS ratio (SA/TEOS). Hierarchical SAPO-5 catalysts were synthesized following the bottom-up synthetic procedure described in subsection 5.2.2.

Synthesis of MCM-41 with enlarged pores: MCM-41 nanoparticles were synthesised following a sol-gel methodology. In a 1000 mL r.b.f., hexadecyltrimethylammonium bromide (CTAB, 1.0 g) was dissolved in deionized water (480 mL) and the suspension was left to stir for 30 min. Sodium hydroxide solution (NaOH, 2M, 3.5 mL) was then added and the solution was further stirred for 30 min. Subsequently, 1,3,5-trimethylbenzene (mesitylene, 3.1 and 18.6 mL for SA/TEOS ratio = 1 and 6 respectively) was added under stirring. After 30 min, tetraethyl orthosilicate (TEOS, 5 mL) was added and the solution was further stirred for 2 h. Filtration, washing with deionized water and ethanol gave a white solid, which was cured in air at 80 °C overnight. Pure MCM-41 was synthesised following

the same procedure, omitting the addition of 1,3,5-trimethylbenzene. For the sake of clarity, the nomenclature MCM-41/x:1, will be hereinafter used, where 'x:1' refers to the molar SA/TEOS ratio used to synthesis MCM-41 precursor.

Synthesis of hierarchical HP-SAPO-5/0.30Si with tuned mesopores: hierarchical SAPO-5 catalysts were synthesised following the bottom-up synthetic strategy described in subsection 5.2.2. MCM-41 materials with tailored pores, containing CTAB micelles swelled on the basis of the SA/TEOS ratio, were used both as silicon source as mesoporegen. 0.30 Si loading was selected, resulting in the following synthesis gel molar composition: 1.0 Al/0.93 P/0.3 Si/0.033 CTAB/0.58 TEA/28 H₂O. For the sake of clarity, the nomenclature HP-SAPO-5/x:1, will be hereinafter used, where 'x:1' refers to the molar SA/TEOS ratio used to synthesis MCM-41 precursor.

5.2.1.3 Characterization

Prior to volumetric and spectroscopic measurements, calcined samples were outgassed at 300 °C overnight and for 2 h, respectively, to remove physisorbed water. Further details on the experimental techniques are reported in Chapter 9/Experimental section.

5.2.2 Results and discussion

5.2.2.1 Structural and textural characterization

X-Ray powder diffraction (XRDP) was performed to investigate the structural features of MCM-41/x:1 and HP-SAPO-5/x:1 (Figure 5.10 A-C). The small-angle XRD pattern of MCM-41/0:1 (pure sample) exhibited four well-resolved signals (Figure 5.10 A), indexable as (100), (110), (200) and (210) reflections associated with *p6mm* hexagonal symmetry. The intense (100) signal reflected a *d* spacing of *ca.* 41 Å and a distance between the centre of adjacent pores of 47 Å (details on the calculations of these values have been reported in Chapter 9/Experimental section). The (100) reflection was detected, although with variable intensity, in the

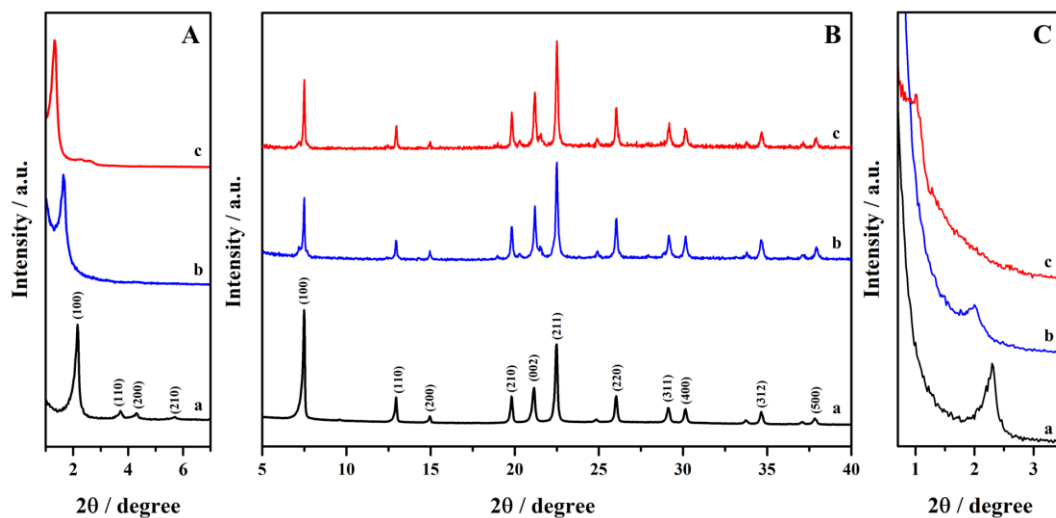


Figure 5.10. The small-angle powder XRD pattern of A) MCM-41/x:1, with x=0 (a, black curve), x=1 (b, blue curve) and x=6 (c, red curve). The B) wide-angle and C) small-angle powder XRD pattern of HP-SAPO-5/x:1, with x=0 (a, black curve), x=1 (b, blue curve) and x=6 (c, red curve).

diffractograms of MCM-41/x:1 swelled samples. By increasing the SA/TEOS ratio from 1:1 to 6:1, a small shift towards smaller 2θ values was observed, reflecting a d spacing of ca. 54 and 66 Å and a distance between adjacent pores of 62 and 76 Å, respectively, thus confirming that the MCM-41 pore enlargement has been successfully performed by using mesitylene as swelling agent. The wide-angle XRD patterns of HP-SAPO-5/6:1 and HP-SAPO-5/1:1 revealed all the characteristic reflections of AFI framework, thus confirming their phase purity and crystallinity (Figure 5.10 B). In addition, small-angle XRD measurements of HP-SAPO-5/x:1 (Figure 5.10 C) evidenced the typical reflection associated with ordered mesoporosity, shifted towards smaller 2θ values with increasing SA/TEOS ratio.

The textural properties of HP-SAPO-5/x:1 were investigated by N_2 adsorption/desorption volumetric analysis at 77 K.^[23] All HP-SAPO-5/x:1 showed Type IV isotherms with a hysteresis loop in the P/P_0 range 0.5-1.0 (Figure 5.11 A), which is typical of a mesoporous material. The pore size distributions of the hierarchical catalysts were determined by means of NLDFT method. HP-SAPO-5/0:1 exhibited mesopores of approximately 30 Å (for further details refer to

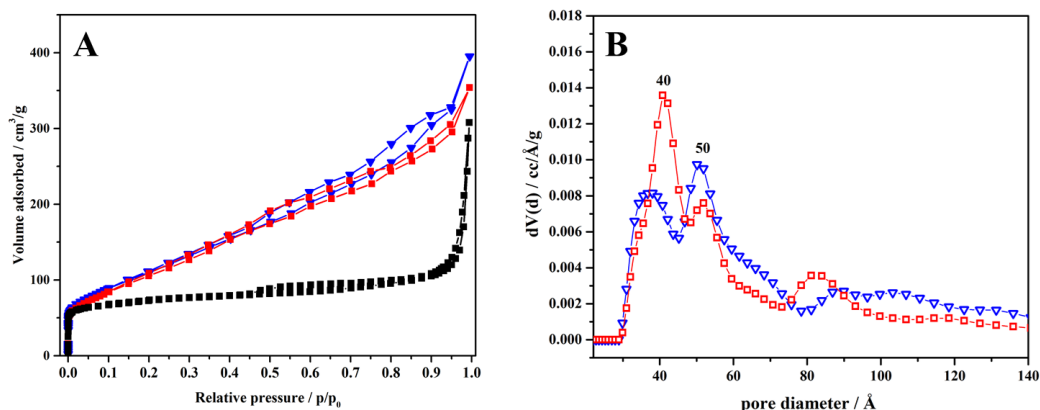


Figure 5.11. A) The N_2 adsorption/desorption isotherms at 77K of HP-SAPO-5/ x :1, with $x=0$ (black curve), $x=1$ (blue curve) and $x=6$ (red curve). B) The pore size distribution in the mesopore range of HP-SAPO-5/1:1 (blue curve) and HP-SAPO-5/6:1 (red curve).

subsection 5.3.1, Figure 5.2 B) whereas HP-SAPO-5/1:1 and HP-SAPO-5/6:1 revealed two family of mesopores at ca. 40 and 50 Å (Figure 5.11 B). Moreover, the micropores volume and surface area of HP-SAPO-5-1:1 and HP-SAPO-5-6:1 were found to be comparable with the one of HP-SAPO-5/0:1, indicating that their micropores textural properties had not been affected by the swelling procedure of CTAB micelles.

5.2.2.2 Spectroscopic characterization

^{27}Al , ^{31}P and ^{29}Si MAS NMR spectroscopy was carried out to confirm that the chemical environment of the framework atoms of HP-SAPO-5/1:1 and HP-SAPO-5/6:1 catalysts had not been altered with respect to HP-SAPO-5/0:1 sample. For all the catalysts, the presence of a single resonance peak in both ^{27}Al and ^{31}P NMR spectra (at about 36 and -30 ppm) confirmed the strict alternation of Al and P atoms at the T-positions of the aluminophosphates framework (Figure 5.12 A and B).^[27] Moreover, the ^{29}Si MAS NMR spectra of HP-SAPO-5/ x :1 revealed multiple signals from -92 to -110 ppm, due to the tetrahedrally-coordinated Si atoms bonded to four, three, two, one and zero Al atoms (Figure 5.12 C).

To assess that the nature of acid sites in HP-SAPO-5/1:1 and HP-SAPO-5/6:1 was analogous to HP-SAPO-5/0:1, FT-IR and ^1H SS NMR spectroscopies were

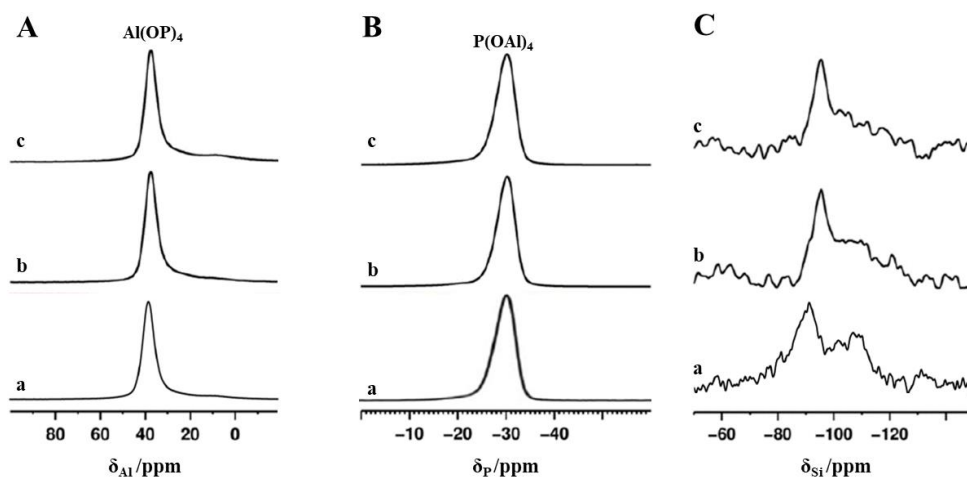


Figure 5.12. The A) ^{27}Al , B) ^{31}P and C) ^{29}Si NMR spectra of HP-SAPO-5/ x :1, with $x=0$ (a), $x=1$ (b) and $x=6$ (c).

performed (Figure 5.13 A and B). Since the same signals were detected with comparable intensities, in FT-IR and ^1H SS NMR spectra of all the catalysts (isolated Si–OH at 3745 cm^{-1} and 1.7 ppm, Al–OH and P–OH at 3680 cm^{-1} and 2.4 ppm, BAS1 at 3630 cm^{-1} and 3.5 ppm, BAS2 at 3513 cm^{-1} and 4.6 ppm, respectively, for further details refers to subsection 5.3.2),^[27,29–32] it was possible to conclude that the nature of the acid sites of the parent HP-SAPO-5/0:1 catalyst had been retained upon the use of swelling agents to prepare MCM-41 precursor.

FT-IR spectroscopy of adsorbed basic NH_3 and 2,6-dTPB was carried out to evaluate the accessibility of the acid sites in HP-SAPO-5/1:1 HP-SAPO-5/6:1 catalysts. Upon the adsorption of 2,6-dTPB (vapour pressure) and NH_3 (90 mbar) and subsequent outgassing at room temperature, the characteristic bands related to the protonate species 2,6-dTBPH $^+$ at 1618 cm^{-1} (ν_{8a}) and NH_4^+ at 1450 cm^{-1} (δ_{asymm}) were detected (Figure 5.14 A and B). Quantifications of the accessible fraction of BAS in hierarchical swelled-templated HP-SAPO-5, estimated by means of Lambert-Beer law (for further explanation refer to Chapter 9/Experimental section), were compared with values obtained for HP-SAPO-5/0:1 (Table 5.6). Although the total number of BAS detected by ammonia adsorption was higher for HP-SAPO-

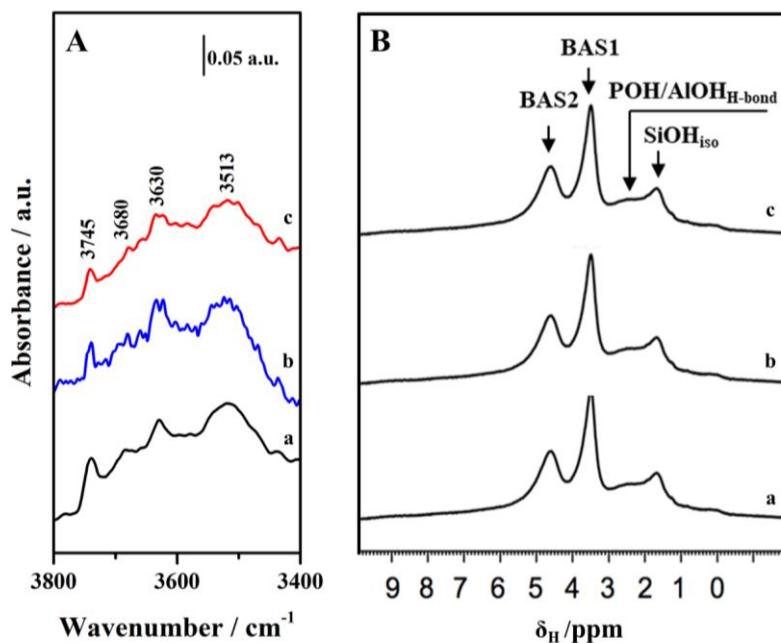


Figure 5.13. The A) FT-IR and B) ¹H SS NMR, of HP-SAPO-5/x:1, with x = 0 (a), x = 1 (b) and x = 6 (c).

5/1:1 and HP-SAPO-5/6:1, the accessibility factor was found to be comparable with respect to the parent hierarchical SAPO-5.

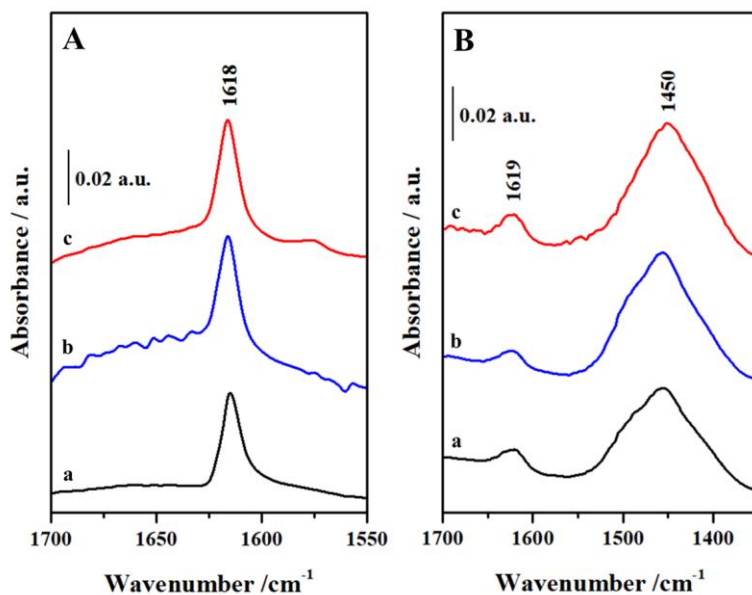


Figure 5.14. FT-IR difference spectra of A) 2,6-dTBP and B) NH₃ of HP-SAPO-5/x:1, with x = 0 (a, black curves), x = 1 (b, blue curves) and x = 6 (c, red curves).

Table 5.6. The accessible fraction of Brønsted acid sites (N) in HP-SAPO-5/x:1 catalysts.

x	NH ₃ adsorption	2,6-dTBP adsorption	AF
	N ^a [μmol g ⁻¹]	N ^b [μmol g ⁻¹]	
0:1	42.8	2.08	0.049
1:1	60.2	2.53	0.042
6:1	62.4	2.87	0.046

^a $\varepsilon = 0.147 \text{ cm}^2 \mu\text{mol}^{-1}$ for NH₄⁺ band^[37]; $\varepsilon = 0.50 \text{ cm}^2 \mu\text{mol}^{-1}$ for 2,6-dTBP⁺ band^[35].

5.2.3 Conclusions

Swelled CTAB micelles, encapsulated in MCM-41 samples, had been used to direct the formation of the mesoporous architecture of hierarchical SAPO-5 catalysts, aiming at increasing the mesopore size by enhancing the swelling agent loading. This strategy has proven to be successful for the enlarging the pore size of MCM-41 samples, indeed by progressively increasing the SA concentration, an increment of the *d* spacing and distance between two adjacent pores was detected. Nevertheless, the same trend was not observed for hierarchical catalysts. Actually, an increase in mesopores diameter from *ca.* 30 to 40-50 Å was detected by volumetric analyses moving from HP-SAPO-5/0:1 to HP-SAPO-5/1:1 and HP-SAPO-5/6:1, but the latter two catalysts displayed the same two mesopores families, with similar dimensions, regardless of the concentration of the swelling agent. FT-IR and SS NMR spectroscopic characterization highlighted the acidic characteristic of the HP-SAPO-5/0:1 had been retained in both the swelled-templated hierarchical SAPO-5 catalysts. Moreover, FT-IR spectroscopy of adsorbed basic probe molecules of different kinetic diameter evidenced the same accessibility factor for all HP-SAPO-5/x:1 samples, with the majority of the BAS located within the microporous framework. Even though a modulation in the mesopore diameter of hierarchical SAPO-5 had not been achieved by increasing the swelling agent loading, the swelling of CTAB micelles nevertheless led to an increase in the mesopores

dimension of HP-SAPO-5/1:1 and HP-SAPO-5/6:1 with respect to parent hierarchical sample. Accordingly, with a view of grafting bulkier organic moieties within the mesopores of a hierarchical SAPO-5, this synthetic strategy should be taken into account.

5.3 Hierarchical SAPO-5 from mesoporous SBA-15 scaffold

In the present section, a soft-templating bottom-up approach to obtain hierarchical SAPO-5 will be investigated.^[22] This synthetic strategy differs from the one described in only for the silicon source and mesoporegen employed, Pluronic123 encapsulated in mesoporous SBA-15 instead of CTAB encapsulated in mesoporous MCM-41. The aim of this methodology was to obtain a hierarchical SAPO-5 with increased mesopores dimensions with respect to HP-SAPO-5 from MCM-41, suitable to graft bulkier organic moieties, whilst simultaneous retention of the acidic properties of parent AFI framework.

5.3.1 Experimental section

5.3.1.1 General

Sodium hydroxide ($\geq 97\%$), Pluronic123, aluminum isopropoxide ($\geq 98\%$), triethylamine ($\geq 99.5\%$), tetraethyl orthosilicate ($\geq 99\%$) and phosphoric acid (85 wt% in H₂O), all used for the synthesis of SAPO-5 catalysts, were purchased by Sigma-Aldrich (Milano, Italy).

5.3.1.2 Synthesis

Hierarchical SAPO-5 was synthesised according to the following hydrothermal procedure, using Pluronic123 encapsulated within ordered mesoporous silica SBA-15 both as silicon source and as mesoporegen.^[22] Aluminium isopropoxide (7.00 g, Sigma Aldrich) was added slowly to deionized water (10 ml) under stirring. Then, triethylamine (TEA, 2.76 ml) was added and the mixture was stirred for 1 h.

Pluronic123-containing SBA-15 (1.5 g, prepared following the methodology reported in literature by Balantseva *et al.*^[52]) was slowly added with deionized water (5 mL) and the mixture was further stirred for 2 h. Phosphoric acid (2.18 mL) was added dropwise under stirring. The gel was vigorously stirred for 30 min to produce a white gel with the following composition: 1.0 Al/0.93 P/0.58 Si/0.068 Pluronic123/0.58 TEA/28 H₂O. The gel was transferred to a Teflon-lined stainless-steel autoclave and crystallized at 473 K for 60 h under autogenous pressure. The solid product from autoclave was then recovered by filtration and washed with water. The as-prepared white solid product was dried in air at 373 K and calcined in a tube furnace under air flow at 873 K for 16 h to remove organic surfactant and micropore template, producing a white crystalline solid. For the sake of clarity, the nomenclature HP-SAPO-5/SBA-15 will be hereinafter used, in order to distinguish this catalyst from HP-SAPO-5/0.6Si (for further details refer to section 5.1-5.4), characterized by the same Si loading but different mesoporegen (CTAB encapsulated in MCM-41). HP-SAPO-5/0.6Si will be hereafter named HP-SAPO-5/MCM-41.

5.3.1.3 Characterization

Before performing volumetric and spectroscopic measurements, calcined samples were outgassed at 300 °C overnight and for 2 h, respectively, to remove physisorbed water. Further details on the experimental techniques are reported in Chapter 9/Experimental section.

5.3.2 Results and discussion

5.3.2.1 Structural and textural characterization

X-Ray powder diffraction (XRD) was carried out to compare the structural features of HP-SAPO-5/SBA-15 catalyst with HP-SAPO-5/MCM-41 and a microporous analogue (Figure 5.15). Typical reflection of AFI framework were detected in the diffractograms of all the sample, thus confirming phase purity and crystallinity also for HP-SAPO-5/SBA-15.

The textural properties of HP-SAPO-5/SBA-15 catalyst were investigated by N₂ adsorption/desorption volumetric analysis at 77 K.^[23] HP-SAPO-5/SBA-15 exhibited Type IV isotherm with a hysteresis loop (Figure 5.16 A), typical of mesoporous materials. With respect to HP-SAPO-5/MCM-41, which was characterized by mesopores of *ca.* 30 Å (for further details, refer to subsection 5.3.1, Figure 5.2 B), HP-SAPO-5/SBA-15 displayed two families of mesopores centred

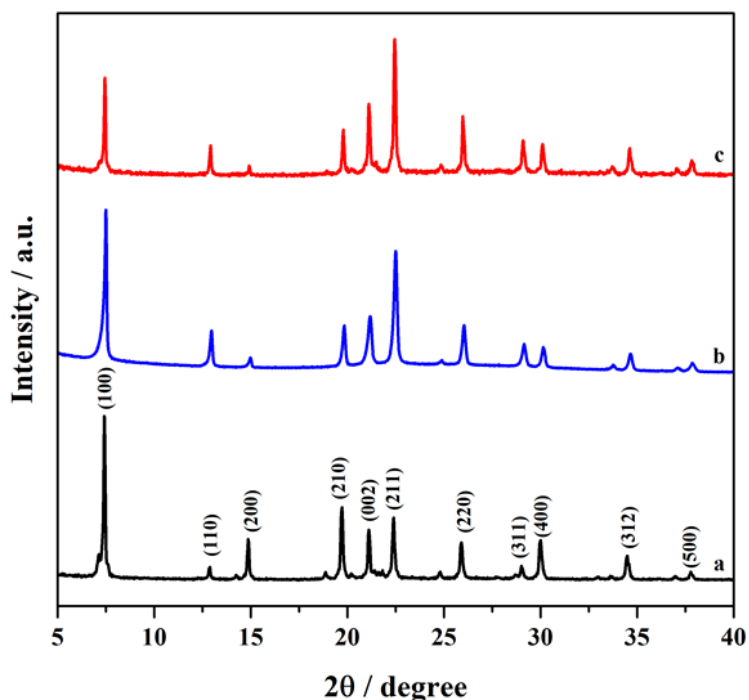


Figure 5.15. The wide-angle powder XRD pattern of microporous SAPO-5 (a, black curve), HP-SAPO-5/MCM-41 (b, red curve) and HP-SAPO-5/SBA-15 (c, blue curve).

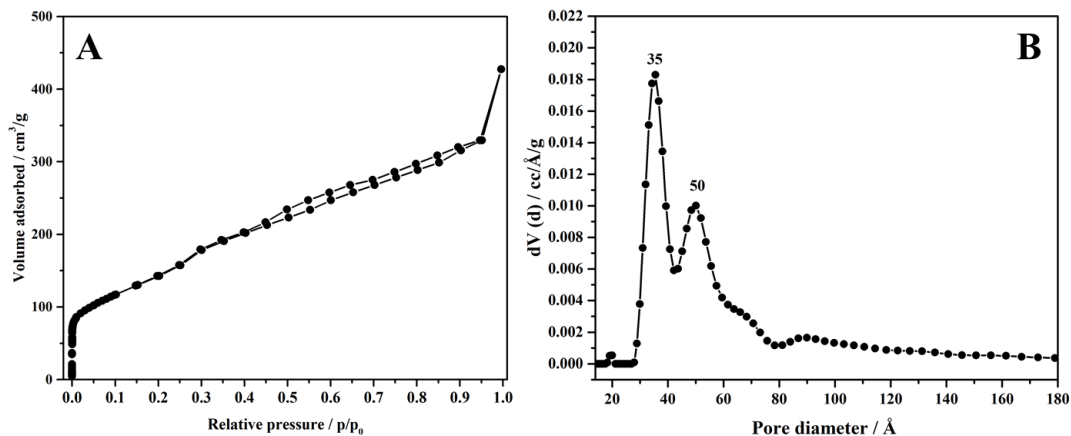


Figure 5.16. A) The N₂ adsorption/desorption isotherm at 77K and B) the pores size distribution of HP-SAPO-5/SBA-15.

approximately at 35 and 50 Å (Figure 5.16 B). Therefore, volumetric analyses confirmed the coexistence of multiple level of porosity within HP-SAPO-5/SBA-15, together with the presence of wider mesopores with respect to HP-SAPO-5/MCM-41 sample.

5.3.2.2 Spectroscopic characterization

²⁷Al, ³¹P and ²⁹Si MAS NMR spectroscopy was performed to confirm that the chemical environment of the framework atoms of HP-SAPO-5/SBA-15 had not been altered with respect to HP-SAPO-5/MCM-41 and microporous analogue. For all the samples, the presence of a single resonance signal in both ²⁷Al and ³¹P NMR spectra (at about 36 and -30 ppm) confirmed the strict alternation of Al and P atoms at the T-positions of the aluminophosphates framework (Figure 5.17 A and B).^[27] In addition, the ²⁹Si MAS NMR spectra of HP-SAPO-5/x:1 revealed multiple signals from -92 to -110 ppm, due to the tetrahedrally-coordinated Si atoms bonded to four, three, two, one and zero Al atoms (Figure 5.17 C).

The nature of acid sites within HP-SAPO-5/SBA-15 catalyst was investigated by means of FT-IR and ¹H SS NMR spectroscopies. FT-IR and ¹H SS NMR spectra of HP-SAPO-5/SBA-15 (Figure 5.18 A and B) exhibited the same signal detected for both HP-SAPO-5/MCM-41 and microporous SAPO-5 samples (Figure 5.6 A and B,

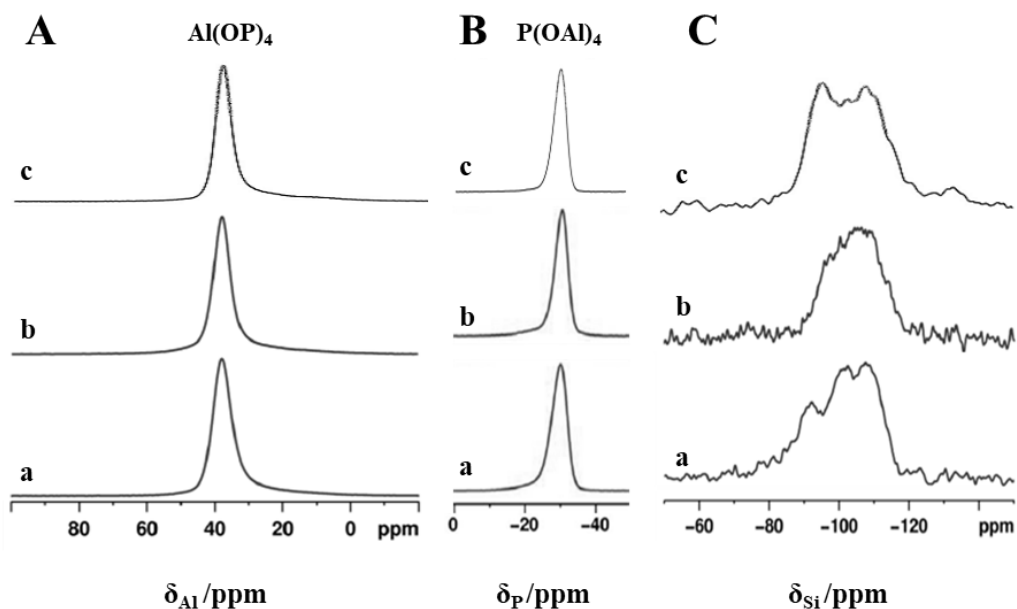


Figure 5.17. The A) ^{27}Al , B) ^{31}P and C) ^{29}Si NMR spectra of microporous SAPO-5 (a), HP-SAPO-5/MCM-41 (b) and HP-SAPO-5/SBA-15 (c).

Figure 5.7 A and B), thus confirming the retention of acidic properties of the AFI framework. Specifically, isolated Si–OH were detected at 3745 cm^{-1} and 1.7 ppm , Al–OH and P–OH at 3680 cm^{-1} and 2.4 ppm , BAS1 at 3630 cm^{-1} and 3.5 ppm , BAS2

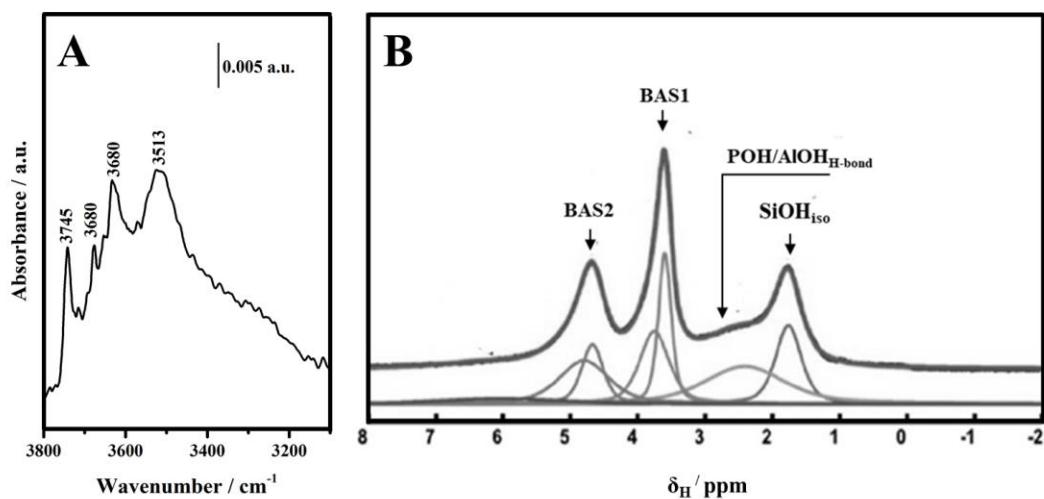


Figure 5.18. The A) FT-IR in the OH stretching region and B) ^1H SS NMR spectra of HP-SAPO-5/SBA-15.

Table 5.7. Proton population distribution obtained from ^1H SS NMR spectra of calcined microporous SAPO-5, HP-SAPO-5/MCM-41 and HP-SAPO-5/SBA-15. FT-IR frequencies of the corresponding OH groups are also reported.

ν_{OH} [cm^{-1}]	^1H Chemical shift [ppm]	Assignment	Microporous SAPO-5	HP-SAPO-5/ MCM-41	HP-SAPO-5/ SBA-15
3745	1.7-2.1	SiOH_{iso}	16	16	15
		AlOH,			
3680	2.2-2.4	POH	19	27	22
		H-bonded			
3630	3.5-3.9	BAS1	17	16	32
3513	4.6-4.9	BAS2	9	11	26

at 3513 cm^{-1} and 4.6 ppm.^[27,29-32] Quantitative analysis obtained by means of ^1H SS NMR is reported in Table 5.7. Surprisingly, HP-SAPO-5/SBA-15 displayed a higher intensity for both BAS1 and BAS1 species with respect to HP-SAPO-5/MCM-41 and microporous SAPO-5 analogue (32 vs. 16 and 17 for BAS1 at 3.5 ppm, and 26 vs. 11 and 9 for BAS2 at 4.6 ppm). The intensity of the signal related to isolated silanols was found to be comparable for all the catalysts (15 vs 16 and 16 at 1.7 ppm).

5.3.3 Conclusions

A distinctive bottom-up method for the synthesis of a hierarchical SAPO-5 has been successfully performed. Compared to the use of CTAB encapsulated in MCM-41, the use of Pluronic, encapsulated within ordered SBA-15, has turned out as an equally valid method to introduce a secondary porosity within the AFI framework. The retention of the Brønsted acidic properties of the AFI framework was assessed by means of FT-IR and SS NMR spectroscopies, together with a comparable number of Si–OH groups with respect to HP-SAPO-5/MCM-41. Moreover, volumetric analysis confirmed the coexistence of multiple levels of porosity within HP-SAPO-5/SBA-15, with mesopores of larger diameter than HP-SAPO-5/MCM-41. In light

of the foregoing, HP-SAPO-5/SBA-15 should be considered a noteworthy inorganic support to anchor bulkier organic molecule, which may not be accommodated in the mesopores of HP-SAPO-5/MCM-41.

5.4 Notes and references

- [1] Pérez-Ramírez, C. H. Christensen, K. Egeblad, C. H. Christensen, J. C. Groen, *Chem. Soc. Rev.* **2008**, 37, 2530.
- [2] L.-H. Chen, M.-H. Sun, Z. Wang, W. yang, Z. Xie, B.-L. Su, *Chem Rev.* **2020**, DOI: <https://doi.org/10.1021/acs.chemrev.0c00016>.
- [3] J.C. Groen, J.C. Jansen, a. Moulijn, J. Pérez-Ramírez, *J. Phys. Chem. B* **2004**, 108, 13062.
- [4] D. Verboekend, M. Milina, J. Pérez-Ramirez, *Chem. Mater.* **2014**, 26, 4552.
- [5] I. Miletto, G. Paul, S. Chapman, G. Gatti, L. Marchese, R. Raja, E. Gianotti, *Chem. Eur. J.* **2017**, 23, 9952.
- [6] I. Miletto, C. Ivaldi, G. Paul, S. Chapman, L. Marchese, R. Raja, E. Gianotti, *ChemistryOpen* **2018**, 7, 297.
- [7] M. Hartmann, L. Kevan, *Chem. Rev.* **1999**, 99, 635.
- [8] E. Gianotti, M. Manzoli, M.E. Potter, V.N. Shetti, D. Sun, J. Paterson, T.M. Mezza, A. Levy, R. Raja, *Chem. Sci.* **2014**, 5, 1810.
- [9] R. J. Pellet, G. N. Long, J. L. Rabo, P. K. Coughlin, US 4,751,340, **1988**.
- [10] R. J. Pellet, G. N. Long, J. L. Rabo, P. K. Coughlin, US 4,740,650, **1988**.
- [11] J.A. Martens, M. Mertens, P.J. Grobet, P.A. Jacobs, in *Innovation in zeolite material science*; P.J. Grobet et al, Eds.; *Stud. Surf. Sci. Catal.* **1988**, 37, p. 97.
- [12] M. Mertens, J.A. Martens, P.J. Grobet, P.A. Jacobs, in *Guidelines for mastering the properties of molecular sieves*; D. Barthomeuf, E.G. Derouane, W. Holderich, EDS.; *NATO ASI Ser. B.* **1990**, 221, p. 1.
- [13] D. Barthomeuf in *Acidity and basicity in solids. Theory, assessment and utility*; J. Fraissard, L. Petrakis, Eds.; *NATO ASI Ser. C* **1993**, 444, p. 375.

- [14] J.A. Martens, P.A. Jacobs, in *Crystalline microporous phosphates. A family of versatile catalysts and adsorbents*; J.C. Janse, M. Stocker, H.G. Karge, J. Weitkamp, Eds.; *Stud. Surf. Sci. Catal.* **1994**, 85, p. 653.
- [15] B. M. Lok, C. A Messina, R. L. Patton, R. T. Gajek, T. R. Cannan, E. M Flanigen, *J. Am. Chem. Soc.* **1984**, 106, 6092.
- [16] J.A. Rabo, in *Zeolite microporous solids: synthesis, structure and reactivity*; E. G. Derouane, F. Lemos, C. Naccache, F. R. Ribeiro, Eds.; *NATO ASI Ser. C* **1992**, 352, p. 531.
- [17] G. Sastre, D. W. Lewis, C.R.A. Catlow, *J. Phys Chem* **1996**, 100, 6722.
- [18] G. Sastre, D. W. Lewis, C.R.A. Catlow, *J. Phys. Chem. B* **1997**, 101, 5249.
- [19] M. Briend, M. Derewinski, A. Lamy, D. Barthomeuf, in *New Frontiers in Catalysis, 10th Intern. Congr. Catal.*, L. Guzzi, F. Solymosi, P. Tetenyi, Eds.; Akademiai Kiado: Budapest, Hungary, **1993**, p. 409.
- [20] D. Barthomeuf, *Stud. Surf. Sci. Catal.* **1997**, 105, 1677.
- [21] D.R. Radu, C.-Y. Lai, K. Jeftinija, E. W. Rowe, S. Jeftinija, V. S.-Y. Lin, *J. Am. Chem. Soc.* **2004**, 126, 13216.
- [22] E. Gianotti, I. Miletto, C. Ivaldi, G. Paul, L. Marchese, M. Meazza, R. Rios, R. Raja, *RCS Adv.* **2019**, 9, 35336.
- [23] K.A. Cychoz, R. Guillet-Nicolas, J. Garcia-Martinez, M. Thommes, *Chem. Soc. Rev.* **2017**, 46, 389.
- [24] W. Lai, S. Yang, Y. Jiang, F. Zhao, Z. Li, B. Zaman, M. Fayaz, X. Li, Y. Chen, *Adsorption* **2020**, 26, 633.
- [25] K.A. Cychoz, R. Guillet-Nicolas, J. Garcia-Martinez, M. Thommes, *Chem. Soc. Rev.* **2017**, 46, 389.
- [26] M. Thommes, K.A. Cychoz, *Adsorption* **2014**, 20, 233.
- [27] B. Zibrowius, E. Loffler, M. Hunger, *Zeolites* **1992**, 12, 167.
- [28] W. Lutz, R. Kurzhals, S. Sauerbeck, H. Toufar, J.-C. Buhl, T. Gesing, W. Altenburg, C. Jger, *Microporous Mesoporous Mater.* **2010**, 132, 31.

- [29] J. Chen, P. A. Wright, S. Natarajan, J. M Thomas, *Stud. Surf. Sci. Catal.* **1994**, 843, 1731.
- [30] S. I. Lee, H. J. Chon, *Chem. Soc. Faraday Trans.* **1997**, 93, 1855.
- [31] G. Müller, J. Bodis, G. Eder-Mirth, J. Kornatowski, J. A. Lercher, *J. Mol. Struct.* **1997**, 410–411, 173.
- [32] E. Gianotti, M. Manzoli, M. E. Potter, V. N. Shetti, D. Sun, J. Paterson, T. M. Mezza, A. Levy, R. Raja, *Chem. Sci.* **2014**, 5, 1810.
- [33] J.M.R. Gallo, C. Bisio, G. Gatti, L. Marchese, H.O. Pastore, *Langmuir* **2010**, 26, 5791.
- [34] A. Zecchina, L. Marchese, S. Bordiga, C. Pazè, E. Gianotti, *J. Phys. Chem B* **1997**, 101, 10128.
- [35] K. Góra-Merek, K. Tarach, M. Choi, *J. Phys. Chem. C* **2014**, 118, 12266.
- [36] K. Sadowska, K. Gorà-Marek, J. Datka, *J. Phys. Chem. C* **2013**, 117, 9237.
- [37] J. Datka, B. Gil, A. Kubacka, *Zeolites* **1995**, 15, 501.
- [38] C.T. Kresge, M.E. Leonowicz, W.J. Roth, J.C. Vartuli, J.S. Beck, *Nature* **1992**, 359, 710.
- [39] J.S. Beck, J.C. Vartuli, W.J. Roth, M.E. Leonowicz, C.T. Kresge, K.D. Schmitt, C.T.W. Chu, D.H. Olson, E.W. Sheppard, S.B. McCullen, J.B. Higgins, J.L. Schlenker, *J. Am. Chem. Soc.* **1992**, 114, 10834.
- [40] A. Sayari, P. Liu, M. Kruk, M. Jaroniec, *Chem. Mater.* **1997**, 9, 2499.
- [41] D. Zhao, J. Feng, Q. Huo, N. Melosh, G.H. Fredrickson, B.F. Chmelka, G.D. Stucky, *Science* **1998**, 279, 548.
- [42] P. Van Der Voort, M. Mathieu, F. Mess, E.F. Vansant, *J. Phys. Chem. B* **1998**, 102, 8847.
- [43] J.S. Beck, J.C. Vartulli, G.J. Kennedy, C.T. Kresge, W.J. Roth, S.E. Schramm, *Chem. Mater.* **1994**, 6, 1816.
- [44] S. Namba, A. Mochizuki, *Res. Chem. Intermed.* **1998**, 24, 561.
- [45] B. Lindlar, A. Kogelbauer, P.J. Kooyman, R. Prins, *Micropor. Mesopor. Mater.* **2001**, 89, 44.

-
- [46] Q. Huo, D.I. Margolese, U. Ciesla, D.G. Demuth, P. Feng, T.E. Gier, P. Sieger, A. Firouzi, B.F. Chmelka, F. Schuth, G.D. Stucky, *Chem. Mater.* **1994**, 6, 1176.
- [47] T. Kimura, Y. Sugahara and K. Kuroda, *J. Chem. Soc., Chem. Commun.* **1998**, 559.
- [48] M. Leuchinger, G.D. Pirngruber, B. Lindar, P. Laggner, R. Prins, *Micropor. Mesopor. Mater.* **2005**, 79, 41.
- [49] J.L. Blin, C. Otjacques, G. Herrier, Bao-Lian Su, *Stud. Surf. Sci. Catal.* **2000**, 129, 75.
- [50] A. Sayari, Y. Yang, M. Kruk, M. Jaroniec, *J. Phys. Chem B* **1999**, 103, 3651–3658.
- [51] A. Corma, Q. Kan, M.T. Navarro, J. Pérez-Pariente, F. Rey, *Chem. Mater.* **1997**, 10, 2123.
- [52] E. Balantseva, I. Miletto, S. Coluccia, G. Berlier, *Micropor. Mesopor. Mater.* **2014**, 193, 103.

6

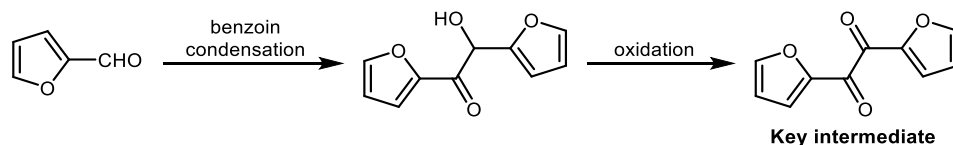
Hybrid catalysts based on N-heterocyclic carbene

In the present chapter, various organic-inorganic hybrid materials based on N-heterocyclic carbene have been investigated. N-heterocyclic carbene (NHC) precursor has been anchored on a range of inorganic supports (Davisil silica, mesoporous MCM-41 and hierarchical SAPO-5 and ZSM-5) with varying textural properties, to obtain hybrid heterogeneous catalysts. The as-synthesised hybrid catalysts were deeply characterised using a multi-technique approach (XRD, volumetric and thermogravimetric analyses, SS NMR and FT-IR spectroscopies), with the aim of establishing structure-property relationship. Moreover, the catalytic activity of the organic-inorganic hybrid materials has been tested in the benzoin condensation reaction of furfural, a base-catalysed reaction.

Introduction

Due to the possibility of combining the advantages of organic and inorganic individual builders, organic inorganic Class II hybrid materials have recently emerged as an important new class of heterogeneous catalysts, rendering solids with high mechanical, structural and hydrothermal stability, together with the flexibility and functionality characteristic of organic compound and polymers.^[1-8] With the aim of combining the soft reaction conditions of organocatalytic chemistry with the recyclability of heterogeneous chemistry, N-heterocyclic carbene organocatalyst was designed and heterogenized on various inorganic supports, for catalysing the benzoin condensation of furfural. Benzoin condensation is an effective strategy to convert biomass into useful chemicals for a range of applications.^[9] Indeed, furfural, hydroxymethylfurfural (HMF) and derivatives can be easily obtained from sugars *via* hydrolysis and dehydration (Scheme 6.1).^[10] Then, the benzoin condensation of

furfural renders furoin, which can be oxidised to furyl, a key intermediate with potential applications in the synthesis of chemicals, sustainable materials and jet or diesel liquid fuels (Scheme 1).^[9]



Scheme 6.1. Benzoin condensation for the synthesis of the key intermediate from furfural.

In this perspective, N-heterocyclic carbene pre-catalyst derived from benzimidazolium salt has been anchored on different inorganic supports, to obtain robust organic-inorganic hybrid catalysts.^[11-13] Initially, NHC moieties were grafted onto a non-ordered mesoporous silica (Davisil), which had been reported by Wang *et al.*^[14] to exhibit remarkable catalytic activity in the benzoin condensation reaction. Subsequently, mesoporous ordered MCM-41, synthesised following the procedure reported by Radu *et al.*,^[15] was employed and compared to a commercial MCM-41. With respect to commercial MCM-41, as-synthesised silica can be obtained both in the calcined form and with surfactant molecules entrapped inside the mesopores, thus paving the way for selective grafting of the NHC precursor on the external or internal mesoporous surface. Lastly, with the aim of combining the Brønsted acidity of zeolite framework with the basic functionality of anchored NHC, hierarchical ZSM-5 and SAPO-5 were used as inorganic support.^[16] This strategy allowed to synthesise a bifunctional acid-base heterogeneous catalyst, with enhanced accessibility of the acid sites through the hierarchical framework, for cascade reactions. The role of the inorganic support, together with the nature of organic-inorganic interface, has been investigated by means of a detailed physico-chemical characterization, using a multi technique approach. Moreover, preliminary catalytic tests in the benzoin condensation of furfural have been also performed to evaluate the catalytic activity of the NHC basic sites. For the sake of clarity, physico-chemical characterization of the various hybrid catalysts will be discussed separately for each one, except for hierarchical materials. After evaluating the catalytic activity, the whole reason some

catalysts exhibited inferior catalytic performances will be investigated. A comparison between the physico-chemical properties of the different catalysts will be made in the Conclusion paragraph, with the aim of establishing preliminary structure-property relationships.

6.1 Experimental section

6.1.1 General

Davisil silica (pore size 150 Å), MCM-41, benzimidazole (98%), NaH (60 % in mineral oil), 1-bromododecane (97%), (3-iodopropyl)trimethoxysilane (95 %) Pluronic123, solvents were purchased from Sigma-Aldrich and used as received. Commercial NH₄-ZSM-5 zeolite was supplied by Zeolyst International with SiO₂/Al₂O₃ = 80 (CBV 8014).

6.1.2 Synthesis of inorganic supports

The synthesis of the inorganic supports was performed at the University of Piemonte Orientale.

Synthesis of MCM-41 nanoparticles: MCM-41 sample was prepared following the methodology reported in literature by Radu *et al.*^[15] and described in Chapter 5, subsection 5.6.2. The as-synthesised material was calcined in a tube furnace in air at 600°C for 10 h to remove the organic surfactant. For the sake of clarity, the nomenclature MCM-41-NPs will be used hereafter, to distinguish this inorganic support from the commercial MCM-41.

Synthesis of hierarchical SAPO-5: hierarchical SAPO-5 catalyst was prepared according to the bottom-up soft-templating strategy described in Chapter 5, subsection 5.10.2, using Pluronic123-containing SBA-15 as both silicon source as mesoporegen.^[16] The as-obtained material was calcined in air at 600 °C for 10 h to remove the organic template.

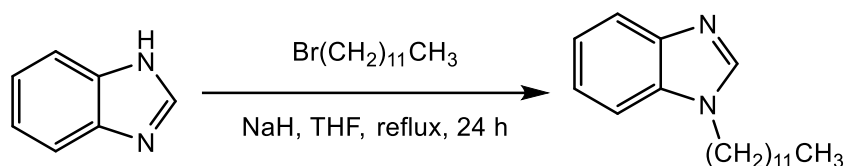
Synthesis of hierarchical ZSM-5: hierarchical ZSM-5 catalyst was synthesised following a top-down approach, consisting in desilication under basic condition to

induce the mesoporosity after the zeolite crystallization.^[17-20] Commercial $\text{NH}_4\text{-ZSM-5}$ zeolite was protonated through calcination at $550\text{ }^\circ\text{C}$ for 16 h under airflow. Subsequently, the zeolite was treated in a 0.2 M NaOH solution (solid/liquid ratio = 22 g L^{-1}) for 3h. In a r.b.f. under stirring, the basic solution was heated at 65°C , the zeolite was subsequently added and the mixture let to stir for 3h. Subsequently, the flask was cooled down with an ice bath and washed with deionized water until pH 7. The as obtained white solid was dried overnight at 80°C . Na-ZSM-5 was then converted to the acidic form by performing a three-times ion exchange with NH_4NO_3 solution (solid/liquid ratio = 6.7 g L^{-1}) at 80°C for 12 h. Finally, H-ZSM-5 was calcined in air at $600\text{ }^\circ\text{C}$ for 16 h.

6.1.3 Synthesis of the N-heterocyclic carbene precursor

The synthesis of N-heterocyclic carbene (NHC) precursor was performed at the University of Southampton, under the supervision of Professor R. Raja and Professor R. Rios.

The first step in the synthesis of the NHC precursor was the 1-alkylation of benzimidazole (Scheme 6.2).

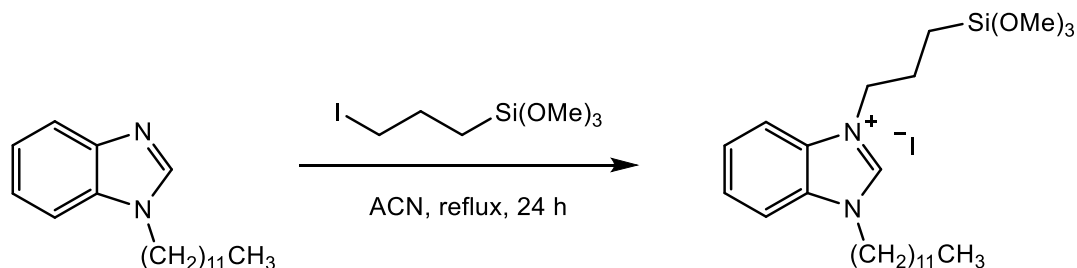


Scheme 6.2. Synthesis of 1-dodecylbenzimidazole.

In a 50 mL r.b.f. under inert atmosphere (Ar), benzimidazole (8.5 mmol) was slowly added to a suspension of NaH (1 eq.) in THF (6 mL) at $0\text{-}5\text{ }^\circ\text{C}$ under stirring and the solution was further stirred for 30 min at room temperature. Subsequently, dodecyl bromide (8.5 mmol) was added dropwise and the solution was left to reflux for 24 h. The solution was filtered and washed with CH_2Cl_2 over a pad of celite. Then the solvent was evaporated, and the product was purified *via* chromatographic column. Yield: 97 %. $^1\text{H-NMR}$ (CDCl_3 , 500 MHz, ppm): 0.90 (t, $-\text{CH}_2-\text{CH}_3$), 1.25–1.35 (m, $\text{N}-\text{CH}_2-\text{CH}_2-(\text{CH}_2)_9-\text{CH}_3$), 1.89 (q, $\text{N}-\text{CH}_2-\text{CH}_2-(\text{CH}_2)_9-\text{CH}_3$), 4.17 (t,

$\text{N-CH}_2\text{-CH}_2\text{-(CH}_2\text{)}_9\text{-CH}_3$), 7.83 (m, Ar), 7.90 (s, N-CH-N). $^{13}\text{C-NMR}$ (CDCl_3 , 125 MHz, ppm): 14 ($\text{-N-(CH}_2\text{)}_{11}\text{-CH}_3$), 22 ($\text{-N-(CH}_2\text{)}_{10}\text{-CH}_2\text{-CH}_3$), 26.8, 29.1, 29.3, 29.4, 29.58, 29.6, 29.85 (aliphatic chain), 31.9 ($\text{N-CH}_2\text{-CH}_2\text{-(CH}_2\text{)}_9$), 45.12 ($\text{N-CH}_2\text{-CH}_2\text{-(CH}_2\text{)}_9$), 109.65, 120.38, 121.98, 122.75, 133.84, 143.90 (aromatic except N-CH-N), 142.93 (N-CH-N).

The second step in the preparation of NHC precursor was the silylation of benzimidazole with an appropriate silane, bearing alkoxy hydrolysable moieties which can condense with Si-OH groups on the inorganic support, thus forming siloxane bridges. The 3-alkylation of benzimidazole was performed following the procedure reported in literature by Wang *et al.* (Scheme 6.3).^[14]



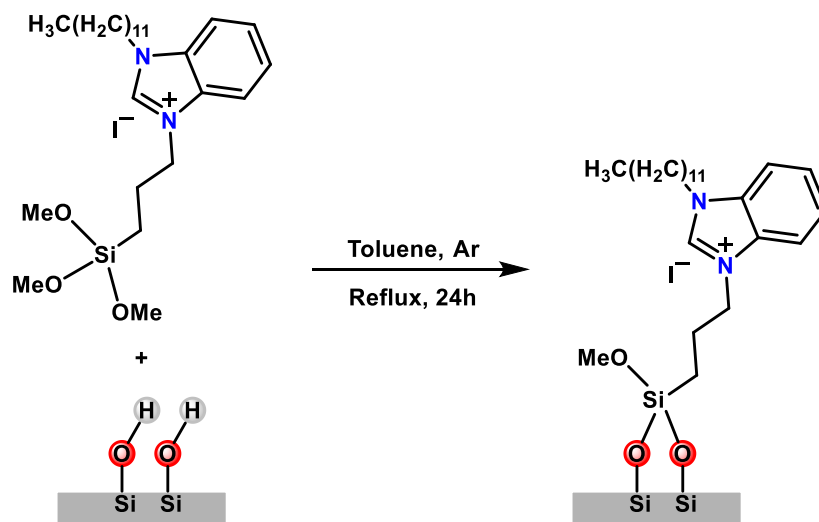
Scheme 6.3. 3-alkylation of benzimidazole.

In a r.b.f under inert atmosphere (Ar) and stirring, 1-alkylated benzimidazole (8.2 mmol) was dissolved in ACN (12 mL). 1-iodo-3-(trimethylsilyloxy)propane (12.3 mmol) was then slowly added. After 30 min of stirring at room temperature, the solution was left to reflux for 24 h under inert atmosphere. Then, the solution was washed with anhydrous pentane. Yield: 95%. $^1\text{H-NMR}$ (CDCl_3 , 500 MHz, ppm): 0.80 (t, $\text{-CH}_2\text{-CH}_3$), 0.699 (O-Si- $\text{CH}_2\text{-CH}_2$), 1.11–1.41 (m, $\text{N-CH}_2\text{-CH}_2\text{-(CH}_2\text{)}_9\text{-CH}_3$), 2 (q, $\text{N}^+\text{-CH}_2\text{-CH}_2\text{-CH}_2\text{-Si}$), 2.11 (q, $\text{N-CH}_2\text{-CH}_2\text{-(CH}_2\text{)}_9\text{-CH}_3$), 3.55 (O- CH_3), 4.53 (t, $\text{N-CH}_2\text{-CH}_2\text{-(CH}_2\text{)}_9\text{-CH}_3$), 4.58 (t, $\text{N}^+\text{-CH}_2\text{-CH}_2\text{-CH}_2\text{-Si}$), 7.58–7.69 (m, Ar), 11.1 (s, N-CH-N). $^{13}\text{C-NMR}$ (CDCl_3 , 125 MHz, ppm): 14 ($\text{-N-(CH}_2\text{)}_{11}\text{-CH}_3$), 22.3, 22.7, 23.3, 26.6, 29, 29.31, 29.37, 29.49, 29.5, 29.57, 31.9, 34.1 (aliphatic chain), 50.8 ($\text{CH}_2\text{-Si-O-(CH}_3\text{)}_3$), 113, 113.24, 127.21, 127.24 (aromatic except N-CH-N), 141.94 (N-CH-N).

6.1.4 Synthesis of hybrid catalysts

NHC-MCM-41, NHC-HP-SAPO-5 and NHC-ZSM-5 catalysts were synthesised during the research period at the University of Southampton. NHC-Davisil silica was synthesised by M. Meazza at the University of Southampton.

Hybrid materials were prepared by post-synthesis grafting with 3-alkylated NHC-precursor (Scheme 6.4).



Scheme 6.4. Graphic representation of NHC grafting on the inorganic support.

In a r.b.f, under stirring and inert atmosphere (Ar), the silylated NHC precursor (0.5 mmol) was dissolved in anhydrous toluene, then the inorganic support (Davisil silica, MCM-41, HP-SAPO-5 and HP-ZSM-5, 0.5 g) was added, and the mixture was let to reflux and stir for 24 h. The reaction was filtered and washed with toluene, giving a yellow solid, which was cured in air at 80 °C overnight.

6.1.5 Characterization

Before performing volumetric analyses and ss NMR and FT-IR spectroscopic measurements, all the samples were outgassed at 200°C for 1h. Further details on the experimental techniques are reported in Chapter 9/Experimental section. The characterization of the hybrids was entirely performed at the University of Piemonte Orientale.

6.1.6 Catalysis

The catalytic tests of the NHC hybrids, with exception of NHC-Davisil silica, were carried out during the research period at the University of Southampton. The catalytic activity of NHC-Davisil silica was evaluated by M. Meazza at the University of Southampton.

The catalytic activity of the NHC hybrids was evaluated in the benzoin self-condensation of furfural to render furoin (Scheme 6.5).



Scheme 6.5. Graphic representation of benzoin condensation reaction.

In a glass vial, at room temperature, were added in sequence the heterogeneous catalyst (10 mol %), anhydrous DMF (0.5 ml), furfural (1 equiv, 0.2 mmol) and DBU (10 mol%). Once the additions were completed, argon was bubbled for 20 minutes, then the vial was closed and left at room temperature without stirring for 20 h. The crude mixture was treated with HCl (0.4 μ mol, 37 %) to regenerate the catalyst precursor (benzimidazolium salt). The crude was then filtered and washed with methanol, dried under vacuum and reused in the next reaction. The conversion of the reaction was monitored by ^1H NMR.

6.2 Results and discussion

6.2.1 Materials

Silylated N-heterocyclic carbene precursor was anchored on the Si–OH groups of different calcined inorganic supports (Davisil silica, HP-ZSM-5, HP-SAPO-5, commercial MCM-41 and MCM-41-NPs) to obtain the corresponding hybrid catalyst (NHC-Davisil silica, NHC-HP-ZSM-5, NHC-HP-SAPO-5, NHC-MCM-41 and NHC-MCM-41-NPs). The role of the long alkyl chain (C_{12}) substituent at the N atom was to prevent NHC deactivation by dimerization and to sterically protect the

Table 6.1. Acronyms, elemental analysis and organic loading of the hybrid catalysts.

Acronym of the hybrid	Organic loading [mmol g ⁻¹]
NHC-Dav150	0.49
NHC-HP-ZSM-5	0.20
NHC-HP-SAPO-5	0.25
NHC-MCM-41	0.46

NHC catalytic site.^[14] The acronyms of the hybrid catalyst, along with their organic loadings determined from elemental analyses, are reported in Table 6.1. The organic loading was found to be similar for hierarchical hybrid materials but lower with respect to NHC-Davisil silica and NHC-MCM-41.

6.2.2 Characterization of NHC-Davisil silica

Thermogravimetric analysis was performed to estimate the organic content and thermal stability of the grafted NHC precursor (Figure 6.1). The thermogram and derivative of NHC-Dav150 exhibited a first weight loss between 30-180 °C, which can be related to the removal of physisorbed water. At higher temperatures, the flat weight loss changed into a rapidly declining profile, ascribable to the decomposition of N-heterocyclic carbene precursor. Moreover, DTG curve revealed that decomposition of NHC precursor started at around 200 °C. The organic content, calculated from the weight loss in the range 180-1100 °C, is reported in Table 6.2 and was found to be consistent with the value obtained from the elemental analysis.

Table 6.2. Weight loss (%) due to physisorbed water and organic content calculated from TGA analysis.

Catalyst	Δw % due to H ₂ O ^a	Δw % due to NHC ^b
Dav150	2.4	-
NHC-Dav150	1.9	16.1

^aCalculated in the range 30-180 °C. ^bCalculated in the range 180-1100 °C

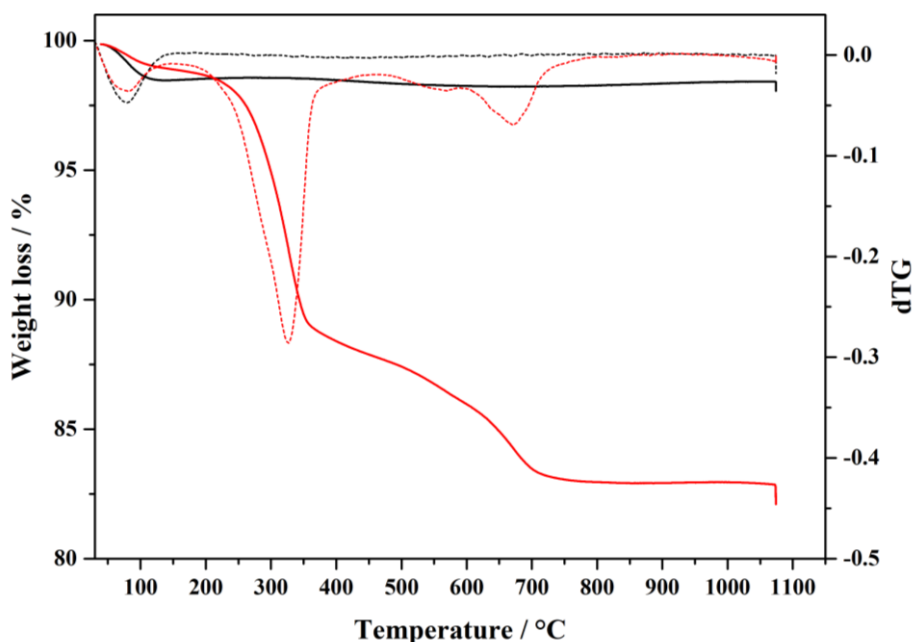


Figure 6.1. TGA/DTG curves of plain Dav150 (black curve) and NHC-Dav150 (red curve).

N_2 adsorption/desorption volumetric analysis at 77 K on NHC-Dav150 and plain Davisil silica was performed to evaluate the textural properties upon the anchoring procedure of NHC precursor.^[21] Both samples revealed type IV isotherms, typical of mesoporous materials (Figure 6.2 A).^[22,23] Pore size distributions, obtained by means of NLDFT (non-localized density functional theory),^[24,25] are reported in Figure 6.2 B, whereas details of the specific surface area and pores volume are listed in Table 6.3. Upon NHC grafting, the N_2 adsorption capacity decreased along with the specific surface area, pore diameter and pore volume, thus confirming the success of the anchoring procedure.

Table 6.3. Textural properties of NHC-Dav150 and plain Dav150.

Sample	SSA _{DFT} [m ² g ⁻¹]	Pore volume [cm ³ g ⁻¹]	Average pore diameter [nm]
Dav150	300	0.98	14
NHC-Dav150	200	0.54	11

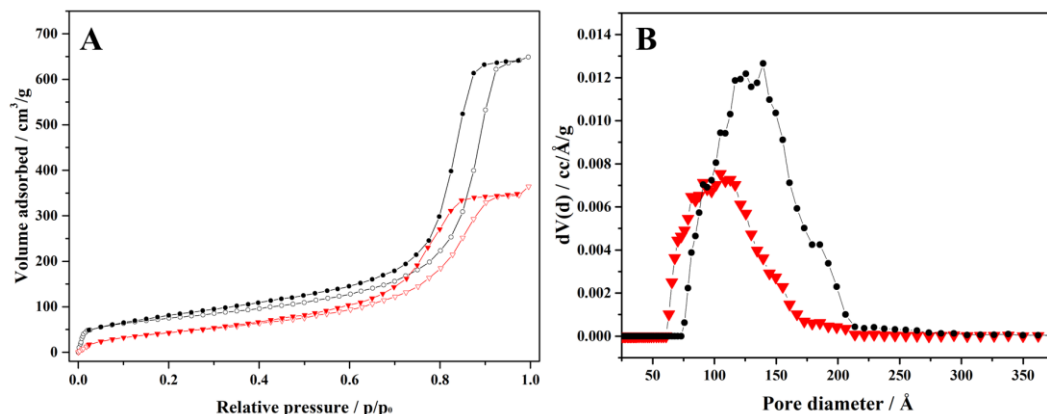


Figure 6.2. A) N₂ adsorption/desorption isotherms at 77 K and B) pore size distribution in the mesopore range of plain Dav 150 (black curve) and NHC-Dav 150 (red curve).

FT-IR spectroscopy at variable temperature was performed with the aim of further investigate the thermal stability of the NHC precursor anchored on the Davisil silica (Figure 6.3 A and B). Upon outgassing the sample at 30 °C, in the high frequency region (4000-2700 cm⁻¹), a broad absorption between 3700 and 3200 cm⁻¹ was recorded, related to the O–H stretching mode of isolated residual silanols and to hydrogen-bonding interactions between surface groups.^[26] Between 3100 and 3000 cm⁻¹, aromatic C–H stretching modes of NHC precursor were detected with very low intensity. In the region 3000-2800 cm⁻¹, the FT-IR spectrum of NHC-Dav150 exhibited the characteristic bands attributed to aromatic C–H stretching vibrations of CH₃ and CH₂ groups of the alkyl chains of NHC precursor. Specifically, signal at 2960 cm⁻¹ can be assigned to ν_{asym} modes of CH₃ groups, whilst bands at 2926 and 2853 cm⁻¹ are related to the asymmetric and symmetric stretching vibration of methylene groups.^[27] In the low frequency region (1700-1300 cm⁻¹), three/four signals due to C=N and C=C stretching modes of aromatic ring are usually detected between 1660-1430 cm⁻¹ for imidazoles. In the spectrum of NHC-Dav150, a band related to the $\nu_{\text{C=N}}$ of benzimidazole ring was identified at 1565 cm⁻¹, whereas signal at 1620 (very low intensity) and 1478 cm⁻¹ might be assigned to $\nu_{\text{C=C}}$ ring vibrations.^[16,27,28] Additional $\nu_{\text{C=C}}$ ring modes might be the band detected at 1428 cm⁻¹ or might fall beneath the signal at 1460 cm⁻¹. Moreover, bands due to the C–H bending

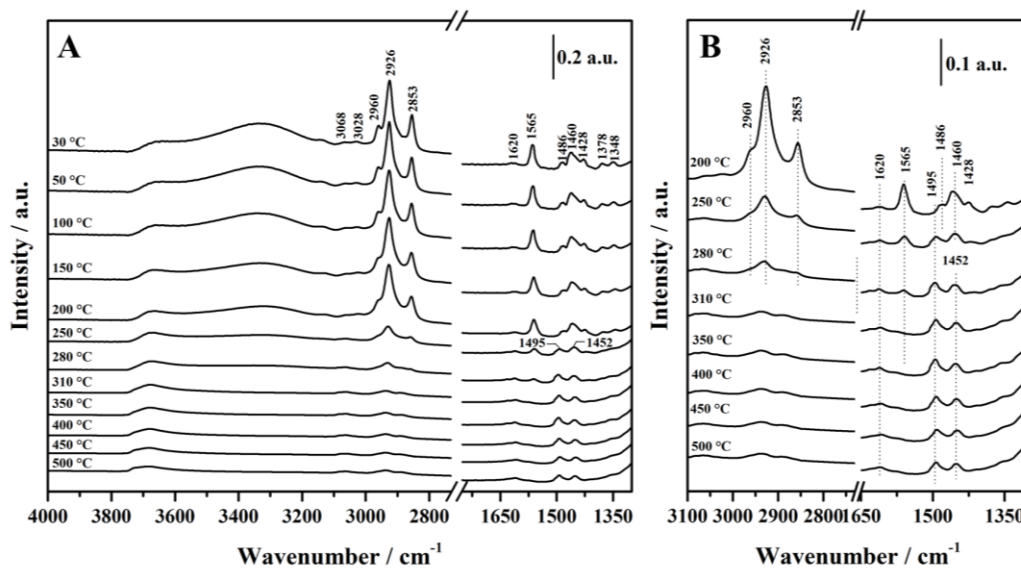


Figure 6.3. A) Variable temperature FT-IR spectra of NHC-Dav150 and B) magnification in the temperature range 200-500 °C.

vibrations were also detected between 1470 and 1300 cm^{-1} . In particular, between 1470 and 1440 cm^{-1} , overlapping of bands related to asymmetric deformation modes of $\text{CH}_3\text{-C}$ (1460 cm^{-1}), symmetric deformation mode of $\text{CH}_3\text{-O}$ (1455 cm^{-1}) and scissoring of CH_2 groups (1450 cm^{-1}) made the assignment difficult.^[29] Conversely, signal due to symmetric bending modes of $\text{CH}_3\text{-C}$ was identified at 1378 cm^{-1} , whereas band at 1348 cm^{-1} can be assigned to C-H in plane deformation of aromatic ring.^[27] By increasing the outgassing temperature, the intensities of the IR signals between 3000-2800 cm^{-1} and 1470-1300 cm^{-1} started decreasing between 200 and 250 °C and almost totally disappeared at 310 °C, thus stressing, in accordance with TGA/DTG data, the progressive decomposition of the NHC precursor in this temperature range (Figure 6.3 A). In particular, the thermal stability of NHC precursor can be monitored by following the reduction in intensity of the unambiguous $\nu_{\text{C=N}}$ stretching mode of the benzimidazole ring. Upon outgassing the sample at 500 °C, signal related to isolated silanols (3745 cm^{-1}) was not detected, indicating that organic decomposition products are deposited on the silica surface. Only band at 1620 cm^{-1} , together with two blue-shifted signals at 1495 and 1452 cm^{-1}

¹ can be appreciate at 500 °C, thus possibly confirming their previous assignation to $\nu_{C=C}$ stretching modes of benzimidazole ring. Indeed, upon thermal treatment, the aromatic ring should be the last portion of the molecule to be decomposed.

Along with FT-IR spectroscopy, ¹H MAS NMR spectroscopy can provide direct information on the different proton sites within the inorganic support (Figure 6.4 A).

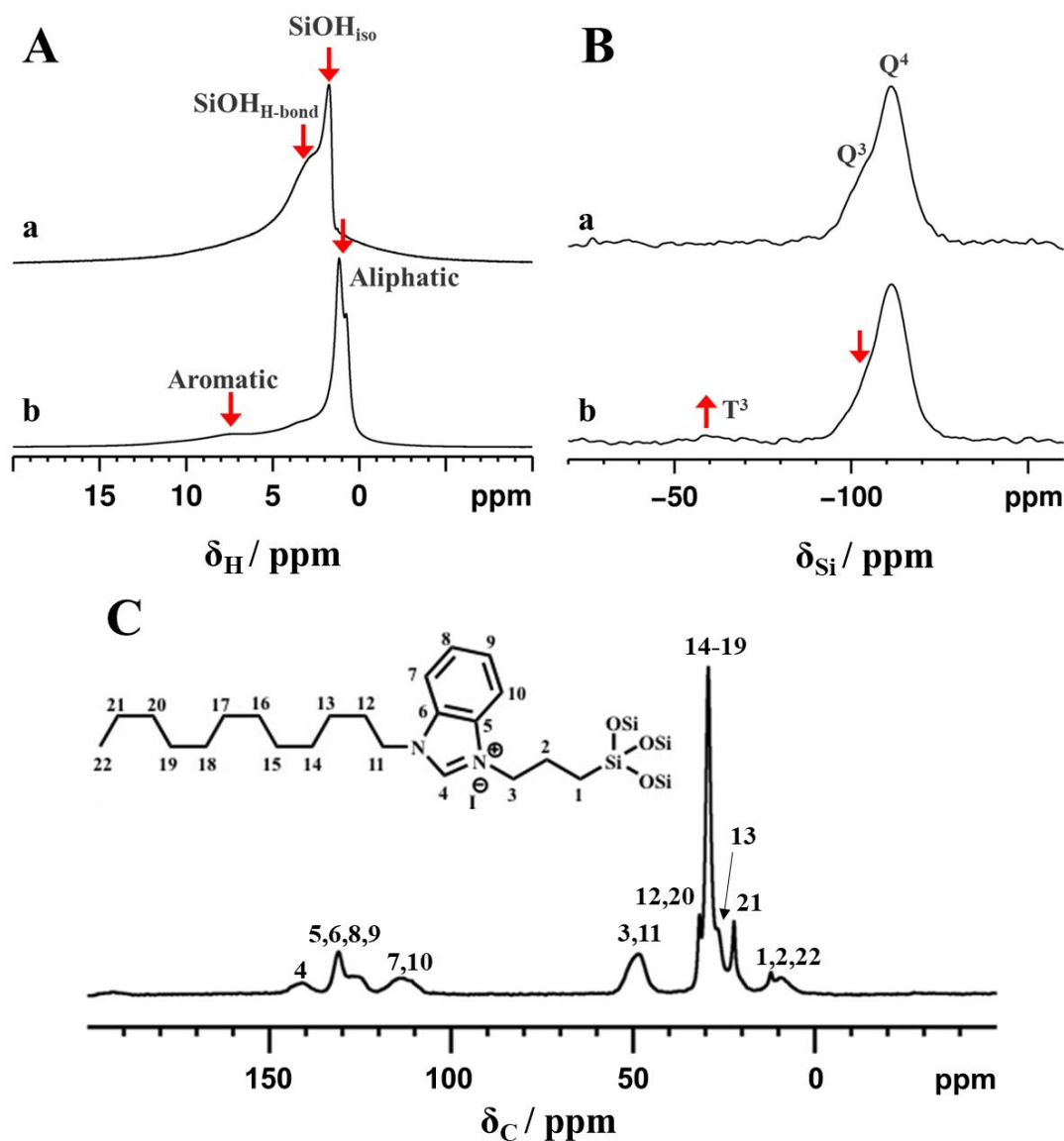


Figure 6.4. A) ¹H, B) ²⁹Si and C) ¹³C CPMAS NMR spectra of plain Davisil silica (a) and NHC-Dav150 (b).

The ^1H NMR spectrum of plain Davisil silica (curve a) exhibited a sharp signal at *ca.* 1.8 ppm, ascribable to isolated Si–OH groups and a broad resonance in the 1.8–3 ppm range due to silanol groups interacting *via* hydrogen bond. Upon NHC grafting (curve b), the resonance peak at 1.8 ppm disappeared, together with the broad resonance due to H-bonded species, indicating that all available Si–OH groups had condensed with alkoxy groups of NHC moieties, as already highlighted by variable temperature FT-IR spectroscopy. Moreover, signal in the 0–3 ppm range, assigned to the aliphatic chain of the N-pyrrolic ring and a broad resonance from 6.5 to 11 ppm, were also detected for NHC-Dav150 catalyst. The successful grafting of NHC precursor was also confirmed by means of ^{29}Si and ^{13}C CPMAS NMR spectroscopy (Figure 6.4 B and C). The ^{29}Si NMR spectrum of plain Davisil silica revealed signals due to Q^4 ($\text{Si}(\text{OSi})_4$) silicon sites at -110 ppm and Q^3 ($\text{Si}(\text{OSi})_3\text{OH}$) sites at -101 ppm (isolated silanols).^[30,31] Upon anchoring of NHC precursor, the resonance peaks due to Q^3 sites disappeared, whilst a signal due to T^3 ($\text{RSi}(\text{OSi})_3$) sites was detected at -65 ppm. In addition, ^{13}C NMR spectrum of NHC-Dav150 exhibited signals due to the terminal CH_3 and CH_2 carbons in the 5–15 ppm range, resonances related to the carbons in aliphatic chains of the NHC moieties in the 20–35 ppm range, signals ascribable to aromatic carbons between 110 and 140 ppm and signal attributed to N– CH_2 groups at around 50 ppm, thus further proving that NHC moieties were covalently bonded to the silica surface.

6.2.3 Characterization of NHC-MCM-41 and NHC-MCM-41-NPs

X-Ray powder diffraction (XRDP) was performed to gain insight into the structural features of nanoparticles and commercial MCM-41 samples, before and after the grafting procedure (Figure 6.5 A and B). The small-angle XRD pattern of both plain nanoparticles and commercial MCM-41 inorganic supports exhibited three well-resolved signals, indexable as (100), (110), and (200) reflections associated with $p6mm$ hexagonal symmetry. In addition, MCM-41-NPs sample revealed additional (210) reflection, indicating a higher degree of crystallinity with

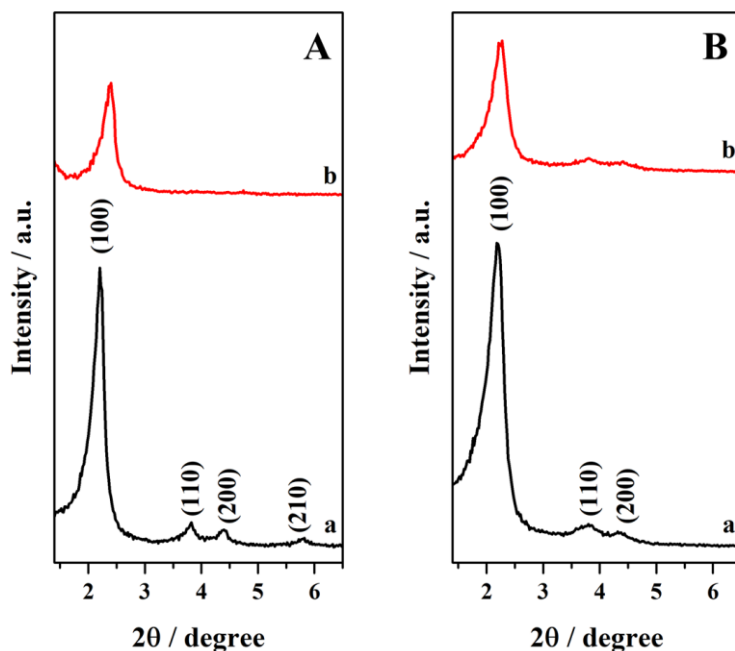


Figure 6.5. The small-angle powder XRD pattern of A) MCM-41-NPs and B) commercial MCM-41 before (a, black curve) and after the NHC precursor grafting (b, red curve).

respect to commercial MCM-41. Upon grafting NHC precursor, a decrease in the intensity of all the characteristic reflections was detected for both NHC-MCM-41-NPs and NHC-MCM-41 hybrid catalysts, corresponding to a lower degree of crystallinity due to the anchoring procedure. Moreover, the small shift towards higher 2θ values detected for (100) reflection, reflecting a lower d spacing, suggested that NHC precursor had been successfully anchored inside the mesopores of MCM-41 in addition to the external surface.

The thermal stability of NHC precursor grafted onto MCM-41-NPs and commercial MCM-41 supports was investigated by means of variable temperature FT-IR spectroscopy (Figure 6.6 A-D). The assignment of the detected bands has already been provided in subsection 6.2.2. In addition, upon outgassing the samples at room temperature, signal related to the $\nu_{\text{O-H}}$ of isolated silanol was detected at 3745 cm^{-1} , at higher intensity for commercial NHC-MCM-41, indicating that a higher fraction of silanol groups had been consumed upon NHC grafting on MCM-41-NPs inorganic support. Nevertheless, a fraction of Si-OH groups was found to be

still available to graft organic moieties for both the catalysts. By increasing the outgassing temperature, $\nu_{C=N}$ vibration of benzimidazole ring started decomposing at around 290 °C for both the catalysts, and was almost totally vanished at *ca.* 350 °C. Noteworthy, NHC precursor was found to be more thermally-stable in NHC-MCM-41-NPs and NHC-MCM-41 catalysts with respect to NHC-Dav150 sample, probably as a result of the confinement effect of NHC moieties grafted inside the mesopores. Furthermore, with respect to Davisil silica (subsection 6.2.1), signal at 3745 cm^{-1} was

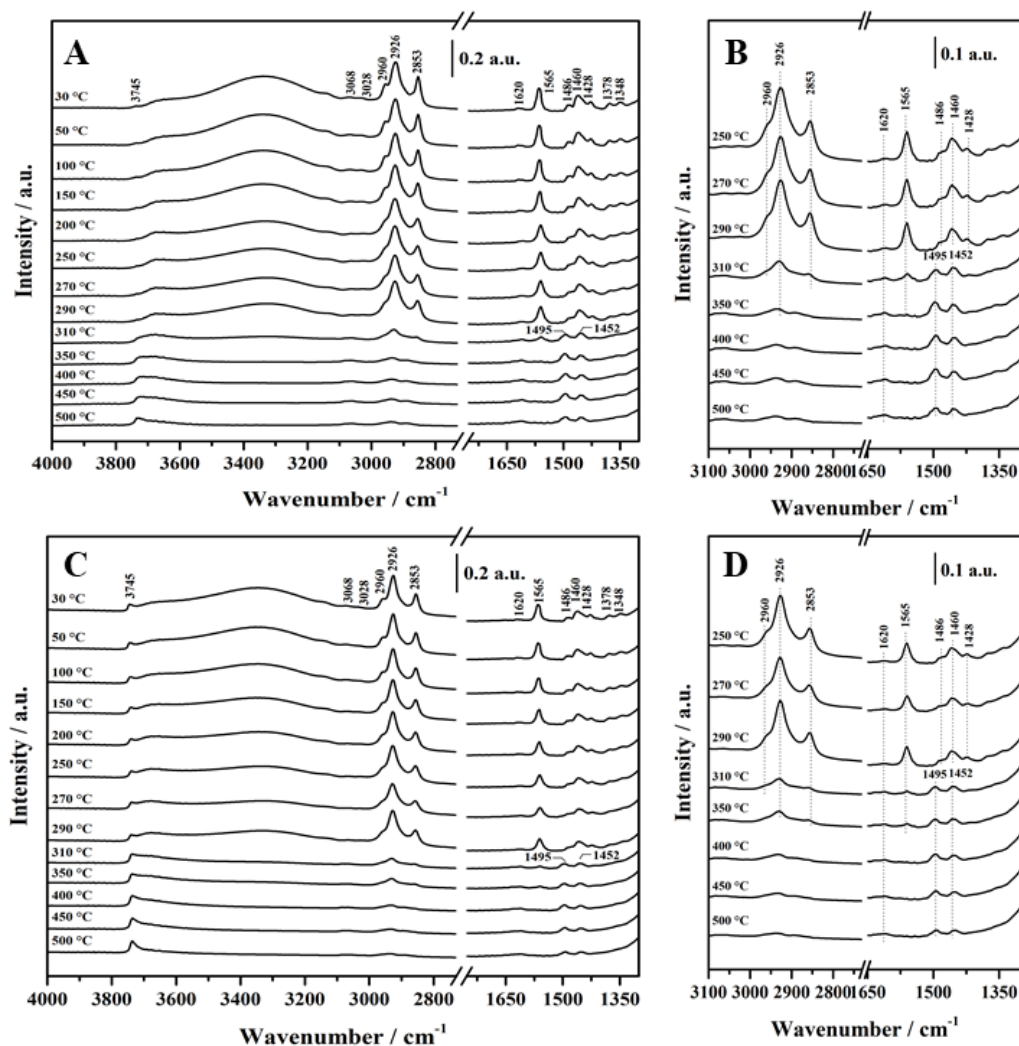


Figure 6.6. Variable temperature FT-IR spectra of A) NHC-MCM-41-NPs and C) commercial NHC-MCM-41 catalysts, with B), D) their respective magnifications in the temperature range 200-500 °C.

detected in the spectra of both MCM-41 samples upon outgassing the sample at 500 °C. In this respect, it is possible that ordered mesoporosity can promote the diffusion of decomposition products within the framework, thus preventing their depositing on the silica surface.

^1H , ^{29}Si and ^{13}C MAS NMR spectroscopy was carried out to confirm the successful grafting of NHC precursor on the different MCM-41 inorganic supports (Figure 6.7 A-C). Upon NHC anchoring, ^1H SS NMR spectra of both NHC-MCM-41-NPs and NHC-MCM-41 catalysts (Figure 6.7 A) exhibited signals between 0 and 3 ppm, ascribable to the aliphatic chain on the N-pyrrolic ring and a broad resonance in the range 6.5-11 ppm, due to aromatic protons. In addition, signal at 1.8 ppm, associated to isolated silanols, was also detected in the NMR spectrum of NHC-MCM-41, thus confirming FT-IR findings. Additionally, ^{29}Si CPMAS NMR spectra of both the sample (Figure 6.7 B) revealed resonance peaks due to Q^4 ($\text{Si}(\text{OSi})_4$) and Q^3 ($\text{Si}(\text{OSi})_3\text{OH}$) silicon sites at -110 and -101 ppm,^[30,31] with the latter more intense than the former. Apart from the characteristic signals of MCM-41 support, resonances arising from T^3 ($\text{RSi}(\text{OSi})_3$) and T^2 ($\text{RSi}(\text{OSi})_2\text{OH}$) sites at -65 and -57 ppm were detected, proving the covalent linkage between NHC precursor and the

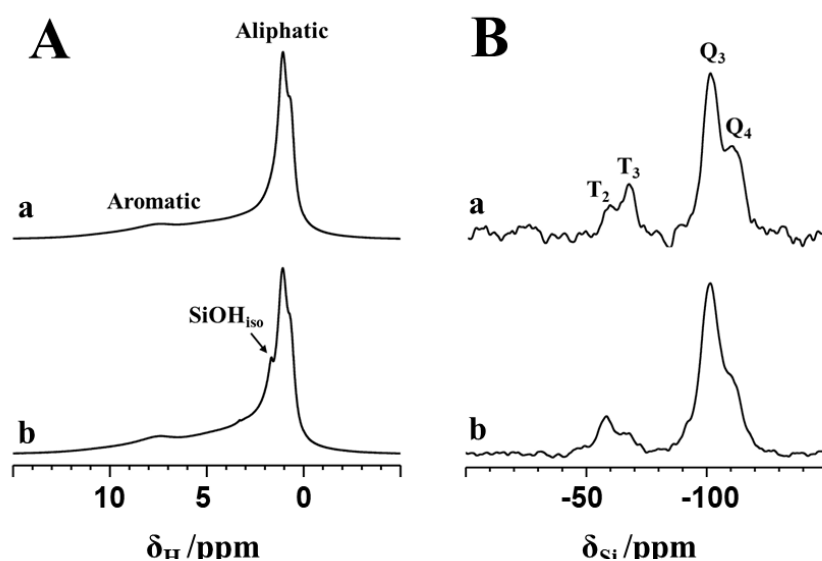


Figure 6.7. Cont.

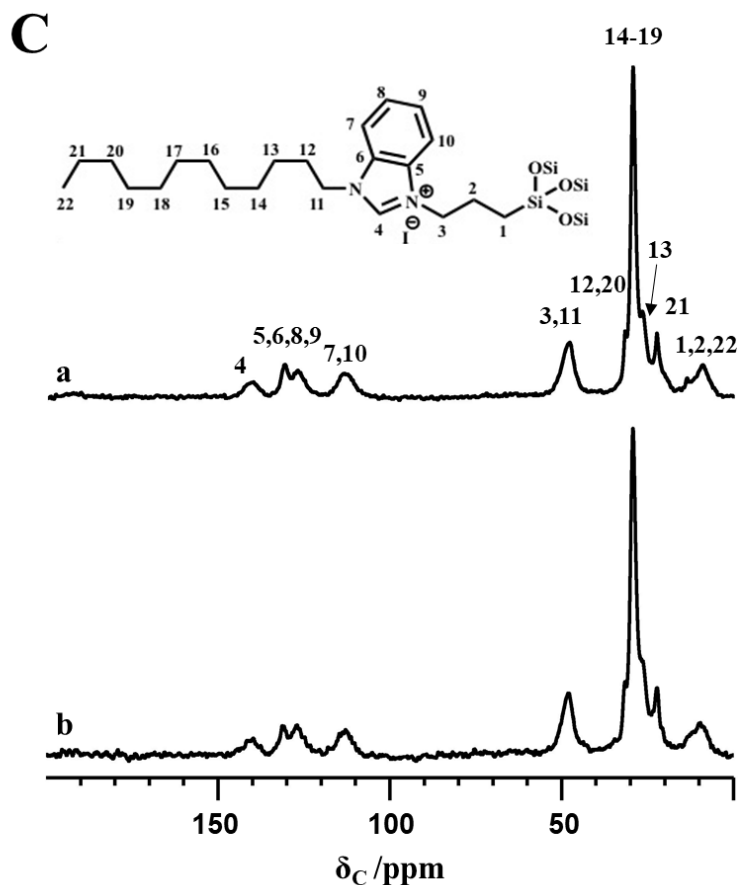


Figure 6.7. A) ^1H SS NMR, B) ^{29}Si and C) ^{13}C CPMAS NMR spectra of NHC-MCM-41-NPs (a) and NHC-MCM-41 (b).

silica surface. Lastly, ^{13}C CPMAS NMR analysis on both the samples (Figure 6.7 C) evidenced the typical signals due to the aliphatic C₁₂ substituent (20-35 ppm), to propyl linker (5-15 ppm), to N-CH₂ groups (50 ppm) and to aromatic carbons of benzimidazole (110-140 ppm).

6.2.4 Characterization of NHC-HP-ZSM-5 and NHC-HP-SAPO-5

X-Ray powder diffraction was performed to assess that the structural properties of hierarchical inorganic supports had not been altered upon the anchoring of NHC moieties (Figure 6.8 A and B). Both NHC-HP-ZSM-5 and NHC-HP-SAPO-5 catalysts exhibited the characteristic reflections of MFI and AFI frameworks with respect to either hierarchical inorganic supports and microporous analogues, thus

confirming phase purity and crystallinity of the hybrids, together with retention of the parent structural features.^[16]

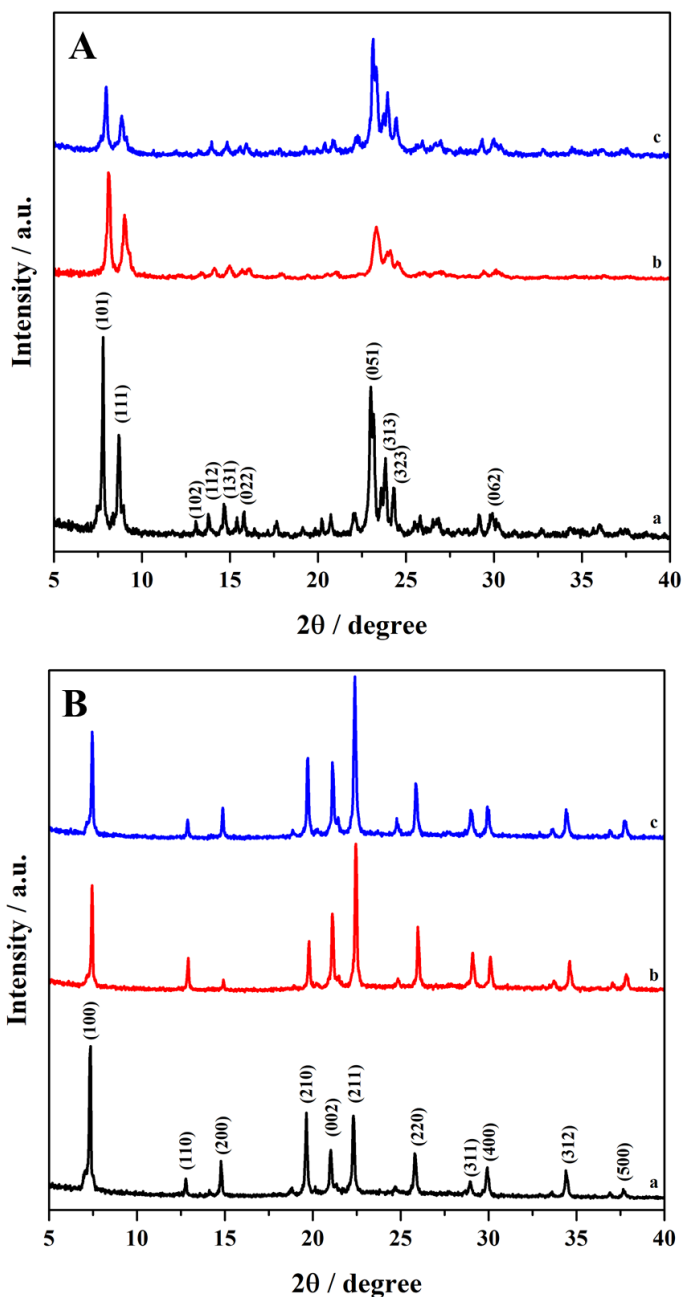


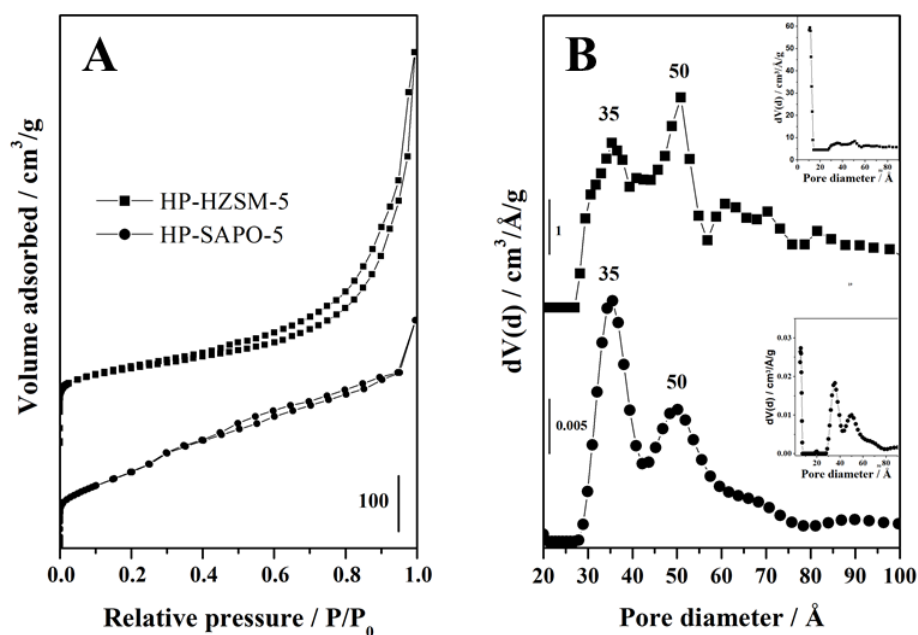
Figure 6.8. XRD patterns of A) microporous ZSM-5 (a, black curve), HP-ZSM-5 (b, red curve) and NHC-HP-ZSM-5 (c, blue curve) and B) microporous SAPO-5 (a, black curve), HP-SAPO-5 (b, red curve) and NHC-HP-SAPO-5 (c, blue curve).

Table 6.3. Textural properties of HP-ZSM-5 and HP-SAPO-5 catalysts.

Sample	S_{BET} [$\text{m}^2 \text{g}^{-1}$]	S_{DFT} [$\text{m}^2 \text{g}^{-1}$]	S_{micro} [$\text{m}^2 \text{g}^{-1}$]	$S_{\text{meso}}^{[a]}$ [$\text{m}^2 \text{g}^{-1}$]	V_{DFT} [$\text{cm}^3 \text{g}^{-1}$]	V_{micro} [$\text{cm}^3 \text{g}^{-1}$]	$V_{\text{meso}}^{[b]}$ [$\text{cm}^3 \text{g}^{-1}$]
HPZSM-5	500	731	516	215	0.82	0.10	0.70
HPSAPO-5	573	508	215	293	0.49	0.05	0.44

^[a] $S_{\text{meso}} = S_{\text{DFT}} - S_{\text{micro}}$; ^[b] $V_{\text{meso}} = V_{\text{DFT}} - V_{\text{micro}}$.

The textural properties of plain and NHC-grafted HP-ZSM-5 and HP-SAPO-5 hybrid catalysts were investigated by means of N_2 adsorption/desorption at 77 K.^[21] Both the hierarchical inorganic supports exhibited Type IV isotherms, with hysteresis loop in the the P/P_0 range 0.5-1.0 (Figure 6.9 A), characteristic of mesoporous materials, whereas microporous analogues revealed type I isotherms (volumetric analysis on microporous SAPO-5 has been shown in Chapter 5, subsection 5.3.1).^[22,23] Pore size distribution, obtained by applying NLDFT method to the adsorption branch of the isotherms,^[24,25] revealed, apart from the micropores typical of MFI and AFI frameworks, additional mesoporosity at 35 and 50 Å (Figure

**Figure 6.9.** *Cont.*

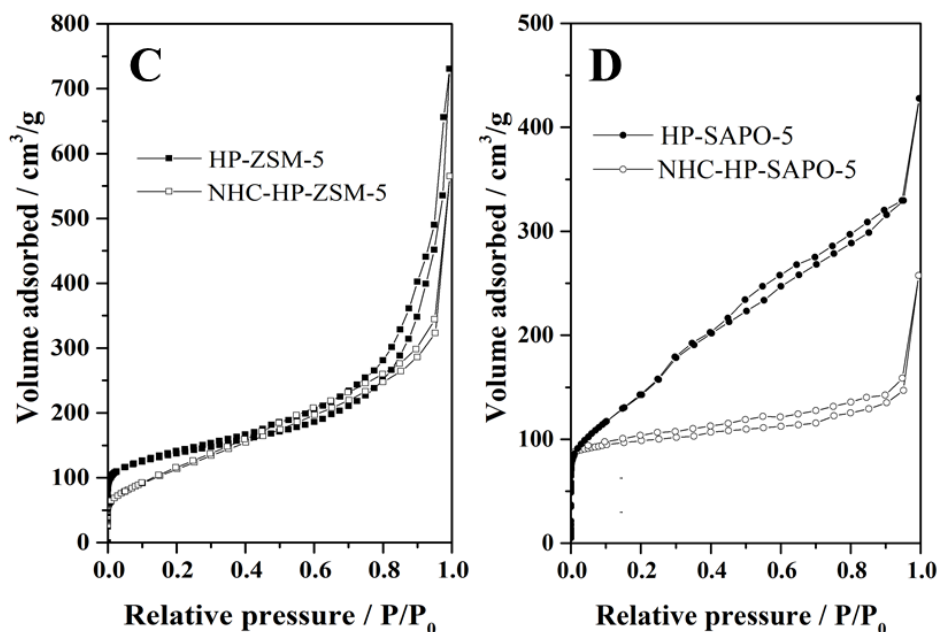


Figure 6.9. A) N_2 adsorption/desorption isotherms of HP-ZSM-5 and HP-SAPO-5 and B) their pore size distributions in the mesopore range with pore size distributions in the micropore range (inset). Comparison between N_2 adsorption/desorption isotherms of C) NHC-HP-ZSM-5 and HP-ZSM-5 and B) NHC-HP-SAPO-5 and HP-SAPO-5.

6.9 B). Details of the specific surface area and pores volume are listed in Table 6.3. Compared to HP-SAPO-5, HP-ZSM-5 exhibited a higher mesopore volume (V_{meso}) and total pore volume (V_{tot}). Upon NHC grafting, for both hierarchical hybrids catalysts a decrease of the N_2 adsorption capacity, specific surface area and pore volume was recorded (Figure 6.9 C and D). Nevertheless, the textural properties of NHC-HP-ZSM-5 were less affected by the NCH presence with respect to NHC-HP-SAPO-5, as a result of the different framework topologies and synthetic methodologies performed to obtain the hierarchical supports.

Thermogravimetric analysis was performed in order to evaluate the thermal stability and organic content of NHC precursor grafted on HP-ZSM-5 and HP-SAPO-5 hybrid catalysts (Figure 6.10 A and B). The thermograms and derivatives of the two hybrid catalysts and parent hierarchical supports exhibited a first weight loss in the 30-180 °C range, due to the removal of physisorbed water. Notably, HP-SAPO-5 revealed a more hydrophilic character with respect to HP-ZSM-5.

However, upon NHC grafting, both hybrid catalysts lost a comparable amount of water. At higher temperatures, the flat weight loss of the hybrid catalysts changed into rapidly declining profiles, corresponding to the decomposition of the organic NHC precursor. In addition, DTG curve revealed that decomposition of NHC precursor started at higher temperature (above 250 °C) with respect to NHC-Dav150. The organic content, estimated from the weight loss in the 180-1000 °C range, is reported in Table 6.4. Notably, TGA results were found to be consistent with data from elemental analysis.

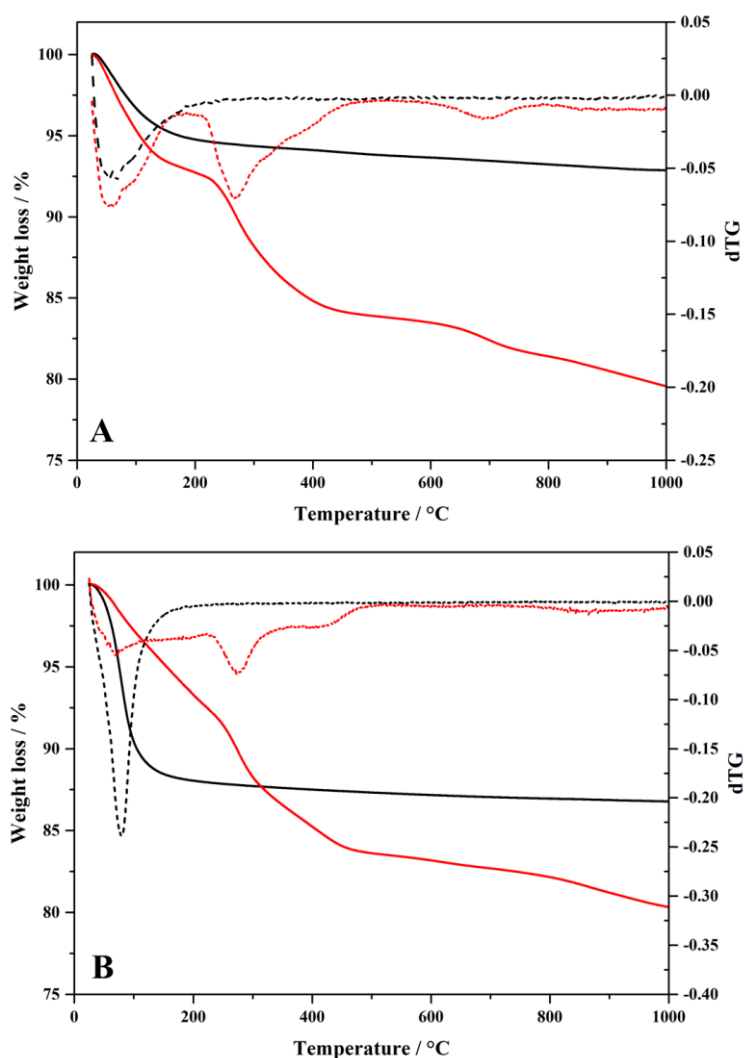


Figure 6.10. TGA/DTG curves of A) HP-ZSM-5 (black curve) and NHC-HP-ZSM-5 (red curve) and B) HP-SAPO-5 (black curve) and NHC-HP-SAPO-5 (red curve)

Table 6.4. Weight loss (%) due to physisorbed water and organic content calculated from TGA analysis.

Catalyst	Δw % due to H ₂ O ^a	Δw % due to NHC ^b
HP-ZSM-5	5	-
NHC-HP-ZSM-5	7	13.5
HP-SAPO-5	12	-
NHC-HP-SAPO-5	6	14

^aCalculated in the range 30-180 °C. ^bCalculated in the range 180-1000 °C

To further investigate the thermal stability of N-heterocyclic carbene precursor anchored on hierarchical inorganic supports, FT-IR spectroscopy at variable outgassing temperature was performed (Figure 6.11 A-D). For further details on the assignment of the detected bands, refer to subsection 6.2.2. The decomposition of NHC precursor was evaluated by monitoring the band at 1565 cm⁻¹, due to the C=N stretching mode of the imidazole ring, during the thermal treatment.^[16,27] For both the hybrids, the signal started decreasing in intensity upon outgassing the samples at 270 °C and totally disappeared at around 400 °C for NHC-HP-SAPO-5 and at *ca.* 450 for NHC-HP-ZSM-5.

With the aim of establishing whether or not the Si–OH groups had been totally consumed upon the NHC anchoring, and if the bridging Si–OH–Al groups (Brønsted acid sites) of the MFI and AFI frameworks had been retained after the grafting procedure, FT-IR spectra in the O–H stretching region of NHC-HP-ZSM-5 and NHC-HP-SAPO-5 were recorded and compared to their respective hierarchical inorganic support (Figure 6.12 A and B). In the FT-IR spectra of both plain inorganic supports (black curves), a band at 3745 cm⁻¹, assigned to the O–H stretching mode of isolated silanol groups, was detected. Upon NHC grafting (red curves), this signal disappeared, indicating that all Si–OH anchoring sites had been consumed. Moreover, both HP-ZSM-5 and HP-SAPO-5 supports displayed bands related to the O–H stretching mode of Brønsted acid sites. The former exhibited a broad band

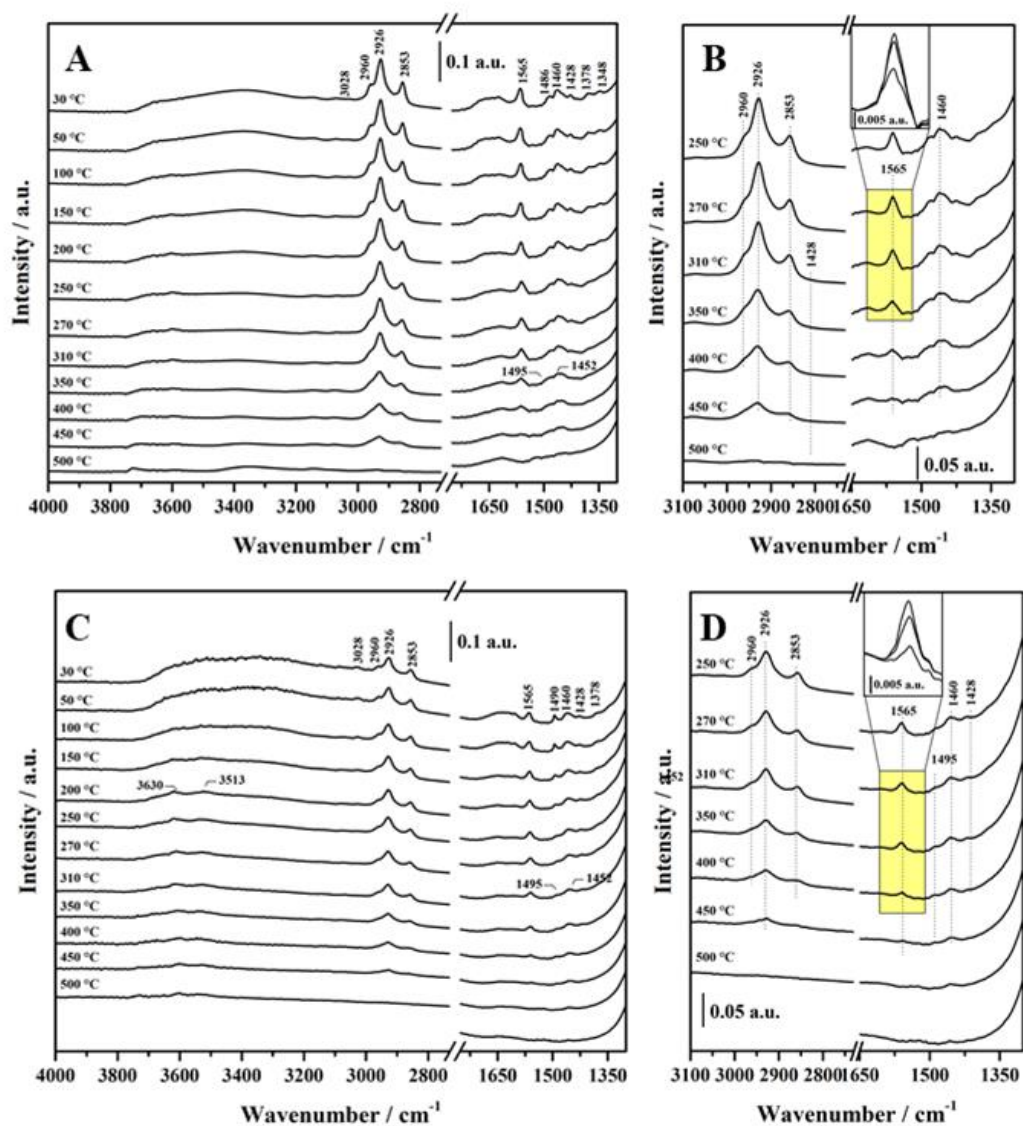


Figure 6.11. Variable temperature FT-IR spectra of A) NHC-HP-ZSM-5 and C) NHC-HP-SAPO-5 catalysts with B), D) their respective magnifications in the temperature range 200–500 °C.

centred 3611 cm^{-1} ,^[20] the latter two distinct signals at 3630 and 3513 cm^{-1} , associated to BAS located at different position within the AFI framework.^[32–34] Characteristic bands of BAS were still detected in the spectra of NHC-HP-ZSM-5 and NHC-HP-SAPO-5, thus confirming the retention of the potential catalytic acid sites upon the anchoring procedure.

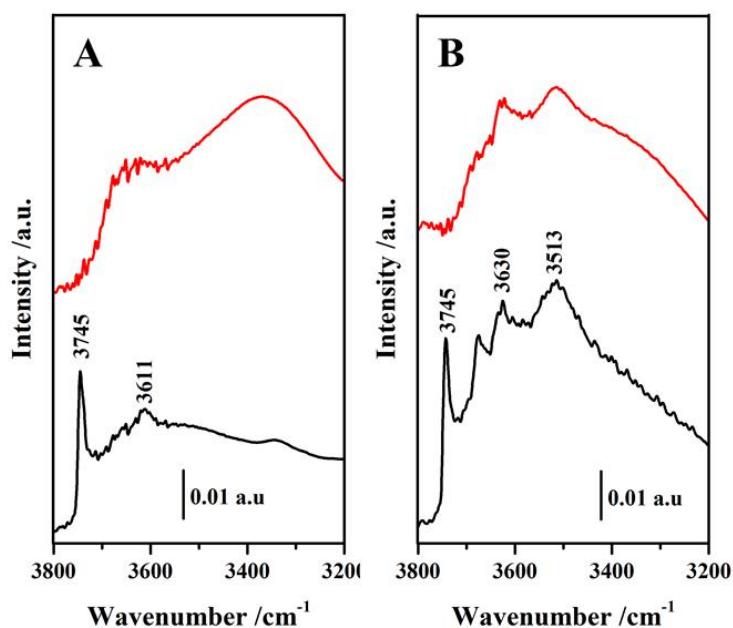


Figure 6.12. FT-IR spectra in the O–H stretching region of A) HP-ZSM-5 (black curve) and NHC-HP-ZSM-5 (red curve) and B) HP-SAPO-5 (black curve) and NHC-HP-SAPO-5 (red curve).

Together with FT-IR spectroscopy, ^1H SS NMR provided direct information about the different proton sites present in the hierarchical supports (Figure 6.13 A). The ^1H NMR spectra of hierarchical supports revealed contributions from isolated Si–OH groups (1.8–2 ppm), hydroxyl units bound to Lewis acid sites (LAS) and extra framework aluminium species (EFAI) through hydrogen bonding (2.4–2.8 ppm), BAS (3.8–5.0 ppm) and H-bonded hydroxyls (5.8 ppm).^[35–37] In accordance with FT-IR measurements, HP-SAPO-5 exhibited two different resonance peaks due to Brønsted acid sites. Quantitative representations of various protonic species are reported in Table 6.5. In order to separate contributions from silanols and BAS, ^{27}Al TRAPDOR NMR spectra were collected (Figure 6.13 B and C). The $^1\text{H}/^{27}\text{Al}$ TRAPDOR NMR method allows to differentiate protons that are dipolar coupled to nearby Al atoms, such as Brønsted and Lewis acid sites as well as Al–OH, from all other protons.^[38] In this perspective, two ^1H spin-echo NMR spectra were recorded, without and with ^{27}Al irradiation. While the former reveals all the protons in the

sample, a difference spectrum will show only protons in close vicinity to ^{27}Al . This experiment allowed to demonstrate that HP-ZSM-5 was characterized by a higher amount of available silanols groups and lower amount of BAS with respect to HP-SAPO-5.

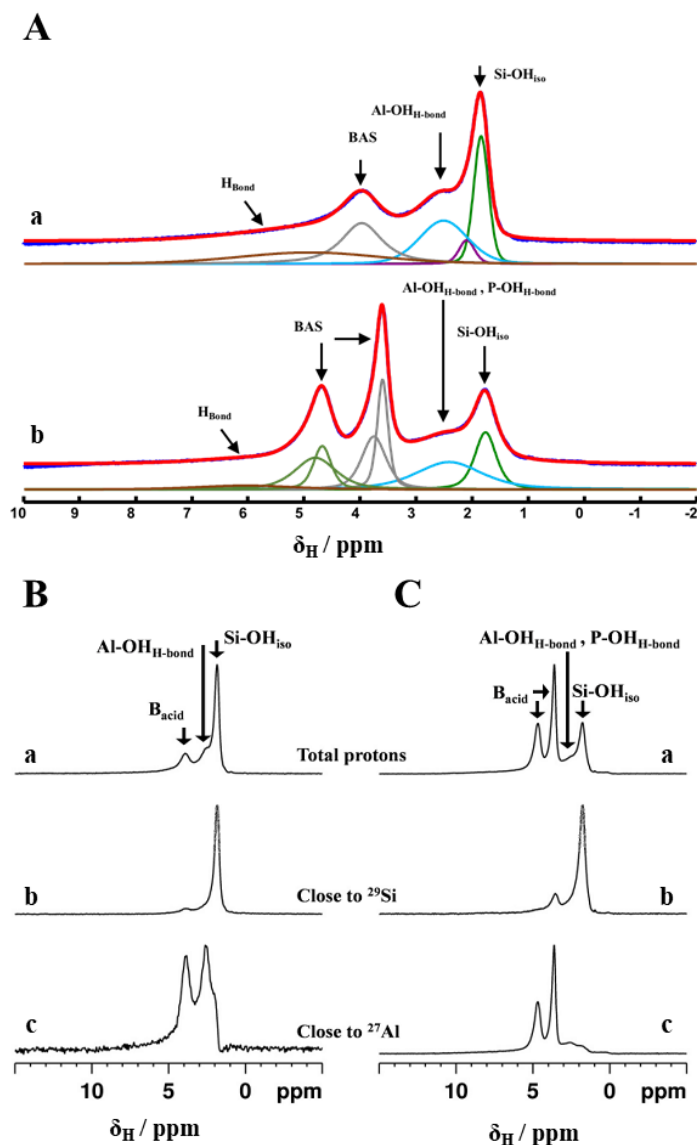


Figure 6.13. A) ^1H MAS NMR spectra of calcined and dehydrated HP-ZSM-5 (a, top) and HP-SAPO-5 (b, bottom). Both experimental and its fitted spectrum with individual contribution from each ^1H sites are shown. ^1H rotor synchronized spin-echo NMR spectra of calcined A) HP-ZSM-5 and C) HP-SAPO-5 recorded without (a, top) and with (b, middle) ^{27}Al irradiation. The difference spectra are shown at the bottom (c).

Table 6.5. Proton population distribution obtained from ^1H SS NMR spectra of calcined HP-ZSM-5 and HP-SAPO-5 supports. FT-IR frequencies of the corresponding OH groups are also reported.

ν_{OH} [cm^{-1}]	^1H Chemical shift [ppm]	Assignment	HP-ZSM-5	HP-SAPO-5
3745	1.7-2.1	Isolated SiOH_{iso}	29	15
	2.4-2.4	OH bound to LAS and EFAI species	26	22
3618-3615	3.8	BAS	26	32
3630	4.8	BAS in small cages	-	26
3513	5.8	H-bonded species	19	5

According to FT-IR evidence, upon N-heterocyclic carbene precursor grafting, resonance peaks at 1.8 ppm due to isolated silanols groups disappeared from the ^1H NMR spectra of NHC-hybrid catalysts, whilst signals related to BAS were retained (Figure 6.14 A), thus providing further confirmation that Si–OH groups had been

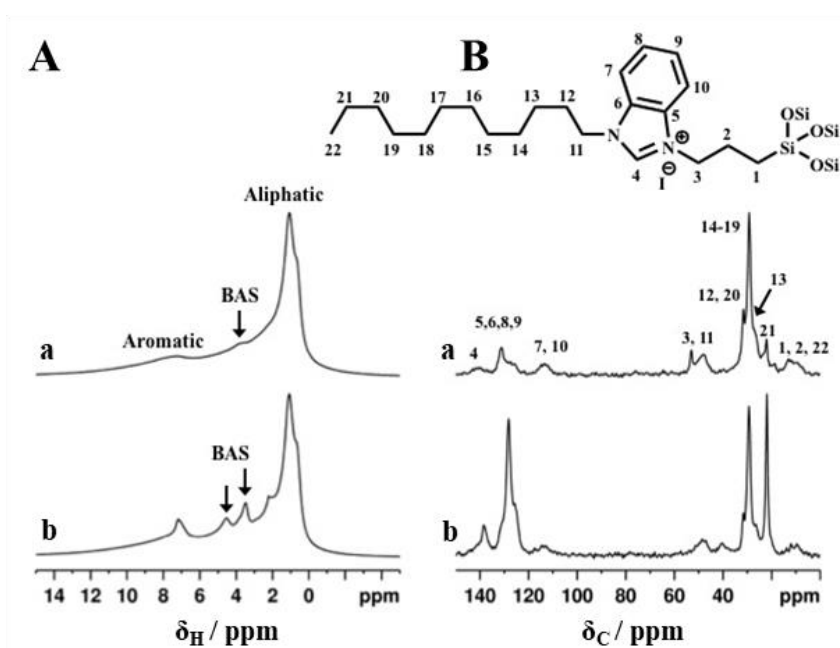


Figure 6.14. A) ^1H MAS NMR and B) ^{13}C CPMAS NMR spectra of calcined and dehydrated HP-ZSM-5 (a, top) and HP-SAPO-5 (b, bottom).

consumed to anchor NHC precursor and BAS had not been affected by its presence. Moreover, signals in the 0-3 ppm range, arising from the aliphatic chain on the N-pyrrolic ring, and a broad resonance from 6.5 to 11 ppm due to aromatic protons were also detected. The successful grafting of NHC organic moieties onto hierarchical supports was further assessed by means of ^{13}C CPMAS NMR spectroscopy (Figure 6.14 B). Indeed, ^{13}C NMR spectra of NHC-HP-ZSM-5 and NHC-HP-SAPO-5 exhibited resonance peaks due to the aliphatic C_{12} substituent (20-35 ppm), to propylic linker (5-15 ppm), to N-CH_2 groups (50 ppm) and to aromatic carbons of benzimidazole (110-140 ppm).

With the aim of probing the chemical environment of the framework atoms in NHC-containing hybrids, ^{27}Al , ^{31}P and ^{29}Si MAS NMR spectroscopy was carried out (Figure 6.15 and Figure 6.16). The ^{29}Si CPMAS NMR spectrum of NHC-HP-ZSM-5 (Figure 6.15 A) revealed resonance peaks related to Q sites at -112 (Q^4 (0Al)), -105 (Q^4 (1Al)), -101 (Q^3 (0Al)) and -90 (Q^2 (0Al)) ppm, owing to tetrahedral Si bound to four, three and two Si atoms and signals due to T sites at -65 (T^3 , $\text{RSi}(\text{OSi})_3$) and -57 (T^2 , $\text{RSi}(\text{OSi})_2\text{OH}$) ppm, confirming the success of the anchoring procedure.^[31] The ^{27}Al MAS NMR spectrum of NHC-HP-ZSM-5 (Figure 6.15 B) exhibited a broad resonance between 1 and 9 ppm, related to six-coordinated Al sites

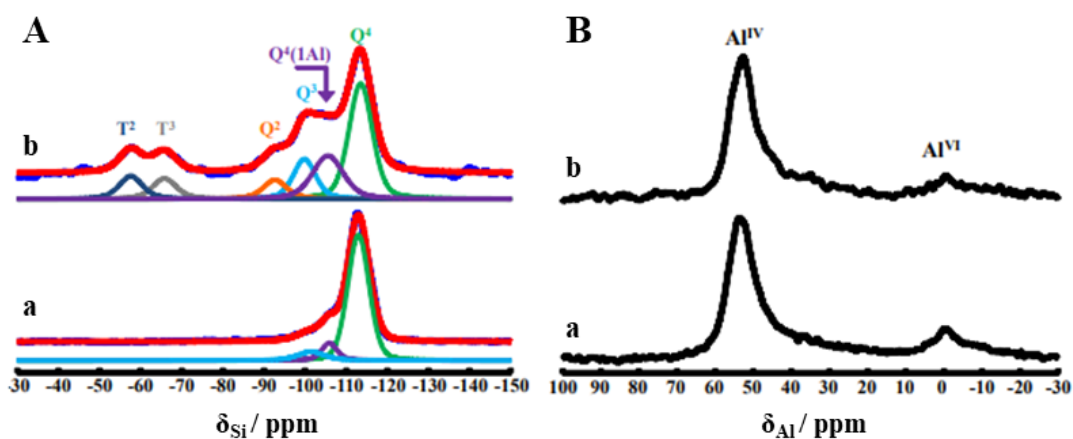


Figure 6.15. A) ^{29}Si and B) ^{27}Al NMR spectra of HP-ZSM-5 (a, bottom curve) and NHC-HP-ZSM-5 (b, top curve).

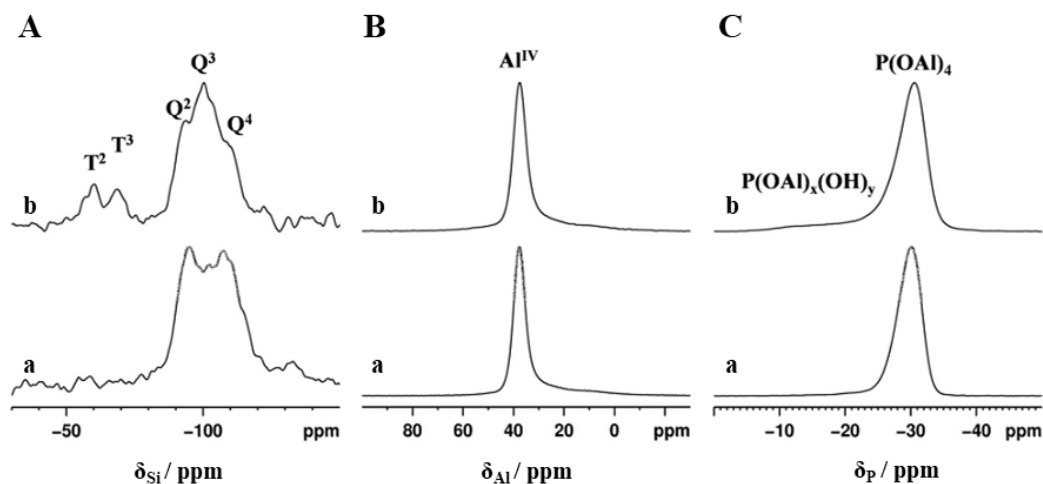


Figure 6.16. A) ^{29}Si , B) ^{27}Al and C) ^{31}P NMR spectra of HP-SAPO-5 (a, bottom curve) and NHC-HP-SAPO-5 (b, top curve).

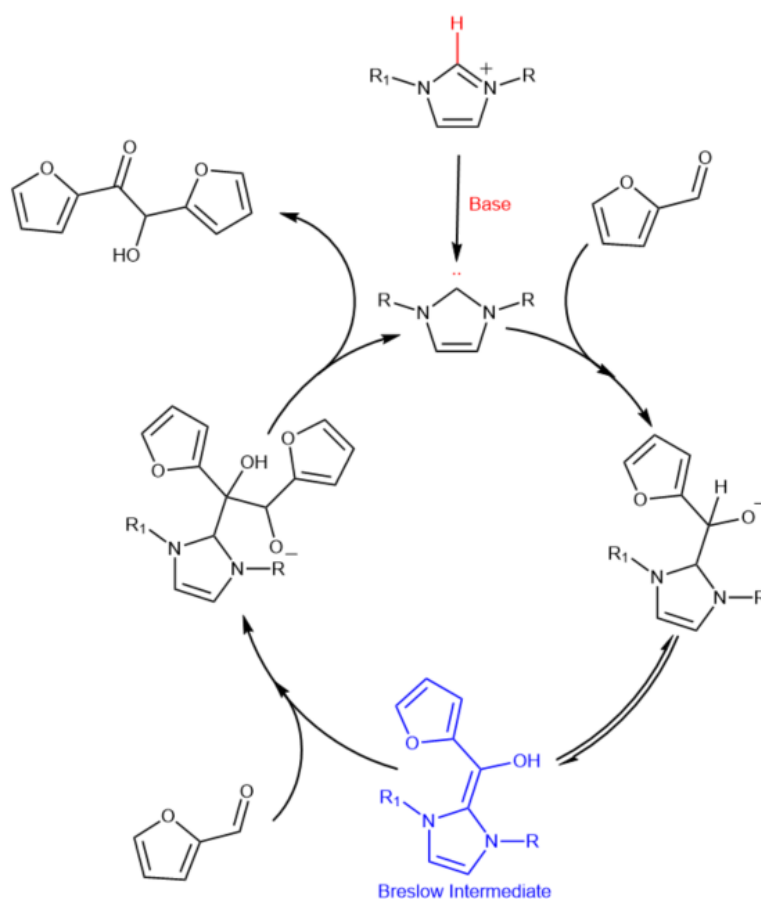
(Al^{IV}) created by the desilication process to obtain a hierarchical framework. Signals related to Q and T sites were detected in the ^{29}Si CPMAS NMR spectrum of NHC-HP-SAPO-5 (Figure 6.16 A), with Q sites characterized by different relative intensities with respect to NHC-HP-ZSM-5, suggesting a different degree of defectivity of the two hybrid catalysts. The ^{27}Al NMR spectrum of NHC-HP-SAPO-5 (Figure 6.16 B) exhibited a resonance peak at ca. 37 ppm, attributed to tetrahedrally-coordinate Al atoms, whilst no signal due to six-coordinated Al was detected. Finally, a single resonance peak at -130.5 ppm, assigned to tetrahedrally-coordinated P atoms, was recorded in ^{31}P MAS NMR spectrum of NHC-HO-SAPO-5 (Figure 6.16 C). Since both ^{27}Al and ^{31}P MAS NMR spectra displayed only a single resonance, it was possible to confirm strictly alternation of Al and P atoms at the T-positions of the AFI framework.^[39]

6.2.5 Catalysis

The catalytic activity of NHC-based hybrids was evaluated in the NHC-catalysed omo-coupling of furfural into furoin.^[9,40] The proposed mechanism for the benzoin condensation reaction is reported in Scheme 6.6. Firstly, the carbene catalyst is activated through in situ deprotonation of the corresponding azolium salt with a base

(1,8-diazabicyclo[5.4.0]undec-7-ene, DBU).^[41-43] Then, nucleophilic attack of one molecule of the furfural by the carbene catalyst generates the carbene-aldehyde zwitterionic adduct. Next, a proton transfer occurs, leading to the formation of the Breslow/Enders intermediate that attacks a second molecule of furfural.^[44-45] After a proton transfer and the release of the carbene catalyst, the furoin product is obtained.

Preliminary results (Figure 6.17) evidenced that NHC-Dav150 gave quantitative conversion in the first reaction, as well as in the first and second recycle, and the third recycle maintained high conversion (85%). When MCM-41-NPs was used as inorganic support, full conversion was achieved in the first reaction and first recycle, then the catalytic activity was found to decrease in the second and third recycle (83% and 73%, respectively). Notably, almost 98% conversion was reached in the first



Scheme 6.6. Catalytic cycle of benzoin condensation reaction.

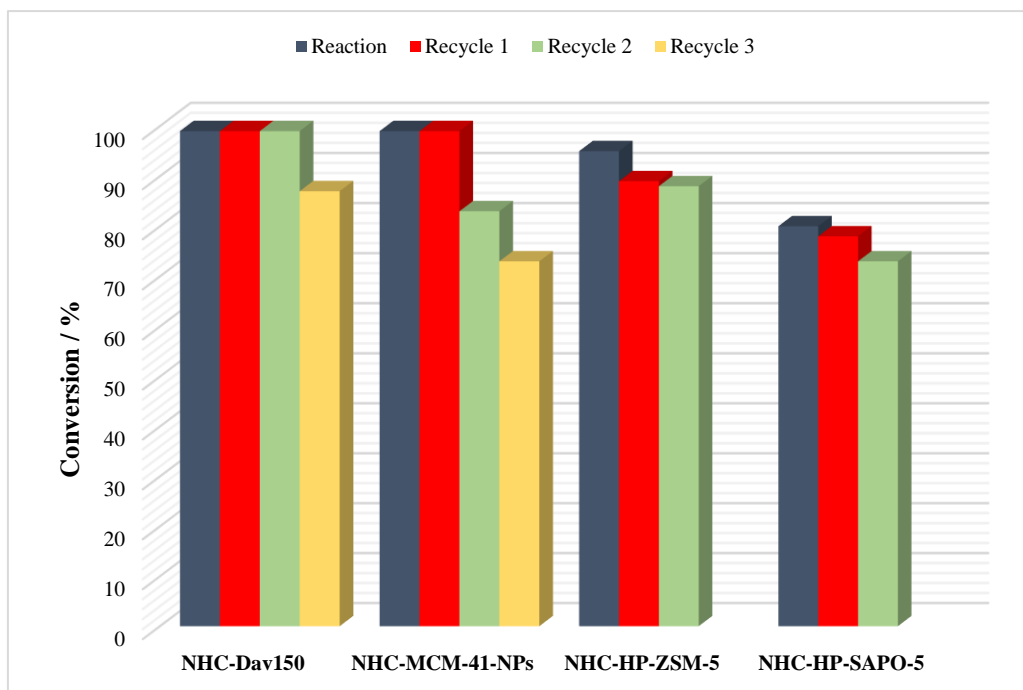


Figure 6.17. Catalytic activity and recycling test of NHC hybrid catalysts in the benzoin condensation reaction. The conversion (%) was estimated after 20 h of reaction.

reaction when NHC-HP-ZSM-5 was used as heterogeneous catalyst, then its catalytic activity slight decreased in the first and second recycle and was completely lost in the third recycle. Conversely, fresh NHC-HP-SAPO-5 revealed a lower 80 % conversion after 20 h of reaction. Similarly to NHC-HP-ZSM-5, the conversion dropped in the first and second recycle (78% and 73%, respectively), losing completely the activity in the third recycle. Control experiments with plain inorganic supports were performed and no reactivity in the benzoin condensation reaction was observed, stressing the role of the anchored N-heterocyclic carbene in the catalytic process.

6.2.6 Unravelling the inferior catalytic performance of NHC-HP-SAPO-5 catalyst

With the aim of clarify the reason of the inferior catalytic activity displayed by NHC-SAPO-5 with respect to the other NHC-based catalysts and in order to explain

the deactivation NHC-based hierarchical supports after the second recycle, a physico-chemical characterization using a multi-technique approach (XRDP, SS NMR and FT-IR spectroscopies) was carried out on the recycled catalyst.

XRDP and ^{27}Al and ^{31}P MAS NMR spectroscopies were performed to confirm that hierarchical AFI framework had not collapsed after the recycling of NHC-HP-SAPO-5 (Figure 6.18 A-C). The XRD pattern of recycled NHC-HP-SAPO-5 showed the characteristic reflections of AFI, also detected with comparable intensities in fresh NHC-HP-SAPO-5 and HP-SAPO-5 samples (Figure 6.18 A). Furthermore, the presence of a single resonance peak in both ^{27}Al and ^{31}P NMR spectra (Figure 6.18 B and C), due to tetrahedrally-coordinated Al and P atoms, at *ca.* 36 and -30 ppm respectively, confirmed the strict alternation of Al and P atoms at the T-positions of the aluminophosphates framework.^[39] Thus, both XRDP and NMR characterization indicated a retention of the structural properties of plain inorganic support in the recycle catalyst.

^1H MAS NMR spectroscopy was used to assess whether or not the acid properties of parent HP-SAPO-5 framework had been retained even after the recycling of the catalyst (Figure 6.19 A). The ^1H NMR spectrum of HP-SAPO-5 (curve a) revealed resonance signals related to isolated silanols (1.8 ppm), Al–OH and P–OH H-bonded (2.4–2.8 ppm) and BAS located at different position of AFI framework (3.8 and 4.6

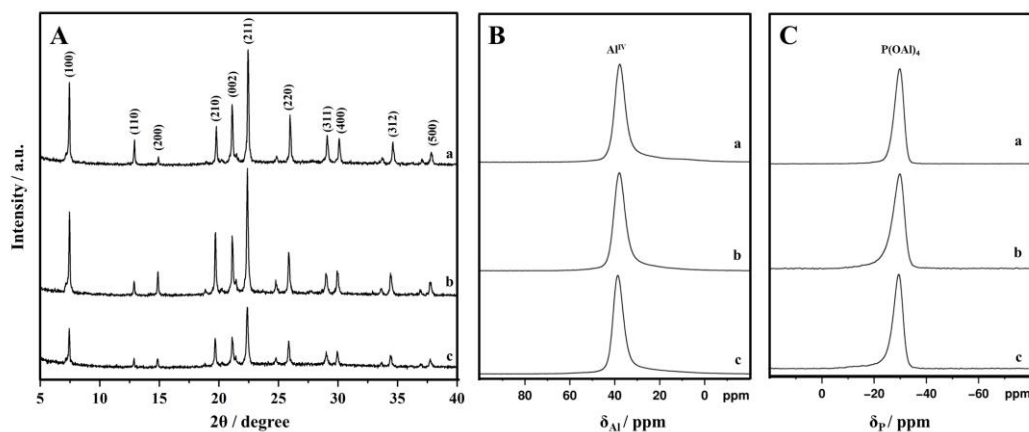


Figure 6.18. A) XRD pattern, B) ^{27}Al and C) ^{31}P NMR spectra of HP-SAPO-5 (a, top curve), fresh NHC-HP-SAPO-5 (b, middle curve) and recycled NHC-HP-SAPO-5 (c, bottom curve).

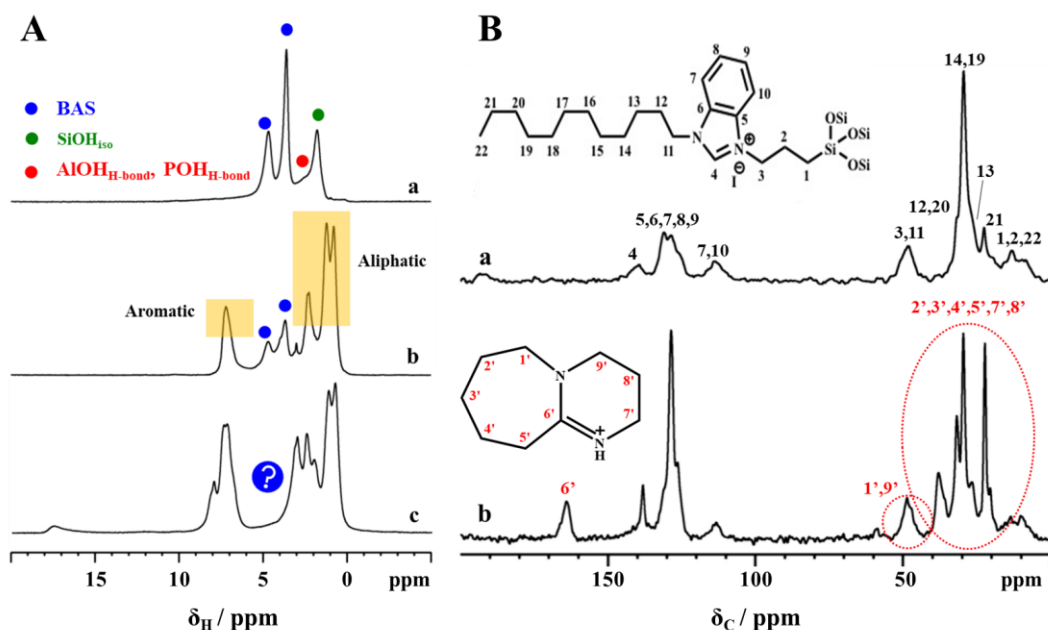


Figure 6.19. A) ^1H MAS NMR spectra of HP-SAPO-5 (a, top curve), fresh NHC-HP-SAPO-5 (b, middle curve) and recycled NHC-HP-SAPO-5 (c, bottom curve). B) ^{13}C CP MAS NMR of fresh NHC-HP-SAPO-5 (a, top curve) and recycled NHC-HP-SAPO-5 (b, bottom curve).

ppm). As already evidenced in subsection 6.2.4, resonance peaks related to isolated Si–OH groups disappeared upon NHC anchoring on the hierarchical support, whereas signals arising from BAS were still detected. Moreover, NHC-HP-SAPO-5 also displayed resonance peaks related to aliphatic (0–3 ppm) and aromatic (6.5–11 ppm) protons of NHC moieties (curve b). Upon recycling, the two well separated resonance bands arising from BAS totally disappeared (curve c), suggesting that the characteristic strong acid sites of AFI framework had been altered over the course of the benzoin condensation reaction. With the aim of getting a deeper insight into the deactivation mechanism of BAS, ^{13}C CPMAS spectroscopy was performed on fresh and recycled NHC-HP-SAPO-5 (Figure 6.19 B). The ^{13}C NMR spectrum of recycled NHC-HP-SAPO-5 exhibited a more complicated pattern (curve b) with respect to the fresh catalyst (curve a), due to the presence of unreacted and product species probably entrapped within the pores architecture. Nevertheless, resonance peaks

arising from the protonated based (DBUH^+) were identified, specifically quaternary carbon at *ca.* 166 ppm and all the other carbons in the range 20-50 ppm.^[46,47]

According to NMR data, FT-IR spectroscopy carried out on fresh and recycled catalysts (Figure 6.20 A and B), evidenced that deprotonation of Brønsted acid sites by DBU had occurred after recycling. In the O–H stretching region (Figure 6.20 A, curve b), bands related to BAS at 3630 and 3513 cm^{-1} were not detected in the FT-IR spectra of recycled NHC-SAPO-5. In the low frequency region (Figure 6.20 B, curve b), in addition to signals evidenced for fresh NHC-HP-SAPO-5 (the $\nu_{\text{C}=\text{N}}$ of benzimidazole ring was identified at 1565 cm^{-1} , $\nu_{\text{C}=\text{C}}$ ring vibrations at 1478 and 1428 cm^{-1} , C–H bending vibrations between 1470 and 1440 cm^{-1}), recycled NHC-HP-SAPO-5 displayed also an intense band at 1677 cm^{-1} , assigned to C=O stretching mode of residual furfural or furoin molecules, and a signal at 1645 cm^{-1} , due to $\nu_{\text{C}=\text{N}}$ of DBUH^+ .^[47,48] Notably, these latter bands were not identified in the FT-IR spectra of recycled NHC-MCM-41-NPs and NHC-Dav150 (Figure 6.21 A and B). All the

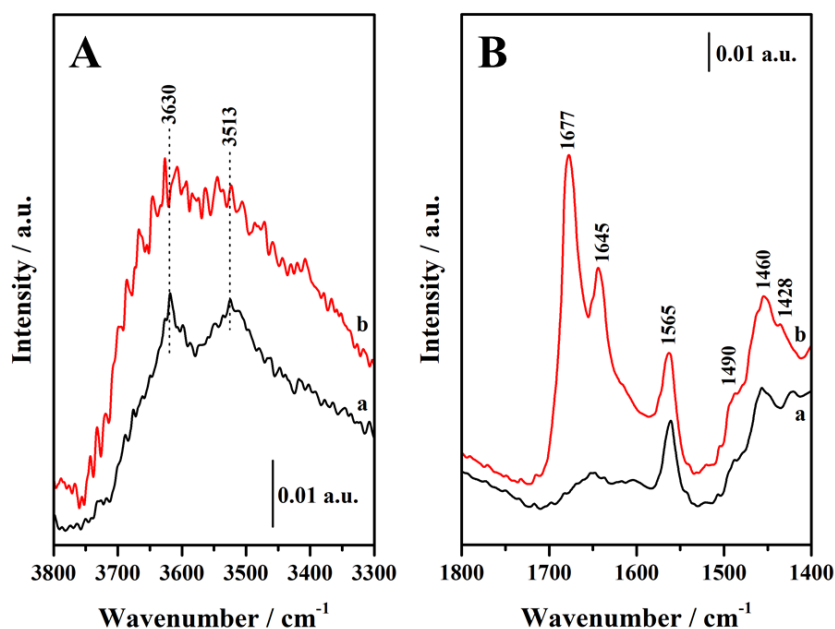


Figure 6.20. FT-IR spectra A) in the O–H stretching region and B) in the low frequency region of fresh NHC-HP-SAPO-5 (a, black curve) and recycled NHC-HP-SAPO-5 (b, red curve).

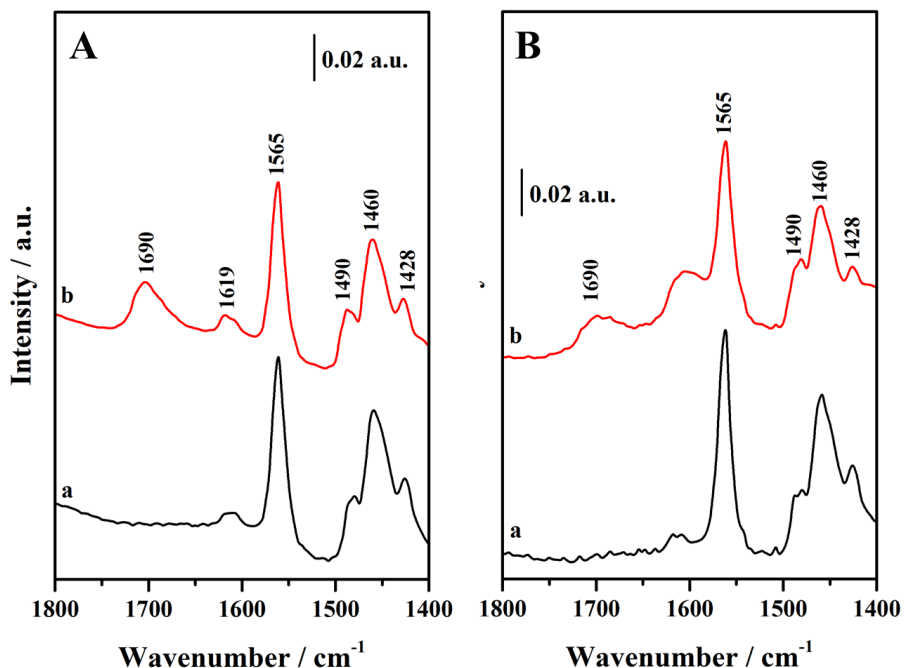
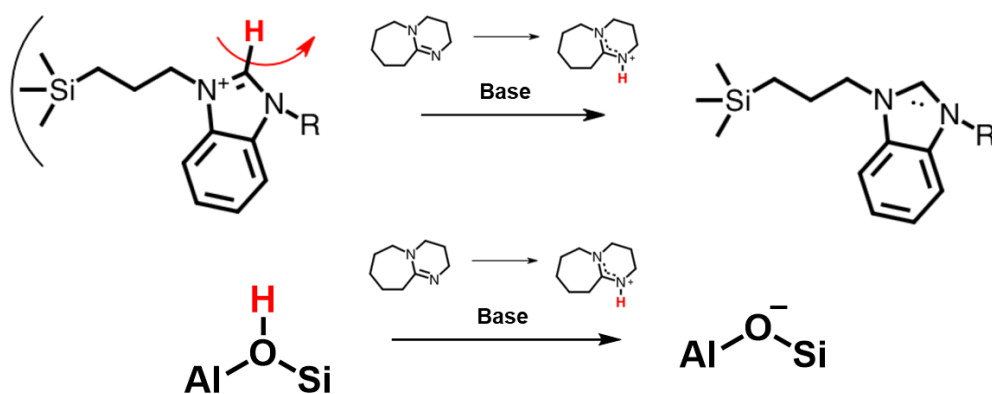


Figure 6.21. FT-IR spectra in the low frequency region of A) fresh NHC-Dav150 (a, black curve) and recycled NHC-Dav150 (b, red curve) and B) fresh NHC-MCM-41-NPs (a, black curve) and recycled NHC-MCM-41-NPs (b, red curve).

previous experimental evidence emphasized that, besides activating the carbene precursor, DBU can also deprotonate and deactivate BAS on the mesopores and within microporous AFI framework of HP-SAPO-5 (Scheme 6.7). Consequently, the



Scheme 6.7. Graphical representation of activation of NHC precursor (top) and deactivation of Brønsted acid site (bottom).

number of activated NHC precursors might decrease at each recycle, leading in a reduction in the catalytic activity of NHC-based hierarchical catalysts with respect to Davisil silica and MCM-41. These data could also explain why the catalytic activity of NHC-SAPO-5 was found to be inferior with respect to NHC-HP-ZSM-5: for comparable NHC-loading, since the former catalysts exhibited a higher amount of BAS (for further details, refer to subsection 6.2.4), a lower fraction of NHC precursors must have been activated by DBU. Furthermore, since the molecular dimensions of DBU (length 5.90 Å, width 3.66 Å, diameter 6.94 Å, approximately) are comparable to micropores diameter of AFI framework (7.3 Å), but larger than the micropore apertures of MFI framework (5.5 Å), DBU within HP-ZSM-5 framework might have deactivated only those BAS located on the mesopore surface or at the micropore mouths.

6.3 Conclusions

N-heterocyclic carbene (NHC) pre-catalyst have been successfully grafted on different inorganic supports. The as-obtained hybrid catalysts have been characterised using a multi-technique approach to establish preliminary structure-property relationships. X-Ray powder diffraction evidence the retention of the structural properties of inorganic supports upon NHC precursor anchoring. ^{29}Si and ^{13}C SS NMR were used to confirm the success of the grafting procedure. Thermogravimetric analyses and variable-temperature FT-IR spectroscopy revealed a different thermal stability of the NHC organic moiety. Specifically, pre-catalyst grafted onto hierarchical supports exhibited a higher thermal stability (at around 300 °C), whereas the NHC decomposition within MCM-41 and Davisil silica was estimated at around 290 and 250 °C, suggesting a dependence on the pore confinement effect. Volumetric analysis performed on hierarchical supports evidenced the existence of multiple levels of porosity within the hierarchical inorganic supports and a retention of the textural properties upon NHC anchoring. Quantification of the proton species via ^1H SS NMR revealed that all the available

silanol groups had been consumed when Davisil silica and hierarchical zeotypes had been used as inorganic supports, whereas NHC-MCM-41 exhibited a fraction of Si-OH groups still available for grafting. Accordingly, an optimization in the NHC loading could be performed on MCM-41 in order to consume all the anchoring groups. In addition, fresh NHC-HP-SAPO-5 and NHC-HP-ZSM-5 also displayed characteristic signals related to BAS, thus proving the retention of the acidic properties of hierarchical framework upon NHC grafting. Then, the catalytic activity of the hybrid materials was evaluated in the benzoin condensation reaction of furfural to render furoin. Notably, NHC-Dav150 and NHC-MCM-41 exhibited full conversion in the first reaction, and good recyclability, whereas HP-ZSM-5 and HP-SAPO-5 showed a 98 % and 80 % conversion after 20 h of reaction. In addition, hierarchical catalysts appeared to be more affected by recycling with respect to mesoporous hybrids. With the aim of unravelling the reason for the inferior catalytic activity of NHC-HP-SAPO-5, SS NMR and FT-IR characterization was performed on the fresh and recycle catalyst. FT-IR and NMR data highlighted that DBU can interact with BAS located within the micropores and on the mesopore surface, deprotonating them instead of activating the NHC pre-catalyst. This mechanism, besides deactivating the acid sites useful to perform tandem reactions, might have led to a decrease in the catalytic activity of NHC-HP-SAPO-5. With a view of exploiting the full potential of hierarchical supports, these drawbacks might be overcome by using a base with larger kinetic diameter, which cannot enter the micropore and deprotonate the BAS *in situ* located. Alternatively, hierarchical supports with smaller micropores, such as hierarchical SAPO-34, might be used to anchor NHC precursor and perform the benzoin condensation reaction.

6.4 Notes and references

- [1] U. Díaz, A. Corma, *Chem. Eur. J.* **2018**, 24, 1.
- [2] A. P. Wight, M. E. Davis, *Chem. Rev.* **2002**, 102, 3589.

- [3] F. Hoffmann, M. Cornelius, J. Morell, M. Fröba, *Angew. Chem., Int. Ed.* **2006**, 45, 3216.
- [4] S.H. Mir, L.A. Nagahara, T. Thundat, P. Mokarian-Tabari, H. Furukawa, A. Khosla, *J. Electrochem. Soc.* **2018**, 165, B3137.
- [5] P. Judeinstein and C. Sanchez, *J. Mater. Chem.* **1996**, 6, 511.
- [6] C. Sanchez, B. Julià, P. Belleville, M. Popall, *J. Mater. Chem.* **2005**, 15, 3559.
- [7] U. Díaz, D. Brunel, A. Corma, *Chem. Soc. Rev.* **2013**, 42, 4083.
- [8] R. Ye, J. Zhao, B. B. Wickemeyer, F. Dean Toste, G. A. Somorjai, *Nat. Catal.* **2018**, 1, 318.
- [9] D. Liu, E. Y.-X. Chen, *Green Chem.* **2014**, 16, 964.
- [10] Selected reviews: a) A.A. Rosatella, S.P. Simeonov, R.F. Frade, C.A.M. Afonso, *Green Chem.* **2011**, 13, 754; b) T. Wang, M.W. Nolte, B.H. Shanks, *Green Chem.* **2014**, 16, 548; c) J.-P. Lange, E. van der Heide, J. van Buijtenen, R. Price, *ChemSusChem* **2012**, 5, 150. d) M.e. Zakrzewska, E. BogelŁukasik, R. BogelŁukasik, *Chem. Rev.* **2011**, 111, 397.
- [11] R. Zhong, A.C. Lindhorst, F. J. Groche, F. E. Kühn, *Chem. Rev.* **2017**, 117, 1970.
- [12] Z. Zhou, Q. Meng, A. Seifert, A. Wagener, Y. Sun, S. Ernst, W. Thiel, *Microporous Mesoporous Mater.* **2009**, 121, 145.
- [13] K.V.S. Ranganath, S. Onitsuka, A. Kiran Kumar and J. Inanaga, *Catal. Sci. Technol.* **2013**, 3, 2161.
- [14] L. Wang, E.Y.-Y. Chen, *ACS Catal.* **2015**, 5 6907.
- [15] D. R. Radu, C.-Y. Lai, K. Jeftinija, E. W. Rowe, S. Jeftinija, V. S.-Y. Lin, *J. Am. Chem. Soc.* **2004**, 126, 13216.
- [16] E. Gianotti, I. Miletto, C. Ivaldi, G. Paul, L. Marchese, M. Meazza, R. Rios, R. Raja, *RSC Adv.* **2019**, 9, 35336.
- [17] D. Verboekend, J. Pérez-Ramírez, *Catal. Sci. Technol.* **2011**, 1, 879.
- [18] X.-Y. Yang, L.-H. Chen, Y. Li, J. C. Rooke, C. Sanchez, B.-L. Su, *Chem. Soc. Rev.* **2017**, 46, 481.
- [19] D.P. Serrano, J.M. Escola, P. Pizarro, *Chem. Soc. Rev.* **2013**, 42, 4004.

- [20] A. Erigoni, S. H. Newland, G. Paul, L. Marchese, R. Raja, E. Gianotti, *ChemCatChem* **2016**, 8, 3161.
- [21] K.A. Cychoz, R. Guillet-Nicolas, J. Garcia-Martinez, M. Thommes, *Chem. Soc. Rev.* **2017**, 46, 389.
- [22] B. Boddenberg, V.R. Rani, R. Grosse, *Langmuir*, **2004**, 20, 10962.
- [23] I. Miletto, G. Paul, S. Chapman, G. Gatti, L. Marchese, R. Raja, E. Gianotti, *Chem. Eur. J.* **2017**, 23, 9952.
- [24] M. Thommes, S. Mitchell, J. Pérez-Ramírez, *J. Phys. Chem. C* **2012**, 116, 18816.
- [25] M. Thommes, K. A. Cychoz, *Adsorption* **2014**, 20, 233.
- [26] G. Paul, G.E. Musso, E. Bottinelli, M. Cossi, L. Marchese, G. Berlier, *ChemPhysChem* **2017**, 18, 839.
- [27] G. Socrates in *Infrared and Raman Characteristic Group Frequencies: Tables and Charts*, John Wiley & Sons Ltd., New York, **2004**.
- [28] V. Arjunan, A. Raj, P. Ravindran, S. Mohan, *Spectrochimica Acta A* **2014**, 118, 651.
- [29] D.W. Mayo, F.A. Miller, R.W. Hannah in *Course notes on the interpretation of IR and Raman spectra*. John Wiley & Sons Inc, Hoboken, NJ, **2004**.
- [30] G. Engelhardt, D. Michel, in *High-Resolution Solid State NMR of Silicates and Zeolites*. John Wiley & Sons Ltd., New York, **1987**; pp. 1.
- [31] G. Paul, C. Bisio, I. Braschi, M. Cossi, G. Gatti, E. Gianotti, L. Marchese, *Chem. Soc Rev.* **2018**, 47, 5684.
- [32] M.E. Potter, M.E. Cholerton, J. Kezina, R. Bounds, M. Carravetta, M. Manzoli, E. Gianotti, M. Lefenfeld, R. Raja, *ACS Catal.* **2014**, 4, 4161.
- [33] S.I. Lee, H. Chon, *J. Chem. Soc., Faraday Trans*, **1993**, 93, 1855.
- [34] G. Müller, J. Bodis, G. Eder-Mirth, J. Kornatowski, J.A. Lercher, *J. Mol. Struct.* **1997**, 410–411, 173.
- [35] Y. Jiang, J. Huang, W. Dai, M. Hunger, *Solid State Nucl. Magn. Reson.* **2011**, 39, 116.

-
- [36] M. Hunger, S. Ernst, S. Steuernagel, J. Weitkamp, *Microporous Mater.* **1996**, 6, 349.
- [37] E.J.M. Hensen, D. G. Poduval, V. Degirmenci, D.A.J.M. Ligthart, W. Chen, F. Mauge, M. S. Rigutto, J.A.R. van Veen, *J. Phys. Chem. C* **2012**, 116, 21416.
- [38] C.P. Grey, A.J. Vega, *J. Am. Chem. Soc.* **1995**, 117, 8232.
- [39] B. Zibrowius, E. Löffler, M. Hunger, *Zeolites* **1992**, 12, 167.
- [40] D. Enders, U. Kallfass, *Angew. Chem. Int. Ed.*, **2002**, 41, 1743.
- [41] M.N. Hopkinson, C. Richter, M. Schedler, F. Glorius, *Nature* **2014**, 510, 485.
- [42] L. Benhamou, E. Chardon, G. Lavigne, S. Bellemin-Laponnaz, V. Cesar, *Chem. Rev.* **2011**, 111, 2705.
- [43] P. de Fremont, N. Marion, S.P. Nolan, *Coord. Chem. Rev.* **2009**, 253, 862.
- [44] R. Breslow, *J. Am. Chem. Soc.* **1957**, 79, 1762.
- [45] R. Breslow, *J. Am. Chem. Soc.* **1958**, 80, 3719.
- [46] D.J. Coady, K. Fukushima, H.W. Horn, J. E. Rice, J.L. Hedrick, *Chem. Comm.* **2011**, 47, 3105.
- [47] S.G. Khokarale, J.-P. Mikkola, *RSC. Adv.* **2018**, 8, 18531.
- [48] S. Basel, K. Bhardwaj, S. Pradhan, S. Tamang, *ACS Omega* **2020**, 5, 6666.

7

Influence of silicodactyly and silicopodality in the design of hybrid materials

In the present chapter, the influence of silicodactyly and silicopodality in the design of a silica-based hybrid catalyst has been deeply investigated by a combined experimental and computational study. With the aim of clarifying how the architecture of anchored organosilane may affect the conformation of organic chains, determining whether or not an interaction between the organic moiety and the inorganic surface, different types of silicodactyl and silicopodal platforms were grafted onto a silica inorganic support. The as-synthesised hybrid materials were characterised using a multi-technique approach (XRD, TGA, ^{29}Si , ^1H and ^{13}C solid-state NMR and FT-IR spectroscopies). Computational studies (molecular dynamics calculations) were carried out to forecast how the different grafting configurations (dactyly) and the variable number of alkyl chains used by the organic platform to grab the inorganic surface (podality) may influence the tendency of the organosilane to lay on the silica surface.

Introduction

In recent years, great progress in the ability to engineer new organic-inorganic hybrid materials, with tailored properties, has been made.^[1-5] Among hybrid silica-based materials, ordered mesoporous silicas such as MCM-41 have been widely used as inorganic supports, thanks to the large specific surface areas and tunable ordered pore arrays with controlled size. Moreover, the huge pores volumes together with the possibility of easy surface functionalization (*e.g.* post-synthetic grafting)^[6], make mesoporous materials extremely suitable for various applications, such as catalytic reactions, molecular capture, enzyme immobilization^[7] and drug delivery^[8,9].

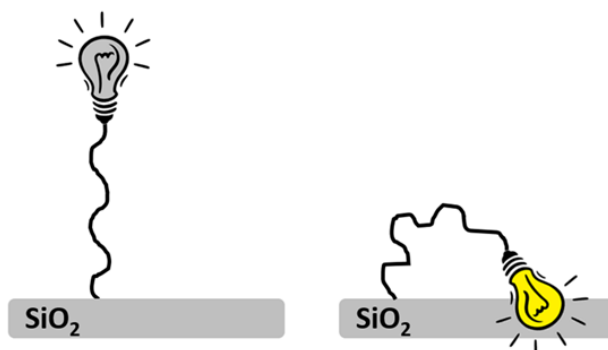


Figure 7.1. Proof of concept of an ideal probe which gives a specific signal when interacting with the inorganic surface.

Besides enabling the embedment of a wide variety of organic moieties within the inorganic framework, surface functionalization also ensures a good dispersion of the organic active sites inside the internal surface of MCM-41, thus minimizing their aggregation and migration. Moreover, post-synthetic grafting prevents the leaching of the organic counterpart, which can affect the traditional physical entrapment methods.^[10] Despite the importance of organic-inorganic hybrid materials in heterogeneous catalysis, the factors (degree of hydrolysis and condensation during the grafting procedure, hydrophilicity of the silica surface, confinement effects, length of the anchoring groups) influencing the conformation of the organic moiety grafted onto a silica surface have not been systematically studied. Specifically, with the view to design a class II hybrid, it should be considered that the reactive organic moiety, covalently bonded to the inorganic support through a linker, may interact with its surface, thus possibly hampering the catalytic activity. Evidently, the best catalytic performances are expected when the organic moiety is able to stick out from the surface, fully available for interactions with substrates. If the catalytic active site gives a specific spectroscopic signal when interacting with the silica surface, it is possible to monitor the behaviour of the system when changing the nature and the length of the linker (Figure 7.1).

In light of the foregoing, the research study described in the present chapter aims at investigating how the architecture of organosilane grafted onto a silica surface

affects the conformation of organic chains, determining whether or not an interaction between the organic moiety and the inorganic surface.^[11] In the design of a hybrid organic-inorganic silica-based material, two important parameters can be easily controlled and varied during the synthesis procedure, as schematized in Figure 7.2. Firstly, each alkoxy silane can bear 1 to 3 hydrolysable groups (typically methoxy or ethoxy groups) which can condense with surface silanols to form siloxane bridges. The number of these covalent bonds depends on the number of hydrolysable tails and on the concentration of surface silanols. This property has been named silicodactyly, since it describes the number of dactyls (from the Greek word meaning fingers) used by the alkoxy silane to grab the silica surface. In Figure 7.2, examples of di-dactyl (a) and tri-dactyl (b) alkoxy silane are reported. Secondly, the catalytic head can be anchored to the surface through a variable number of alkylsilane chains. This property has been named silicopodality and, depending on the number of leg(s), a monopodal or multipodal system can be formed (Figure 7.2., (a) and (b), (c) respectively). The influence of silicodactyly and silicopodality has been elucidated by a combined experimental (XRD, TGA/DTG, ^{29}Si , ^1H and ^{13}C solid-state NMR and FT-IR spectroscopies) and computational (Molecular Dynamics calculations) approach. Computational studies have been used to forecast the influence of the different grafting configurations (dactyly) and the influence of the number of

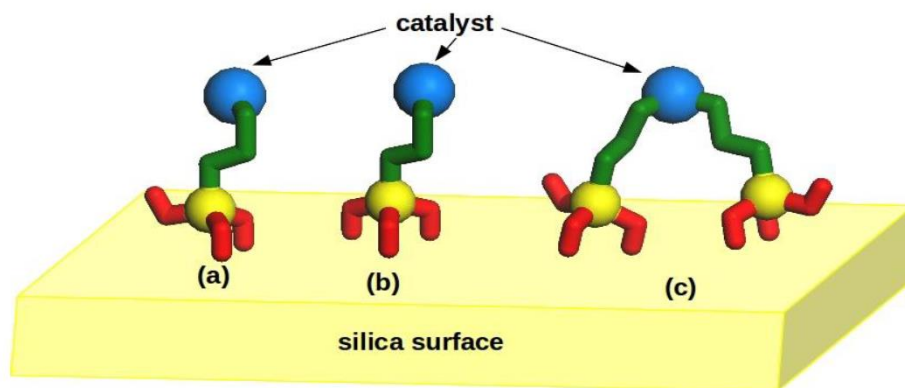


Figure 7.2. Examples of different silicodactyly (a,b) or silicopodality (c) affecting the conformations of the organic moiety with respect to the surface. Yellow sphere: silicon; red: hydrolysable groups; green: alkyl chain; blue: catalytic active site.

alkylsilane chains by which the catalytic site is anchored to the inorganic support (podality) on the tendency of the silane to lay on the inorganic surface.

7.1 Influence of silicodactyly

In order to investigate the effect of silicodactyly on the conformation of the alkoxy silane chains, (3-mercaptopropyl)alkoxy silanes bearing different number of hydrolysable methoxy groups (the remaining ‘fingers’ being substituted by methyl groups) have been grafted on an ordered mesoporous silica, MCM-41. Mercapto-functional mesoporous silicas have received great attention as heavy metal ion-trapping agents.^[12] Furthermore, thiol groups may represent the branching point to anchor a possible organo-catalyst or can be oxidized to form sulfonic acid active centres, suitable for applications in heterogeneous acid catalysis.^[13]

7.1.1 Experimental section

7.1.1.1 General

MCM-41, methylmagnesium bromide and solvents were purchased from Sigma-Aldrich and used as received. (3-mercaptopropyl)trimethoxysilane and (3-mercaptopropyl)dimethoxymethylsilane were purchased from TCI Europe and employed as received. (3-mercaptopropyl)methoxydimethylsilane was synthesised by CAGE Chemicals S.r.l., one of the MULTI2HYCAT project partners, under the supervision of Prof. Giovanni Battista Giovenzana, slightly modifying a reported procedure.^[14]

7.1.1.2 (3-Mercaptopropyl)methoxydimethylsilane synthesis

In a 250 mL r.b.f. under inert atmosphere (N_2), (3-mercaptopropyl)trimethoxysilane (8.0 mL, 43 mmol) was dissolved in anhydrous THF (25 mL) and cooled to 0–5 °C with an ice bath. Methylmagnesium bromide (3M in diethyl ether, 43 mL, 129 mmol) was added dropwise at such a rate to maintain $T < 10$ °C. The olive-green mixture was stirred at 0–10 °C for 75 min during

which the colour gradually disappears. Dry methanol (25 mL) was then added (caution, foaming) and the milky-white suspension was diluted with a THF/diethyl ether (5 mL/40 mL) mixture. Filtration on a sintered glass frit under N₂ atmosphere and evaporation of the solvents gave a liquid residue, fractionally distilled under vacuum to give the title product (4.9 g). Clear colourless liquid; yield, 69%; b.p. 70–75 °C (60 mmHg). ¹H-NMR (CDCl₃, 300 MHz, ppm): 3.39 (s, 3H, CH₃O), 2.50 (q, 2H, J = 7.3 Hz, CH₂S), 1.62 (m, 2H, C-CH₂-C), 1.30 (t, 1H, J = 8.0 Hz, -SH), 0.66 (m, 2H, CH₂-Si), 0.07 (s, 6H, CH₃-Si). ¹³C-NMR (CDCl₃, 75.6 MHz, ppm): 50.2 (CH₃), 28.1 (CH₂), 27.9 (CH₂), 15.2 (CH₂), -2.7 (CH₃).

7.1.1.3 Synthesis of hybrid materials

Hybrid materials were prepared by post-synthesis grafting with (3-mercaptopropyl)alkoxysilane: MCM-41 (0.3 g), dried overnight at 100 °C, was suspended in anhydrous toluene (30 mL). The suspension was heated at 120 °C under stirring. (3-mercaptopropyl)alkoxysilane (0.77 mmol) was then added dropwise and the mixture was refluxed for 18 h. Filtration and washing of the mixture with toluene, ethanol and deionized water gave a white solid, which was cured in air at 80 °C overnight.

7.1.1.4 Characterization

Before recording solid state NMR spectra, all the samples were outgassed at 200°C for 1h. Further details on the experimental techniques are reported in Chapter 9/Experimental section.

7.1.1.5 Computational details

Design of models: the structures of (3-mercaptopropyl)alkoxysilanes were grafted on a silica surface (slab) with density 2.4 OH/nm². The atomic structure of the slab was taken from literature (Uliengo *et al.*)^[15] The thickness of the layer was 13.96 Å. The horizontal dimensions of the simulation box were 25.34 × 26.55 Å²,

the vertical dimension was 50.00 Å. Periodic boundary conditions in all dimensions were employed. In Figure 7.3, one example of simulation box is reported.

General settings of molecular dynamics (MD): starting configurations of the molecular dynamics were generated performing partial energy minimization to adjust atom coordinates in the box. Only atomic position of (3-mercaptopropyl)alkoxysilane derivatives, together with silicon and oxygen atoms of the slab directly bonded to these, were minimized. The remaining atoms were kept fixed. Conjugate Gradients algorithm were used, by specifying an energy tolerance of 1.0×10^{-3} kcal/mol and force tolerance of 0.5 kcal/mol/Å. QEq charge equilibration method was employed to generate atomic partial charge, indicating a convergence limit of 1.0×10^{-6} e, using the 'Qeq' package implemented in Material Studio suite.^[16] Coulombic interactions were computed by means of standard Ewald summation with accuracy of 1.0×10^{-6} kcal/mol. Van der Waals interactions were calculated as sum of 12-6 Lennard Jones (LJ), setting a cutoff of 20 Å. σ and ϵ parameters were extracted from UFF force field^[17] and their amounts were calculated

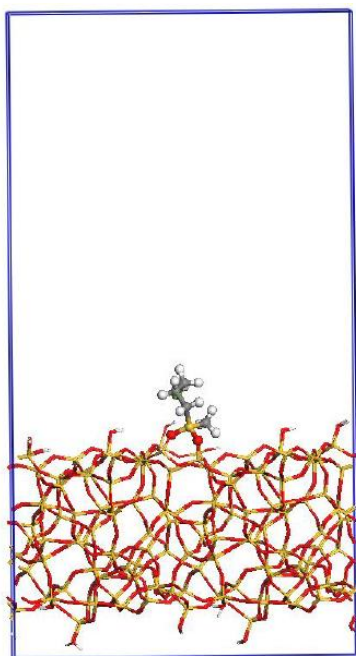


Figure 7.3. Simulation box containing one (3-mercaptopropyl)alkoxysilane grafted on a slab silica.

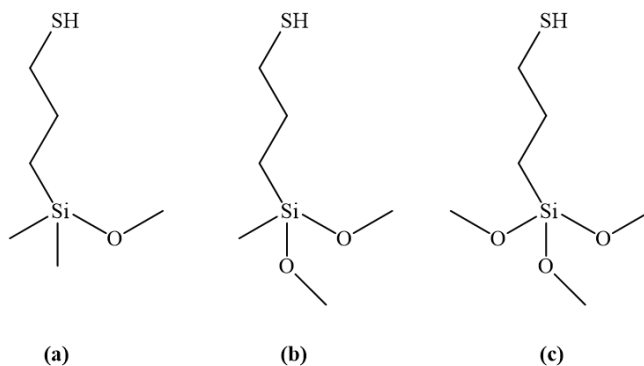


Figure 7.4. Different (3-mercaptopropyl)alkoxysilane derivatives: (a) (3-mercaptopropyl)methoxydimethylsilane, (b) (3-mercaptopropyl)dimethoxymethylsilane and (c) (3-mercaptopropyl)trimethoxysilane.

based on the Lorentz-Berthold relationship. Molecular dynamics simulations were performed in canonical (n,V,T) ensemble in vacuum at 298 K (using Langevin thermostat to maintain the temperature constant)^[18] for 1 ns using the LAMMPS simulation package.^[19]

7.1.2 Results and discussion

7.1.2.1 Hybrid structures

Three different (3-mercaptopropyl)alkoxysilane derivatives, bearing a different number of hydrolysable species (one, two or three, Figure 7.4), were grafted on an ordered mesoporous MCM-41. With the aim of preventing island-type grafting due to condensation and clustering of the silylation agents and favouring homogeneous distribution of the alkoxy silanes, the grafting procedure was performed in a non-polar solvent (like toluene) with a clean inorganic surface.^[20] In Table 7.1 the acronyms of the hybrid materials are listed.

Table 7.1. Acronyms of hybrid materials.

Acronyms	Alkoxy silane derivative grafted on MCM-41
MeO-MCM-41	(3-mercaptopropyl)methoxydimethylsilane
DiMeO-MCM41	(3-mercaptopropyl)dimethoxymethylsilane
triMeO-MCM-41	(3-mercaptopropyl)trimethoxysilane

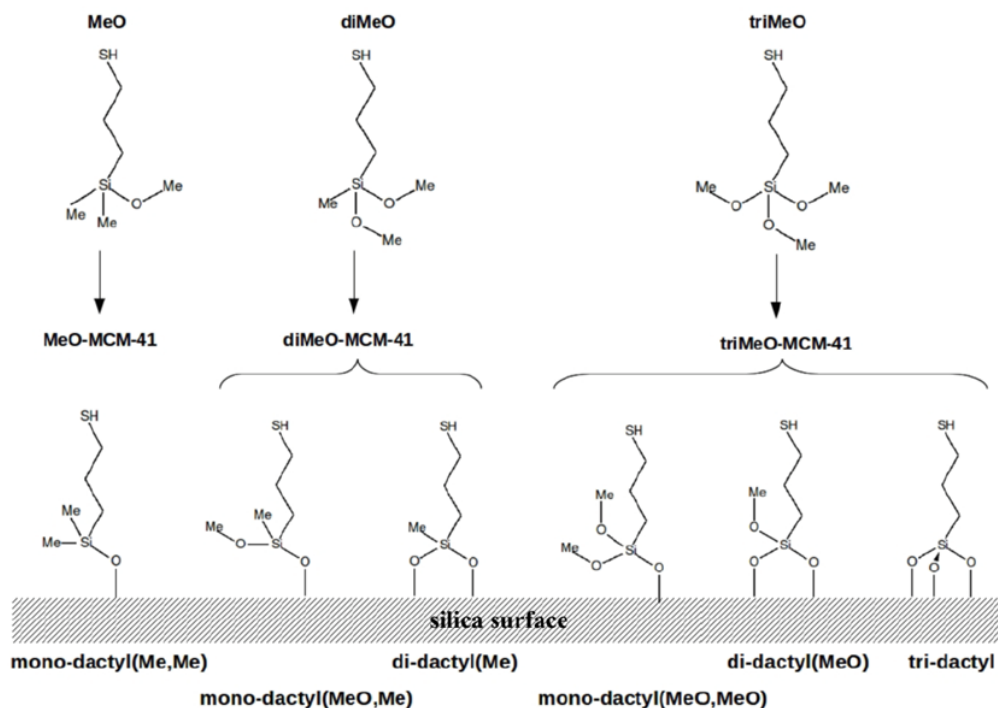


Figure 7.5. Grafting configurations possibly obtained by anchoring (3-mercaptopropyl)alkoxysilanes on MCM-41. The name at the bottom evidences the dactyl of the particular configuration and the nature of the non-grafted dangling groups.

According to the number of methoxy groups which are actually hydrolysed, six different dactyls can be obtained, as reported in Figure 7.5, wherein a nomenclature of the different possible grafting configurations is also proposed.

7.1.2.2 XRD and TGA analyses

X-Ray powder diffraction was performed to assess that ordered MCM-41 had not been affected by the grafting procedure (Figure 7.6). Upon the anchoring of the three different alkoxy silanes, all hybrids exhibited the same characteristic Bragg reflections of plain hexagonally ordered MCM-41, confirming the retention of the structural properties of the inorganic support.^[21]

Thermogravimetric analysis was carried out to estimate the organic content, thermal stability of the grafted mercaptoalkoxysilanes and the hydrophobic/hydrophilic character of the resulting hybrid materials (Figure 7.7). The

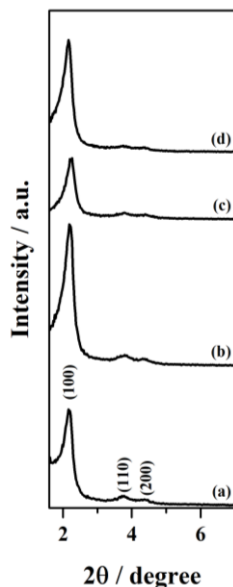


Figure 7.6. The powder XRD pattern of a) plain MCM-41, b) MeO-MCM-41, c) diMeO-MCM-41 and d) triMeO-MCM-41.

thermograms and derivatives of all the hybrid samples and plain MCM-41 exhibited a first weight loss at around 30-150 °C, which can be assigned to the removal of water weakly bonded to the surface. Specifically, MeO-MCM-41 revealed a weight loss due to physisorbed water which is similar to plain MCM-41, whilst diMeO-MCM-41 and triMeO-MCM-41 lost a lower amount of water, meaning a higher hydrophobic character of these latter functionalized materials. At higher temperatures (150-550 °C), flat weight loss profiles of the hybrids changed into a rapidly declining profile, corresponding to the decomposition of the alkoxy silane derivatives. In particular, triMeO-MCM-41 exhibited a higher loss of organic content

Table 7.2. Weight loss (%) due to water and organic content calculated from TGA analysis.

Sample	$\Delta\text{wt}\%$ due to $\text{H}_2\text{O}^{\text{a}}$	$\Delta\text{wt}\%$ due to mercaptoalkoxysilane ^b
MCM-41	1.25	-
MeO-MCM-41	1.13	6.30
diMeO-MCM-41	0.45	8.20
triMeO-MCM-41	0.74	8.90

^a Calculated from 30 °C to 150 °C. ^b Calculated from 150 °C to 550 °C.

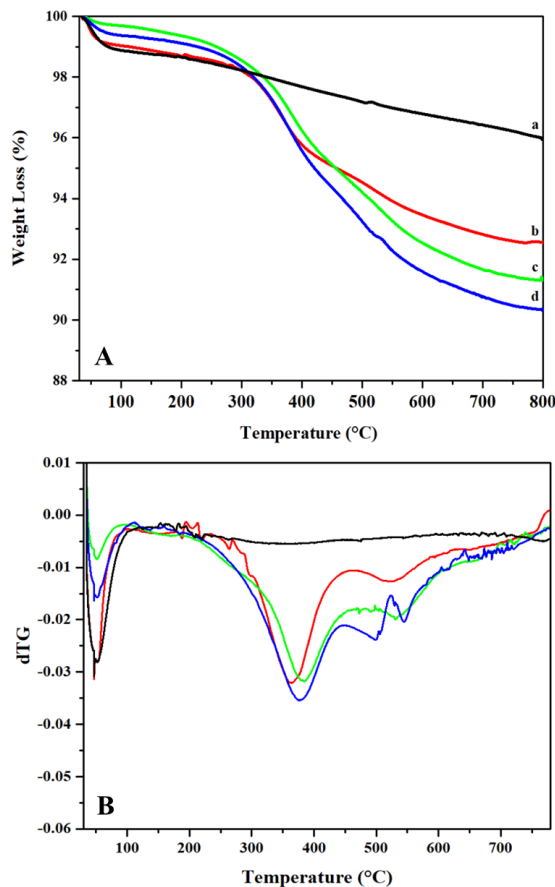


Figure 7.7. A) TGA and B) DTG curves of MCM-41 (a, black curve), MeO-MCM-41 (b, red curve), diMeO-MCM-41 (c, green curve) and triMeO-MCM-41 (d, blue curve).

in this temperature range with respect to the other hybrids. Moreover, DTG curves (Figure 7.7 B) showed that the temperature of weight loss due to the (3-mercaptop)alkoxysilane decomposition for MeO-MCM-41 is slightly lower. The organic content, calculated from the weight loss in the range 150-550 °C, is reported in Table 7.2. The further weight loss in the 550-800 °C range observed for plain MCM-41 can be attributed to the silanol condensation forming siloxane bridges.

7.1.2.3 FT-IR spectroscopy

FT-IR spectroscopy performed at different temperatures was used in order to gain insight into the thermal stability of the different grafted (3-mercaptop)alkoxysilane derivatives (Figure 7.8-7.10). Upon outgassing the samples at 30°C, FT-IR spectra

of the three hybrid materials exhibited at high wavenumbers a weak signal at 3745 cm^{-1} , which is attributed to the O–H stretching mode of isolated residual silanols and is less intense in triMeO-MCM-41 sample. Between 3700 and 3000 cm^{-1} , a broad absorption related to hydrogen-bonding interactions between surface groups, was detected.^[22] The FT-IR spectra of the hybrids showed in the region between 3000 and 2800 cm^{-1} signals characteristic of the grafted organosilane, which can be assigned to C–H stretching modes of methyl and methylene groups of (3-mercaptop)alkoxysilanes. Specifically, bands at 2962 cm^{-1} and 2872 cm^{-1} are assigned to the asymmetric and symmetric methyl C–H stretching modes, whereas signals at 2926 cm^{-1} and 2853 cm^{-1} are due to ν_{asym} and ν_{sym} modes of CH_2 groups of the propyl chain. Bands related to the C–H bending vibrations were also detected in the range 1470 – 1300 cm^{-1} , but unambiguous assignment was not possible due to the low intensity and overlapping (in this respect, in linear hydrocarbons, antisymmetric deformation modes of CH_3 –C are typically found at 1460 cm^{-1} , symmetric deformation mode of CH_3 –C, CH_3 –O and CH_3 –Si groups are observed at 1378 cm^{-1} , 1455 cm^{-1} and 1255 cm^{-1} , respectively, whereas scissoring of CH_2 groups are

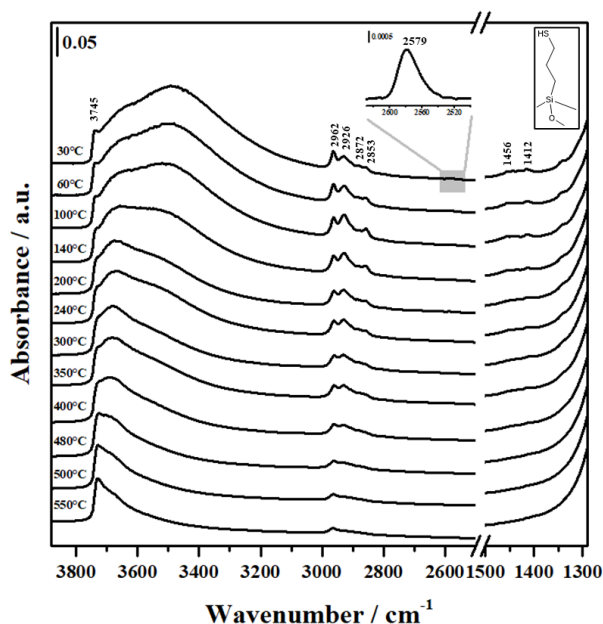


Figure 7.8. Variable temperature FT-IR spectra of MeO-MCM-41.

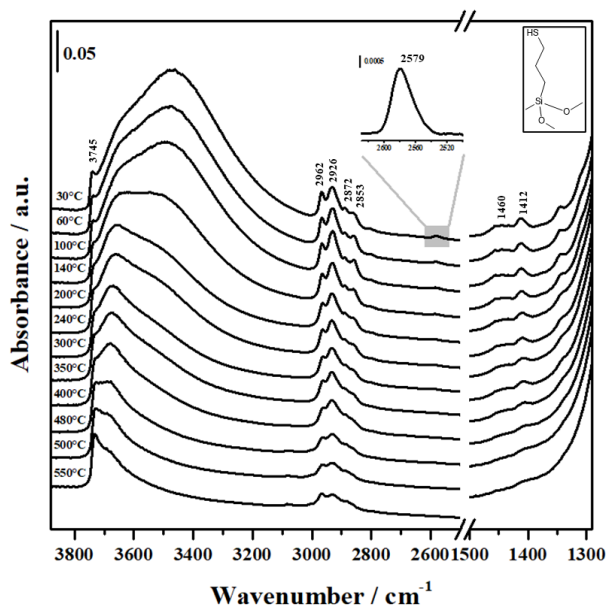


Figure 7.9. Variable temperature FT-IR spectra of diMeO-MCM-41.

detected at 1450 cm^{-1} .^[23] Moreover, symmetric bending vibrations of $\text{CH}_3\text{-Si}$ groups are not detectable since these signals fall beneath the broad and intense absorption in the region $1250\text{-}1000\text{ cm}^{-1}$, assigned to the asymmetric stretching modes of Si-O-Si of the silica framework. A weak signal at 2579 cm^{-1} , due to the S-H stretching

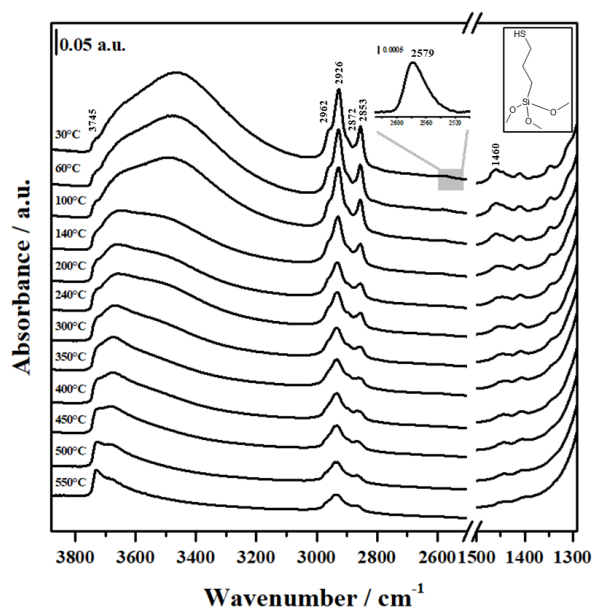


Figure 7.10. Variable temperature FT-IR spectra of triMeO-MCM-41.

mode of thiol groups, was observed in the spectra of all the samples (Figure 7.8-7.10, inset).^[24-26] By increasing the outgassing temperature, intensities of the IR signals between 3000-2800 cm^{-1} and 1470-1300 cm^{-1} progressively decreased, indicating the gradual decomposition of the alkoxy silane derivatives, which started at ca. 240 °C in all the hybrid samples. In accordance with TG analysis, FT-IR spectra evidenced that the organic counterpart of MeO-MCM-41 hybrid was totally decomposed at ca. 400 °C, while in the other two hybrid materials the alkoxy silane derivatives decomposed at temperatures slightly higher than 400 °C.

7.1.2.4 Solid state NMR spectroscopy

Despite the FT-IR analysis evidenced the successful grafting of the various alkoxy silanes on MCM-41, ^{13}C and ^{29}Si CPMAS NMR can provide additional information on surface silicon environments and attached silanes, specifically in their grafting mechanism. With the aim of confirming the effective condensation of the alkoxy silane precursors with silica support silanols, ^{13}C CPMAS NMR analysis was performed (Figure 7.11). The signals at -3.6 and -5.2 ppm can be assigned to the Si-CH₃ dangling groups in the spectra of MeO-MCM-41 (curve a) and diMeO-MCM-41 (curve b) hybrids, respectively. Furthermore, the Si-CH₂ resonances were detected at 15.7, 14 and 9.8 ppm in the spectra of MeO-MCM-41, diMeO-MCM-41 and triMeO-MCM-41 (curve c) respectively. Finally, the peaks of the remaining methylene carbons (-CH₂-CH₂-CH₂-SH) were observed at around 26.5 ppm in all the hybrid materials. Resonance peaks at ca. 49 ppm, ascribable to residual non-hydrolysed methoxy groups, were particularly evident in the spectrum of triMeO-MCM-41, meaning that the presence of three alkoxy groups in the alkoxy silane precursor does not ensure the complete condensation with three surface silanols.^[27,28]

^{29}Si CPMAS analysis, which enhances, by magnetization transfer, the sensitivity and detection of the silicon atoms nearby to protons, can be used in order to gain insight in structural species and surface OH groups of solid samples, by referring to ^{29}Si isotropic chemical shifts of tetrahedrally coordinated silicon atoms (Figure 7.12

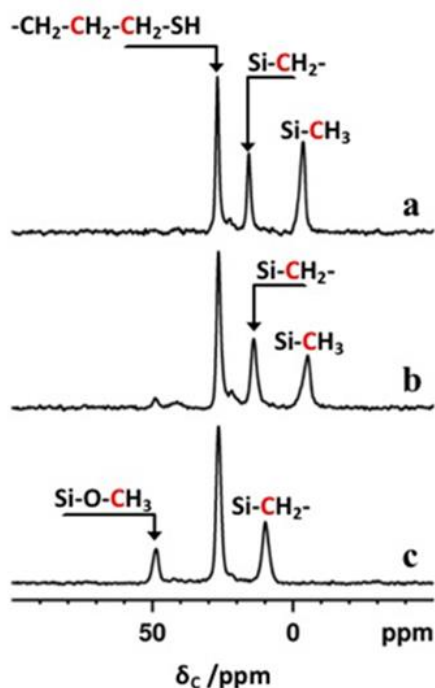


Figure 7.11. ^{13}C CPMAS NMR spectra of MeO-MCM-41 (curve a), diMeO-MCM-41 (curve b) and triMeO-MCM-41 (curve c).

A). Specifically, this NMR technique was performed with the aim of thoroughly characterize the surface species located at the interface between the organic counterpart and the silica support. The crystallographic distinct Si sites can be identified according to the commonly used Q^n and $\text{T}^n/\text{D}^n/\text{M}^n$ notations (Figure 7.12 C), where the capital letter indicate the number of oxygens directly bonded to the Si atom, whereas n is related to the number of Si atoms of the second coordination sphere.^[29] Systematic changes in the chemical shift values are observed when the second coordination sphere is changed from Si to other atoms.^[30] The ^{29}Si NMR chemical shifts of various silicon sites were detected in the following ranges. Q^4 ($\text{Si}(\text{OSi})_4$) silicon sites at -110 ppm, Q^3 ($\text{Si}(\text{OSi})_3\text{OH}$) sites at -101 ppm, Q^2 ($\text{Si}(\text{OSi})(\text{OH})_2$) sites at -91 ppm, T^3 ($\text{RSi}(\text{OSi})_3$) sites at -67 ppm, T^2 ($\text{RSi}(\text{OSi})_2\text{OH}$) sites at -57 ppm, T^1 ($\text{RSi}(\text{OSi})_1(\text{OH})_2$) sites at -48 ppm, D^2 ($\text{R}_2\text{Si}(\text{OSi})_2$) sites at -16 ppm, D^1 ($\text{R}_2\text{Si}(\text{OSi})(\text{OH})$) sites at -9 ppm and M^1 ($\text{R}_3\text{Si}(\text{OSi})$) sites at $+15$ ppm. In all hybrids materials, Q^4 , Q^3 and Q^2 resonances peak arising from MCM-41 silica

support, were detected, although with different intensities.^[31] Apart from the Q^n signals, upon silylation, MeO-MCM-41 hybrid (curve a) showed M^1 signal at ca. 15 ppm, whilst diMeO-MCM-41 sample (curve b) exhibited two resonance peaks at ca. -9 and -16 ppm, due to D^1 and D^2 sites, respectively. Particularly, diMeO-MCM-41 exhibited more intense D^1 than D^2 sites, indicating that the difunctional organosilane has reacted preferentially in a mono-dentate manner with the silica support. TriMeO-MCM-41 (curve c) showed more intense signal arising from T^2 than T^1 sites (-57 and -48 ppm, respectively), suggesting that in this case the surface grafting mechanism has preferentially occurred with a mono- or di-dentate chelation, with the di-dactyl system more prevalent than the mono-dactyl. Very weak signal due to T^3 sites at around -68 ppm confirmed the presence of a very low fraction of tri-dentate silane grafted onto MCM-41 silica support, meaning, in accordance with the Si-O-CH₃ signal in the ¹³C CPMAS NMR spectrum, that the presence of three alkoxy groups in the alkoxy silane precursor does not ensure the complete condensation with three surface silanols. Borrego *et al.* have reported similar observations when they have

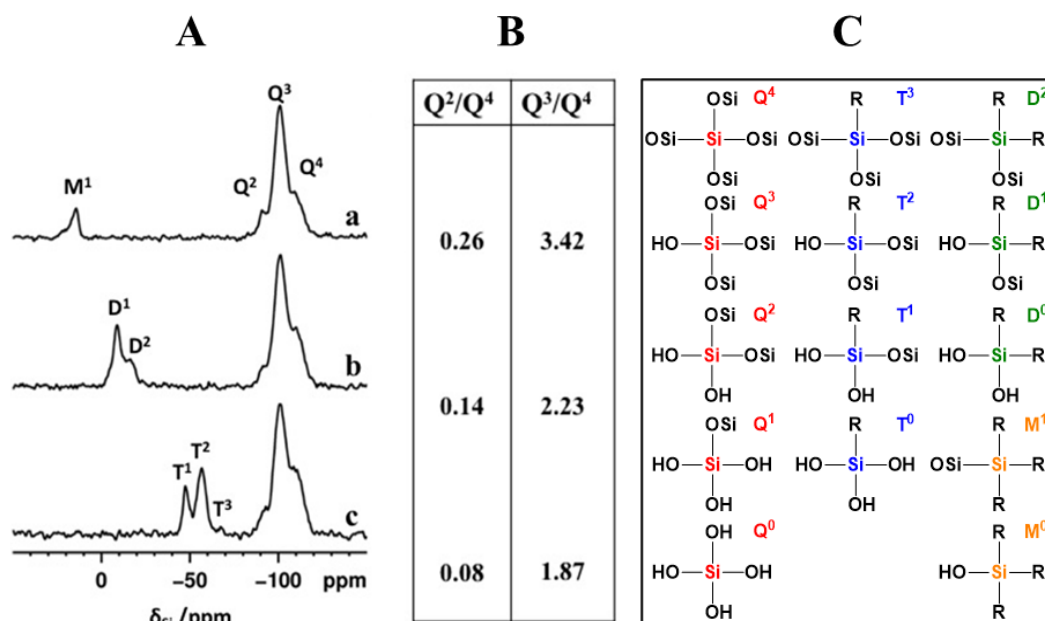


Figure 7.12. A) ²⁹Si CPMAS NMR spectra of MeO-MCM-41 (curve a), diMeO-MCM-41 (curve b) and triMeO-MCM-41 (curve c). B) Area ratios derived from the deconvolution of ²⁹Si CPMAS NMR data. C) Schematic representation of Q^n / T^n / D^n / M^n silicon sites

grafted (3-mercaptopropyl)trimethoxysilane on mesoporous solids.^[32] A possible explanation for such behaviour may be found in the hydrophobic nature of the methyl on the organosilane which might impede the complete hydrolysis and multidentate condensation on a hydrophilic surface like that of the MCM-41.^[33]

Concerning the Q^n sites typical of siliceous matrices, it should be emphasised that in the organosilane grafting process onto a silica support, the Q^3 and Q^2 sites plays the most important role since they provide Si-OH groups (one or two, respectively) for the silane anchoring.^[32] On the other hand, Q^4 sites are not involved in the functionalization process as they lack OH groups. Against this background, although the deconvolution data from CPMAS experiments are not quantitative, a trend in the grafting process can be derived from Q^2/Q^4 and Q^3/Q^4 ratios. Specifically, the decrease of Q^2/Q^4 and Q^3/Q^4 ratios can indicate which type of silanol, isolated (Q^3) or geminal (Q^2), reacts preferentially with the given alkoxy silane. The Q^2/Q^4 and Q^3/Q^4 ratios decreased from monoMeO-MCM-41 to triMeO-MCM-41, thus confirming the mono and/or bidentate (and, in much less extent, tridentate) connectivity to the silica surface (Figure 7.12 B). Furthermore, the highest decrease in Q^2/Q^4 ratio occurred in triMeO-MCM-41, since geminal (Q^2) silanols react preferably with tri-dactyl alkoxy silanes. Such a reaction pathway involving Q^2 sites may lead to either mono- or bi-dentate grafting as evidenced in triMeO-MCM-41.

With the aim of obtaining additional information on the different proton environments and grafted organosilane, 1H ECHO MAS NMR analysis was performed. The 1H NMR spectra of hybrid materials (Figure 7.13) consist mainly of contributions from organosilane alkyl chains, unhydrolyzed methoxy species, methyl dangling groups as well as isolated silanols or silanols interacting *via* hydrogen bond. The resonance of $-SH$ proton along with the physisorbed water signal, are difficult to distinguish in the 1H NMR spectra, anyway their contributions fall beneath the broad peak in the range 3–8 ppm. Consistently with ^{13}C and ^{29}Si CPMAS NMR analyses, proton NMR data evidenced the presence of a large and

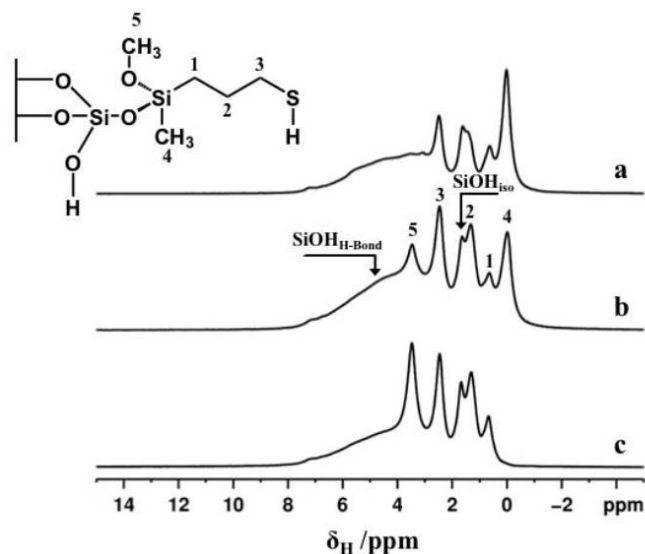


Figure 7.13. A) ^1H ECHO MAS NMR spectra of MeO-MCM-41 (curve a), diMeO-MCM-41 (curve b) and triMeO-MCM-41 (curve c).

moderate amount of unhydrolyzed methoxy groups in triMeO-MCM-41 and diMeO-MCM-41 hybrids, respectively. Furthermore, in agreement with FT-IR analysis, resonance peak attributed to isolated silanols was found to be less intense in diMeO-MCM-41 and triMeO-MCM-41, emphasising the multidentate bonding on the silica surface. Finally, the interaction between thiol groups and silanols or physisorbed water was further confirmed by preliminary analysis with variable contact time 2D proton-silicon correlation NMR experiments.

7.1.2.5 Computational modeling

Classical molecular dynamics were exploited in order to gain microscopic insight on the hybrid structures. Six models, corresponding to six possible grafting configurations depicted in Figure 7.5, were prepared by linking the proper (3-mercaptopropyl)alkoxysilane to a periodic model of MCM-41 surface with a silanol density of 2.4 OH/nm^2 , in accordance with the experimental evaluation by TG analysis on plain MCM-41. Notably, the try-dactyl system could not be easily prepared on this kind of surface, unlike the mono- and di-dactyls, due to the lack of silanols in fit positions. Finally, the tri-dentate hybrid was obtained by condensing

two methoxy groups with geminal silanols, resulting in a quite strained structure. This is in accordance with ss-NMR findings, which evidenced the presence of a weak T^3 signal in the triMeO-MCM-41 sample, recommending a more hydrophilic (i.e., with higher density of silanols) silica surface to obtain a higher concentration of tri-dactyl systems. Then 1ns MD runs at 298 K were performed for each model, after suitable thermalization cycles. During the simulations, the distance between the sulphur atom and the MCM-41 surface was monitored, to evaluate the tendency of organic moiety to interact with the silica surface.

The time evolution of the sulphur-surface distance for the six hybrid models, and the corresponding average distances, are reported in Figure 7.14 and Table 7.3,

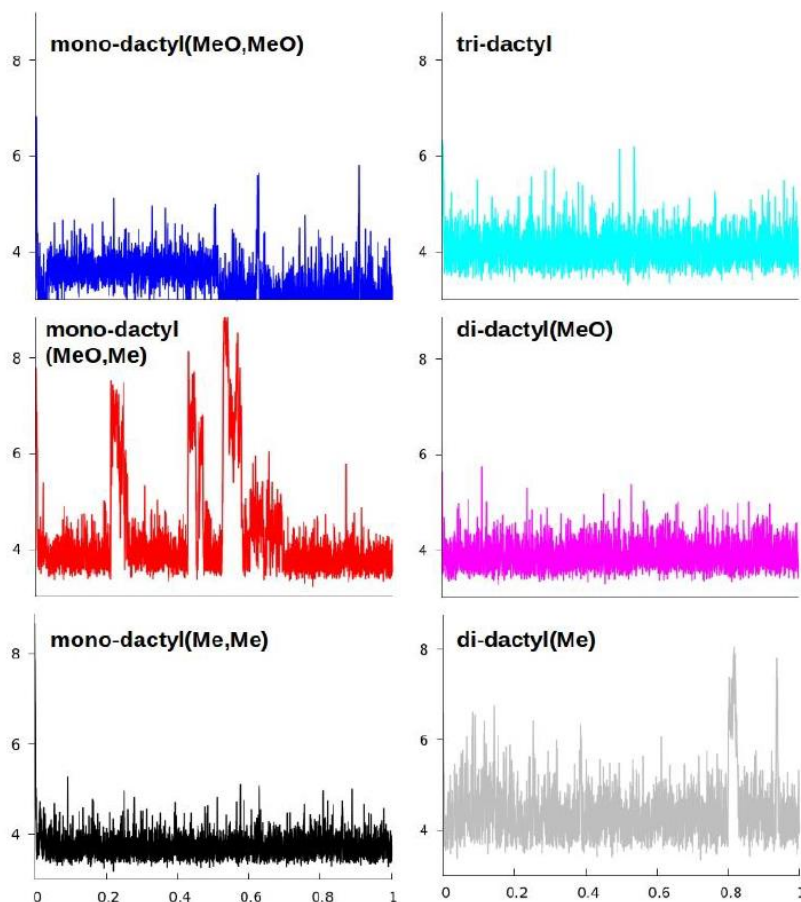


Figure 7.14. Time (ns) evolution of the Sulphur-silica surface distance (Å) for the six hybrid models.

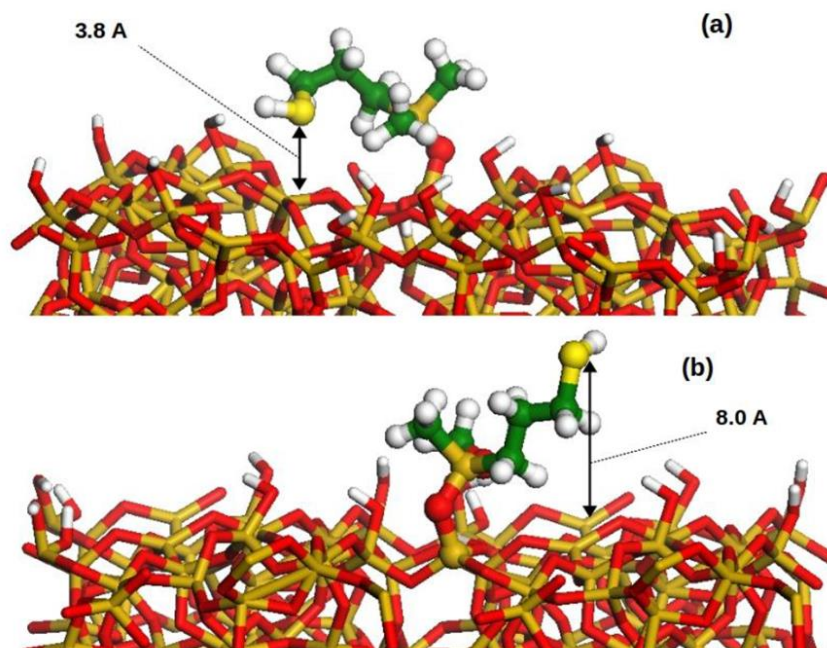


Figure 7.15. Snapshot of MD simulations of (a) mono-dactyl(Me,Me) with the organic chain laying close to the surface, (b) mono-dactyl(MeO,Me) with the chain in an extended conformation.

respectively. Referring to the snapshots extracted from the dynamics, reported in Figure 7.15 to facilitate the interpretation of the time evolution graphs, it is possible to notice that a distance around 4 \AA or below relates to a structure strongly bent and close to the surface (panel a), whereas in a standing, extended structure the sulphur-silica distance can reach $8\text{--}9 \text{ \AA}$ (panel b).

Table 7.3. Average sulfur-silica surface distance and standard deviation during the MD simulations of hybrid materials.

Hybrid structures	Average distance (\pm stdev)/ \AA
tri-dactyl	4.09 (\pm 0.35)
di-dactyl(MeO)	3.90 (\pm 0.29)
di-dactyl(Me)	4.42 (\pm 0.63)
mono-dactyl(MeO,MeO)	3.42 (\pm 0.44)
mono-dactyl(MeO,Me)	4.29 (\pm 1.05)
mono-dactyl(Me,Me)	3.75 (\pm 0.03)

Molecular dynamics results highlighted that silicodactyly *in se* plays a marginal role in determining the average hybrid conformations: tri-dactyl (triMeO-MCM-41 hybrid), di-dactyl(MeO) (triMeO-MCM-41) and two mono-dactyl (mono-dactyl(Me,Me) (MeO-MCM-41) and mono-dactyl(MeO,MeO) (triMeO-MCM-41)) structures laid close to the surface for all the simulations, with average distances in the 3.4–4.1 Å range. Specifically, monodactyl(MeO,MeO) spent half of the time very close to the silica surface, with distances around 3 Å. In contrast, di-dactyl(Me) (diMeO-MCM-41 hybrid) was susceptible of a stronger oscillation, spending most of the time with a sulphur-surface distance of 4.5 Å. Mono-dactyl(MeO,Me) (diMeO-MCM-41 hybrid) was found to be the most mobile system, the only one observed several times in an extended conformation. Although the average distance for this structure is not the largest, it is associated with the highest standard deviation, accounting for the different conformations sampled in the dynamics.

Classical molecular dynamics calculations revealed that dispersion forces (included in the force field through a 6–12 Lennard-Jones term) have a stronger contribution to the organosilane-surface interaction energy, with respect to H-bonds between silanols and chain oxygen or sulphur atoms. The latter effect is expected to become more significant as the density of silanols on the silica surface, together with the hydrophilicity of MCM-41, increases. No relevant differences between methoxy and methyl groups were detected, with respect to the tendency of the organic moiety to interact with the silica surface. Both the dandling groups showed steric effects during MD simulations, and methoxy groups sometimes were engaged in loose hydrogen bonds with silanols, but this interaction does not seem to correlate with the chain conformation.

7.1.3 Conclusions on silicodactyly

Through a combined experimental and computational approach, the influence of silicodactyly in the designing and engineering of hybrid catalysts with accessible organic active sites has been elucidated.

Experimental and computational data have highlighted that the number of the siloxane bridges, which the (3-mercapto)alkoxysilane can form with the silica surface, are strictly correlated with the number of hydrolysable alkoxy groups (dactyly) of the organosilane and with the silanol density of the silica support. Specifically, a one to one correspondence between the number of hydrolysable alkoxy moieties and the number of siloxane bridges is not guaranteed, especially for low silanol density inorganic supports. In this respect, solid state NMR analyses evidenced that the grafting mechanism for diMeO-MCM-41 hybrid, bearing two hydrolysable methoxy groups, has preferentially occurred in a mono-dentate manner, whereas the trifunctional alkoxysilane has preferentially reacted to form a mono- or bi-dentate adduct, with the di-dactyl system more prevalent than the mono-dactyl, with a very low fraction of tri-dentate grafted organosilane. Moreover, molecular dynamics calculations have also highlighted the difficulty in modelling the tri-dentate adduct, unless the condensation reaction occurs with geminal silanols. Consequently, to obtain a higher concentration of tri-dactyl systems, a more hydrophilic silica surface is recommended.

TGA and variable temperature FT-IR analyses have emphasized a correlation between the number of siloxane bridges actually formed and the thermal stability of the organic moiety, with mono-dentate adducts being decomposed at lower temperatures than di- and tri-dactyl systems. On the basis of these considerations and with the aim of preventing the leaching of the organic counterpart, alkoxysilanes bearing two or three hydrolysable moieties should be preferred to mono-dactyl adducts.

Finally, regardless of the particular silicodactyly of the organosilane, molecular dynamics simulations have clearly predicted the tendency of (3-mercapto)alkoxysilane derivatives to lay on the silica surface, with the largest contribution to the molecule-surface interaction energy coming from dispersion forces. This relevant aspect should be primarily taken into account when designing an active hybrid catalyst.

7.2 Influence of silicopodality

With the aim of elucidating the role of silicopodality (number of alkylsilane chains through which a catalytic organic active site is linked to a silica surface) in determining the final conformation of the organosilane with respect to the silica surface, different pyridine derivatives, with fixed di-dactyly and variable podality, were grafted onto an ordered mesoporous MCM-41 (Figure 7.16). Concerning the dactyly, tri-dactyl structures were not considered since it has been proved that the formation of three siloxane bridges from three hydrolysable alkoxy groups is statistically unlikely, unless a very hydrophilic silica is used. Mono-dactyl systems were excluded since the linkage via one siloxane bridge is easily susceptible to leaching. Anyway, in the previous section it has already been shown that the organo-inorganic interface conformation is not much affected by the silicodactyly parameter.^[11] A pyridine derivative was chosen since pyridine (Py) is a useful basic probe to assess whether or not an interaction between this catalytic active centre and the silica surface exists. In fact, hydrogen bonding interactions between Py and Si–OH groups can be easily detected through FT-IR and NMR spectroscopies.^[29,34-36] Thus, by coupling an experimental multi-technique approach with a predictive computational modelling, a deeper insight in the organo-silica interface was gained.

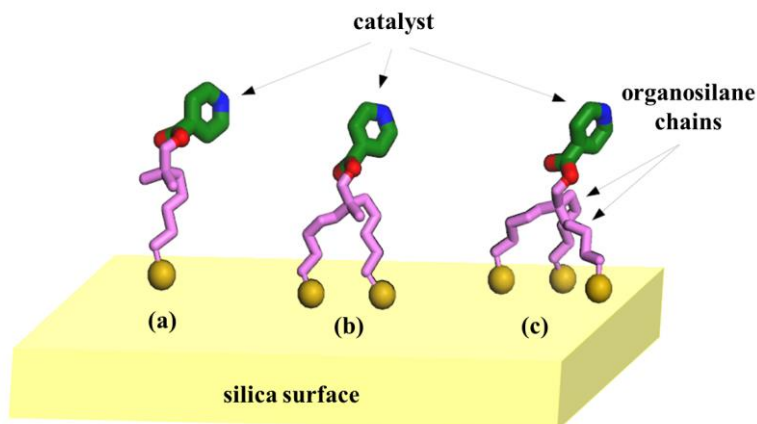


Figure 7.16. Scheme of possible architectures obtained varying the number of alkylsilane chains: (a) monopodal, (b) dipodal and (c) tripodal system.

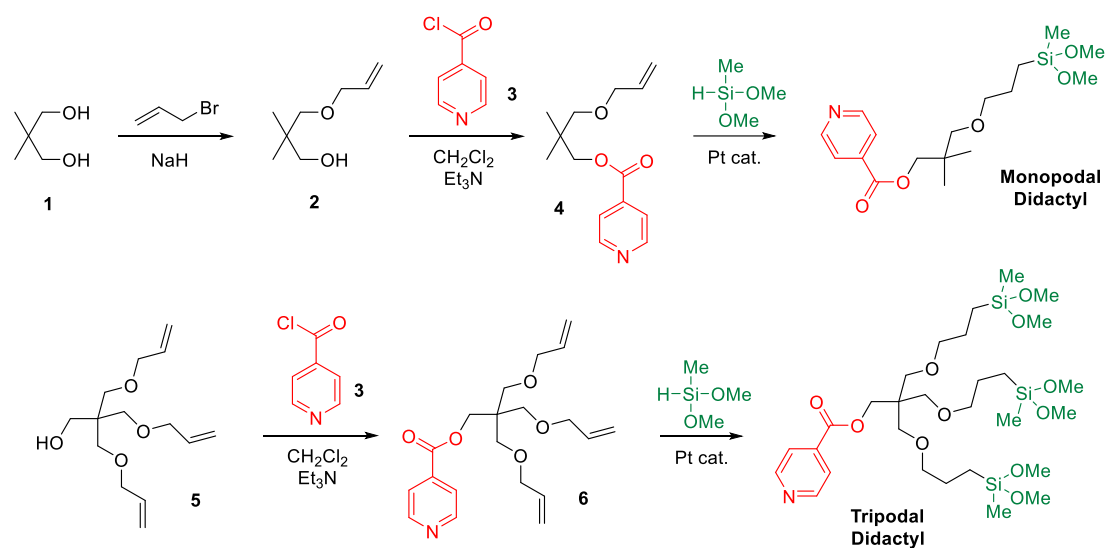
7.2.1 Experimental section

7.2.1.1 General

MCM-41, reagents and solvents were purchased from Sigma-Aldrich and used as received. Pyridine derivatives were prepared by CAGE Chemicals S.r.l.

7.2.1.2 7.2.1.3 Synthesis of multipodal pyridine derivatives

The monopodal and dipodal derivatives, with silicodactyl fixed at didactyl were prepared, with a pyridine residue as the molecular probe. The preparation of these derivatives is summarized in Scheme 7.1.



Scheme 7.1. Scheme of the synthesis strategy to obtain the multipodal didactyl systems.

The commercially available polyols 2,2-dimethyl-1,3-propanediol **1** was used as the starting materials for the monopodal and dipodal derivatives. Monoallylation of **1** was accomplished through a classic Williamson synthesis, by treating a THF solution of the polyol with sodium hydride, followed by reaction with allyl bromide. Separation of the monoallyl derivative **2** from variously allylated derivatives was obtained by column chromatography. Triallylpentaerythritol **5** is the starting material for the preparation of the tripodal derivative. It is commercially available as a mixture of allylated pentarhythritols, enriched in the triallyl derivative (assay

~70%), from which the pure **5** may be obtained by simple displacement chromatography. The pyridine ring was introduced in the structure through an esterification, taking advantage of the purposefully residual alcoholic group in each of the allylated derivatives. Isonicotinic acid was activated by conversion into the corresponding acid chloride **3**, isolated as the hygroscopic crystalline hydrochloride. Reaction of **3** with the allylated derivatives **2** and **5** provided the corresponding esters **4** and **6**, respectively. Then, each of the mono-, di- and tripodal esters was hydrosilylated with methyldimethoxysilane. The latter reacts with alkenes in the presence of a platinum catalyst (Karstedt catalyst was used), adding to the double bond with anti-Markovnikov selectivity, and leading to the introduction of the didactyl reactive silicon-based functional group and leading to the monopodal and tripodal didactyl derivatives.

7.2.1.3 Synthesis of hybrid materials

Hybrid materials were synthesised *via* post-synthesis grafting with pyridine 4-substituted derivatives. MCM-41 (0.3 g), dried overnight at 100 °C, was suspended in dry toluene (30 mL). The suspension was heated at 120 °C under stirring. Pyridine derivatives (mmol) were then added dropwise the mixture was refluxed for 18 h. The reaction solution was filtered and washed with toluene, ethanol and deionized water. The obtained white solid was cured in air at 80°C overnight.

7.2.1.4 Characterization

Before recording FT-IR and solid NMR spectra, all the samples were outgassed at 200°C for 1h. Further details on the experimental techniques are reported in Chapter 9/Experimental section.

7.2.1.5 Computational details

Design of the models: the structures of pyridine 4-substituted derivatives, with a variable number of leg(s), were grafted on a silica surface (slab) with density 2.4 OH/nm². The atomic structure, the thickness, the horizontal and vertical dimensions

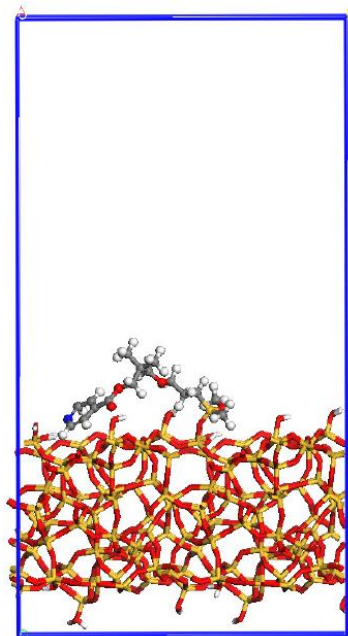


Figure 7.17. Simulation box containing one monopodal pyridine 4-substituted derivatives anchored on a slab silica.

of the slab employed are the ones described in Paragraph 7.1.1.5. In Figure 7.17, one example of simulation box is reported.

General settings of molecular dynamics: starting configurations of the molecular dynamics were obtained performing partial energy minimization to adjust atom coordinates in the box. Only atomic position of pyridine 4-substituted derivatives together with oxygen and silicon atoms of the slab directly bonded to these have been minimize, while the remaining atoms were kept fixed. TIP3P model of Price *et al.*^[37] was employed to simulate the solvent effect on the arrangement of the catalyst on silica slab, fixing atomic parameters of water molecule by SHAKE procedure.^[38] Conjugate Gradients algorithm and QEq charge equilibration method were used with the same specification reported in Paragraph 7.1.1.5. Coulombic and Van der Waals interactions were computed with the same procedure described in Paragraph 7.1.1.5. Molecular dynamics simulations were performed in canonical (n,V,T) ensemble in vacuum at 298 K (using Langevin thermostat to maintain the temperature constant)^[18] for 1 ns using the LAMMPS simulation package.^[19]

7.2.2 Results and discussion

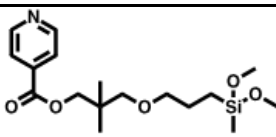
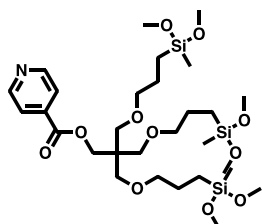
7.2.2.1 Hybrid structures

Two different di-dactyl pyridine 4-substituted derivatives, bearing different number of alkylsilane chains (one or three), were anchored on an ordered mesoporous silica MCM-41. In order to promote homogeneous distribution of the silylation agents and to prevent island-type grafting, the anchoring procedure was carried out in a non-polar solvent (toluene) and clean inorganic surface.^[20] The acronyms of the hybrid materials and chemical structures of pyridine derivatives are reported in Table 7.4.

7.2.2.2 XRD and TGA analyses

To confirm the retention of structural properties of the inorganic silica support upon the grafting procedure, X-Ray powder diffraction was performed on hybrid materials and plain MCM-41 (Figure 7.18). Notably, all hybrids showed all the characteristic reflections of plain hexagonally-ordered MCM-41,^[21] though lowered in intensity as a result of a partial loss of structural order upon the anchoring procedure.

Table 7.4. Acronyms of hybrid materials and chemical structure of pyridine derivatives.

Acronyms	Chemical structure of pyridine derivative grafted on MCM-41	Podality
Py-MP-MCM-41		Monopodal
Py-TP-MCM-41		Tripodal

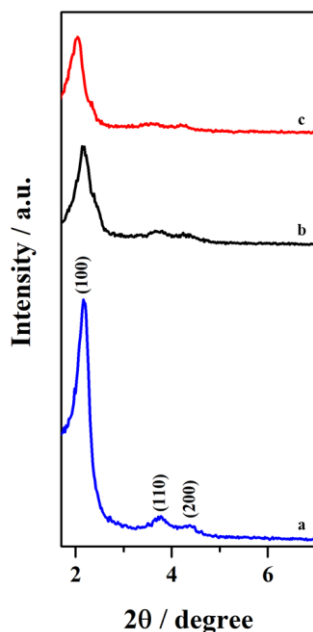


Figure 7.18. The powder XRD pattern of a) plain MCM-41 (blue curve), b) Py-MP-MCM-41 (black curve) and c) Py-TP-MCM-41 (red curve).

Thermogravimetric analysis was performed to determine the thermal stability of grafted pyridine 4-substituted derivatives and to gain insight in the organic content and hydrophobic/hydrophilic nature of the resulting hybrid materials. Thermograms and derivatives (Figure 7.19 A and B) of both hybrid materials and plain MCM-41 showed a first weight loss, in the range 30-150°C, ascribable to the removal of physisorbed water. In particular, Py-TP-MCM-41 exhibited a slightly higher weight loss due to the removal of weakly bonded water compared to Py-MP-MCM-41 and plain MCM-41, meaning a higher hydrophilic character of tripodal functionalized hybrid material. At higher temperature, a second weight loss at around 350-550 °C, attributed to the decomposition of grafted pyridine derivatives, was detected for both the hybrid materials. Specifically, Py-MP-MCM-41 revealed a slightly higher loss of organic content with respect to Py-TP-MCM-41. Moreover, DTG curve of Py-MP-MCM-41 highlighted two different weight loss, at 380 and 465 °C, whilst for Py-TP-MCM-41 only a single contribution, centred at 465 °C, was detected. A possible explanation for this behaviour might be that, being equal the weight loading

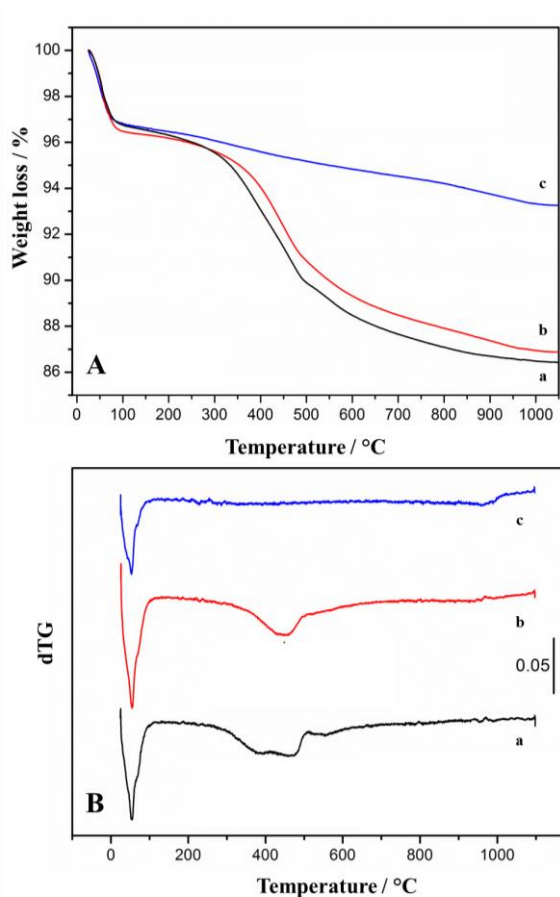


Figure 7.19. A) TGA and B) DTG curves of Py-MP-MCM-41 (a, black curve), Py-TP-MCM-41 (b, red curve) and plain MCM-41 (c, green curve).

of the grafting agent and greater the number of legs of the tripodal system compared to the monopodal, Py-TP-MCM-41 will expose a lower number of pyridine active sites. Thus, in Py-MP-MCM-41 two contributions, assigned at lower temperature to the decomposition of the catalytic head, and at higher temperature to the decomposition of the remaining organosilane, can be distinguished, whereas only an average weight loss for Py-TP-MCM-41 hybrid can be appreciated.

7.2.2.3 FT-IR spectroscopy

FT-IR spectra of Py-MP-MCM-41 and Py-TP-MCM-41 hybrids were recorder in order to provide confirmation of successful grafting of pyridine 4-substituted derivatives on MCM-41 and compared (Figure 7.20 A and B). In the high frequency

region ($4000\text{-}2700\text{ cm}^{-1}$), the FT-IR spectra of Py-MP-MCM-41 and Py-TP-MCM-41 hybrids (Figure 7.20 A) showed a weak band at 3745 cm^{-1} and a broad absorption between 3700 and 2500 cm^{-1} , which can be assigned to the O–H stretching mode of isolated residual silanols and to hydrogen-bonding interactions between surface groups^[22], respectively. In the region $3100\text{-}3000\text{ cm}^{-1}$, aromatic C–H stretching vibrations were detected with very low intensity (Figure 7.20 A, inset). Between 3000 and 2800 cm^{-1} , signals due to C–H stretching modes of methyl and methylene groups of pyridine 4-substituted derivatives were recorded. Particularly, bands at 2962 cm^{-1} and 2872 cm^{-1} are assigned to the asymmetric and symmetric methyl C–H stretching vibrations, whereas signals at 2926 cm^{-1} and 2853 cm^{-1} are related to ν_{asym} and ν_{sym} modes of CH_2 groups of the alkyl chains. In the low frequency region ($1800\text{-}1300\text{ cm}^{-1}$), the FT-IR spectra of hybrid materials (Figure 7.20 B) exhibited C=O stretching mode in the range $1722\text{-}1750\text{ cm}^{-1}$. Notably, for Py-MP-MCM-41 hybrid, this band is characterized by a main contribution at 1722 cm^{-1} , with a weak shoulder at 1749 cm^{-1} . Conversely, in the spectrum of Py-TP-MCM-41, two components of equal intensity were detected at 1722 cm^{-1} and 1749 cm^{-1} . Between 1600 and 1400 cm^{-1} , the spectra of both hybrid materials revealed characteristic C–C aromatic ring vibrations. Specifically, ν_{8a} , ν_{8b} and ν_{19b} were detected at 1608 cm^{-1} , 1566 cm^{-1} and 1414 cm^{-1} , respectively.^[39-41] Moreover, bands due to the C–H bending vibrations were also identified between 1480 and 1300 cm^{-1} . In particular, in the region $1470\text{-}1440\text{ cm}^{-1}$, overlapping of bands related to asymmetric deformation modes of $\text{CH}_3\text{-C}$ (1460 cm^{-1}), symmetric deformation mode of $\text{CH}_3\text{-O}$ (1455 cm^{-1}) and scissoring of CH_2 groups (1450 cm^{-1}) made the assignment difficult.^[23] Conversely, signal due to symmetric bending modes of $\text{CH}_3\text{-C}$ was detected at 1378 cm^{-1} , whereas band at 1328 cm^{-1} can be assigned to C–H in plane deformation of aromatic ring.^[42] Finally, symmetric bending vibration of $\text{CH}_3\text{-Si}$ groups (1255 cm^{-1}), together with C–O–C stretching modes (1280 cm^{-1} and 1100 cm^{-1}) could not be detected in the spectra of hybrid materials since they fall beneath the

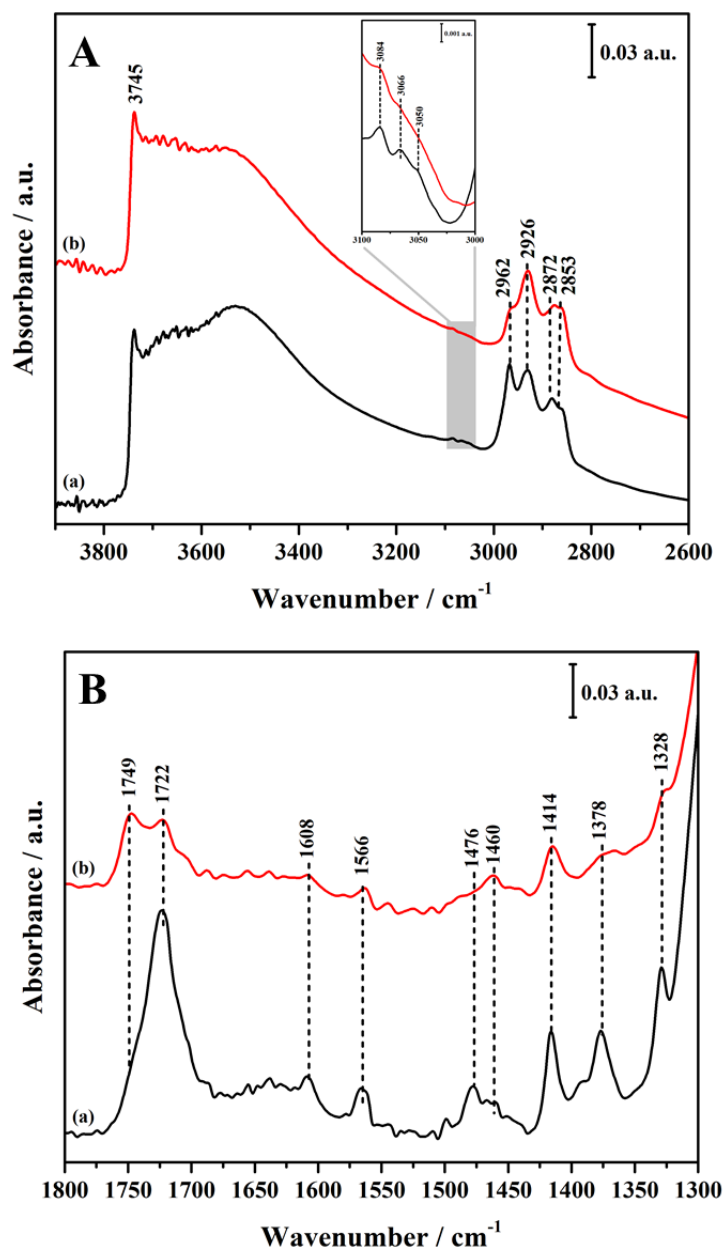


Figure 7.20. FT-IR spectra Py-MP-MCM-41 (a, black curve), Py-TP-MCM-41 (b, red curve) in the region A) 4000–2600 cm^{-1} , with inset between 3100 cm^{-1} and 3000 cm^{-1} , and B) 1800–1300 cm^{-1} .

broad and intense absorption in the region 1250–1000 cm^{-1} , attributed to the asymmetric stretching modes of Si–O–Si of the silica framework.^[43]

With the aim of gaining insight in the nature of organic-inorganic interface after the anchoring procedure, FT-IR spectra of Py-MP-MCM-41 and Py-TP-MCM-41 hybrids were compared with the ones of pyridine 4-substituted derivatives adsorbed in MCM-41 and diluted in KBr (Figure 7.21 A, B, C, D). Upon the grafting procedure, signals attributed to vibrational frequencies of the organic derivatives were shifted to higher frequencies, stating a variation of the chemical environment which pyridine derivatives are affected by, thus confirming a successful anchoring on the silica support. Notably, a shift of some of the vibrational modes can also be appreciated in the spectrum of organic derivatives adsorbed in MCM-41, indicating that confinement effect and dispersion forces in determining their frequency values. Interestingly, both the spectra of pyridine 4-substituted derivatives impregnated in MCM-41 and diluted in KBr exhibited a single band for C=O stretching mode at 1733 cm^{-1} (Figure 7.21 A and C). Conversely, $\nu_{\text{C=O}}$ signal is split into two components in the spectra of Py-MP-MCM-41 and Py-TP-MCM-41 hybrids, with the former characterized by a weak shoulder at 1749 cm^{-1} , associated with the main peak at 1722 cm^{-1} , the latter composed of two distinct signals of equal intensity. This experimental evidence may be explained by hypothesizing two prevailing conformations of the organic molecules with respect to the inorganic surface, one in which the molecule is able to stick out from the surface ($\nu_{\text{C=O}}$ detected at higher frequency, 1749 cm^{-1}), the other resulting in hydrogen-bonding interaction between C=O groups and Si-OH groups of silica support or physisorbed water ($\nu_{\text{C=O}}$ shifted at lower frequency, 1722 cm^{-1}).^[23] Notably, the number of organic derivatives interacting with physisorbed water is lower for the tripodal hybrid than for the monopodal, thus emphasizing a correlation between the number of legs and the tendency of the pyridine derivative to lay on the surface. Finally, it should be possible to assert whether or not an interaction *via* hydrogen bonding occurs between the nitrogen of the pyridine ring and surface silanols, by evaluating the perturbation of C-C aromatic ring stretching vibrations of pyridine derivatives upon grafting on MCM-41.^[34-35] Although frequency shifts of ν_{8a} , ν_{8b} and ν_{19b} modes were found to

be consistent with this hypothesis of H-bonding interaction, since upon grafting a similar shift towards higher wavenumber can be detected for all signals related to organic molecule, it has not been possible to exclude that the perturbation of C-C ring vibrations, especially for ν_{8b} and ν_{19b} modes, was just ascribable to a changing in the chemical environment of the grafted organic moieties due to the anchoring procedure or to a combined effect.

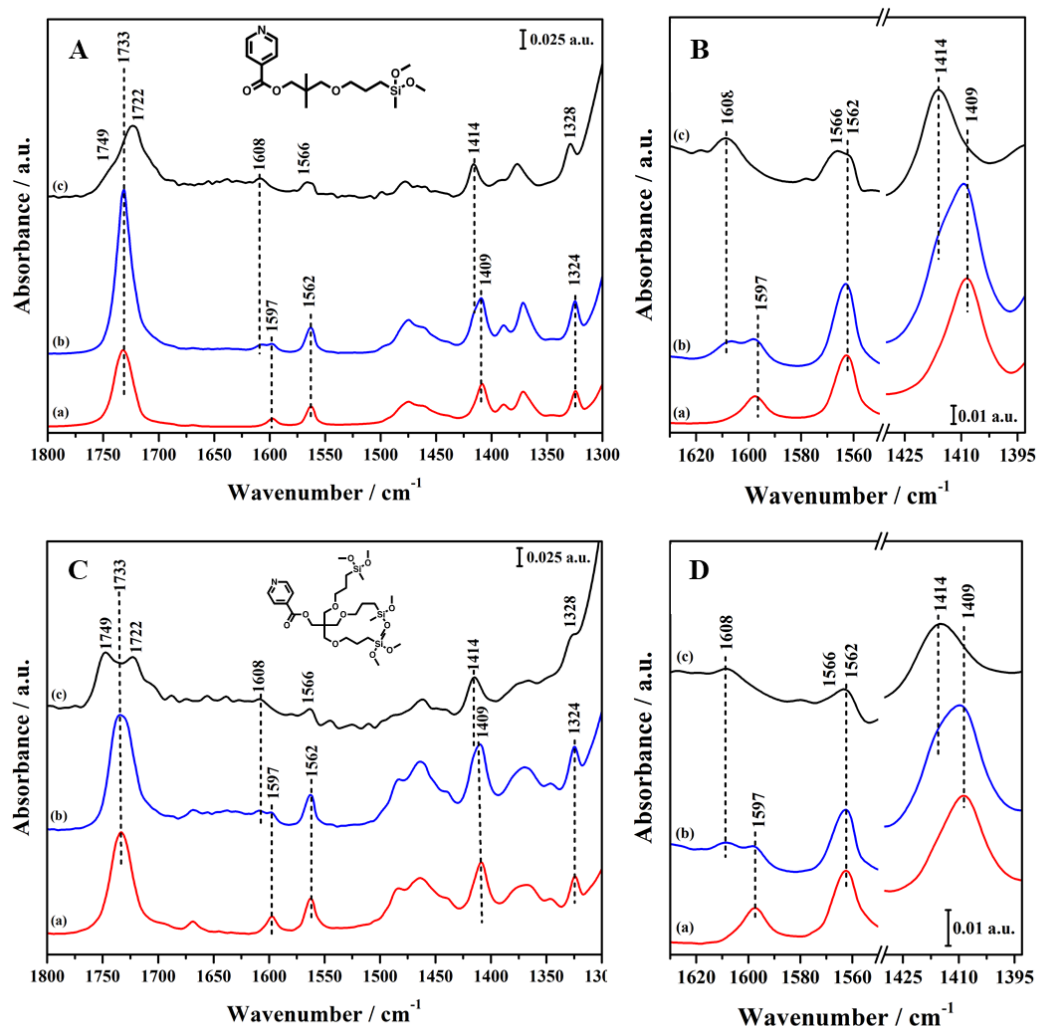


Figure 7.21. FT-IR spectra of pyridine derivatives diluted in KBr (a, red curve), MCM-41 impregnated with pyridine 4-substituted derivatives (b, blue curve) and (A,B) Py-MP-MCM-41, (C,D) Py-TP-MCM-41 (c, black curve). Magnifications in the C-C ring stretching vibrations region is also provided (B,D).

FT-IR spectroscopy at variable temperature was performed to investigate the thermal stability of the grafted pyridine 4-substituted derivatives (Figure 7.22-7.23). Assignment of the detected signals has already been provided in the first section of the present paragraph. By increasing the outgassing temperature from 30 °C to 500 °C, the intensity of the broad absorption between 3700 and 2500 cm^{-1} gradually decreased, indicating the removal of physisorbed water (30-150 °C) and the progressive weakening of hydrogen-bonding interactions between surface Si-OH groups (150-500 °C). In accordance with TGA/DTG analyses, the gradual decomposition of the organic grafted moieties, which can be monitored by following the progressive decrease of IR intensities of vibrational modes related to pyridine 4-substituted derivatives (aliphatic ν_{CH_3} , ν_{CH_2} between 3000-2800 cm^{-1} , $\nu_{\text{C=O}}$ between 1700-1750 cm^{-1} , ν_{8a} , ν_{8b} and ν_{19b} in the region 1610-1400 cm^{-1} , CH_2 and CH_3 bending modes between 1470-1300 cm^{-1}) started at ca. 300°C and was almost completed at 450 °C for both Py-MP-MCM-41 and Py-TP-MCM-41 hybrids. Interestingly, as the outgassing temperature increased, the intensity of $\nu_{\text{C=O}}$ component at 1722 cm^{-1}

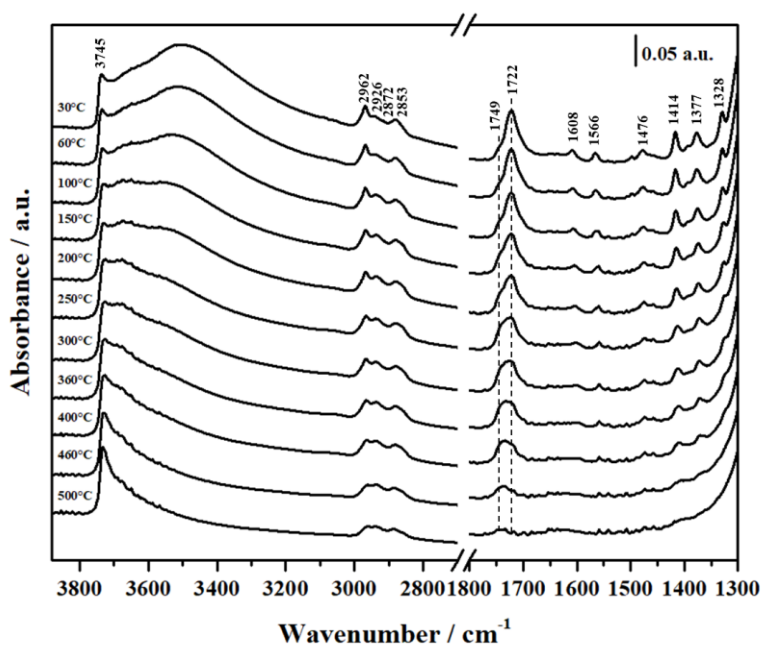


Figure 7.22. Variable temperature FT-IR spectra of Py-MP-MCM-41.

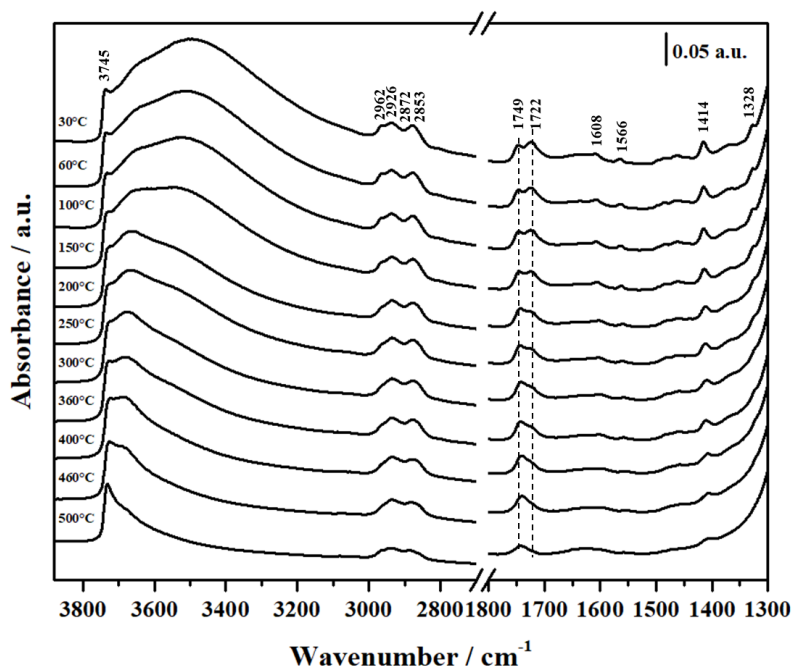


Figure 7.23. Variable temperature FT-IR spectra of Py-TP-MCM-41.

gradually decreased, while the contribution at 1749 cm^{-1} became predominant in both the spectra of hybrid materials. A possible explanation for this behaviour, in agreement with previous observations, might be that, by increasing the thermal agitation, H-bonding interactions are progressively weakened, with extended conformations of the organic moieties becoming favourable with respect to the ones close to silica surface.

7.2.2.4 Solid state NMR spectroscopy

^{13}C and ^{29}Si CPMAS NMR spectroscopies were performed to further confirm successful organosilane functionalization and getting a deeper insight on the grafted mechanism of attached pyridine 4-substituted derivatives (Figure 7.24). ^{29}Si CPMAS NMR can be used to provide information on surface silicon environments, by referring to ^{29}Si isotropic chemical shifts of tetrahedrally coordinated silicon atoms (Figure 7.24 A). Both Py-MP-MCM-41 and Py-TP-MCM-41 hybrids exhibited Q^4 , Q^3 and Q^2 resonance peaks at -110 , -101 and -91 ppm, related to MCM-41 inorganic

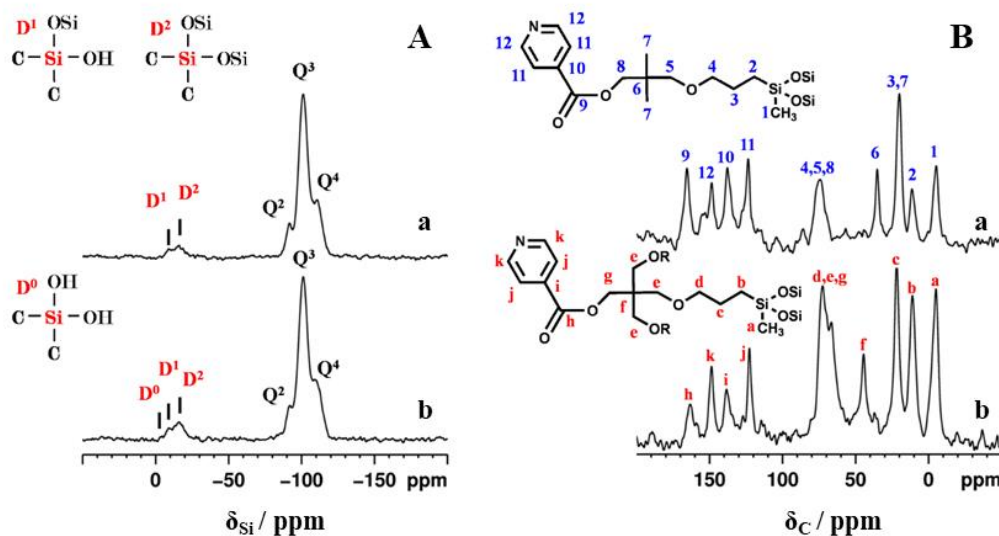


Figure 7.24. A) ^{29}Si and B) ^{13}C CPMAS NMR spectra and of Py-MP-MCM-41 (curve a) and Py-TP-MCM-41 (curve b).

support.^[29,31] In accordance with previous study on silicodactyl^[11], upon grafting, both di-dactyl monosilane and trisilane functionalized materials showed D^1 and D^2 signals, at ca. -9 and -16 ppm respectively, with D^2 resonances more intense than D^1 , suggesting that the condensation of pyridine derivatives has preferentially occurred forming bi-dentate adducts. In addition, for Py-TP-MCM-41 sample, D^0 signal, due to non-condensed organosilane Si sites, was detected at around -3 ppm with low intensity, meaning the presence, for the tripodal system, of a few legs not anchored to the silica surface.

The integrity of pyridine 4-substituted derivatives after functionalization was assessed by ^{13}C CPMAS NMR spectroscopy (Figure 7.24 B). The assignment of resonance peaks was carried out with the support of liquid-state ^{13}C NMR spectra. In both Py-MP-MCM-41 and Py-TP-MCM-41 hybrids, ^{13}C resonance signals can be clearly attributed to the organosilane units, demonstrating the integrity of organic pendent groups as well as the success of the grafting procedure. Notably, a close examination of the spectra revealed that certain ^{13}C nuclei displayed multiple peaks associated with different environments, specifically, carbon in position 12 in Py-MP-MCM-41 (curve a) and carbon in position h in Py-TP-MCM-41 (curve b).

^1H NMR spectroscopy was performed to probe proton environments and to provide additional information on the nature of organic-inorganic interface, with particular emphasis on clarifying if an interaction between the organic pendent groups and surface silanols and/or physisorbed water might occur. The NMR spectra were recorded on pristine as well as vacuum treated samples (Figure 7.25 A and B) and the spectral deconvolution has been applied to separate the resonances originating from organic pendant groups and MCM-41. ^1H NMR spectra of Py-MP-MCM-41 (panel A) and Py-TP-MCM-41 (panel B) hybrids revealed multiple environments for proton associated to organic pendant groups and to MCM-41. The pristine Py-MP-MCM-41 showed narrow resonances due to organic pendant groups while broad resonances were associated with MCM-41. The most intense peak in both pristine samples was in the range 3.5 to 4.0 ppm and can be attributed to

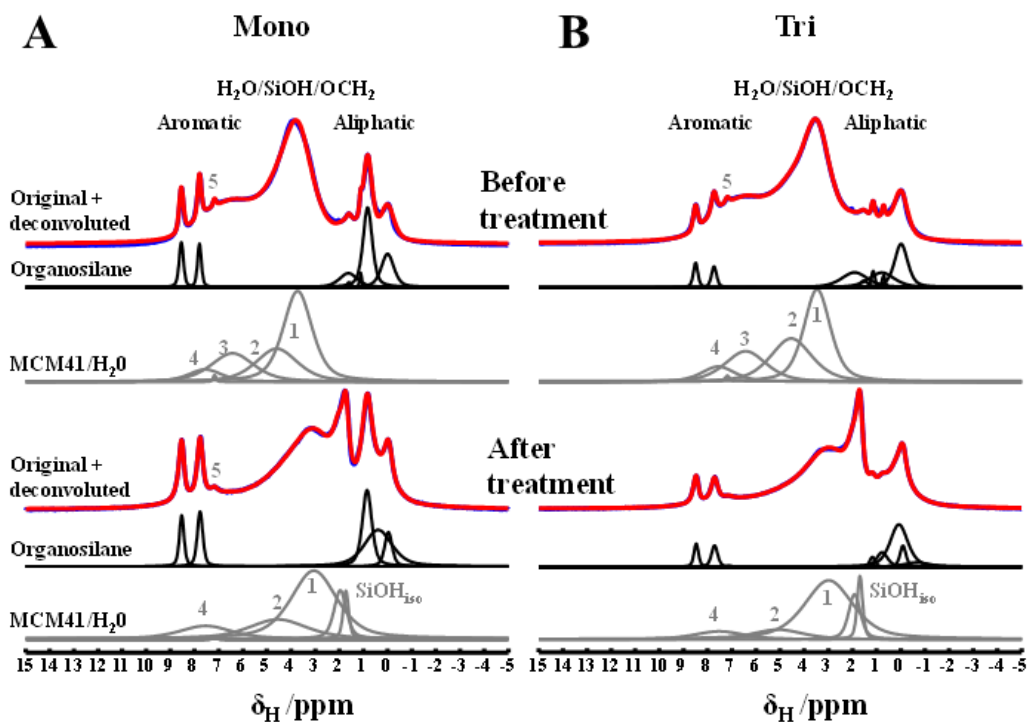


Figure 7.25. ^1H NMR spectra of A) Py-MP-MCM-41 and B) Py-TP-MCM-41 hybrids. Deconvoluted spectra are shown to distinguish the contribution of pyridine derivatives and MCM-41.

physisorbed water, hydrogen bonded silanols and O-CH₂ moieties from the organosilanes. A narrow resonance peak at around 0 ppm was also visible in both samples and was due to methyl protons directly bonded to silicon atom of organosilanes. Additional resonances were also visible in the aliphatic region due to organosilanes. Two broad signals in the range 3-6 ppm (marked as 1 and 2) were due to physisorbed water and hydrogen bonded silanols. Interestingly, two additional broad resonances (marked as 3 and 4) appeared in the range 5-9 ppm and are attributed to silanols interacting with the pyridine nitrogen.^[44,45] Besides the two intense narrow aromatic peaks at 7.8 and 8.5 ppm from pyridine units, an additional sharp signal at 7.2 ppm was also detected (marked as 5) in this sample whose assignment is not straight forward. However, upon thermal treatment of pristine Py-MP-MCM-41 sample under vacuum the broad peak (marked as 3), associated to silanols interacting with the pyridine nitrogen, disappeared and concomitantly additional resonances appeared at around 1.8 ppm and are attributed to isolated silanols. More importantly, not all interacting silanols become isolated ones upon the mild thermal treatment (see peaks 4 and 5) highlighting the strong organic pendent group-surface silanol interactions through the pyridine nitrogen, probably assisted by water molecules. The sharp peak at 7.2 ppm could arise from the interaction of carbonyl carbon with either silanols or water molecules as has been pointed out in the FT-IR data. Summarising, pristine Py-MP-MCM-41 contains some adsorbed water, which interacts with the silanol groups and organo-pyridine units. In addition, proton resonance peaks appeared as sub-resonance broad peaks separated from the main signals, suggests the existence of pyridine groups residing on the silica surface in different environments, interacting with Si-OH groups. A comparable behaviour by anchored organo-silanes on mesoporous silica has been reported in the past.^[22]

A similar ¹H MAS NMR spectrum (Figure 7.25 B) was displayed by pristine Py-TP-MCM-41 sample except the fact that the amplitude of the organosilane signals were lower intense than in the previous sample. Interestingly, ¹H MAS NMR spectrum of Py-TP-MCM-41, after thermal treatment under vacuum, also showed

the generation of peaks associated to isolated silanols. However, the intensity of the broad sub-resonance, associated to the strong interactions between silanols and pyridine nitrogen (peak 4, after thermal treatment), was much lower suggesting an extended organosilane conformation (away from the surface) for majority of the anchored tripodal derivatives.

In order to establish the nature of the protons responsible for sub-resonance peaks detected in Py-MP-MCM-41 hybrid, ^1H NMR spectra were recorded upon exchange with D_2O (Figure 7.26 A and B). It is noteworthy that only protons from water molecules and from Si–OH residing on silica surface are exchangeable, whereas protons of organic moieties are not. In accordance with FT-IR findings, disappearance of sub-resonance peaks upon deuteration confirmed a dependence of these signals on exchangeable protons of water molecules and silanols, thus confirming the tendency of the monopodal hybrid to lay on the silica surface, especially upon solvation. Conversely, the absence of resonance signals in Py-TP-MCM-41 hybrid suggested an extended conformation for the majority of anchored tripodal derivatives even upon solvation. Furthermore, the true identities of the protons interacting with pyridine nitrogen were confirmed by recording a ^1H MAS

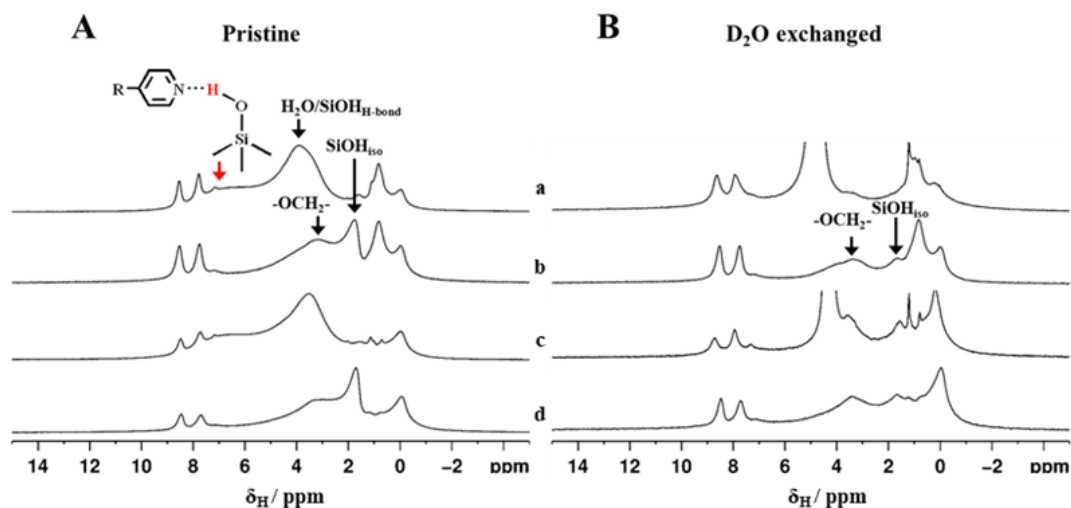


Figure 7.26. ^1H NMR spectra of Py-MP-MCM-41 (a,b) and Py-TP-MCM-41 (c,d) hybrids A) before and B) after performing exchange with D_2O .

spectra with pre-saturating the water signal. The notion behind such a technique is to selectively saturate the water signal before the excitation of the organosilane and silanol protons and subsequent acquisition of their signals. The saturation can be spread to labile protons in the system via chemical exchange by propagating through the spin system by spin diffusion and all protons associated with water molecules as well as those in exchange with them will not be detected in the spectrum. In fact, the broad resonance peaks in the range 5-9 ppm associated to silanols interacting with the pyridine nitrogen remained in the spectra of both samples confirming the organic-inorganic interface interactions.

7.2.2.5 Computational modeling

Classical molecular dynamics calculations were used to investigate at atomistic scale the nature of organic-inorganic interface. Bearing in mind ^{29}Si CP MAS NMR results on different dactyly configurations, four different models were prepared, corresponding to the structures illustrated in Figure 7.27. By referring to the nomenclature proposed for dactyly^[11], two structures can be classified as di-dactyl(Me), the other two as mono-dactyl(MeO,Me), indicating in parenthesis the

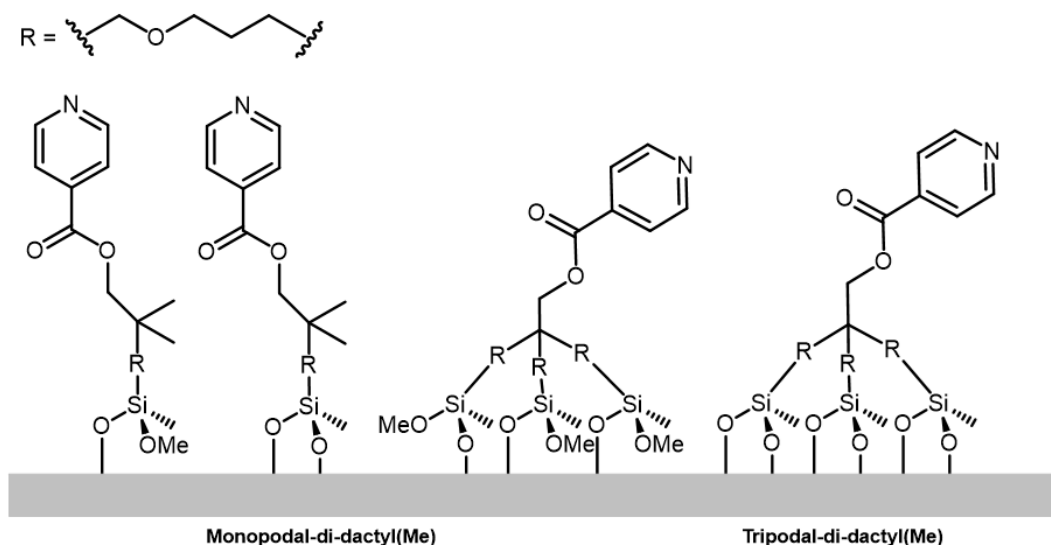


Figure 7.27. Structure of the models of multipodal pyridine derivatives. The name at the bottom evidences the podality and the dactyly of the particular configuration, as well as the nature of the non-grafted dangling groups.

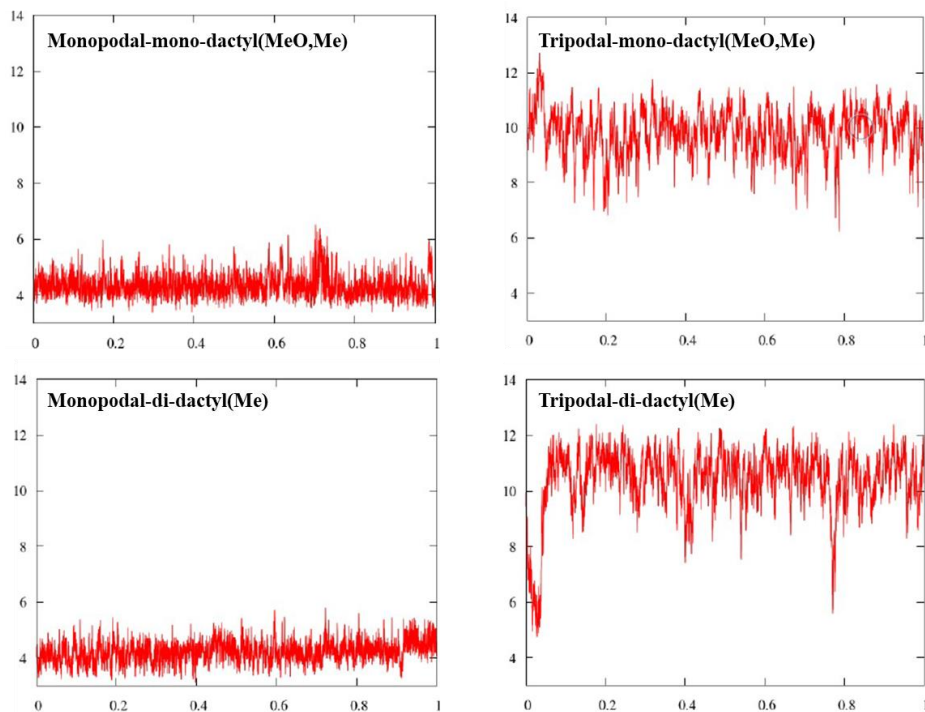


Figure 7.28. Time (ns) evolution of the pyridine-silica surface distance (\AA) for the four hybrid models.

dangling groups remaining unbound. Tri-dactyl adducts were not considered since the formation of three siloxane bridges by a single chain is energetically unlikely, unless a very hydrophilic silica is used. Then preliminary 1ns MD runs at 298 K in vacuum were performed for each model, after suitable thermalization cycles. During the simulations, the distance between nitrogen atom of pyridine derivatives and MCM-41 surface was monitored, in order to evaluate the tendency of the organic chain to lie on the surface. The time evolution of the nitrogen-surface distance for the four hybrid models are reported in Figure 8.28. It should be stressed that a distance around 4 \AA or below indicates a structure strongly bent and close to the surface, whereas in a non-interacting, extended structure the nitrogen-silica distance can reach 8-9 \AA .

In accordance with experimental evidence, molecular dynamics preliminary results evidenced the tendency of the monopodal derivative (both mono- and di-dactyl adducts) to interact with the silica surface, with average distances in the range

of 4-4.5 Å. On the contrary, tripodal system has been observed the majority of the time in extended conformation.

7.2.3 Conclusions on silicopodality

The influence of silicopodality in the designing of organic-inorganic silica-based hybrid catalysts has been clarified by a detailed experimental characterization, with the support of molecular Dynamics calculations.

Experimental and computational results have evidenced a correlation between the number of legs and the tendency of the organic moieties to interact with the silica surface. Specifically, FT-IR and NMR data have revealed the presence of two different conformations of the organic molecules with respect to the silica surface for both Py-MP-MCM-41 and Py-TP-MCM-41 hybrids. In the tripodal hybrid, extended conformations were equally probable with respect to interacting ones, whereas in Py-MP-MCM-41 the majority of pyridine derivatives was found to be involved in interactions with Si-OH groups of the silica support and/or physisorbed water. Preliminary molecular dynamics simulations in vacuum results have predicted strong interaction between monopodal pyridine derivative and silica surface and the tendency of tripodal organosilane to stick out from the silica surface. This partial disagreement between computational and experimental data can be explained bearing in mind that MD simulations were performed on a plain silica surface, whereas the confinement effect typical of porous systems might determine an interaction between organic pendant groups and silanols located on the pore walls of MCM-41. Moreover, the few tripodal adducts with non-bonded legs, detected by ^{29}Si CPMAS NMR spectroscopy, possess a higher mobility compared to fully condensed ones, thus they might have more similar behaviour to monopodal derivatives. With the aim of confirming this hypothesis, further step of experimental work will be focused on the synthesis and characterization of the dipodal hybrid material. Moreover, computational simulations of mono- di- and tripodal hybrids will be

performed in various solvents, to evaluate the effect of solvation on the tendency of organic moieties to interact with the silica surface.

7.3 Notes and references

- [1] U. Díaz, A. Corma, *Chem. Eur. J.* **2018**, 24, 1.
- [2] S.H. Mir, L.A. Nagahara, T. Thundat, P. Mokarian-Tabari, H. Furukawa, A. Khosla, *J. Electrochem. Soc.* **2018**, 165, B3137.
- [3] A.P. Wight, M.E. Davis, *Chem. Rev.* **2002**, 102, 3589.
- [4] F. Hoffmann, M. Cornelius, J. Morell, M. Froba, *Angew. Chem. Int. Ed.* **2006**, 45, 3216.
- [5] G. Férey, *Chem. Soc. Rev.* **2008**, 37, 191.
- [6] C. Ivaldi, I. Miletto, G. Paul, G.B. Giovenzana, A. Fraccarollo, M. Cossi, L. Marchese, E. Gianotti, *Molecules* **2019**, 24,848.
- [7] X. Feng, G.E. Fryxell, L.-Q. Wang, A. Y. Kim, J. Liu, K.M. Kemner, *Science* **1997**, 276, 923.
- [8] Y. Mori, T.J. Pinnavaia, *Chem. Mater.* **2001**, 13, 2173.
- [9] E.V. Agina, A.S. Sizov, M.Y. Yablokov, O.V. Borschev, A.A. Bessonov, M.N. Kirikova, M.J.A. Bailey, S.A. Ponomarenko, *ACS Appl. Mater. Interfaces* **2015**, 7, 11755.
- [10] P. Ugliengo, M. Sodupe, F. Musso, I.J. Bush, R. Orlando, R. Dovesi, *Adv. Mater.* **2008**, 20, 4579.
- [11] *Materials Studio 6.0*, Accelrys Software Inc.: San Diego, CA, USA, **2011**.
- [12] A.K. Rappe, C.J. Casewit, K.S. Colwell, W.A. Goddard, W.M. Skiff, *J. Am. Chem. Soc.* **1992**, 114, 10024.
- [13] T. Schneider, E. Stoll, *Phys. Rev. B* **1978**, 17, 1302.
- [14] S. Plimpton *J. Comp. Phys.* **1995**, 117, 1.
- [15] D. Brunel, A. Cauvel, F. Di Renzo, F. Fajula, B. Fubini, B. Onida, E. Garrone, *New J. Chem.* **2000**, 24, 807.

- [16] J.S. Beck, J.C. Vartuli, W.J. Roth, M.E. Leonowicz, C.T. Kresge, K.D. Schmitt, C.T.W. Chu, D.H. Olson, E.W. Sheppard, S.B. McCullen, Y.B. Higgins, and I.L. Schelenker, *J. Am. Chem. Soc.* **1992**, 114,10834.
- [17] G. Paul, G.E. Musso, E. Bottinelli, M. Cossi, L. Marchese, G. Berlier, *ChemPhysChem.* **2017**, 18, 839.
- [18] D.W. Mayo, F.A. Miller, R.W. Hannah in *Course notes on the interpretation of IR and Raman spectra*. John Wiley & Sons Inc, Hoboken, NJ, **2004**, p. 33.
- [19] D. Margolese, J.A. Melero, S.C. Christiansen, B.F. Chmelka, G.D. Stucky, *Chem. Mater.* **2000**, 12, 2448.
- [20] S. Shylesh, S. Sharma, S.P. Mirajkar, A.P. Singh, *J. Mol. Catal. A: Chem.* **2004**, 212, 219.
- [21] E. Gianotti, U. Diaz, A. Velty, A. Corma, *Catal. Sci. Technol.* **2013**, 3, 2677.
- [22] E. Bayer, K. Albert, J. Reiners, M. Nieder, D. Müller, *J. Chromatogr.* **1983**, 264, 197.
- [23] N. García, E. Benito, J. Guzmán, P. Tiemblo, *J. Am. Chem. Soc.* **2007**, 129, 5052.
- [24] G. Paul, C. Bisio, I. Braschi, M. Cossi, G. Gatti, E. Gianotti, L. Marchese, *Chem. Soc Rev.* **2018**, 47, 5684.
- [25] H. Koller, M. Weiß, in *Solid State NMR*. Ed. J. C. C. Chan, Springer Berlin Heidelberg, Berlin, Heidelberg, **2011**, 306, p. 189.
- [26] G. Engelhardt, D. Michel, in *High-Resolution Solid State NMR of Silicates and Zeolites*. John Wiley & Sons Ltd., New York, **1987**, p. 1.
- [27] T. Borrego, M. Andrade, M.L. Pinto, A.R. Silva, A.P. Carvalho, J. Rocha, C. Freire, J. Pires, *J. Colloid Interface Sci.* **2010**, 344, 603.
- [28] G. Paul, S. Steuernagel, H. Koller, *Chem. Commun.* **2007**, 5194.
- [29] S. Bordiga, C. Lamberti, F. Bonino, A. Travert, F.T. Starzyk, *Chem. Soc. Rev.* **2015**, 44, 7262.
- [30] I. Miletto, G. Paul, S. Chapman, G. Gatti, L. Marchese, R. Raja, E. Gianotti, *Chem. Eur. J.* **2017**, 23, 9952.

-
- [31] I. Miletto, C. Ivaldi, G. Paul, S. Chapman, L. Marchese, R. Raja, E. Gianotti, *ChemistryOpen* **2018**, 7, 297.
- [32] D.J. Price, C.L. Brooks, *The Journal of Chemical Physics* **2004**, 121, 10096.
- [33] J-P. Ryckaert, G. Ciccotti, H.J. Brendsen, *Journal of Computational Physics* **1977**, 23, 327.
- [34] P. Koczoń, J. Piekut, M. Borawska, W. Lewandowski, *J. Mol. Struct.* **2003**, 651.
- [35] K. Badjor, P. Koczoń, E. Wieckowska, W. Lewandowski, *Int. Quant. Chem.* **1997**, 62, 385.
- [36] G. Versanyi in *Assignment for vibrational spectra of 700 benzene derivatives*, Akademiai Kiado, Budapest, **1973**.
- [37] G. Socrates in *Infrared and Raman Characteristic Group Frequencies: Tables and Charts*, John Wiley & Sons Ltd., New York, **2004**, p. 183.
- [38] J.M. Chalmers, P.R. Griffiths in *Handbook of vibrational spectroscopy: theory and instrumentations*, John Wiley & Sons Ltd., Chichester, **2002**, 1, p. 1825.
- [39] I. G. Shenderovich, G. Buntkowsky, A. Schreiber, E. Gedat, S. Sharif, J. Albrecht, N.S. Golubev, G.H. Findenegg, H.-H Limbach, *J. Phys. Chem. B* **2003**, 107, 11924.
- [40] A. A. Gurinov, Y. A. Rozhkova, A. Zikal, J. Čejka, and I.G. Shenderovich, *Langmuir* **2011**, 27, 12115.

8

Conclusion and perspectives

The main object of this Ph.D. thesis was the design of hierarchically-porous hybrid catalysts, which represent a prominent and new class of organic-inorganic hybrids to perform multi-step catalytic processes.

In this regard, a general introduction to Class II organic-inorganic hybrid materials has been given in *Chapter 1*, focusing in particular on advantages and drawbacks of the synthetic methods available for their preparation and describing in details the catalytic active sites associated with inorganic framework, which possess an active role in catalytical process or can influence the catalytic activity of the organic counterpart. Then, the potential of hierarchically-porous hybrid materials as heterogeneous catalysts to perform tandem and cascade reactions, due to their superior physico-chemical properties (high mechanical and thermal stability, enhanced molecular diffusion due to the presence of different porous architectures within a single framework, tunable porosity and acidic properties, possibility of speciation of the active sites within the hierarchical framework) has been deeply investigated. Moreover, the synthetic strategies which can be performed to obtain hierarchical zeotype materials have been discussed, together with the importance of establishing structure-property relationship in order to pave the way for further catalyst optimization and application-oriented design.

In *Chapter 2*, a general overview of the Ph.D. research work has been reported, as well as its location in the framework of the European Union's Horizon2020 funded MULTI2HYCAT (multi-site organic-inorganic hybrid catalysts for multi-step chemical processes) project.

In *Chapter 3*, a novel and low-cost bottom-up synthetic strategy for the preparation of hierarchical SAPO-34, using mono- and di- saccharides to direct the formation of the additional mesoporous network, has been explored. Physico-chemical and catalytic tests confirmed the successful preparation of hierarchical inorganic supports by using fructose and saccharose as mesoporogen, thus mitigating the need for sophisticated and expensive surfactants. Beside retention of structural, acidic and textural properties characteristic of the microporous CHA framework, assessed by means of X-ray powder diffraction, ^1H SS NMR coupled with FT-IR spectroscopy and volumetric analysis, both the saccharide-templated materials exhibited substantial enhancements in mesopore volume and mesopore surface area with respect to a microporous analogue. In addition, probe-based FT-IR spectroscopy evidenced that a fraction of the Brønsted acid centres had been made accessible by the hierarchical framework. On the basis of this promising characterization result, the catalytic activity of the SAPO-34 was evaluated in the liquid-phase Beckmann rearrangement of cyclohexanone oxime to ϵ -caprolactam (the industrially-significant precursor to Nylon-6), a BAS acid catalysed reaction carried out at low temperatures (130 °C) with respect to the vapour-phase Beckmann rearrangement (320°C). Notably, sucrose-templated hierarchical SAPO-34 exhibited very promising results, with a three-fold increase in conversion and yield with respect to the microporous analogue and the hierarchical sample obtained using glucose as mesoporogen. In contrast, fructose-templated sample revealed inferior catalytic performances with respect to the saccharide-templated SAPO-34 catalysts, probably as a result of an impeded diffusion within its mesoporous network. The selectivity of all the hierarchical saccharide-templated catalysts was found to be comparable with the microporous analogue, thus stressing that the microporous textural features, as well as the Brønsted acidity, had been retained in the hierarchical materials.

In *Chapter 4*, a distinctive bottom-up soft-templating synthetic strategy for the preparation of a hierarchical SAPO-34 (HP-SAPO-34), using cetyl

trimethylammonium bromide (CTAB) encapsulated within an ordered mesoporous silica (MCM-41) as both the silicon source as mesopore directing agent and mitigating the need for sophisticated and specifically-synthesised organosilanes, has been described. The as-obtained hierarchical material exhibited superior textural properties with respect to microporous analogue, with simultaneous retention of structural, textural and acidic properties of the microporous CHA framework. FT-IR of adsorbed alkyipyridine evidenced that the introduction of additional mesoporous network had greatly enhanced the accessibility of the acid active site. Furthermore, HP-SAPO-34 showed noteworthy catalytic activity in the vapour-phase Beckmann rearrangement of cyclohexanone oxime to ϵ -caprolactam with respect to both microporous SAPO-34 and MCM-41. In addition, the mediocre yield of caprolactam achieved using a physical mixture of mesoporous MCM-41 and microporous SAPO-34, stressed the importance of designing a single, harmonized hierarchical system which can host, contemporarily, both micro- and mesopores. Besides improving accessibility and ensuring retention of Brønsted acidity, this bottom-up synthetic strategy has proven to be a viable method to introduce defecting pendant silanols within hierarchical framework, which can be used to anchor tailored organic functionalities. Indeed, the number of Si–OH groups, obtained via ^1H SS NMR quantifications, was found to be higher with respect to the hierarchical SAPO-34 obtained using saccharides as mesopore directing agents. As a conclusion, this bottom-up synthetic strategy has proven to be effective in generating a hierarchical inorganic support, characterised by superior textural and acidic properties, which can be further employed to synthesise hierarchically porous hybrid materials.

In light of the promising results and conclusions exposed in Chapter 4, the synthetic strategy using CTAB encapsulated in mesoporous MCM-41 as both silicon source as mesopore directing agent, performed to obtain a hierarchical SAPO-34, was also adopted to synthesis a hierarchical SAPO-5 (HP-SAPO-5/MCM-41). In addition, a hierarchical SAPO-5 was also obtained using Pluronic-containing SBA-15 to serve as silicon source as mesopore directing agent (HP-SAPO-5/SBA-15). Both the

synthetic methodologies, described in *Chapter 5*, has proven to be effective means of introducing a secondary porosity within AFI structure, leading to a substantial enhancement in mesopore volume and mesopore surface areas, whilst retaining the acidic properties of the parent framework. With respect to HP-SAPO-5/MCM-41 catalyst, HP-SAPO-5/SBA-15 sample revealed the presence of mesopores of larger diameter and, notably, ^1H SS NMR evidenced a comparable number of Si–OH groups. In light of the foregoing, HP-SAPO-5/SBA-15 should be considered a useful inorganic support to anchor bulkier organic molecule, which may not be accommodated in the mesopores of HP-SAPO-5/MCM-41. Furthermore, an optimization of the mesopore dimensions and of the silicon loading was performed on CTAB-containing MCM-41 hierarchical SAPO-5 (HP-SAPO-5/x:1 and HP-SAPO-5/xSi). The modulation of mesopore diameter can be obtained by using suitable organic swelling agents (SA) to expand the surfactant micelles. Despite the pore size of MCM-41 had been progressively enlarged by increasing the SA/TEOS ratio of MCM-41 synthesis, the same trend was not observed for hierarchical SAPO-5. Upon the introduction of trimethylbenzene, an increase in the mesopore diameter from 30 to 40–50 Å was evidenced, but no modulation was achieved for HP-SAPO-5/6:1 with respect to HP-SAPO-5/1:1. Conversely, the optimization of the silicon (and mesopore) loading yielded more promising results. Noteworthy, by increasing the silicon loading, more silanol groups available to anchor organic functionalities on the inorganic support were produced at the expense of the number of Brønsted acid sites preferentially located on the mesopore surface rather than within microporous framework. Indeed, probe-based FT-IR spectroscopy evidenced a comparable density of BAS located in the micropores for HP-SAPO-5/xSi, regardless of the Si loading, and a higher accessibility factor of HP-SAPO-5/0.30Si with respect to HP-SAPO-5/0.6Si and HP-SAPO-5/0.9Si. Thus, a modulation of the density of Si–OH groups was successfully achieved without severely affecting the acidic properties of the microporous framework. Moreover, the speciation of the active sites within the two different level of porosity, combined with the enhanced

accessibility of the hierarchical architecture which can favour their cooperativity (confirmed by the catalytic test in the aldol condensation/crotonization reaction of FF with MIBK), made hierarchical SAPO-5 catalysts viable inorganic supports to synthesise organic-inorganic hybrids with application in tandem and/or cascade reactions.

In **Chapter 6** the heterogenization of a N-heterocyclic carbene (NHC) pre-catalyst on a range inorganic supports (Davisil silica, mesoporous MCM-41 and hierarchical SAPO-5 and ZSM-5) with varying textural, performed *via* grafting methodology, has been described. The as-obtained hybrid catalysts were deeply characterised using a multi-technique approach (XRD, volumetric and thermogravimetric analyses, SS NMR and FT-IR spectroscopies), with the aim of establishing preliminary structure-property relationship. Upon the same NHC precursor loading, all the silanol groups had been consumed in Davisil silica and hierarchical zeotype materials, whilst MCM-41 displayed a fraction Si–OH groups still available for grafting, opening the possibility for further loading optimization. NHC functionality covalently anchored on ordered porous materials was found to decompose at higher temperature with respect to Davisil silica, stressing the role of the confinement effect in enhancing its thermal stability. The detailed physico-chemical characterization provided confirmation of the retention of the structural, textural and acidic properties of the parent framework, as well as the successful anchoring of the NHC moieties. The catalytic activity of the organic-inorganic hybrid materials was then evaluated in the benzoin condensation reaction of furfural, a base-catalysed reaction. Despite all the hybrid catalysts had exhibited high conversion to the desired product, hierarchical hybrids, especially NHC-HP-SAPO-5, appeared to be more affect by recycling with respect to Davisil Silica and MCM-41. The reason of the inferior catalytic performance of NHC-HP-SAPO-5 was clarified by means of SS NMR and FT-IR spectroscopies, which had evidenced that, due to its small molecular diameter, the organic base (1,8-diazabicyclo[5.4.0]undec-7-ene, DBU) responsible for in situ deprotonation and activation of the N-heterocyclic carbene precursor, can also

interact with, deprotonate and deactivate the Brønsted acid sites located on the mesopore and within the microporous architecture, thus compromising the acid characteristics of the parent framework as well as its potential application in tandem reactions. With a view in exploiting the full potential of hierarchical supports, these drawbacks might be overcome by using a base with larger kinetic diameter, which cannot enter the micropore and deprotonate the BAS *ivi* located. Alternatively, hierarchical supports with smaller micropores, such as hierarchical SAPO-34, might be used to anchor NHC precursor and perform the benzoin condensation reaction. Overall, this example strongly evidenced the prominent role of the physico-chemical characterization in unravelling possible issues which can occur during the design of novel hybrid materials and in providing additional approaches to overcome these drawbacks. Apart from optimizing the NHC precursor loading, improving the recyclability of hierarchical hybrids whilst simultaneously retaining their strong acid properties, future perspectives will be focus on the selective grafting of the NHC-pre-catalyst on the external and internal surface of a ordered MCM-41 inorganic support, with the aim of investigating the nature of organic-inorganic interface and the confinement effects. The selective anchoring within the external surface can indeed be achieved by grafting the organic functionalities on a CTAB-containing MCM-41 and by subsequent extraction of the surfactant. Conversely, the selective grafting within the mesopore can be obtained by capping the external silanols with small silylating agents (i.e. trimethoxymethylsilane), followed by CTAB extraction and NHC precursor anchoring. Furthermore, catalytic data from benzoin condensation reaction seemed to evidence a role of silanol groups in favouring, in presence of oxygen, the oxidation of furoin to furyl, paving the way for performing tandem benzoin condensation-oxidation of furfural. In this perspective, research studies on the selective capping of groups on MCM-41 and periodic mesoporous organosilicas (PMOs) will be performed to evaluate the hydrophobic/hydrophilic character of the resulting hybrids and to clarify the role of Si–OH groups during the catalysis.

In *Chapter 7*, the influence of silicodactyly (*i.e.* the number of hydrolysable alkoxy groups which can be used by the organosilane to grab the inorganic surface) and silicopodality (*i.e.* number of alkyl chains through which the organosilane is anchored to the surface) in the design of a Class II hybrid material, based on strong covalent interactions between the organic and inorganic building blocks, has been deeply elucidated through a combined experimental and computational approach. This research work was carried out with a view in establishing the best grafting conditions and configurations to host organic moieties fully available for interactions with substrates, avoiding configurations which might favour the hampering of the catalytic activity as a result of the tendency of the organic functionality to lay on the inorganic support surface. Overall, the aim was to get a deeper insight into the nature of organic-inorganic interface in order to ultimately improve the catalytic performances. Concerning silicodactyly, experimental and computational data excluded a one to one correspondence between hydrolysable alkoxy moieties and the number of siloxane bridges is not guaranteed, especially for low silanol density inorganic supports, for which tridentate adducts are uncommon. As expected, the thermal stability of the hybrids was found to correlate with the number of siloxane bridges effectively formed, with mono-dentate adducts being decomposed at lower temperatures than di- and tri-dactyl systems. Nevertheless, as highlighted by molecular dynamics simulations, the organic-inorganic interface conformation was not much affected by the silicodactyly parameter. Indeed, regardless to the number of covalent bonds with the inorganic surface, the tendency of organosilane was to lay on the silica surface, with the largest contribution to the molecule-surface interaction energy coming from dispersion forces. Conversely, with regard to silicopodality, a correlation between the number of legs and the tendency of the organic moieties to lay on the silica surface was evidenced. Specifically, both computational and experimental results highlighted that, by increasing the podality from a monopodal to a tripodal system, fully extended conformations were favoured with respect to interactions with Si–OH groups of the inorganic support and/or

physisorbed water. To clarify the influence of solvation in determining the most probable conformations with respect to the inorganic surface, computational simulation will be performed in various solvents. Moreover, a dipodal system, which should conceptually have an intermediate behaviour, will be synthesised, anchored and the resulting hybrid materials will be deeply characterised. This research study strongly evidenced the potential of a combined experimental and computational approach in properly performing the design and optimization of a hybrid catalyst.

In conclusion, the physico-chemical approach to the design and multi-technique investigation of novel hybrid materials allows a fine tuning and optimization of both inorganic and organic moieties, ensuring the effective synergic effect. This research work contributed in the understanding of the key parameters underlying the design of efficient and robust hybrid catalysts.

9

Experimental section

Before undertaking volumetric and spectroscopic characterization, all the samples were outgassed at a temperature reported in the “Materials and Methods” section of the corresponding chapter, to remove physisorbed water.

Scanning electron microscopy (SEM) images at different magnifications were recorded on a Quanta 200 FEI Philips Scanning Electron Microscope equipped with an EDAX energy dispersive spectroscopy (EDS) attachment. The electron source was a tungsten filament operating at 25 keV. The samples were coated with a thin gold layer to ensure surface conductivity (Chapters 3 and 4).

X-ray powder diffraction (XRDP) patterns were recorded using an ARL XTRA48 diffractometer with $\text{Cu}_{\text{K}\alpha}$ radiation ($\lambda=1.54062 \text{ \AA}$). Diffractograms were recorded at room temperature (RT) in the high angles (5° - $50^\circ 2\theta$) and low angles (1° - $10^\circ 2\theta$) range with a rate of $1.0^\circ/\text{min}$. The X-ray profiles at low angles were collected with narrower slits (Chapters 3, 4, 5, 6, 7). The d spacing was calculated referring to the Bragg’s law: $n\lambda = 2d\sin\theta$, where $n=1$, λ is the $\text{Cu}_{\text{K}\alpha}$ radiation and θ was the half of the reflecting angle. The distance between two adjacent pores (a) was computed according to the equation $\sqrt{3}a = 2d$ (Chapter 5).

To perform **Inductively-coupled plasma (ICP) analyses**, samples were digested under acidic conditions before being aspirated into a Varian Vista MPX CCD simultaneous axial ICP-OES instrument (Chapters 3 and 4).

Elemental analysis was collected on Thermo Scientific Flash EA 1112 Series (CHNS), with sulfanilamide used as the standard for calibration purposes (Chapter 6).

N₂ and Ar physisorption analyses were carried out at 77 K in the relative pressure range from 1×10^{-6} to $1 P/P_0$ by using a Quantachrome AsiQ instrument. Prior to the analysis, the samples were outgassed overnight at the temperature reported in corresponding “Characterization” paragraph (residual pressure lower than 10^{-6} torr). Specific surface areas were determined using the Brunauer-Emmett-Teller (BET) equation, in the relative pressure range from 0.01 to 0.1 P/P_0 . The desorption branch of the N₂ physisorption isotherm was analysed by means of the non-local density functional theory (NLDFT) method, to obtain the pore size distribution of the materials (Chapters 3, 4, 5 and 6).

Thermogravimetric analyses (TGA) were carried out on a:

- SETSYS Evolution TGA-DTA/DSC thermobalance, under argon flow at a gas flow rate of 100 mL min^{-1} . The samples were heated from $40 \text{ }^\circ\text{C}$ to $1000 \text{ }^\circ\text{C}$ at a heating rate of $5 \text{ }^\circ\text{C min}^{-1}$ (Chapters 3).
- Mettler TGA/SDTA 851e instrument, under nitrogen flow, at a gas flow rate of 60 mL min^{-1} . The samples were heated from 30 to $1000 \text{ }^\circ\text{C}$ at a heating rate of $20 \text{ }^\circ\text{C min}^{-1}$ (Chapter 6).
- TA Q500 instrument, in nitrogen flow, at a gas flow rate of 60 mL min^{-1} . The samples were heated from $35 \text{ }^\circ\text{C}$ to $800 \text{ }^\circ\text{C}$ at a heating rate of $10 \text{ }^\circ\text{C min}^{-1}$ (Chapters 7).

FT-IR analyses of self-supporting pellets were performed under vacuum conditions (residual pressure $< 10^{-4}$ mbar) using a Bruker Equinox 55 spectrometer equipped with a pyroelectric detector (DTGS type) with a resolution of 4 cm^{-1} . FT-IR spectra were normalized with respect the pellet weight and, when even specified, are reported in difference-mode by subtracting the spectrum of the sample in vacuum from the spectrum of the adsorbed molecule (Chapters 3, 4, 5, 6 and 7).

Variable temperature FT-IR measurements were performed in the $30\text{-}500 \text{ }^\circ\text{C}$ temperature range, using a specifically designed cell permanently connected to the vacuum line (Chapters 6 and 7).

When probe molecules were employed, CO was adsorbed at 77 K, whereas NH₃, 2,4,6-trimethylpyridine (2,4,6-TMP, collidine) and 2,6-di-*tert*-butylpyridine (2,6-dTBP) were adsorbed at room temperature using specifically design cells permanently connected to a vacuum line to perform adsorption-desorption in situ measurements (Chapters 3, 4 and 5).

When basic probe molecules were adsorbed to perform accessibility studies, the total number of Brønsted acid sites was estimated using Lambert-Beer law in the form $A = \varepsilon N \rho$, where A is the integrated area of the bands of the protonated species ($\text{cm}^2 \mu\text{mol}^{-1}$), N is the concentration of the vibrating species ($\mu\text{mol g}^{-1}$) and ρ is the density of the disk (mass/area ratio of the pellet, mg cm^{-2}) (Chapters 3, 4 and 5).

The choice of the proper basic probe molecule used to assess the accessibility of acid sites in hierarchical samples (Chapter 3, 4 and 5) was performed according to the following arguments. Initially, to evaluate BAS accessibility in HP-SAPO-34/MCM-41 sample (Chapter 4), three different probe molecules of increasing kinetic diameter (pyridine (Py), 0.54 nm, 2,4,6-trimethylpyridine (2,4,6-TMP), 0.74 nm and 2,6-di-*tert*-butylpyridine (2,6-dTBP), 1.05 nm), unable to enter the micropores, were used and their adsorption compared to NH₃ adsorption, leading to a comparable accessibility factor for both 2,4,6-TMP and 2,6-dTBP (0.037 and 0.038, respectively) and to a higher AF for pyridine (0.107), due to its ability to interact with BAS located also on the micropores mouths. On the basis of this experimental evidence, pyridine was no longer employed and the accessibility of acid sites in hierarchical SAPO-34 catalysts synthesised using mono- and disaccharides as mesoporegen (Chapter 3) was estimated using 2,4,6-TMP. Since the micropore diameter of SAPO-5 (0.73 nm) is comparable to the kinetic diameter of 2,6-dTBP (0.74 nm), to assess the accessibility of acid sites of hierarchical SAPO-5 samples (Chapter 5), the more sterically hindered 2,6-dTBP was employed.

Liquid state ¹H and ¹³C NMR spectra were recorded with a

- Bruker DPX400 NMR operating at 9.39 T with frequencies for ¹H, and ¹³C of 400 MHz and 100.7 MHz, respectively (Chapter 6).

- with a Jeol Eclipse ECP300 spectrometer (Jeol Ltd. Tokyo, Japan) operating at 7.05 T with frequencies for ^1H , and ^{13}C of 300.5 MHz and 75.6 MHz, respectively (Chapter 7).

Chemical shifts are reported in ppm with the protic impurities of the deuterated solvent as internal reference.

Solid-state NMR spectra were acquired on a Bruker Avance III 500 spectrometer and a wide bore 11.7 Tesla magnet with operational frequencies for ^1H , ^{29}Si , ^{31}P , ^{27}Al and ^{13}C of 500.13, 99.35, 202.45, 130.33 and 125.77 MHz, respectively. A 4 mm triple resonance probe with magic angle spinning (MAS) was employed in all the experiments and the samples were packed on a Zirconia rotor and spun at a MAS rate between 10 and 15 kHz. The magnitude of radio frequency (RF) fields was 100, 83, and 42 kHz for ^1H , ^{31}P , and ^{29}Si , respectively. The ^{27}Al MAS spectra were acquired on large sweep width with small pulse angle ($\pi/12$) to ensure quantitative interpretation. In the case of ^{29}Si , ^{31}P , and ^{27}Al MAS NMR, high-power proton decoupling was applied. The relaxation delay, $d1$, between accumulations was 5, 1, 30, and 60 s for ^1H , ^{27}Al , ^{31}P , and ^{29}Si MAS NMR spectroscopy, respectively. For the ^{13}C and ^{29}Si Cross Polarization (CP) MAS experiments, the RF fields of 55 and 28 kHz were used for initial proton excitation and decoupling, respectively. During the CP period the ^1H RF field was ramped using 100 increments, whereas the $^{13}\text{C}/^{29}\text{Si}$ RF fields were maintained at a constant level. During the acquisition, the protons are decoupled from the carbons/silicons by using a two-pulse phase-modulated (TPPM) decoupling scheme. A moderate ramped RF field of 62 kHz was used for spin locking, while the carbon/silicon RF field was matched to obtain optimal signal and the CP contact time of 2 ms were used. All chemical shifts were reported by using the δ scale and are externally referenced to tetramethylsilane (TMS) for ^1H , ^{13}C and ^{29}Si NMR spectra, $\text{Al}(\text{H}_2\text{O})_6^{3+}$ ion in 1.0 M AlCl_3 solution for ^{27}Al NMR spectra and H_3PO_4 (85%) for ^{31}P NMR spectra. The chemical shifts reported for ^{27}Al are not corrected for second-order quadrupole

effects. ^1H MAS NMR spectra were fitted with DMFIT functions for quantitative deconvolution of overlapping peaks.

The choice of the **catalytic tests** was strictly correlated with the overall activities of the MULTI2HYCAT partners.

- The catalytic activity of saccharide-templated SAPO-34 samples (Chapter 3) and hierarchical SAPO-34 catalysts obtained using CTAB encapsulated in MCM-41 (Chapter 4) was assessed in the liquid-phase and vapour phase Beckmann rearrangement of cyclohexanone oxime to ϵ -caprolactam (the industrially-significant precursor to Nylon-6), respectively, in partnership with the University of Southampton, under the supervision of Prof. Robert Raja. The role of strong Brønsted acid sites and weak acid sites (*e.g.* Si–OH groups) and, eventually, their synergy has to be investigated to determine structure-property relationships and mechanistic insight. Specifically, whilst BAS plays a crucial role in the liquid-phase Beckmann rearrangement, nest silanols are effective active centres in the vapour-phase. Thus, the catalytic activity of the silanols rich HP-SAPO-34/MCM-41 was tested in the vapour-phase Beckmann rearrangement, whilst liquid phase should be preferred for silanols poor saccharide templated hierarchical SAPO-34.
- The catalytic activity of HP-SAPO-5/xSi materials (Chapter 5) was preliminary tested in the aldol condensation/crotonization of furfural with methyl isobutyl ketone, by the Eco-Efficient Products and Processes Laboratory (E2P2L), UMI 3464 CNRS-Solvay, under the supervision of Prof. M. Pera-Titus. Both furfural and 5-hydroxymethylfurfural, which can be accessed by the acid-catalysed dehydration of hexoses and pentoses, respectively, are considered as two of the most value-added biomass building blocks or platform chemicals. Both bio-based furanic derivatives can be further oxidized, hydrolysed or reduced to generate valuable downstream chemicals. In this perspective, considerable research has been carried out in the last year to develop simple, accessible and robust heterogeneous catalysts affording multi-step reactions and preventing the

separation of intermediates. Among the various heterogeneous catalyst that can be used, hierarchical silicoaluminophosphates, such as SAPO-5, represent a viable alternative to traditional catalysts for performing aldol condensation reactions, due to their superior diffusion within the framework and their acidic properties.

- The catalytic activity of N-heterocyclic carbene organocatalyst heterogenized on different inorganic support (commercial Davisil Silica, mesoporous MCM-41, hierarchical ZSM-5 and hierarchical SAPO-5 using Pluronic encapsulated in SBA-15 as mesopore) was tested in the benzoin condensation reaction of furfural in partnership with the University of Southampton, under the supervision of Prof. Robert Raja. Benzoin condensation is an effective strategy to convert biomass into useful chemicals for a range of applications, as already described in Chapter 6/Introduction.

List of Publications

1. **C. Ivaldi**, I. Miletto, G. Paul, G. B. Giovenzana, A. Fraccarollo, M. Cossi, L. Marchese, E. Gianotti, “Influence of silicopodality in the design of hybrid materials”. In preparation.
2. L. Gao, I. Miletto, **C. Ivaldi**, G. Paul, L. Marchese, S. Coluccia, F. Jiang, E. Gianotti, M. Pera-Titus, “Rational design of bifunctional hierarchical Pd/SAPO-5 for the synthesis of tetrahydrofuran derivatives from furfural”, submitted to *Journal of Catalysis*.
3. W. R. Webb, M. E. Potter, D. J. Stewart, S. J. Elliott, P. J. A Sazio, Z. Zhang, H-K. Luo, J. Teng, L. Zhang, **C. Ivaldi**, I. Miletto, E. Gianotti, R. Raja, “The significance of metal coordination in imidazole-functionalized metal organic frameworks for carbon dioxide utilization”, *Chem Eur. J.* **2020**, DOI: 10.1002/chem.202001561.
4. E. Gianotti, I. Miletto, **C. Ivaldi**, G. Paul, L. Marchese, M. Meazza, R. Rios, R. Raja, “Hybrid catalysts based on N-heterocyclic carbene anchored on hierarchical zeolites”, *RSC Adv.* **2019**, 9, 35336–35344, DOI: 10.139:C9RA07516J.
5. **C. Ivaldi**, I. Miletto, G. Paul, G. B. Giovenzana, M. Cossi, L. Marchese, E. Gianotti, “Influence of silicodactyly in the preparation of hybrid materials”, *Molecules* **2019**, 24, 848-863, DOI: 10.3390/molecules24050848.
6. I. Miletto, E. Catizzone, G. Bonura, **C. Ivaldi**, M. Migliori, E. Gianotti, L. Marchese, F. Frusteri, G. Giordano, “In-situ FT-IR characterization of CuZnZr/ferrierite hybrid catalysis for one pot CO₂-to-DME conversion, *Materials* **2018**, 11, 2275-2289, DOI:10.3390/ma11112275.
7. I. Miletto, **C. Ivaldi**, G. Paul, S. Chapman, L. Marchese, R. Raja, E. Gianotti, “Hierarchical SAPO-34 architectures with tailored acid sites using sustainable sugar templates”, *ChemistryOpen* **2018**, 7, 297-301, DOI: 10.1002/open.201800001.

Acknowledgements

Vorrei innanzitutto porgere i miei più sentiti ringraziamenti alla Prof. Enrica Gianotti, relatrice di questa tesi di Dottorato, per gli importanti insegnamenti che ha saputo e voluto trasmettermi nel corso di questi anni, per la disponibilità nel chiarire i miei dubbi, per il supporto e la fiducia dimostrata, grazie alla quale ho potuto maturare una buona autonomia di lavoro e di pensiero, nonchè per essere una costante fonte di ispirazione scientifica.

Ringrazio immensamente la Dr. Ivana Miletto, per me esempio di grande dedizione, impegno e passione per il proprio lavoro. Oltre ad esserle grata per avermi pazientemente insegnato i “trucchi del mestiere”, la ringrazio sia per il supporto fornitomi in campo scientifico e non, sia per i divertenti e piacevoli momenti trascorsi nel corso di questa esperienza.

I would like to thank Prof. Robert Raja, Prof. Ramon Rios and Dr. Marta Meazza for supervising me during the research period at the University of Southampton.

Ringrazio poi tutti i tesisti che hanno contribuito alla realizzazione di questo progetto.

Un ringraziamento sincero va infine a tutti i colleghi che hanno contribuito a rendere, ognuno a suo modo, questa esperienza più divertente e formativa, sia dal punto di vista umano che scientifico.



UNIVERSITÀ DEL PIEMONTE ORIENTALE

DOTTORATO DI RICERCA
IN CHEMISTRY & BIOLOGY

Via Duomo, 6
13100 – Vercelli (ITALY)

DECLARATION AND AUTHORISATION TO ANTIPLAGIARISM DETECTION

The undersigned **CHIARA IVALDI** student of the Chemistry & Biology Ph.D.
course (**XXXIII – 33°** Cycle)

Declares:

- to be aware that the University has adopted a web-based service to detect plagiarism through a software system called “Turnit.in”,
- his/her Ph.D. thesis was submitted to Turnit.in scan and reasonably it resulted an original document, which correctly cites the literature;

Acknowledges:

- his/her Ph.D. thesis can be verified by his/her Ph.D. tutor and/or Ph.D. Coordinator in order to confirm its originality.

Date: **15/11/2020**

Signature:

